

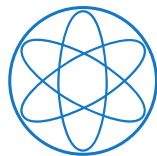


Fakultät für Physik der Technische Universität München

Max-Planck-Institut für Physik
(Werner-Heisenberg-Institut)

Limitations of Rare Event HPGe Experiments due to Muon-Induced Neutron Background

Laura Vanhoefer



Dissertation
München
2018



Fakultät für Physik der Technische Universität München

Max-Planck-Institut für Physik
(Werner-Heisenberg-Institut)

Limitations of Rare Event HPGe Experiments due to Muon-Induced Neutron Background

Laura Vanhoefer

Vollständiger Abdruck der von der Fakultät für Physik der Technische Universität
München zur Erlangung des akademischen Grades

Doktors der Naturwissenschaften (Dr.rer.nat.)

genehmigten Dissertation.

Vorsitzende/-r:

Prüfende/-r der Dissertation:

1. Priv.-Doz. Dr. Béla Majorovits
- 2.
- 3.

Die Dissertation wurde am _____ bei der Technischen Universität München
eingereicht und durch die Fakultät für Physik am _____ angenommen.

Abstract

Experiments searching for neutrinoless double beta ($0\nu\beta\beta$) decay which could occur if neutrinos are Majorana particles require very low background due to the very long expected half-life. The GERDA experiment uses germanium detectors operated in liquid argon to search for $0\nu\beta\beta$ decay of ^{76}Ge . Since the signature is a peak at the Q-value of 2039 keV, any energy deposition around the Q-value is potential background. Neutrons can produce such background due to the production of long-lived radioisotopes which are hard to veto. Long-lived isotopes can be produced either during processing of the detector materials above ground or by muon-induced neutrons below ground.

Monte Carlo simulations of the propagation of cosmic-ray neutrons and the production of muon-induced neutrons for different commonly used shielding materials were performed. They were used to estimate the total neutron flux and spectra for different shielding configurations.

Muon-induced neutron production rates, especially for high-Z materials, are not well understood. The MINIDEX experiment located at the Tübingen Shallow Underground Laboratory aims to investigate the muon-induced neutron production rates for high-Z materials. The muon flux inside the laboratory was simulated which was used as input for Monte Carlo simulations of the expected muon-induced neutron production rates in MINIDEX.

While muon-induced radionuclides are not the dominant background for current experiments searching for $0\nu\beta\beta$ decay, this kind of background becomes more relevant for future experiments like LEGEND. A relevant background contribution in the region of interest is expected from beta decay of $^{77(m)}\text{Ge}$ which can be produced by capture of muon-induced neutrons on ^{76}Ge . The predicted production rates of $^{77(m)}\text{Ge}$ in GERDA from different Monte Carlo simulations differ by a factor of two.

GERDA data were analyzed to search for signatures of the $^{77(m)}\text{Ge}$ and $^{75(m)}\text{Ge}$ production. No signal was found. Upper limits on the production rates of 4.1 nuclei/(kg yr) (90% CI) for $^{77(m)}\text{Ge}$ and of 0.63 nuclei/(kg yr) (90% CI) for $^{75(m)}\text{Ge}$ were set. Using this result an upper limit on the expected background due to the decay of $^{77(m)}\text{Ge}$ can be extracted. After applying analysis cuts, the upper limit is $\text{BI} < 6.4 \cdot 10^{-5}$ cts/(keV kg yr) and $\text{BI} < 4.7 \cdot 10^{-5}$ cts/(keV kg yr) for coaxial detectors and BEGe detectors, respectively. Limits on the integrated neutron flux around the GERDA detector array were derived to be $\Phi_n < 36$ n/(m² h).

The set limits are 1 – 2 orders of magnitude larger than the ones expected from simulations. LEGEND-200 will have the capability to determine the $^{77(m)}\text{Ge}$ and $^{75(m)}\text{Ge}$ production rates as well as the BI from $^{77(m)}\text{Ge}$ beta decay. This will allow to verify that this background component will not deteriorate the sensitivity of future tonne-scale experiments.

Zusammenfassung

Experimente, die nach dem neutrinolosen Doppel-Beta-Zerfall ($0\nu\beta\beta$) suchen, der auftreten kann, wenn Neutrinos Majorana-Teilchen sind, benötigen auf Grund der sehr langen erwarteten Halbwertszeit einen sehr geringen Untergrund. Das GERDA-Experiment verwendet Germaniumdetektoren, die in flüssigem Argon (LAr) betrieben werden, um nach dem $0\nu\beta\beta$ -Zerfall von ^{76}Ge zu suchen. Da die gesuchte Signatur ein Peak im Energiespektrum beim Q-Wert von 2039 keV ist, stellt jede Energiedeposition um diesen Q-Wert potenziell Untergrund dar. Neutronen können solchen Untergrund erzeugen, indem sie langlebige, radioaktive Kerne erzeugen. Diese lassen sich nur schwer mit Vetos reduzieren. Langlebige Isotope können entweder oberirdisch beim Prozessieren der Detektormaterialien oder unterirdisch durch Myon-induzierte Neutronen entstehen.

Monte-Carlo-Simulationen der Propagation von Neutronen der kosmischen Strahlung sowie von Myon-induzierten Neutronen wurden für verschiedene Abschirmmaterialien durchgeführt, um den gesamten Neutronenfluss sowie die Spektren für verschiedene Abschirmkonfigurationen zu bestimmen.

Myon-induzierte Neutronproduktionsraten sind insbesondere für Materialien mit hohem Z-Wert nicht gut verstanden. Das MINIDEX-Experiment, das sich im Tübinger Untergrundlabor befindet, hat zum Ziel, die Myon-induzierten Neutronproduktionsraten für Materialien mit hoher Massenzahl zu bestimmen. Der Myonenfluss, der als Input für die Simulation der erwarteten Neutronenrate in MINIDEX dient, wurde mit Monte-Carlo-Simulationen bestimmt.

Während für aktuelle Experimente, die nach dem $0\nu\beta\beta$ -Zerfall suchen, diese Art von Untergrund nur eine untergeordnete Rolle spielt, wird er für künftige Experimente wie LEGEND von größerer Bedeutung sein. Ein relevanter Beitrag wird vom Beta-Zerfall von $^{77(m)}\text{Ge}$, das durch Neutroneneinfang an ^{76}Ge entsteht, erwartet. Die simulierten $^{77(m)}\text{Ge}$ -Produktionsraten für GERDA unterscheiden sich für verschiedene Simulationen um den Faktor zwei.

GERDA-Daten wurden analysiert, um nach Signaturen von $^{77(m)}\text{Ge}$ und $^{75(m)}\text{Ge}$ zu suchen. Es wurde kein Signal gefunden. Die gesetzten oberen Limits für die Produktionsraten sind 4,1 Kerne/(kg yr) (90% CI) für $^{77(m)}\text{Ge}$ und 0,63 Kerne/(kg yr) (90% CI) für $^{75(m)}\text{Ge}$. Aus dem $^{77(m)}\text{Ge}$ -Limit konnte eine obere Grenze auf den erwarteten Untergrund von $^{77(m)}\text{Ge}$ -Zerfällen gesetzt werden. Nach dem Anwenden aller Cuts beträgt diese $\text{BI} < 6,4 \cdot 10^{-5} \text{ cts}/(\text{keV kg yr})$ für Koaxial-Detektoren und $\text{BI} < 4,7 \cdot 10^{-5} \text{ cts}/(\text{keV kg yr})$ für BEGe-Detektoren. Es konnte auch ein oberes Limit auf den integrierten Neutronenfluss von $\Phi_n < 36 \text{ n}/(\text{m}^2 \text{ h})$ gesetzt werden.

Die gesetzten Limits sind 1 – 2 Größenordnungen größer als die Erwartungen von Monte-Carlo-Simulationen. Mit LEGEND-200 wird es möglich sein, die Produktionsraten von $^{77(m)}\text{Ge}$ und $^{75(m)}\text{Ge}$ sowie den Untergrundbeitrag von $^{77(m)}\text{Ge}$ -Zerfällen zu bestimmen. Dies würde es ermöglichen zu überprüfen, ob die Sensitivität eines künftigen Tonnen-Experiments von dieser Untergrundkomponente beeinträchtigt werden wird.

Table of Contents

1	Introduction	3
2	Neutrinos and Neutrinoless Double Beta Decay	7
2.1	Neutrinos	8
2.2	Neutrinoless Double Beta Decay	10
2.3	Searching for Neutrinoless Double Beta Decay	13
3	Cosmic Rays and Cosmic-Ray-Induced Background	17
3.1	Cosmic-Rays	17
3.1.1	Primary Cosmic Rays	17
3.1.2	Secondary Cosmic Rays	19
3.2	Attenuation of Muons in Matter	22
3.2.1	Neutron Interactions	25
3.3	Cosmic-Ray-Induced Background	25
3.3.1	Background Reduction	26
3.3.2	Simulation of Cosmic-Ray-Induced Background	27
3.3.3	Neutron Flux and Radio-Nuclei Production in GERDA	28
4	Cosmic-Ray Shielding Simulations with GEANT4	29
4.1	Backscattering Effect	31
4.2	Cosmic-Ray Neutron Simulations	33
4.3	Muon Simulations	39
4.4	Muon-Induced Neutrons	43
4.5	Total Neutron Flux	47
5	The MINIDEX Experiment	53
5.1	Principle and Setup	53
5.2	Run Configurations	55
5.3	Analysis and Background	56
5.4	Cosmic-Ray Simulations	56
5.5	Comparison with Muon-Map Measurements	68
5.6	Discussion	70

6	The GERDA Experiment	71
6.1	Set-Up	71
6.2	Analysis Results	74
6.2.1	Analysis Cuts	74
6.2.2	Pulse Shape Discrimination	75
6.2.3	Half-Life of Double Beta Decay	77
6.2.4	Half-Life of Neutrinoless Double Beta Decay	77
6.3	Background in GERDA	79
6.4	Next Generation of ^{76}Ge Experiments	81
7	Muon-Induced Radionuclide Search in GERDA	83
7.1	Signatures	84
7.2	Monte Carlo Simulations	89
8	GERDA Muon-Induced Radionuclide Search Results	97
8.1	Datasets and Data Selection	99
8.2	Signal and Background Extraction	104
8.3	Efficiencies and Expectation	111
8.4	Results	114
9	Conclusion and Outlook	121
A	Used Physics Models and Cross Sections	125
B	Material Compositions of Simulated Materials	127
C	Number of Simulated Neutrons	129
D	Shielding Index s of Cosmic-Ray Neutrons	131
E	Maximum Muon-Induced Neutron Flux Depths	135
F	Attenuation Index s of Muon-induced Neutrons	137
G	Depth of Equality of the Neutron Fluxes	139
H	Total Neutron Capture Detection Efficiencies	143
I	Likelihood of the Radionuclide Search	149
J	GERDA Energy Reconstruction Efficiencies	153
K	Data Set Detector Configurations	171

Chapter 1

Introduction

Since the postulation of neutrinos in 1930 and their discovery in 1956, a lot has been learned about their properties. In the Standard Model of particle physics, neutrinos are only weakly interacting and are considered to be massless. It is nowadays well established that neutrinos are mixing among their flavor eigenstates. Since this mixing is only possible if neutrinos are not massless, this means physics beyond the Standard Model. Most of the mixing parameters have already been measured but not the CP violating phase(s). The absolute values of the neutrino masses have not been measured yet since the mixing depends only on the mass differences (see chapter 2). Also the nature of neutrinos is still an open question: since neutrinos are electrically neutral particles, there exists another solution apart from the standard solution for the Dirac equation which was found by Ettore Majorana in 1937 [1]. If neutrinos are Majorana particles, they would be their own antiparticles.

To answer the question about the nature of neutrinos, one can search for the neutrinoless double beta ($0\nu\beta\beta$) decay (see chapter 2). This decay could only occur if neutrinos are indeed Majorana particles [2]. One of the experiments searching for the $0\nu\beta\beta$ decay is the GERDA experiment which is described in chapter 6.

The signature of $0\nu\beta\beta$ decay is a peak at the end-point $Q_{\beta\beta}$ of the double-beta ($2\nu\beta\beta$) decay energy spectrum. Since the expected signal rates are very low due to the expected very long half-lives for the $0\nu\beta\beta$ decay, the background rate must be as low as possible.

Cosmic-rays can create background by activating the material. If the created radionuclides decay with a Q-value above or around $Q_{\beta\beta}$, these nuclei can create background events. If the half-life is long, these kind of events are hard to veto and are therefore dangerous background. To suppress the cosmic-induced background, the experiments are running in deep underground laboratories which most of the cosmic rays do not reach. Only muons and neutrinos can penetrate and reach the experiments.

Muons can not only deposit energy around $Q_{\beta\beta}$ inside the detector or produce radionuclides, but they can also induce neutrons. These neutrons can also produce further

radionuclides. Energy depositions by muons and short-lived radionuclides can be vetoed by identifying muon events. If the half-lives are longer than a few ms, these events are hard to veto. If the muon-induced neutron rate or the nuclei production rate are known, this background component can be estimated. So far, the muon-induced background component for the GERDA experiment has only been determined by Monte Carlo simulations [3] [4]. It was found that the beta decay of ^{77}Ge and its meta-stable state ^{77m}Ge contribute mostly to the muon-induced background [3].

So far, the muon-induced background was not the dominant remaining background after applying all vetoes and cuts. Since the background has to be further reduced for a tonne-scale experiment, this kind of background may be a limiting factor. This has to be investigated before building the experiment. If this kind of background becomes a limiting factor, a different location or set-up with a lower neutron flux has to be chosen. Also the reliability of simulations needs to be improved.

The aim of this thesis is to investigate the muon-induced radionuclide production in GERDA—especially for $^{77(m)}\text{Ge}$ production. For known radionuclide production rates, the expected background in the region of interest (ROI) as well as the integrated neutron flux can be calculated. Also the reliability of the simulations can be tested by comparing the measured values with the values from Monte Carlo simulations. This is important for estimating the expected background of a future tonne-scale experiment such as LEG-END.

From neutron yield measurements it is known that there are discrepancies between data and Monte Carlo simulations (see chapter 3). Especially for heavy elements like lead which is often used as shielding material, the muon-induced neutron rate is not well understood. Measurements of processes that allow to extract information on the in-situ neutron flux are therefore of great importance.

The MINIDEX experiment aims to investigate the muon-induced neutron rates for different materials at shallow depths [5]. In order to investigate the quality of Monte Carlo simulations, the MINIDEX measurements have to be compared with Monte Carlo simulations. For these simulations the muon flux inside the shallow underground laboratory has to be known. Monte Carlo simulations were conducted to obtain this flux (see chapter 5).

Radio-active nuclei can also be produced during times above ground when the material is not shielded by the overburden of the underground laboratory. To reduce the number of produced radio-nuclei, times above ground have to be as short as possible and the material must be shielded against neutrons from cosmic rays [6]. The reduction of the integrated neutron flux depends on the shielding material and its thickness. Muons which penetrate the shielding material induce neutrons and hence increase the neutron flux first. Only for certain depths more neutrons are shielded than produced depending on the material. This has to be considered for planning a shielding for the detector components. Monte Carlo simulations were conducted to investigate the neutron flux behavior for often used

shielding materials for different shielding depths (see chapter 4).

The structure of this thesis is the following: First, the neutrino properties and the neutrinoless double beta decay are introduced in chapter 2. In chapter 3, cosmic rays and the interactions of muons and neutrons with matter are introduced. Also the cosmic-ray induced background is discussed. Chapter 4 and chapter 5 present the shielding and MINIDEX simulations. In chapter 6, the GERDA experiment and its background components are described. The signatures for the muon-induced radionuclide search are described in chapter 7 as well as the conducted Monte Carlo simulations. Radionuclides produced by neutron capture on the two most abundant germanium isotopes ^{76}Ge and ^{74}Ge as well as neutron capture on ^{40}Ar were investigated. The results of the muon-induced radionuclide search are presented in chapter 8.

Chapter 2

Neutrinos and Neutrinoless Double Beta Decay

In the Standard Model of particle physics, neutrinos are only weakly interacting particles which are considered to be massless. Neutrinos were suggested by Wolfgang Pauli in 1930 to explain the continuous energy spectrum of the beta decay:

$$(Z, A) \longrightarrow (Z + 1, A) + e^- + \bar{\nu}_e. \quad (2.1)$$

Before this suggestion it was assumed that during beta decay only one electron is emitted which would lead to a mono-energetic peak (since only the electron could get the released energy). This was contradicted by measurements of the electron energy spectrum from beta decays which showed that this energy spectrum is continuous. Without a second particle this would mean that energy and momentum would not be conserved.

Not until more than twenty years later, the neutrino was first detected by Clyde L. Cowan and Frederick Reines in 1956. They used the inverse beta decay

$$\bar{\nu}_e + p \longrightarrow n + e^+ \quad (2.2)$$

to detect electron antineutrinos $\bar{\nu}_e$ from a reactor of the Savannah River Plant. [7]

Few years later, the muon neutrino which is produced during muon decay

$$\mu^- \longrightarrow e^- + \nu_\mu + \bar{\nu}_e \quad (2.3)$$

$$\mu^+ \longrightarrow e^+ + \bar{\nu}_\mu + \nu_e \quad (2.4)$$

was discovered by investigating accelerator neutrinos from pion decays

$$\pi^- \longrightarrow \mu^- + \nu_\mu \quad (2.5)$$

$$\pi^+ \longrightarrow \mu^+ + \bar{\nu}_\mu \quad (2.6)$$

at Brookhaven [8]. After the discovery of the tau lepton in the 1970s [9], the tau neutrino ν_τ was postulated which should be produced during tau decay. At the beginning of the 21st century the tau neutrino was discovered by the DONUT experiment with a neutrino beam at Fermilab [10].

The neutrino properties will be discussed in section 2.1. One open question is the nature of neutrinos. To answer this question one can search for the neutrinoless double beta ($0\nu\beta\beta$) decay. If neutrinos are their own antiparticles (Majorana particles), it is possible that during a double beta ($2\nu\beta\beta$) decay no neutrinos—just electrons—are emitted. The $0\nu\beta\beta$ decay will be discussed in section 2.2 and how to search for the $0\nu\beta\beta$ decay will be discussed in the last section.

2.1 Neutrinos

In the Standard Model (SM) of particle physics, it was first assumed that neutrinos are massless. On the effective electron anti-neutrino mass $m_{\bar{\nu}_e}$, only upper limits have been set so far by analyzing the electron energy spectrum of beta decays. The maximum energy which the electron can have depends on the neutrino mass, since the released energy—the so-called Q-value of the beta decay—is split between the electron and the neutrino which are released during the decay. Upper limits from tritium decay experiments are

$$m_{\bar{\nu}_e} \leq 2.3 \text{ eV at } 95\% \text{ C.L.} \quad (2.7)$$

by the Mainz experiment [11] and

$$m_{\bar{\nu}_e} < 2.05 \text{ eV at } 95\% \text{ C.L.} \quad (2.8)$$

by the Troitsk experiment [12].

After it had been discovered that neutrinos oscillate, the neutrinos could not longer be considered to be massless. The SM had to be expanded, since neutrino oscillations require differences of the neutrino mass eigenstates. Solar neutrino experiments like the Homestake experiment [13] had measured a neutrino flux much lower than the neutrino flux predicted by the standard solar model (SSM) [14]. This reduced flux could be explained if electron neutrinos produced in the Sun would be transformed to ν_μ and ν_τ . The experiments using chloride or gallium could only measure the ν_e flux via the inverse beta decay

$$\nu_e + (Z, A) \longrightarrow (Z + 1, A) + e^-. \quad (2.9)$$

At the beginning of the 21st century, the transformation of solar ν_e to ν_μ and ν_τ could be shown by the water Cherenkov experiment SNO¹ [15]. SNO used ultra-pure heavy water D₂O to detect the neutrinos via the charge current (CC), neutral current (NC) and the elastic scattering (ES) reactions:

$$\nu_e + d \longrightarrow p + p + e^- \quad (\text{CC}), \quad (2.10)$$

$$\nu_x + d \longrightarrow p + n + \nu_x \quad (\text{NC}), \quad (2.11)$$

$$\nu_x + e^- \longrightarrow \nu_x + e^- \quad (\text{ES}). \quad (2.12)$$

The electron neutrino flux was much lower than expected from SSM calculations, but the total neutrino flux measured via the NC reaction, which is equally sensitive to all three neutrino flavors ν_e , ν_μ and ν_τ , was consistent with the SSM calculations. This shows that ν_e had been transformed into ν_μ and ν_τ . [15]

Neutrino-antineutrino oscillations were suggested by B. Pontecorvo in the 1950's [16]. Z. Maki, M. Nakagawa and S. Sakata proposed that the flavor eigenstates of neutrinos are linear combinations of the neutrino mass eigenstates which would lead to neutrino mixing [17]. Neutrino oscillation data collected so far can be described by 3-flavor neutrino mixing [18]. The flavor eigenstates $|\nu_\alpha\rangle$ ($\alpha = e, \mu, \tau$) are connected to the three mass eigenstates $|\nu_i\rangle$ ($i = 1, 2, 3$) via the so-called Pontecorvo-Maki-Nakagawa-Sakata (PMNS) neutrino mixing matrix U :

$$|\nu_\alpha\rangle = \sum_j U_{\alpha j} |\nu_j\rangle. \quad (2.13)$$

The mixing matrix U is a 3×3 matrix in case of three neutrino flavors and three massive neutrinos and depends on three mixing angles (θ_{12} , θ_{23} , θ_{13}), one Dirac CP violating phase δ and—if neutrinos are Majorana particles—two Majorana phases (α_{21} , α_{31}):

$$U = \begin{pmatrix} c_{12}c_{13} & s_{12}c_{13} & s_{13}e^{-i\delta} \\ -s_{12}c_{23} - c_{12}s_{23}s_{13}e^{i\delta} & c_{12}c_{23} - s_{12}s_{23}s_{13}e^{i\delta} & s_{23}c_{13} \\ s_{12}s_{23} - c_{12}c_{23}s_{13}e^{i\delta} & -c_{12}s_{23} - s_{12}c_{23}s_{13}e^{i\delta} & c_{23}c_{13} \end{pmatrix} \cdot \begin{pmatrix} 1 & 0 & 0 \\ 0 & e^{i\frac{\alpha_{21}}{2}} & 0 \\ 0 & 0 & e^{i\frac{\alpha_{31}}{2}} \end{pmatrix} \quad (2.14)$$

with $c_{ij} = \cos \theta_{ij}$ and $s_{ij} = \sin \theta_{ij}$.

In 1937, Ettore Majorana published in [1] another possible solution for the Dirac equation [19]. This solution allows electrically neutral particles like the neutrino to be their own antiparticles and there would be no lepton number conservation. If neutrinos are Dirac particles, the neutrino mixing matrix U would just depend on one CP violating phase and not on three CP violating phases.

If neutrinos are Majorana particles, the smallness of neutrino masses could be explained by the seesaw mechanism. In addition to the Dirac mass term by the Higgs

¹SNO: Sudbury Neutrino Observatory

mechanism, a right-handed Majorana mass term is introduced. This would imply an effective Majorana mass term for left-handed flavor neutrinos. [20]

The generation of the baryon asymmetry of the Universe could be explained via the leptogenesis mechanism [21]. At high temperatures, the right handed neutrino could decay via

$$N_R \longrightarrow l_L + \bar{\phi} \quad (2.15)$$

or

$$N_R \longrightarrow \bar{l}_L + \phi \quad (2.16)$$

with ϕ being the standard Higgs doublet. The branching ratios of reaction 2.15 and reaction 2.16 differ if CP is violated due to one-loop radiative corrections by a Higgs particle. [21]

This scenario requires a Majorana mass term. So far, the nature of the neutrino—Dirac or Majorana—is unknown. With neutrino oscillation experiments neither the nature of neutrinos nor the absolute neutrino masses can be determined. Only the mixing angles, the Dirac CP violating phase and the mass square differences Δm_{21}^2 , Δm_{31}^2 and Δm_{32}^2 with

$$\Delta m_{ij}^2 = m_i^2 - m_j^2 \quad (2.17)$$

can be determined via neutrino oscillations. So far, only the sign of Δm_{21}^2 (see [18]) could be determined. Therefore the ordering of the neutrino masses is unknown and two possibilities exist:

$$m_1 < m_2 < m_3 \quad (\text{normal}), \quad (2.18)$$

$$m_3 < m_1 < m_2 \quad (\text{inverted}). \quad (2.19)$$

The nature of neutrinos, the absolute mass scale and the mass ordering can be investigated by searching for neutrinoless double beta ($0\nu\beta\beta$) decay which is discussed in the next section.

2.2 Neutrinoless Double Beta Decay

Neutrinoless double beta ($0\nu\beta\beta$) decay

$$(Z, A) \longrightarrow (Z + 2, A) + 2e^- \quad (2.20)$$

was suggested by Wendell Furry in 1939 [22]. This decay could only occur if neutrinos are their own antiparticles (Majorana particles) according to the Schechter-Valle theorem. Then the two neutrinos could be exchanged during double beta decay. The neutrino-accompanied double beta ($2\nu\beta\beta$) decay

$$(Z, A) \longrightarrow (Z + 2, A) + 2e^- + 2\bar{\nu}_e \quad (2.21)$$

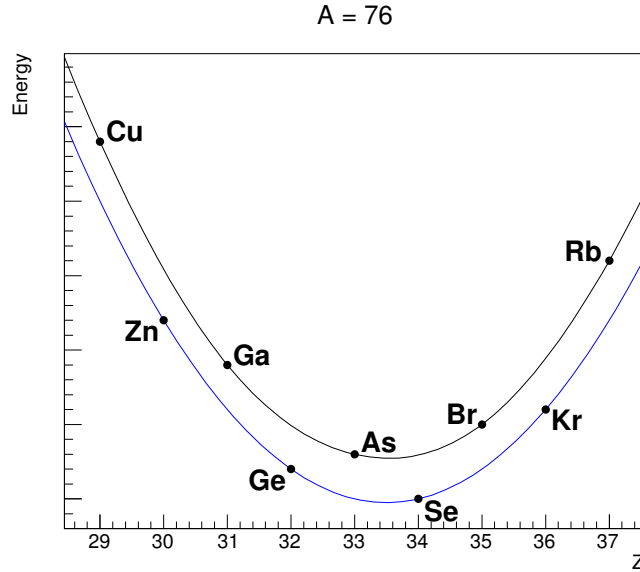


Figure 2.1: Mass parabola for nuclei with the atomic mass number $A=76$. Nuclei with even numbers of protons Z and even numbers of neutrons N lie on the lower parabola. Nuclei with odd Z and odd N lie on the upper parabola.

was suggested in 1935 by Maria Goeppert-Mayer [23]. Beta decay takes place due to the weak interaction and can only occur if the energy of the daughter nucleus is smaller than the energy of the mother nucleus. During beta decay one neutron is transformed to a proton

$$\beta^- : (Z, A) \longrightarrow (Z + 1, A) + e^- + \bar{\nu}_e \quad (2.22)$$

or a proton is transformed to a neutron

$$\beta^+ : (Z, A) \longrightarrow (Z - 1, A) + e^+ + \nu_e. \quad (2.23)$$

Therefore the number of nucleons and the atomic mass number A are conserved. Due to beta decay the binding energy of the nucleus is reduced.

The binding energies of nuclei with fixed A lie on two smooth curves depending on the atomic number Z (see Fig. 2.1): Nuclei with even numbers of protons and neutrons lie on the lower curve, nuclei with odd numbers of protons and neutrons lie on the upper curve. Both curves have a parabolic shape. A nucleus which does not have the lowest possible binding energy is unstable and is decaying until the minimum binding energy is reached. If the binding energy of the next atomic number Z is higher, the nucleus cannot undergo beta decay—even if the nucleus has not yet reached the minimum binding energy. For these nuclei Maria Goeppert-Mayer suggested that $2\nu\beta\beta$ decays could take place at the same time and her calculations showed that this would be a rare process with half-lives longer than 10^{17} years [23]. In 1950, the first observation of a $2\nu\beta\beta$ was published by a

Table 2.1: Half-lives of the $2\nu\beta\beta$ decay $T_{1/2}^{2\nu}$ for different isotopes at 90% C.L.

Experiment	Isotope	$T_{1/2}^{2\nu}$ [yr]
NEMO-3 [26]	^{48}Ca	$[6.4_{-0.6}^{+0.7}(\text{stat.})_{-0.9}^{+1.2}(\text{syst.})] \times 10^{19}$
GERDA [27]	^{76}Ge	$(1.84_{-0.10}^{+0.14}) \times 10^{21}$
NEMO-3 [28]	^{82}Se	$[9.6 \pm 0.3(\text{stat.}) \pm 1.0(\text{syst.})] \times 10^{19}$
NEMO-3 [29]	^{96}Zr	$[2.35 \pm 0.14(\text{stat.}) \pm 0.16(\text{syst.})] \times 10^{19}$
NEMO-3 [28]	^{100}Mo	$[7.11 \pm 0.02(\text{stat.}) \pm 0.54(\text{syst.})] \times 10^{18}$
NEMO-3 [30]	^{116}Cd	$[2.74 \pm 0.04(\text{stat.}) \pm 0.18(\text{syst.})] \times 10^{19}$
CUORE-0 [31]	^{130}Te	$[8.2 \pm 0.2(\text{stat.}) \pm 0.6(\text{syst.})] \times 10^{20}$
EXO-200 [32]	^{136}Xe	$[2.165 \pm 0.016(\text{stat.}) \pm 0.059(\text{syst.})] \times 10^{21}$
NEMO-3 [33]	^{150}Nd	$[9.34 \pm 0.22(\text{stat.})_{-0.60}^{+0.62}(\text{syst.})] \times 10^{18}$

geo-chemical experiment using ^{130}Te [24]. So far, 35 possible candidates undergoing $2\nu\beta\beta$ decay have been identified [25]. For some of these isotopes, the $2\nu\beta\beta$ decay has been observed (see Table 2.1).

The $0\nu\beta\beta$ decay could only occur if neutrinos are their own antiparticles. Thus, observation of the $0\nu\beta\beta$ decay would imply the existence of a Majorana mass term [2]. This makes it possible to investigate the nature of neutrinos by searching for the $0\nu\beta\beta$ decay.

Since the decay rate due to the exchange of a light neutrino

$$\Gamma^{0\nu} = |m_{\beta\beta}|^2 |M^{0\nu}|^2 G^{0\nu}(Q, Z) \quad (2.24)$$

depends not only on the phase-space factor $G^{0\nu}$ and the nuclear matrix element $M^{0\nu}$, but also on the effective Majorana mass term

$$m_{\beta\beta} = \sum_i U_{ei}^2 \cdot m_i = c_{12}^2 c_{13}^2 \cdot m_1 + s_{12}^2 c_{13}^2 e^{i\alpha_{21}} \cdot m_2 + s_{13}^2 e^{i(\alpha_{31}-2\delta)} \cdot m_3, \quad (2.25)$$

also the absolute neutrino mass scale and the mass ordering can be investigated. From Eq. 2.25 one can see that the effective Majorana mass depends on the neutrino masses, the mixing angles and all three CP violating phases of the neutrino mixing matrix. One can also see from Eq. 2.25 that $0\nu\beta\beta$ decay requires that at least one neutrino mass is not zero. This is known to be true due to neutrino oscillation experiments (see section 2.1).

In Fig. 2.2, the effective Majorana mass $|m_{\beta\beta}|$ as function of the smallest neutrino mass m_{min} is shown. The neutrino oscillation parameters were taken from a global fit [34] and the two CP violating phases α_{21} and α_{31} were varied in the whole allowed range. It can be seen from Fig. 2.2 that the value of $|m_{\beta\beta}|$ depends on the mass hierarchy: the normal

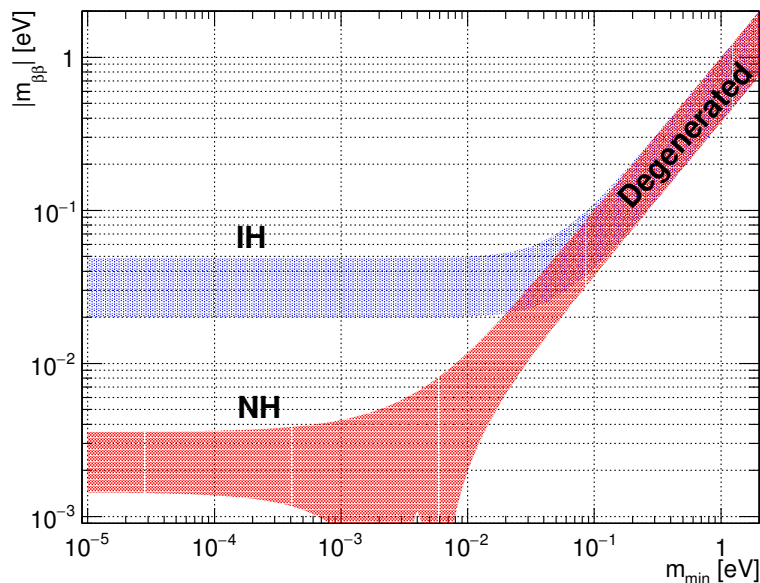


Figure 2.2: The effective majorana mass $|m_{\beta\beta}|$ as function of the smallest neutrino mass m_{min} for the normal (NH) and the inverted (IH) mass hierarchy. Values for the neutrino oscillation parameters were taken from the global fit of [34]. The two CP violating phases α_{21} and α_{31} were varied in the interval $[0, 2\pi]$.

mass hierarchy (NH), the inverted mass hierarchy (IH) and the degenerate mass hierarchy ($m_1 \simeq m_2 \simeq m_3$).

The largest uncertainties in calculating $|m_{\beta\beta}|$ from an observed decay rate arise from uncertainties of the nuclear matrix element $M^{0\nu}$. Complicated nuclear many-body problems must be solved for which no exact analytical solutions exist. The calculations of different models deliver values for $M^{0\nu}$ which deviate up to a factor of three. Since $M^{0\nu}$ depends on the decaying isotope, it is not straight forward to compare the results of experiments using different isotopes. [20]

2.3 Searching for Neutrinoless Double Beta Decay

To search for the $0\nu\beta\beta$ decay, one needs an isotope as source which can undergo $2\nu\beta\beta$ decay. There are 35 known candidates for observing $2\nu\beta\beta$ decay; for 10 nuclei $2\nu\beta\beta$ decay could already be observed: ^{48}Ca , ^{76}Ge , ^{82}Se , ^{96}Zr , ^{100}Mo , ^{116}Cd , ^{128}Te , ^{130}Te , ^{150}Nd and ^{238}U [25]. Some of them which are often used for $0\nu\beta\beta$ decay experiments are shown in Table 2.2. During $0\nu\beta\beta$ decay only two electrons are released. Their summed energy together with the recoil energy of the nucleus is equal to the Q-value of the decay (the energy difference between the mother and daughter nucleus).

The sensitivity on the half-life $T_{\frac{1}{2}}^{0\nu}$ of a $0\nu\beta\beta$ decay experiment depends on the detection efficiency ϵ , the mass of the $\beta\beta$ isotope M , the measuring time t , the energy resolution

Table 2.2: Isotopes undergoing $2\nu\beta\beta$ decay which are often used in $0\nu\beta\beta$ decay experiments. The values of the natural abundance are taken from [35].

Isotope	Q-value [keV]	Natural Abundance [%]
^{48}Ca	4267.98(32) [36]	0.187
^{76}Ge	2039.006(59) [37]	7.44
^{82}Se	2997.9(3) [38]	8.73
^{96}Zr	3355.85(15) [39]	2.80
^{100}Mo	3034.40(17) [40]	9.63
^{116}Cd	2813.50(13) [41]	7.49
^{130}Te	2526.97(23) [41]	33.80
^{136}Xe	2457.83(37) [42]	8.9
^{150}Nd	3371.38(20) [43]	5.64

ΔE and the background rate B :

$$S^{0\nu} \propto \epsilon \sqrt{\frac{Mt}{B\Delta E}} \quad [44]. \quad (2.26)$$

From Eq. 2.26 one can see that the sensitivity depends linearly on the detection efficiency. Therefore the detection efficiency should be as high as possible. The sensitivity increases with the square root of the mass and the measuring time. The measuring time is typically fixed for only some years. However, the mass could be increased to further increase the sensitivity. One can also see from Eq. 2.26 that the sensitivity increases for a better energy resolution and that the background should be as low as possible.

Equation 2.26 is only valid in the presence of background. As long as the background rate in the energy region of interest is so low that during measurement time t zero background events are expected, the sensitivity depends linearly on the mass and the measuring time

$$S^{0\nu} \propto \epsilon Mt \quad (2.27)$$

and does no longer depend on the energy resolution and the background rate [44].

The sensitivity is also influenced by the choice of isotope, since the phase-space factor $G^{0\nu}$ (and therefore also the decay probability) is proportional to the Q-value:

$$G^{0\nu} \propto Q^5 \quad [44]. \quad (2.28)$$

For higher Q-values, the decay probability is increasing.

The background rate increases with increasing detector mass including also non $2\nu\beta\beta$ undergoing isotopes. The sensitivity on the other hand increases only with the square root of the mass. Therefore the isotope abundance should be as high as possible. This

Table 2.3: Limits on the half-lives of the $0\nu\beta\beta$ decay $T_{1/2}^{0\nu}$ for different isotopes and the effective Majorana mass $m_{\beta\beta}$ at 90%C.L.

Experiment	Isotope	$T_{1/2}^{0\nu}$ [yr]	$m_{\beta\beta}$ [meV]
ELEGANT VI [50]	^{48}Ca	$> 5.8 \times 10^{22}$	$< 3500 - 22000$
GERDA [46]	^{76}Ge	$> 5.3 \times 10^{25}$	$< 150 - 330$
NEMO-3 [28]	^{82}Se	$> 1.0 \times 10^{23}$	$< 1700 - 4900$
NEMO-3 [29]	^{96}Zr	$> 9.2 \times 10^{21}$	$< 7200 - 19500$
NEMO-3 [51]	^{100}Mo	$> 1.1 \times 10^{24}$	$< 330 - 620$
NEMO-3 [30]	^{116}Cd	$> 1.0 \times 10^{23}$	$< 1400 - 2500$
CUORE-0 + Cuoricino [47]	^{130}Te	$> 4.0 \times 10^{24}$	$< 270 - 760$
EXO-200 + KamLAND-Zen [48]	^{136}Xe	$> 3.4 \times 10^{25}$	$< 120 - 250$
NEMO-3 [33]	^{150}Nd	$> 2.0 \times 10^{22}$	$< 1600 - 5300$

can be achieved by choosing an isotope with a high natural abundance or by choosing an isotope which can be easily enriched.

There are two approaches for $0\nu\beta\beta$ decay experiments: the detector can be made of the $2\nu\beta\beta$ -decay undergoing isotope or source and detector can be separated. The last option opens the possibility to use isotopes considered unsuitable for detector construction. It is also possible to investigate many different isotopes at the same time.

The NEMO collaboration uses the latter approach. The NEMO sources are thin foils made of $2\nu\beta\beta$ decaying isotopes. The NEMO 3 detector consists of a tracking and a calorimeter part which allows to reconstruct the full event topology. In $0\nu\beta\beta$ decay, the released energy which is equal to the mass difference of the mother and the daughter nuclei is divided between the two emitted electrons. In the NEMO 3 experiment, the energies of both electrons as well as their summed energy can be reconstructed. The drawback of this approach is the low detection efficiency² and a high energy resolution of (14.1 – 17.7)% FWHM. [28] [33]

If source and detector are identical, the detection efficiency is usually much higher: the detection efficiency of the EXO-200 experiment which uses liquefied xenon as a time projection chamber is 71% [45]. Also the energy resolution can be much better. For germanium detectors and TeO_2 bolometers, energy resolutions of (2.6 – 4.4) keV FWHM at 2.6 MeV [46] and (5.1 ± 0.3) keV FWHM [47] can be reached respectively. There is also the possibility to load a liquid scintillator with a $2\nu\beta\beta$ isotope which is done by KamLAND-Zen [48] and SNO+ [49]. With the loaded liquid scintillator approach, huge source masses can be obtained. However, the obtained energy resolution is relatively poor leading to a good limit setting sensitivity but a low sensitivity for a discovery.

Table 2.3 shows the results of some $0\nu\beta\beta$ decay experiments. So far, no $0\nu\beta\beta$ decay has

²detection efficiency of 3.87% for ^{150}Nd [33] and of $(1.8 \pm 0.1)\%$ for ^{116}Cd [30]

been observed. There had been a claim from part of the Heidelberg-Moscow collaboration to have seen the $0\nu\beta\beta$ decay of ^{76}Ge with $T_{1/2}^{0\nu} = (2.23_{-0.31}^{+0.44}) \times 10^{25}$ yr [52]. This claim has already been excluded by other experiments like the KamLAND-Zen experiment at more than 97.5% C.L. [48]. Since KamLAND-Zen is using ^{136}Xe and not ^{76}Ge , this comparison depends on the matrix element calculations. For proving or disproving the Heidelberg-Moscow claim, it is therefore an advantage to also use ^{76}Ge . Then, the comparison of the half-lives does not depend on the matrix element calculations; the results are directly comparable.

^{76}Ge does not have the highest Q-value or the highest natural abundance, but one can build detectors which are enriched in ^{76}Ge with $\sim 86\%$. Germanium is a semiconductor and detectors made from germanium diodes have a very good energy resolution. The GERDA experiment is using this approach. The data of Phase I have already strongly disfavored the claim of the Heidelberg-Moscow experiment with a Bayes factor of 2×10^{-4} [53].

Chapter 3

Cosmic Rays and Cosmic-Ray-Induced Background

Particles and nuclei produced outside the solar system as well as particles from solar flares reach Earth's atmosphere and produce further particles while interacting with the nuclei of the atmosphere (see section 3.1). Among particles reaching the ground, muons and neutrinos are the only particles which penetrate deeply and can reach deep underground laboratories. There they can create background events. Especially muons can induce further particles (like neutrons) which can produce background events.

Section 3.1 is about the composition of cosmic rays and their origin. In sections 3.2, interactions of muons and neutrons with matter are described. In section 3.3 the background induced by cosmic rays is discussed with a focus on the GERDA experiment.

3.1 Cosmic-Rays

3.1.1 Primary Cosmic Rays

Primary cosmic rays consist of electrons, protons, helium and other nuclei synthesized in stars like carbon, oxygen and iron. Most of the primary nucleons are free protons (79%), about 70% of the rest are nucleons bound in helium nuclei. [18]

Primary cosmic rays are accelerated at astrophysical sources. For high energetic Galactic cosmic rays supernova remnants are the most plausible source [54]. There, the particles are accelerated in supernova remnant shock fronts created in explosion of a massive star. However, charged particles can only be accelerated up to a maximum energy.

The main part of cosmic rays originates from within our Galaxy. The ultra-high-energy cosmic rays may also have an extragalactic origin. So far, their origin as well as the acceleration mechanism to the high energy is not well understood [54].

Cosmic rays mainly consist of charged particles [54]. Since charged particles are affected by the turbulent magnetic field in the Galaxy, the directional information gets lost

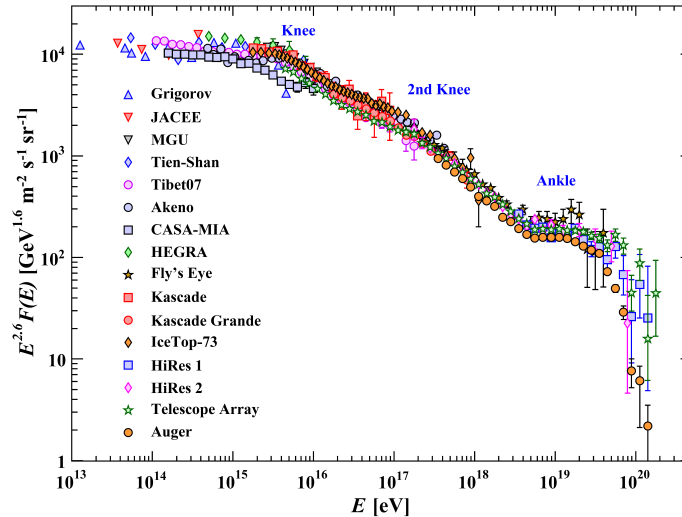


Figure 3.1: The all-particle spectrum as a function of E (energy-per-nucleus) from air shower measurements. [18]

and they become nearly isotropically distributed. This makes it hard to find the source positions and therefore hides the hints on possible acceleration mechanisms.

The cosmic-ray particles are not only affected by the Galactic magnetic fields but also by interactions with the interstellar medium in which secondaries can be produced. During these interactions also spallation processes can take place in which other nuclei are created. Therefore particles lose energy while propagating through the Galaxy. The ratio of secondary to primary nuclei is observed to decrease with increasing energy and mean free paths decrease with energy [18].

The majority of cosmic rays comes from outside the solar system. Due to a magnetized wind from the Sun, which decelerates the incoming charged particles, the low-energy particles do not reach the inner solar system. For cosmic rays with energies below 10 GeV an anticorrelation between intensity and solar activity is observed. The intensity is alternating in an eleven-year cycle [18].

Propagation of charged low-energy cosmic rays is influenced by the geomagnetic field. Therefore the intensity of cosmic-ray components depends on the location on Earth.

Figure 3.1 shows the flux of all particles from air shower measurements. Individual parts of the spectrum can be described by a power law E^{-x} . At $3 \cdot 10^{15}$ eV the spectral slope of the differential flux changes from ~ 2.7 to ~ 3.1 [54]. This steepening is called "knee". Around $10^{18.5}$ eV another feature called "ankle" is visible [18]. The ankle may be the result of the extragalactic flux dominating over the galactic flux [18] [55]. The knee could be the result of most cosmic accelerators in the Galaxy having reached their maximum energy [18].

3.1.2 Secondary Cosmic Rays

Secondary cosmic rays are produced in the atmosphere by interactions of primary cosmic rays with the air. If the energy of cosmic rays is high enough, the created air shower can be detected on ground as well. The shower consist of a hadronic core with electromagnetic sub-showers mostly originating from π^0 decays

$$\pi^0 \longrightarrow \gamma\gamma. \quad (3.1)$$

Electromagnetic showers consist of positrons and electrons which are the most numerous particles in the shower [18]. The showers are electron-rich for heavy chemical compositions and electron-poor for a light chemical composition [54].

Charged mesons are created in the atmosphere as well. By their decay chains muons and neutrinos are produced high in the atmosphere (at ~ 15 km). Neutrinos are mainly produced by π^\pm decays with a ratio of

$$\nu_e : \nu_\mu : \nu_\tau = 1 : 2 : 0 \quad (3.2)$$

but since neutrinos oscillate, the number of arriving ν_e and ν_μ is similar. [18]

Due to an excess of protons to neutrons in the primary spectrum, the fraction of π^+ and K^+ is higher than the fraction of π^- and K^- [18]. Therefore also more μ^+ than μ^- are produced. The muon charge ratio is $\mu^+/\mu^- \sim 1.25$ [56] and increases with muon energy. Muons lose typically ~ 2 GeV before they reach the ground where the mean muon energy is ~ 4 GeV [18].

Low-energetic muons can decay and produce the main part of low-energy electrons at sea-level. Also photons, protons, neutrons and charged pions reach sea-level. The relative ratio of the secondaries charged pions : protons : electrons : neutrons : muons is about 1 : 13 : 340 : 480 : 1420 [57]. From that it follows that $\sim 63\%$ of all these particles are muons and $\sim 21\%$ are neutrons. Thus, the ratio between neutrons and muons at sea-level is 1:3.

Figure 3.2 shows the muon energy spectrum which was measured at two different locations by [58] and [59]. The shapes of both measured energy spectra are the same. The angular distribution follows a $\cos(\theta)^2$ distribution [18].

Figure 3.3 shows the measured neutron energy spectrum measured by [60] on ground. In contrast to the muon angular distribution, the angular distributions of neutrons on ground is not precisely known. For high-energetic cosmic-ray neutrons ($E \geq 10$ MeV) reaching the ground, A. Nesterenok [61] suggested following distribution

$$J(\theta) = J_0 \exp[\alpha(1 - \cos \theta)] \quad (3.3)$$

with $\alpha = -2.5$, the flux in the vertical direction J_0 and the nadir angle θ . This angular

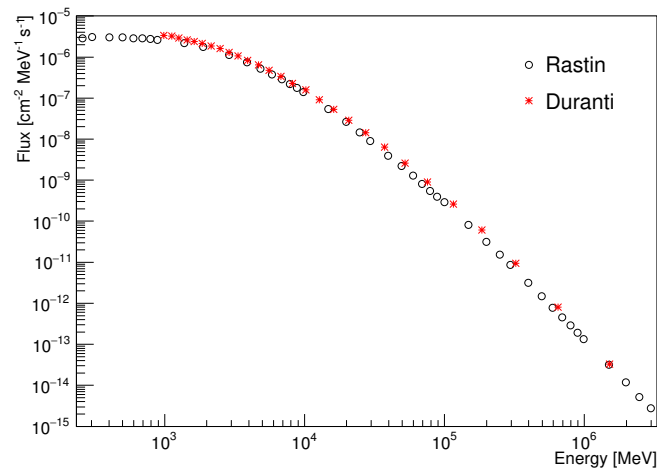


Figure 3.2: Measured energy spectra on ground. Data points are taken from [58] and [59].

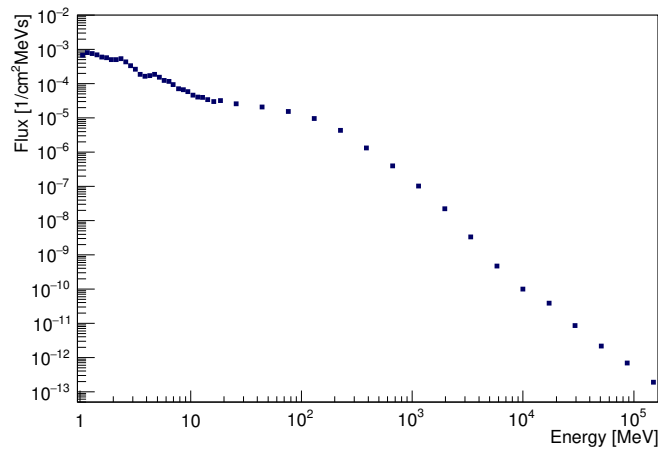


Figure 3.3: Measured neutron energy spectrum on ground. Data points are taken from [60].

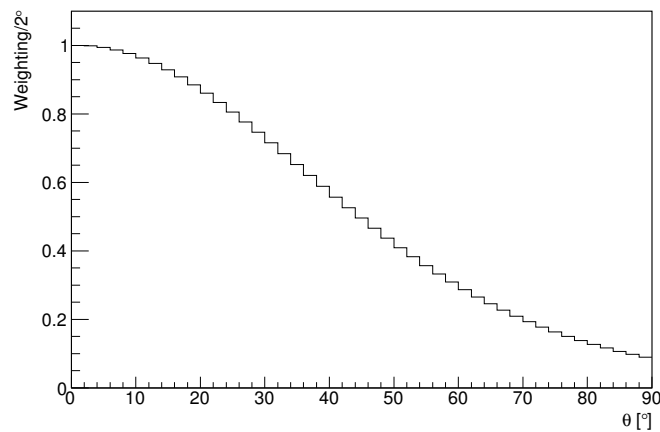


Figure 3.4: Angular distribution of the nadir angle for high-energy neutrons ($E \geq 10$ MeV) on ground suggested by [61].

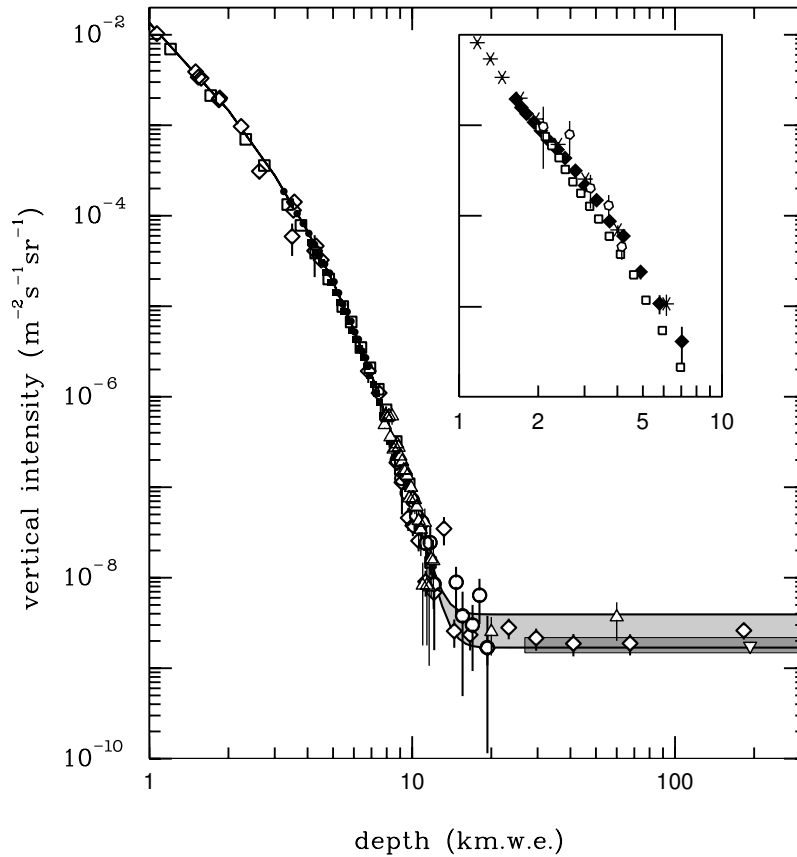


Figure 3.5: Vertical muon intensity vs depth. [18]

distribution is shown in Fig. 3.4.

Cosmic rays induce too much background in low-rate experiments (like experiments searching for $0\nu\beta\beta$ decay) at sea-level. Therefore these experiments usually are built in deep underground laboratories.

Through interactions with matter during penetration of the overburden, muons lose energy by ionization and radiative processes (see next section) and produce tertiary fluxes of photons, electrons and hadrons [18]. With increasing depth the muon flux is decreasing while their mean energy is increasing. Muons can be also produced by charge-current interactions of ν_μ

$$\nu_\mu + e^- \longrightarrow \mu^- + \nu_e. \quad (3.4)$$

Since neutrinos are only weakly interacting, nearly all of them are traversing the whole Earth. Neutrino-induced muons can thus enter the laboratory also from below and not only from above. Thus, the muon flux is not changing anymore at very large depths (see Fig. 3.5).

3.2 Attenuation of Muons in Matter

When muons propagate through matter they interact with the nuclei and lose energy by ionization and radiative processes. The most important among these are bremsstrahlung, direct e^+e^- pair production, μ -nuclear and photonuclear interactions. Interactions of either muons or of muon-induced particles with nuclei can lead to muon spallation. This can produce further hadrons. The remaining nucleus can be highly excited and is often unstable. The nuclear remnants can afterwards emit evaporation nucleons which are often in the MeV range [62]. The number of emitted evaporation neutrons is increasing with higher atomic number and higher neutron content [62].

Also the muon-induced particles can interact with further nuclei while propagating through matter. A hadronic cascade is developed which can include not only neutrons and protons but also pions and other hadrons. Also electromagnetic showers can develop via photo production and π^0 decay. Latter showers consist mostly of photons [63] but also of electrons and positrons. Most neutrons are not created by muon-spallation reactions but by muon-initiated hadronic and electromagnetic cascades [64]. With decreasing muon energy the neutron yield decreases. At low energies the neutron production is dominated by real photonuclear interactions in electromagnetic cascades while for increasing muon energy the production in hadronic cascades becomes more important [64]. The neutron production cross-section is very large for high-energy muons propagating through high-A materials [65].

Neutrons from muon spallation and other relativistic particles move in forward direction of the shower and are concentrated along the shower core while evaporation neutrons and moderated neutrons are predominantly isotropically distributed and spread out.

The muon-induced cascade needs a certain length within a material to develop and to reach equilibrium depending on the penetrated material. In equilibrium, the energy spectra as well as shower composition are not changing anymore. Only the number of particles is decreasing.

The shielding depth is often expressed in term of meter water equivalent (mwe). It is a standard measure for the cosmic-ray attenuation where the depth is expressed in terms of an equivalent water shielding thickness for which cosmic rays would have the same attenuation. It is calculated by multiplying the depth with the material density of the overburden.

After equilibrium is reached, the decreasing flux with increasing shielding depth can be described by a power law [66]:

$$y = 10^{sx+a} \quad (3.5)$$

with the shielding depth x , the flux $y(x)$, the shielding index s and a fit constant a .

For large depths h in the range of (1 – 10) kilometer water equivalent (km.w.e), the differential muon intensity

(in $\text{m}^{-2} \text{s}^{-1} \text{sr}^{-1}$) can be expressed by

$$I(h) = I_1 \cdot e^{-\frac{h}{\lambda_1}} + I_2 \cdot e^{-\frac{h}{\lambda_2}} \quad (3.6)$$

with the parameters $I_1 = (8.60 \pm 0.53) \cdot 10^{-6} \text{ cm}^{-2} \text{ s}^{-1} \text{ sr}^{-1}$, $\lambda_1 = (0.45 \pm 0.01) \text{ km.w.e}$, $I_2 = (0.44 \pm 0.06) \cdot 10^{-6} \text{ cm}^{-2} \text{ s}^{-1} \text{ sr}^{-1}$ and $\lambda_2 = (0.87 \pm 0.02) \text{ km.w.e}$ with an overall accuracy of $\sim 5\%$ [67]. The differential muon intensity for different shielding depths is shown in Fig. 3.6. For a flat overburden with a vertical depth h_0 in km.w.e, the muon rate (in $\text{cm}^{-2} \text{s}^{-1}$) is

$$I_\mu(h_0) = 67.97 \cdot 10^{-6} \cdot e^{-\frac{h_0}{0.285}} + 2.071 \cdot 10^{-6} \cdot e^{-\frac{h_0}{0.698}} \quad [67]. \quad (3.7)$$

The muon energy spectrum is shown in Fig. 3.8 and can be described by

$$\frac{dN}{dE_\mu} = A \cdot e^{-bh(\gamma_\mu-1)} \cdot [E_\mu + \epsilon_\mu \cdot (1 - e^{-bh})]^{-\gamma_\mu} \quad (3.8)$$

and the average muon energy (see Fig 3.7) with

$$\langle E_\mu \rangle = \frac{\epsilon_\mu \cdot (1 - e^{-bh})}{\gamma_\mu - 2} \quad (3.9)$$

with the parameters $b = 0.4 \text{ km.w.e}^{-1}$, $\gamma_\mu = 3.77$ and $\epsilon_\mu = 693 \text{ GeV}$ [67].

Muons are decelerated by the interactions and are eventually stopped if they do not decay beforehand. Muons at rest decay purely leptonically

$$\mu^- \longrightarrow e^- + \nu_\mu + \bar{\nu}_e \quad (3.10)$$

$$\mu^+ \longrightarrow e^+ + \bar{\nu}_\mu + \nu_e \quad (3.11)$$

or are being captured by a nucleus (only for μ^-). If a negative muon gets captured, a muonic atom is created and energy is released which is transferred to Auger electrons (electrons which are emitted from the atom). The captured muons have different lifetimes depending on the element on which they were captured [68]. If the 1s state of the muonic atom is reached, the muon decays or is captured on a bound proton

$$\mu^- + p \longrightarrow n + \nu_\mu. \quad (3.12)$$

Except very light nuclei, muon capture is more likely than muon decay [68]. The capture probability increases strongly with Z [57]. After muon capture the nucleus is excited and often one or more neutrons are emitted. At shallow depths, stopped negative muons often dominate the nucleonic production [57]. For large depths, the ratio of stopping muons to through-going muons is less than 0.5% and therefore negligible [67].

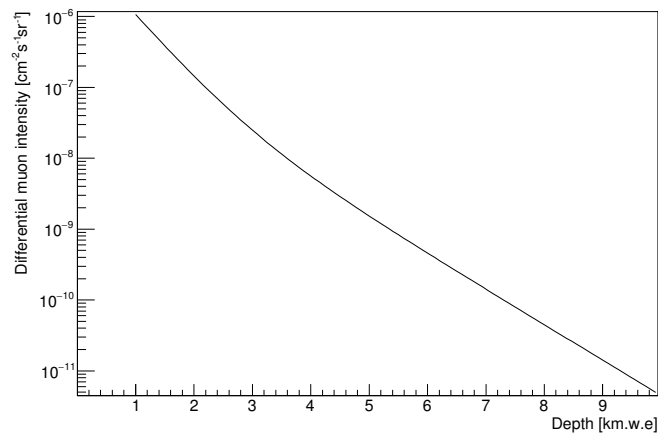


Figure 3.6: Differential muon intensity for different depths using the parameterization of [67].

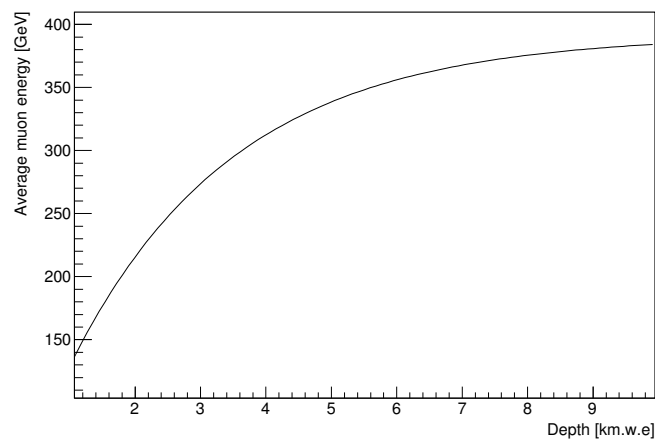


Figure 3.7: Average muon energy spectrum for different depths using the parameterization of [67].

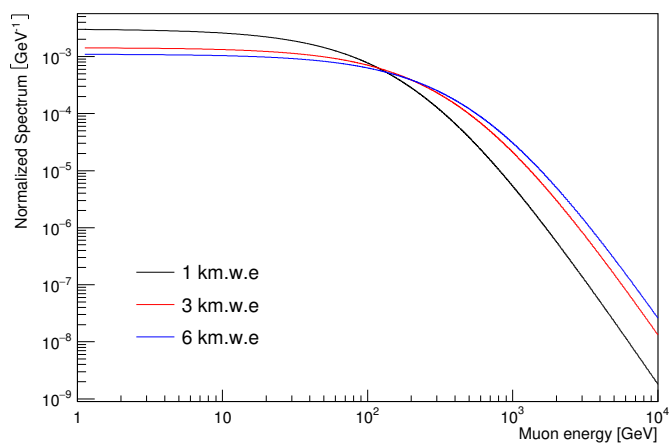


Figure 3.8: Muon energy spectrum for different depths using the parameterization of [67].

3.2.1 Neutron Interactions

The created neutrons in the shower interact with other nuclei with elastic and inelastic scattering and get moderated. In inelastic reactions further neutrons and radio-nuclei are produced. If a neutron is slow enough, it can get captured by a nucleus



The moderation and capture takes place at μs time-scales [62]. In lead, for example, the average time for a fast neutron to be thermalized and to be captured is about $900 \mu\text{s}$ [57]. For a moderator substance this time is much shorter.

By neutron capture, an highly excited nucleus is created. The binding energy of the additional neutron is released by the emission of γ 's. Nuclei decays via γ cascades to the ground state do not only happen after neutron capture but also after inelastic reactions where also highly excited nuclei can be created.

These gammas as well as produced unstable nuclei in the shower can lead to background in experiments searching for rare events such as $0\nu\beta\beta$ decay.

3.3 Cosmic-Ray-Induced Background

Cosmic rays can induce energy depositions around $Q_{\beta\beta}$ and thus contribute to the background. The used material in the experiment can be activated above ground by cosmic rays or in the underground laboratory by muons and muon-induced neutrons. Background for the $0\nu\beta\beta$ decay search can be produced by

- muon energy loss
- inelastic scattering (de-excitation gammas)
- neutron capture cascade and
- radioactive decays of isotopes with $Q > Q_{\beta\beta}$.

Radio-nuclei for example can be produced by

- muon spallation
- muon capture
- (p,x) reactions
- (n,x) reactions and
- neutron capture.

By fast neutron interactions with stable germanium isotopes, ^{60}Co ($T_{1/2} = 5.2714$ yr, $Q = 2823.9$ keV [35]) as well as ^{68}Ge ($T_{1/2} = 270.8$ d, $Q = 106$ keV [35]) can be produced. The latter isotope undergoes electron capture (EC)



to ^{68}Ga ($T_{1/2} = 67.629$ min, $Q = 2921.1$ keV [35]).

By (n,p) reactions with germanium, unstable gallium isotopes with $Q > Q_{\beta\beta}$ like ^{74}Ga ($T_{1/2} = 8.12$ min, $Q_{\beta} = 5368$ keV [35]) and ^{76}Ga ($T_{1/2} = 32.6$ s, $Q_{\beta} = 7010$ keV [35]) can be produced.

Not only cosmic-ray interactions with germanium can produce background but also the interactions of the cosmic rays with material of the surrounding (like argon). Due to cosmogenic activation of natural argon, ^{42}Ar ($T_{1/2} = 32.9$ yr, $Q_{\beta} = 599$ keV [35]) can be produced. Its Q -value is lower than $Q_{\beta\beta}$. However, ^{42}Ar decays to ^{42}K ($T_{1/2} = 12.36$ h, $Q_{\beta} = 3525.4$ keV [35]) whose decay contributes to the background.

If a neutron gets captured, not only gammas from the de-excitation of produced highly-excited nuclei can be background, but also gammas from following decays (if produced nuclei are unstable). Neutron capture on ^{76}Ge , for example, produces ^{77}Ge whose Q -value $Q_{\beta} = 2702$ keV [35] is higher than $Q_{\beta\beta}$. If a neutron gets captured on ^{40}Ar , ^{41}Ar ($T_{1/2} = 109.34$ min, $Q_{\beta} = 2491.6$ keV [35]) is produced whose decay also contributes to the background.

3.3.1 Background Reduction

Radioactive isotopes are mainly produced on ground [69]. Thus, exposure to cosmic rays has to be reduced to minimize the background creation. This can be done by shielding the detector material and by running the experiment underground. Then, the long-lived cosmogenic activity is dominated by the activation of the detector material at the surface [67]. In order to reduce the amount of produced long-lived radioisotopes, the time above ground has to be as short as possible and the detector material should be shielded during transportation as well as possible [6].

Deep underground the muon and neutron fluxes are reduced by the overburden by orders of magnitude compared to the surface fluxes depending on depth. Since long-lived radioisotopes produced at the surface will decay and less radioisotopes are produced, the amount of long-lived radioisotopes and thus the induced background gets reduced over time.

The natural radioactivity comes not only from the underground environment (from rock, cavity walls etc.) but also from the experimental setup. Therefore the used material in the experiment should be as clean as possible.

Although neutrons from natural radioactivity dominate at large depths, their energy

is typically less than 8 MeV. Thus, they are relatively straight forward to shield. The detectors of the GERDA experiment for example are shielded by water and liquid argon (see chapter 6).

Muon events as well as prompt induced background from de-excitation gammas and very short-lived radioisotopes can be vetoed by detecting through-going muons. However, produced long-lived radioisotopes are hard to veto and potentially limit the reachable sensitivity. For improving sensitivity, this kind of background becomes more relevant [65]. Therefore it is important to investigate and understand this background using available data and Monte Carlo simulations.

3.3.2 Simulation of Cosmic-Ray-Induced Background

The reliability of Monte Carlo simulations is influenced by the choice of models. Simulations of neutron fluxes have a large degree of uncertainty and should be tested against measurements [70]. The significant uncertainty in simulating muon-induced neutron rates is stressed by the fact that the neutron production is changing with every GEANT4 version and also if a different physics list is used [65].

The physics list contains the used models. For different particles and energy ranges different models are applied. If energy ranges between models overlap, a specific model is randomly chosen for each interaction in the simulation with the probability to choose this model starting from zero and increasing to one at the energy at which it becomes the only applicable model.

Also the results of different simulation toolkits differ. Comparisons of GEANT4 simulations with FLUKA simulations show that the muon-induced neutron production in GEANT4 is generally lower (but this difference is typically smaller than a factor of 2) [64]. The simulation of neutron propagation through different materials shows a good agreement and differs at most by 20% when comparing GEANT4 with MCNPX [71].

Comparing the time structure of hadronic showers between data and Monte Carlo simulations shows an overall good agreement if low-energy neutrons are treated with high precision models [62]. Some experiments on neutron production in heavy targets show that both FLUKA and GEANT4 may underestimate the neutron production [64]. For low-A targets the agreement between different measurements and simulation toolkits is reasonable [65]. The accuracy of simulations is limited by a lack of data for muon-induced interactions in medium dense materials [67]. For heavy targets experimental data for neutron production is scarce. The number of neutrons per muon is the least known quantity. The average multiplicity in FLUKA is smaller than the measured values [67].

To improve the Monte Carlo toolkits further accurate data on muon-induced neutron production in several materials [65] as well as for high-energy muon interactions are needed [67]. MINIDEX aims to measure the muon-induced neutron production in lead and other materials in shallow underground laboratories (see chapter 5).

Table 3.1: Muon-induced isotope production and background index (BI) from different radioisotopes estimated with Monte Carlo simulations for phase II by [3]. Only statistical errors and upper limits at 90% C.L. are quoted.

Isotopes	$^{74}\text{Ga}/^{75}\text{Ga}/^{76}\text{Ga}$	^{68}Ge	^{69}Ge	$^{77}\text{Ge}/^{77m}\text{Ge}$
$T_{1/2}$	8.1 m/126 s/33 s	271 d	39 h	11.3 h/53 s
Q-value [keV]	5368/3392/7010	106	2227	2702/2861
Rate [nuclei/(kg y)]	< 0.1	0.8 ± 0.03	1.8 ± 0.2	0.51 ± 0.09
BI [cts/(kg keV y)]	$< 4 \cdot 10^{-5}$	$(5 \pm 2) \cdot 10^{-6}$	$(5.0 \pm 0.6) \cdot 10^{-6}$	$(1.1 \pm 0.2) \cdot 10^{-4}$

The right choice of models influences also the reliability of the simulations. With detailed Monte Carlo simulations an absolute agreement between simulation and data of $\sim 25\%$ for muon-induced neutrons can be reached even for lead [65]. Therefore the Monte Carlo simulations should be compared to measurements to validate the choice.

3.3.3 Neutron Flux and Radio-Nuclei Production in GERDA

At large depths like at the Gran Sasso underground laboratory, the muon-induced neutron flux is about three orders of magnitude lower than the flux from natural activity [57]. Fission neutrons and neutrons from (α, n) reactions build up most of the neutron flux background. The (α, n) reactions do not only take place in the rock and the cavity walls but are also induced by α 's from radon decay. Thus, the neutron flux is also influenced by the radon concentration which depends on the air circulation.

Since the neutron flux depends on the used materials, it can not be measured in advance but can only be determined for a running experiment. Otherwise it has to be simulated. For the GERDA experiment, the expected integrated neutron flux close to the detector array was investigated using Monte Carlo simulations and was found to be

$$(5.72 \pm 0.04) \text{ neutrons/m}^2 \text{ h [3]}. \quad (3.15)$$

If a newer GEANT4 version (10.3) and another implemented setup is used, the resulting neutron flux is $1.6 \text{ m}^{-2} \text{ h}^{-1}$ [4]. The difference is a factor of ~ 3.6 . Thus the simulated neutron flux depends strongly on the used GEANT4 version and implemented setup. It was found that only muon-induced neutrons generated in the LAr or the LAr cryostat walls contribute to the neutron flux around the detector array [4].

Also the production rate of dangerous isotopes for the GERDA experiment and their background indices were investigated by [3] and are shown in Table 3.1. One can see from Table 3.1 that ^{77}Ge is the isotope with the highest expected background index. It is produced by neutron capture on ^{76}Ge .

Chapter 4

Cosmic-Ray Shielding Simulations with GEANT4

To reduce the induced background above ground, a good shielding design for the transportation of the detector material is needed. For its design, the knowledge of shielding properties is an important input. The properties of different materials were estimated by simulating the penetration of cosmic-ray neutrons and muons through different material blocks. The GEANT4 [72] based framework MaGe [73] developed by the GERDA and MAJORANA collaborations was used for these simulations. Special care was taken to avoid double counting due to particles crossing boundaries multiple times (backscattering) which would lead to wrong estimation of shielding powers. The backscattering effect was investigated using neutron simulations and is discussed in section 4.1.

For simulating neutrons and muons penetrating different material blocks, the Geant4 version 9.6 patch 2 was used together with CLHEP¹ 2.1.3.1. The default physics lists implemented in MaGe were used. For hadronic processes, the physics list QGSP_BERT_HP is used. Above 12 GeV, reactions of pions, kaons and nucleons happen according to theory-driven quark-gluon string models (QGSP). Hadrons are treated as QCD strings which collide with nucleons in the nucleus forming more strings which later hadronize producing secondary particles. For the de-excitation of the remnant nucleus, the GEANT4 precompound and de-excitation sub-models are used.

Below 10 GeV, reactions happen according to the Bertini cascade (BERT) model. The final state of hadron inelastic scattering is generated by simulating the intra-nuclear cascade. The target nucleus is treated as an average nuclear medium to which excitons (particle-hole states) are added after each collision. The excited nucleus is a sum of particle-hole states. For its decay, pre-equilibrium, nucleus explosion, fission and evaporation methods are used.

For neutrons from thermal energies up to 20 MeV, high-precision data-driven models (NeutronHP) are used. Cross-section data from the ENDF/B-VII database [74] is used

¹CLHEP: Class Library for High Energy Physics

Table 4.1: Properties of different materials. For used material composition see appendix B.

Material	Density [g cm ⁻³]	Avg. mass [amu]	Avg. neutron density 10 ²⁴ [cm ⁻³]
Air	0.00129	14.4	0.00039
PE	0.92	4.7	0.24
Water	1.00	6.0	0.27
Soil	1.65	11.7	0.59
Concrete	2.3	18.7	0.69
LNGS rock	2.71	25.5	0.82
Steel	7.90	55.1	2.52
Copper	8.960	63.6	2.89
Lead	11.340	207.2	4.12

to model neutron capture, elastic and inelastic scattering.

For electromagnetic interactions, low-energy models based on the Livermore data library are used. Further information about used models can be found in Appendix A.

Cosmic-ray neutrons and muons (μ^- and μ^+) at sea-level were simulated. As generator input the measured muon energy spectrum of [58] and the measured neutron energy spectrum of [60] were used (see section 3.1). Since the cosmic-ray neutron angular distribution is not precisely known, the influence of the chosen angular distribution for the neutron shielding properties was also investigated (see section 4.2). Three different angular distributions were used: vertically downwards going neutrons, an isotropic distribution and a distribution suggested by A. Nesterenok [61] for high energetic neutrons (see section 3.1).

A generation plane of 1.5 m \times 1.5 m is used which is centered and located above the material blocks. The blocks are 200 m \times 200 m \times x m large to make sure that all neutrons enter the shielding material. The length in the z direction x corresponds to the shielding thickness.

In Table 4.1 the properties of the used materials are shown: plastic (polyethylene PE, C₂H₄), water, soil, concrete, LNGS rock, stainless steel, copper and lead. It can be seen from Table 4.1 that the densities for water and plastic are similar. Therefore they should have similar shielding properties. It can also be seen that the average neutron density is also higher for an higher density for all chosen materials but air. The used material compositions can be found in Appendix B.

To avoid double counting due to backscattering, the material blocks with different thicknesses were placed in vacuum and only outgoing neutrons or muons were counted. Only the information of particles crossing a boundary like momentum, energy and position were saved. Counting particles inside the material block could lead to double counting of particles. Thus, only outgoing particles were counted. Only for investigating the backscattering effect (see section 4.1), neutrons were counted within the block.

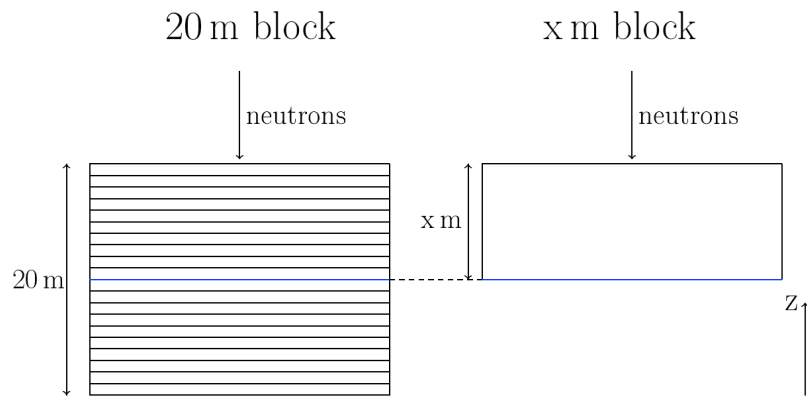


Figure 4.1: Illustration of the backscattering effect investigation.

The results of the muon shielding simulations are discussed in section 4.3 and the results of muon-induced neutron production for different shielding materials are discussed in section 4.4. Combining the shielded cosmic-ray neutron rate with the muon-induced neutron rate, the total neutron flux can be estimated. The total estimated neutron fluxes are given in section 4.5.

4.1 Backscattering Effect

To save computing time for the shielding simulations, one could use only one block for each material and could count the neutrons within the block for different shielding thicknesses like it was done in [66]. Since backscattered neutrons can not be recognized by this approach, this would lead to multiple counting of neutrons. Therefore this approach can only be used, if the contribution of backscattered neutrons is negligible. This has to be verified. Within the framework of this thesis, the backscattering effect was investigated for plastic, water, soil and steel by comparing the number of outgoing neutrons leaving material blocks with different thicknesses (in the range of 1 m–20 m) with the number of neutrons at the corresponding depth of a 20 m block. Since the particle information is only saved if the particle is crossing a boundary, the 20 m block was divided into 20 sub-blocks. This is illustrated in Fig. 4.1.

To be able to distinguish between the backscattering effect and the effect of different angular distributions, only vertically downwards going neutrons ($9.99 \cdot 10^6$ for each material) were injected. For the sub-blocks, all neutrons passing the boundary as well as only downwards going neutrons were counted, since upwards going neutrons have scattered back at least once. The result for comparing the number of only downwards going neutrons to the number of neutrons leaving a block with the corresponding thickness x is shown in Fig. 4.2. Since steel shields more neutrons than the other materials, there are

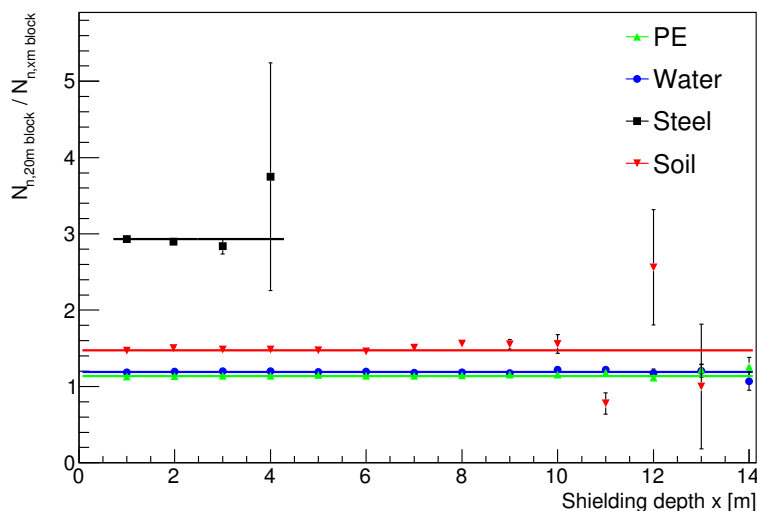


Figure 4.2: Ratio of only downwards going neutrons counted inside a block and neutrons leaving a block with the corresponding thickness.

Table 4.2: Number of neutrons from the 20 m block at a certain depth divided by the number of neutrons of a block with the corresponding thickness.

Material	All neutrons	Downwards going neutrons	Upwards going neutrons
Plastic	1.3552 ± 0.0006	1.1370 ± 0.0005	0.218 ± 0.001
Water	1.4918 ± 0.0005	1.1899 ± 0.0004	0.3019 ± 0.0008
Soil	2.1718 ± 0.0005	1.4723 ± 0.0004	0.700 ± 0.001
Steel	5.340 ± 0.002	2.9322 ± 0.0009	2.408 ± 0.008

hardly any neutrons at depths larger than 4 m.

It can be seen from Fig. 4.2 that the backscattering rate is independent of the shielding depth for the simulated materials and depths. Therefore a constant function was fitted to the data for each material. The fit results are shown in Table 4.2. The fraction of upwards going neutrons was calculated by subtracting the number of downwards going neutrons from all counted neutrons. If there is no backscattering effect, the ratio would be one for the downwards going neutrons and zero for the upwards going neutrons, since upwards going neutrons are always backscattered neutrons. If also backscattered neutrons contribute, the ratio would be larger than one. The larger the ratio is the more neutrons have scattered back. The ratio is the largest, if all (downwards and upwards going) neutrons are counted. By counting only downwards going neutrons, the ratio gets smaller.

From Table 4.2, it can be seen that the backscattering properties of water and plastic are similar. This is due to their similar properties. It can also be seen that for materials with higher average atomic number like steel the number of backscattered neutrons is larger.

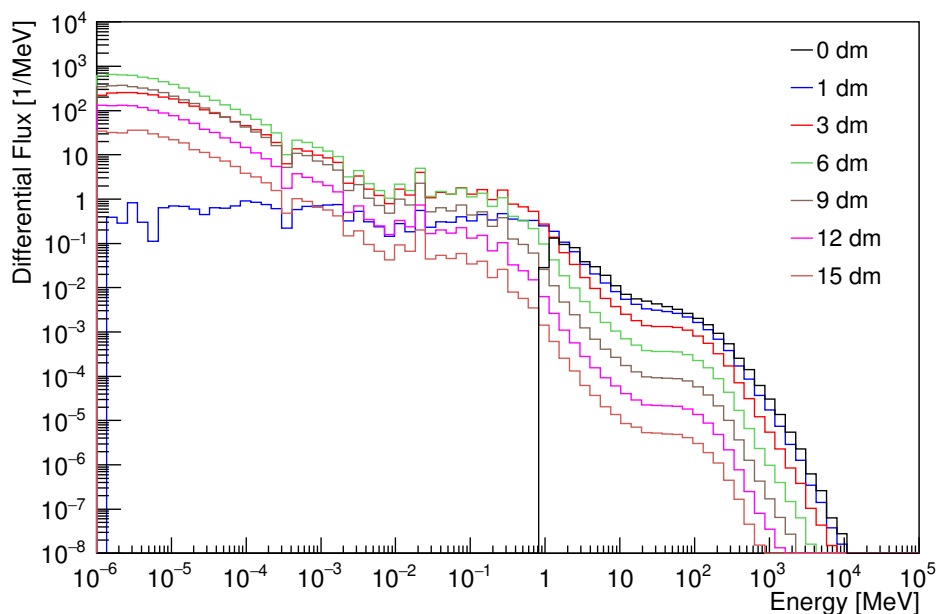


Figure 4.3: Neutron energy spectrum at different depths for steel. Only downwards going neutrons were injected.

It can clearly be seen from Table 4.2 and Fig. 4.2 that the backscattering effect is significant and not negligible. Using only one block for each material and counting also the neutrons within the block would lead to incorrect results. Therefore many blocks have to be used for each material: one block for each shielding thickness. This was done for the other simulations whose results are presented in the next sections.

4.2 Cosmic-Ray Neutron Simulations

To get the shielding properties of concrete, copper, lead, LNGS rock, soil, steel, plastic and water, blocks with different thicknesses were simulated. The number of simulated neutrons as well as the thicknesses is adjusted to the shielding power and thus different for each material and angular distribution. A step-size of 1 m was chosen for plastic, water and soil and a step-size of 0.1 m was chosen for concrete, copper, LNGS rock and lead. For steel, a step-size of 1 m was chosen for only vertically downwards going neutrons and of 0.1 m for isotropically distributed neutrons and neutrons distributed according to Nesterenok. For numbers of simulated neutrons depending on the shielding thickness and used angular distribution see Appendix C. The number of outgoing neutrons were counted and normalized to the number of incoming neutrons. While penetrating the material, some neutrons are shielded, but new neutrons are created as well.

Figure 4.3 shows the energy spectrum of cosmic-ray neutrons shielded by different steel depths. If the neutrons have not penetrated any material yet (0 m), the energy spectrum is equal to the injection spectrum which is the spectrum of [60] (see Fig. 3.3

Table 4.3: Depths d_{equ} at which the equilibrium has been reached for different materials. The smallest block thickness of plastic, water or soil was 1 m at which the equilibrium has already been reached.

Material	Plastic	Water	Soil	Concrete	LNGS rock	Steel	Copper	Lead
Depth [dm]	< 10	< 10	< 10	1 ± 0.5	6 ± 0.5	6 ± 0.5	7 ± 0.5	16 ± 0.5

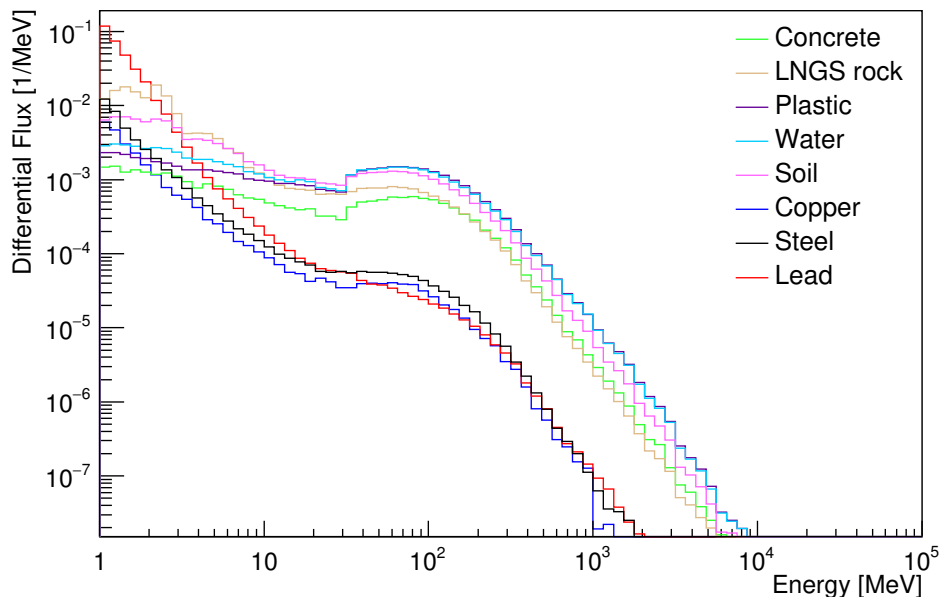


Figure 4.4: Neutron energy spectrum for different materials at 1 m, if only downwards going neutrons were injected.

of chapter 3). From Fig. 4.3 it can be seen that only neutrons with energy $E \geq 1$ MeV are injected and that the neutrons are shifted to smaller energies while penetrating the shielding material. The shape of the energy spectrum for increasing shielding depths is changing until equilibrium of the particle shower has been reached at a certain depth. After equilibrium has been reached, only the total number of neutrons decreases, but the shape of the energy spectrum does not change anymore.

Table 4.3 shows the depths d_{equ} at which the equilibrium has been reached for different materials. It was found that d_{equ} is the same for all three angular distributions. From Table 4.3, it can be seen that the equilibrium depth depends on the material. For materials with higher average masses and higher densities, a longer distance is needed to reach equilibrium.

Since the thicknesses of the smallest block made of plastic, water or soil was 1 m, the values for these materials were not evaluated. All these materials are lighter than concrete. Therefore it can be expected that the shape of the energy spectrum is not changing anymore at 1 dm.

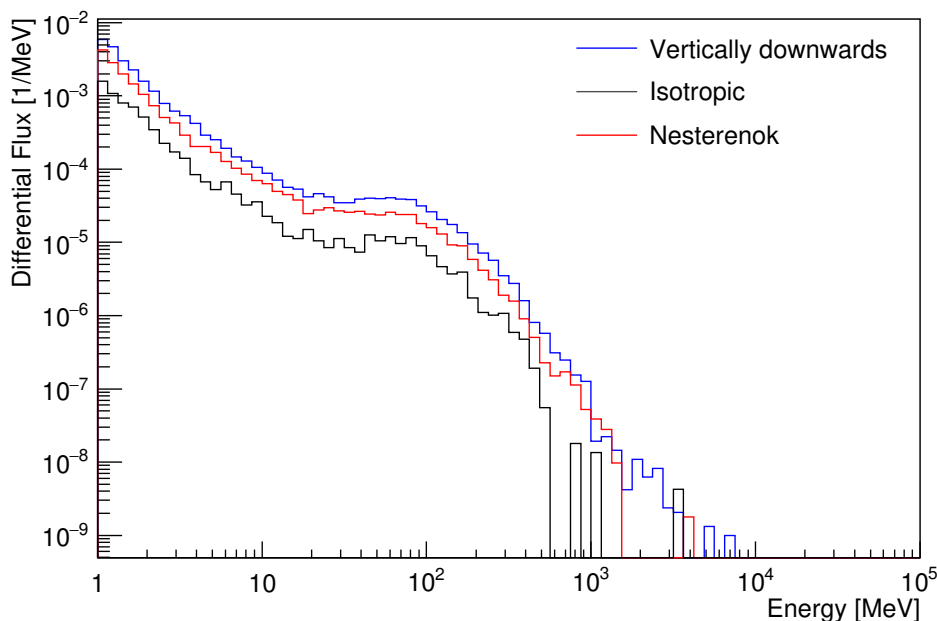


Figure 4.5: Neutron energy spectrum for different angular distributions after 1 m copper shielding.

Figure 4.4 shows the neutron energy spectrum for different materials at 1 m if only downwards going neutrons were injected. For all materials but lead the equilibrium has been reached at this depth. It can be seen from Fig. 4.4 that the shape of the energy spectrum depends on the material. For heavier materials like steel, copper and lead, the fraction of less energetic neutrons is higher, since their slopes in the energy range (1 – 10) MeV are larger than the slopes of the other materials.

Figure 4.5 shows the energy spectra for different angular distributions: vertically downwards going neutrons, an isotropic distribution and a distribution suggested by A. Nesterenok [61] for high energetic neutrons (see Eq. 3.3). In contrast to the choice of material, the choice of different angular distributions hardly affects the shape of the energy spectrum. The number of neutrons is different since the on average penetrated distance depends on the angular distribution. If the neutrons have to penetrate a larger distance, more neutrons are shielded. The on average penetrated distance is the largest for the isotropic distribution. Less neutrons are shielded if only vertically downwards going neutrons are injected.

The number of outgoing neutrons normalized to the number of incoming neutrons for different block thicknesses and materials is shown in Fig. 4.6 and in Fig. 4.7. For Fig. 4.7 the unit mwe (meter water equivalent) was used which is defined as the product of depth and the density of the penetrated material. For heavier materials (like steel, copper and lead) more neutrons are produced than shielded at small shielding depths. Only after equilibrium has been reached the neutron flux is decreasing with increasing shielding depth.

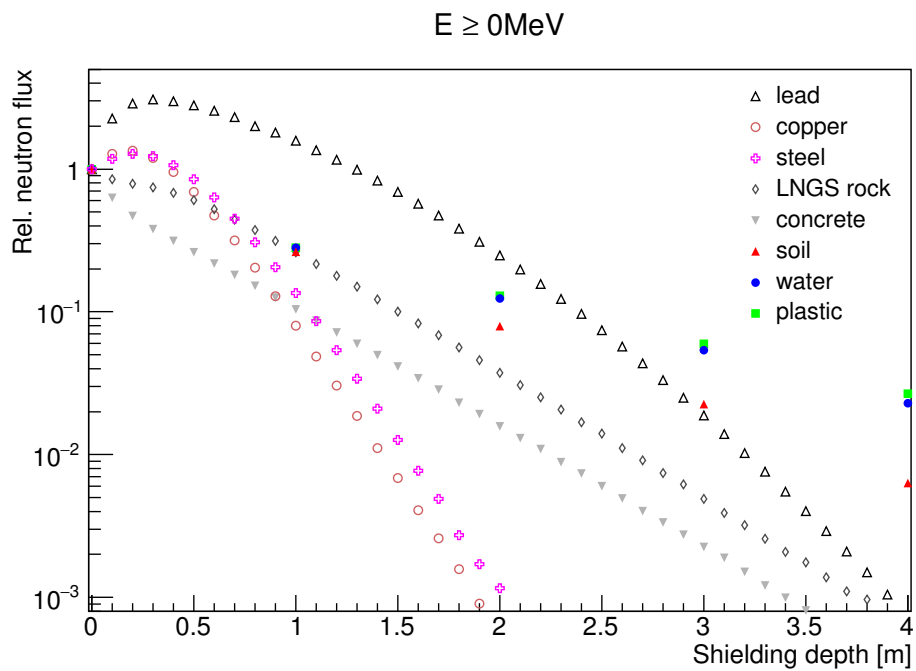


Figure 4.6: Neutron flux at different shielding depths normalized to the incoming neutrons for different materials. The angular distribution suggested by [61] (see Eq. 3.3) was used for injection.

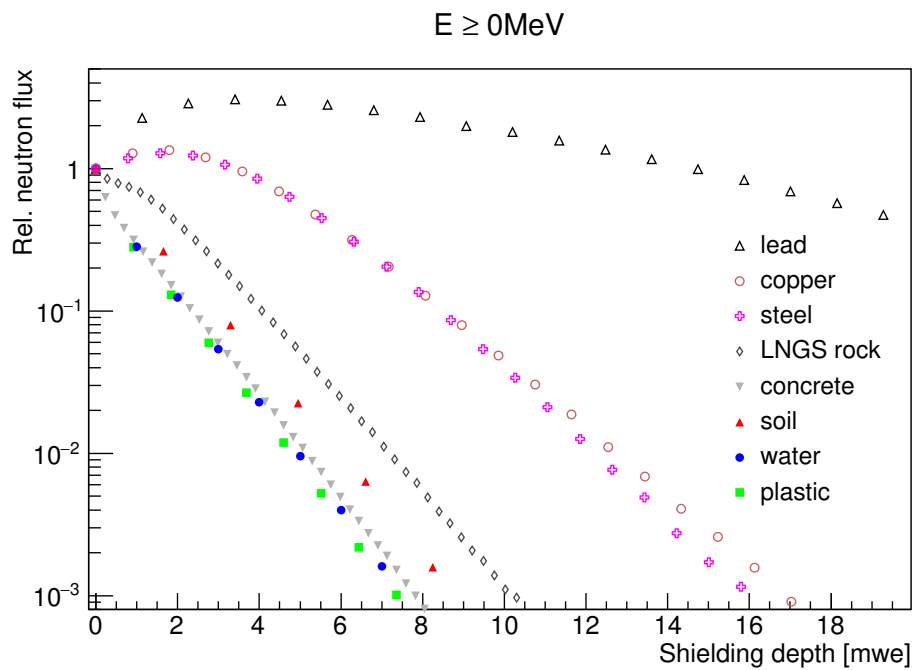


Figure 4.7: Neutron flux at different shielding depths normalized to the incoming neutrons for different materials. The angular distribution suggested by [61] (see Eq. 3.3) was used for injection.

Table 4.4: Depths d_s at which there are less neutrons than neutrons which have arrived for different materials, angular distributions and energy thresholds.

Material	Angular distribution	Threshold [MeV]	Shielding depth [m]	Shielding depth [mwe]
Steel	Isotropic	0	0.30 ± 0.05	2.4 ± 0.4
	Nesterenok	0	0.40 ± 0.05	3.2 ± 0.4
	Vertically downwards	0	0.50 ± 0.05	4.0 ± 0.4
Copper	Isotropic	0	0.30 ± 0.05	2.7 ± 0.4
	Nesterenok	0	0.40 ± 0.05	3.6 ± 0.4
	Vertically downwards	0	0.40 ± 0.05	3.6 ± 0.4
Lead	Isotropic	0	1.10 ± 0.05	12.5 ± 0.6
	Nesterenok	0	1.30 ± 0.05	14.7 ± 0.6
	Only downwards going	0	1.40 ± 0.05	15.9 ± 0.6
Lead	Isotropic	1	0.30 ± 0.05	3.4 ± 0.6
	Nesterenok	1	0.30 ± 0.05	3.4 ± 0.6
	Vertically downwards	1	0.40 ± 0.05	4.5 ± 0.6

The depths at which the total neutron flux induced by cosmic-ray neutrons is lower than the unshielded flux d_s depends on the shielding material and is shown in Table 4.4 for different angular distributions. For the evaluation of d_s , the smallest simulated block thickness has to be smaller than d_s . If no energy threshold is set, d_s can only be evaluated for steel copper and lead. If only neutrons with $E \geq 1$ MeV are counted at the different shielding depths, d_s can only be evaluated for lead.

From Table 4.4 it can be seen that the heavier the material is the thicker the shielding has to be to effectively shield neutrons. For lighter materials or higher energy thresholds this depth decreases. The thickness needed to shield neutrons depends also on the angular distribution of injected neutrons. The depth becomes smaller if the neutrons penetrate on average a larger distance (like for the isotropic distribution).

Figure 4.8 shows the neutron flux at different depths for different energy cuts. Only neutrons with higher energies than the cut value were counted at the given shielding depths. The number of neutrons decreases with increasing threshold energy. From Fig. 4.8 it can be seen that most of the new produced neutrons are low energetic.

Table 4.5 shows the depths d_{max} at which the total neutron flux reaches its maximum. For heavier materials this depth is reached at larger shielding depths. For different angular distributions, the d_{max} values are similar. The depth at which the maximum neutron flux is reached depends not only on the material but also on the threshold energy. With increasing threshold d_{max} is decreasing.

To estimate the shielding index s , a power law fit was applied to the simulated neutron fluxes (see Eq. 3.5). The shielding index s is a measure of shielding power. The smaller the shielding index the more effectively neutrons are shielded. The fit was only applied

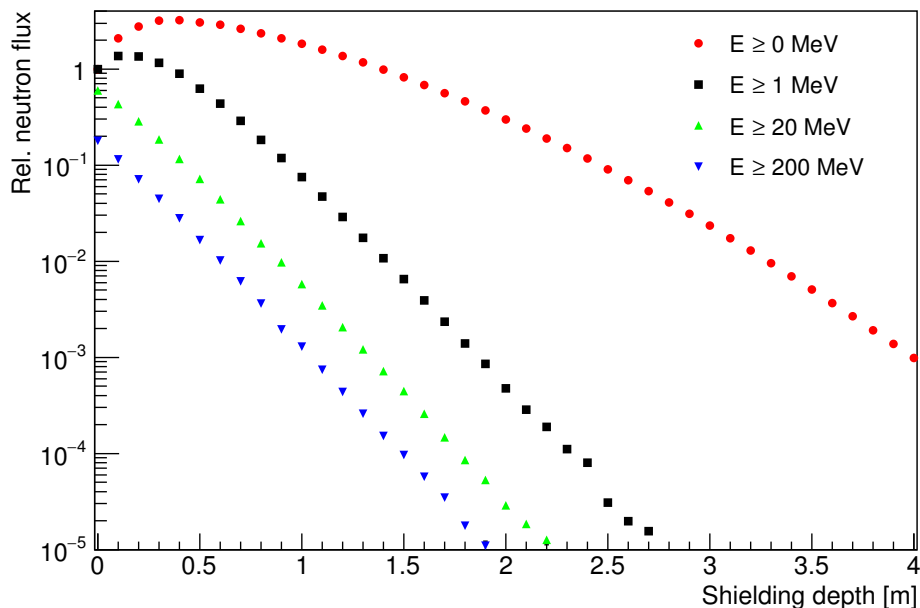


Figure 4.8: Neutron flux at different shielding depths normalized to the incoming neutrons for lead, if different neutron energy cut were set. Only vertically downwards going neutrons were injected.

Table 4.5: Depths d_{max} at which the neutron flux is highest for different materials, angular distributions and energy thresholds.

Material	Angular distribution	Threshold [MeV]	Maximum [m]	Maximum [mwe]
Steel	Isotropic	0	0.10 ± 0.05	0.8 ± 0.4
	Nesterenok	0	0.20 ± 0.05	1.6 ± 0.4
	Vertically downwards	0	0.20 ± 0.05	1.6 ± 0.4
Copper	Isotropic	0	0.10 ± 0.05	0.9 ± 0.4
	Nesterenok	0	0.20 ± 0.05	1.8 ± 0.4
	Vertically downwards	0	0.20 ± 0.05	1.8 ± 0.4
Lead	Isotropic	0	0.20 ± 0.05	2.3 ± 0.6
	Nesterenok	0	0.30 ± 0.05	3.4 ± 0.6
	Vertically downwards	0	0.40 ± 0.05	4.5 ± 0.6
Lead	Isotropic	1	0.10 ± 0.05	1.1 ± 0.6
	Nesterenok	1	0.10 ± 0.05	1.1 ± 0.6
	Vertically downwards	1	0.10 ± 0.05	1.1 ± 0.6

Table 4.6: Shielding index s [1/m] for different materials and angular distributions ($E \geq 0$ MeV).

Material	Vertically downwards	Nesterenok	Isotropic
Plastic	-0.354 ± 0.003	-0.366 ± 0.002	-0.388 ± 0.005
Water	-0.372 ± 0.003	-0.397 ± 0.007	-0.418 ± 0.005
Soil	-0.57 ± 0.01	-0.584 ± 0.007	-0.611 ± 0.009
Concrete	-0.822 ± 0.006	-0.855 ± 0.004	-0.91 ± 0.02
LNGS rock	-0.850 ± 0.003	-0.897 ± 0.005	-0.961 ± 0.009
Steel	-2.01 ± 0.02	-2.12 ± 0.02	-2.22 ± 0.03
Copper	-2.10 ± 0.02	-2.15 ± 0.01	-2.22 ± 0.02
Lead	-1.368 ± 0.009	-1.39 ± 0.01	-1.42 ± 0.01

for depths $d > d_{equ}$ at which equilibrium has been reached. The results are shown in Table 4.6 if no energy threshold is set. For the shielding index values in mwe and the shielding index values if different energy cuts are set see Appendix D.

From Table 4.6 it can be seen that the shielding index is smaller for heavier materials. Only for lead, which is the heaviest material, the shielding power is lower than for copper and steel. It can also be seen that the influence of the chosen material is much larger than the influence of the used angular distribution.

4.3 Muon Simulations

The energy spectrum of [58] was used as injection spectrum (see chapter 3). For investigating the production of muon-induced neutrons, the same simulations were used (see section 4.4). A shielding thickness range of (1 – 20) m with a step-size of 1 m was chosen for plastic, water, soil and steel. For concrete, copper, LNGS rock and lead, a thickness range of (0.1 – 4) m with a step-size of 0.1 m was chosen. For each muon charge (μ^+ or μ^-) and shielding thickness, 10^6 (for concrete, copper, LNGS rock and lead) or $9.99 \cdot 10^6$ muons (for plastic, water, soil and steel) were injected.

Figure 4.9 shows the simulated energy spectrum at different depths if μ^- penetrate plastic. From Fig. 4.9, it can be seen that only muons with an energy higher than 260 MeV are injected. Like for neutrons, muons are shifted to smaller energies due to energy loss during penetration. After the muons have penetrated a certain depth, equilibrium is reached and the shape of the energy spectrum is not changing anymore. Low energetic muons are either decaying or are being captured. Latter process is only possible for μ^- .

In Fig. 4.10 the energy spectra of μ^- and μ^+ are compared. It can clearly be seen that the spectra do not differ much if the same material is penetrated. In Fig. 4.11, energy spectra of μ^- for different materials at 2 m are compared. It can be seen that heavier

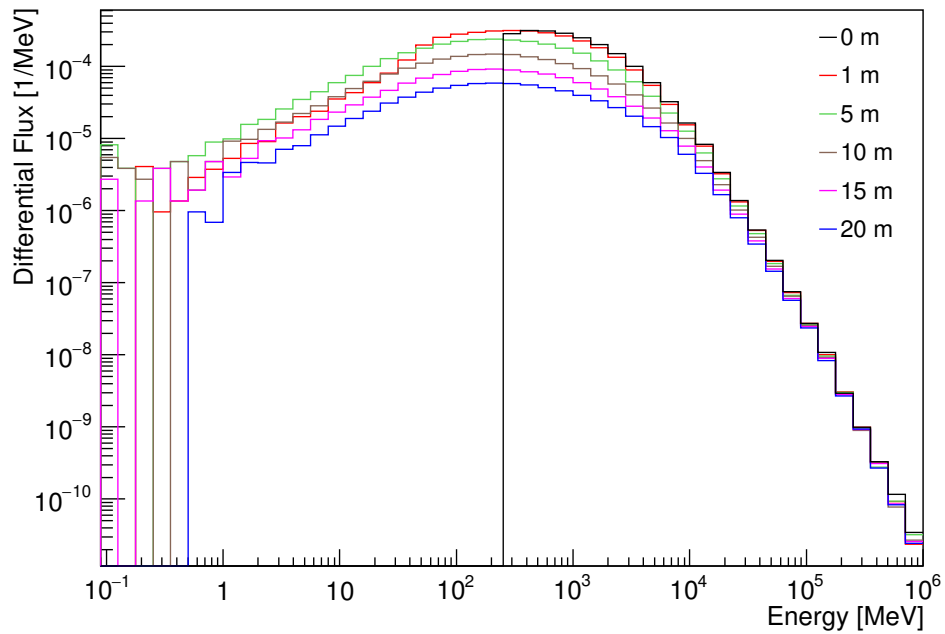


Figure 4.9: Muon energy spectrum of μ^- after different depths of plastic shielding.

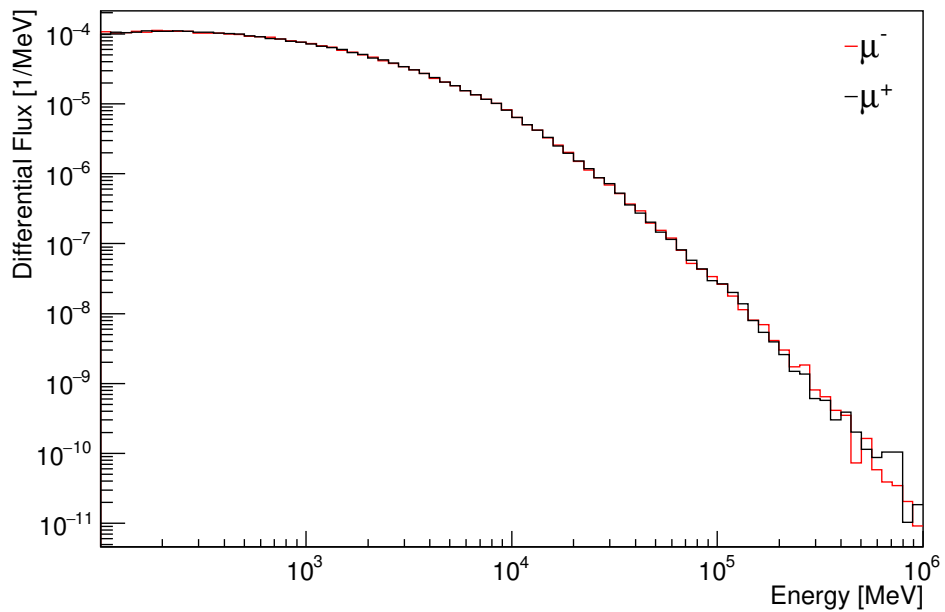


Figure 4.10: Comparison of the μ^- and μ^+ energy spectrum after 2 m copper shield.

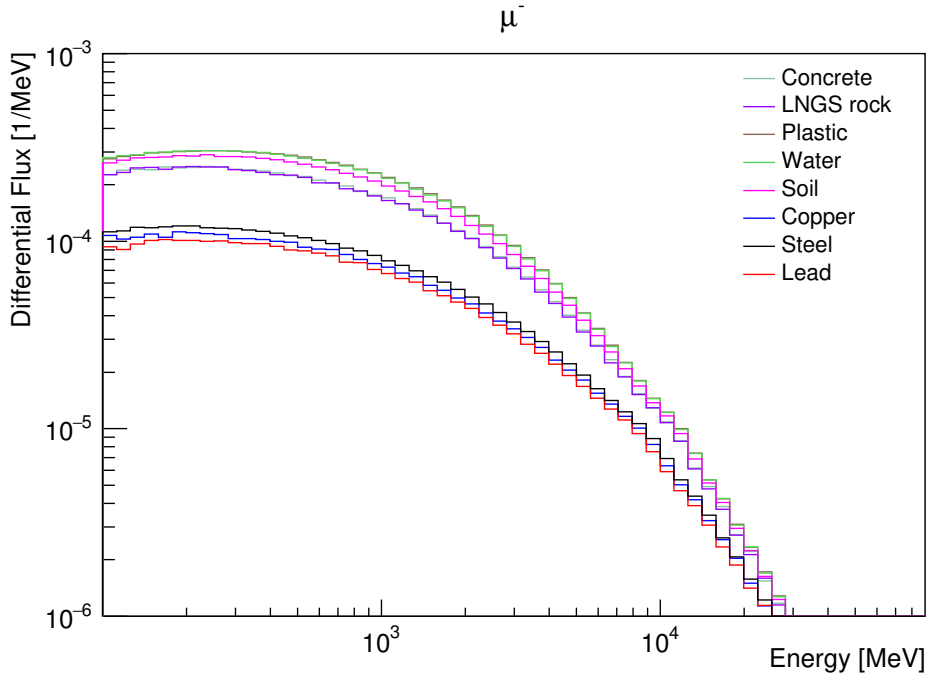


Figure 4.11: Muon energy spectra (μ^-) for different materials at 2 m.

materials shields muons more effectively. However, the shapes of the muon energy spectra are similar.

Figure 4.12 shows the μ^- and μ^+ flux at different depths and their deviations, if the muons penetrate LNGS rock. The shielding efficiencies for μ^- and μ^+ are the same within the uncertainties. To estimate the shielding index, the fit of Eq. 3.5 was applied. The results of the fit are shown in Table 4.7. The shielding indices for μ^- and μ^+ are the same within uncertainties. Since less muons are shielded than neutrons, the muon shielding indices are larger than the neutron shielding indices (see Table 4.6). Like the neutron shielding indices the muon shielding indices are smaller for heavier materials.

Table 4.7: Muon shielding index s for different materials in [1/m] and [1/mwe] if no threshold is set on the muon energy ($E \geq 0$ MeV).

Material	μ^+ [m^{-1}]	μ^- [m^{-1}]	μ^+ [mwe^{-1}]	μ^- [mwe^{-1}]
Plastic	-0.0313 ± 0.0004	-0.0313 ± 0.0004	-0.0341 ± 0.0005	-0.0340 ± 0.0005
Water	-0.0326 ± 0.0005	-0.0325 ± 0.0005	-0.0326 ± 0.0005	-0.0325 ± 0.0005
Soil	-0.0396 ± 0.0008	-0.0395 ± 0.0008	-0.0240 ± 0.0005	-0.0239 ± 0.0005
Concrete	-0.0840 ± 0.0002	-0.0837 ± 0.0002	-0.03652 ± 0.00009	-0.03641 ± 0.00009
LNGS rock	-0.0872 ± 0.0002	-0.0869 ± 0.0002	-0.03216 ± 0.00008	-0.03205 ± 0.00008
Steel	-0.149 ± 0.008	-0.149 ± 0.008	-0.019 ± 0.001	-0.019 ± 0.001
Copper	-0.177 ± 0.002	-0.177 ± 0.002	-0.0198 ± 0.0002	-0.0198 ± 0.0002
Lead	-0.186 ± 0.002	-0.186 ± 0.002	-0.0164 ± 0.0002	-0.0164 ± 0.0002

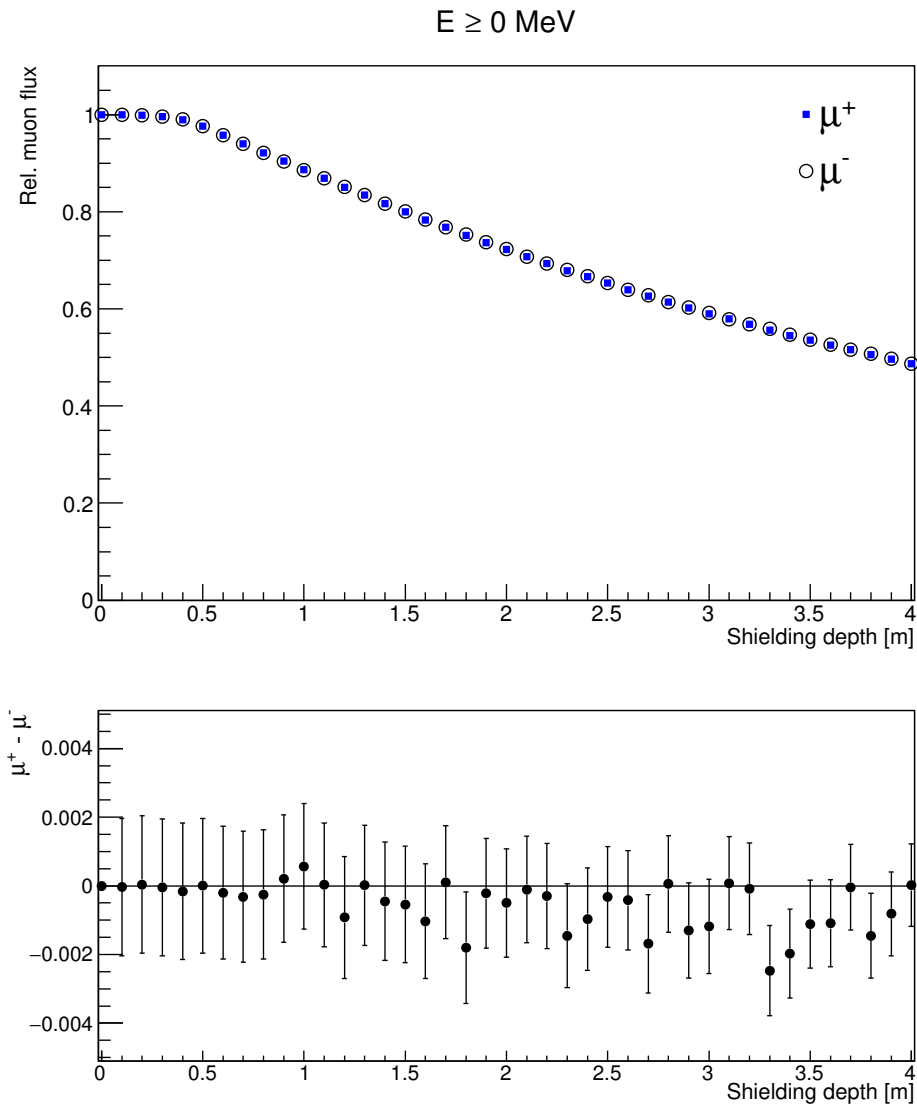


Figure 4.12: Muon flux at different shielding depths for LNGS rock for μ^+ and μ^- and their deviations. The fluxes are normalized to the incoming muon flux.

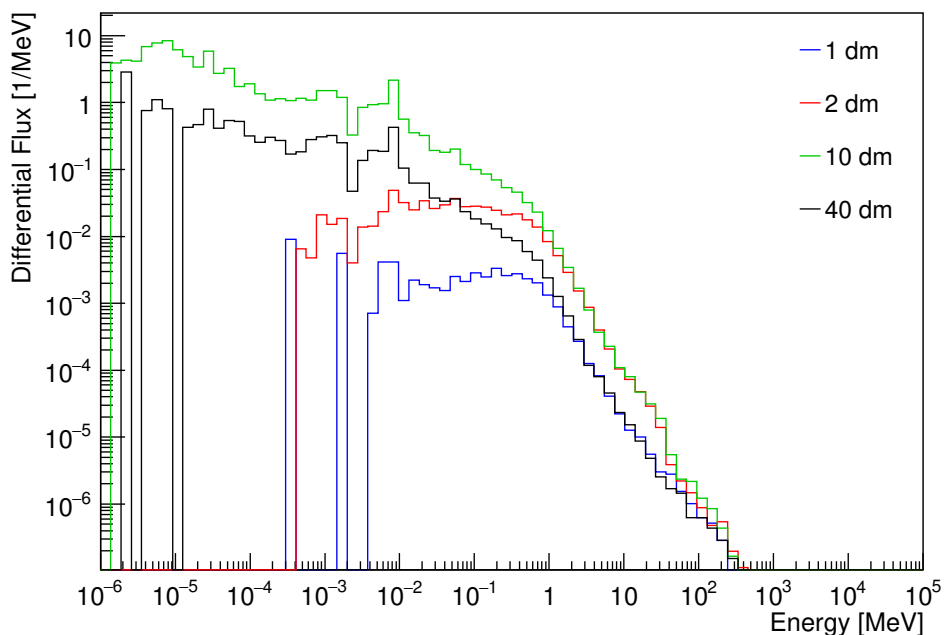


Figure 4.13: Energy spectrum of μ^- -induced neutrons after different depths of copper shielding.

4.4 Muon-Induced Neutrons

For investigating the production of muon-induced neutrons, the simulations of the muon shielding were used (see section 4.3). The number of outgoing neutrons behind a given shield thickness were counted and normalized to the number of incoming muons. Figure 4.13 shows the muon-induced neutron energy spectrum of neutrons leaving the shield at different depths of copper being penetrated by μ^- . Muon-induced neutrons are shifted to lower energies during penetration and some are shielded. After the particle shower has reached equilibrium at a certain depth d_{equ} , more muon-induced neutrons are shielded than produced and the shape of the energy spectrum is not changing anymore. Only the number of muon-induced neutrons decreases.

In Fig. 4.14 the energy spectra of μ^- -induced and μ^+ -induced neutrons after 2 m shield of copper are shown. Unlike the muon energy spectra (see Fig. 4.10) the muon-induced neutron energy spectra differ for μ^+ and μ^- . They undergo similar reactions, but only μ^- can be captured which results in production of neutrons (see section 3.2). Low energetic μ^+ can only decay without production of neutrons. Therefore μ^- 's induce more neutrons than μ^+ 's. At higher energies the energy spectra become similar.

Figure 4.15 shows the muon-induced neutron energy spectra if μ^- have penetrated 2 m of different shielding materials. It can be seen that the shape depends on the penetrated material. More neutrons are produced if muons penetrate material with higher atomic mass—especially at low energies.

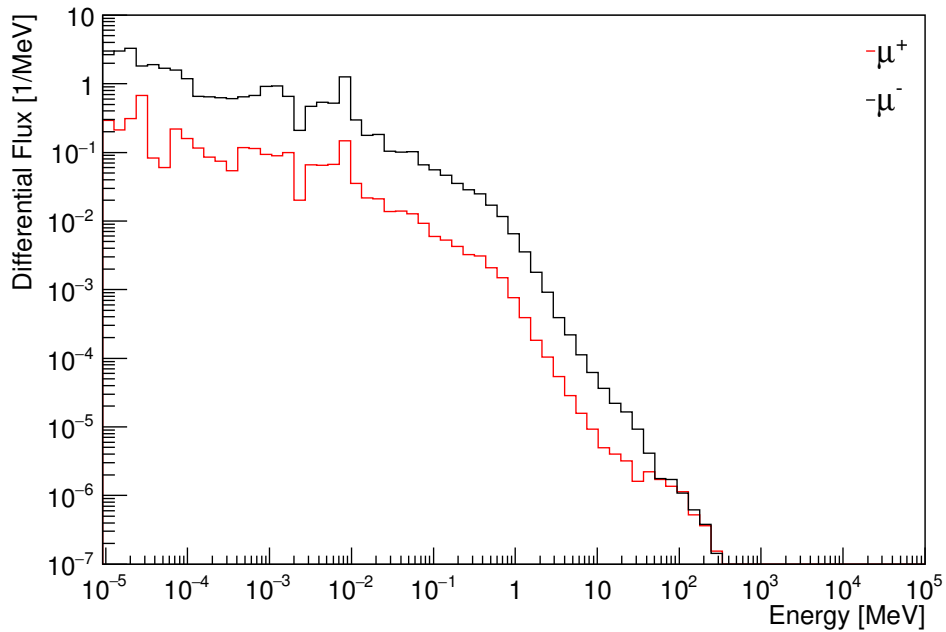


Figure 4.14: Comparison of the μ^- -induced and μ^+ -induced neutron energy spectrum after the muons have penetrated 2 m of copper. The only difference between μ^- and μ^+ is that only μ^- can undergo muon capture on nuclei.

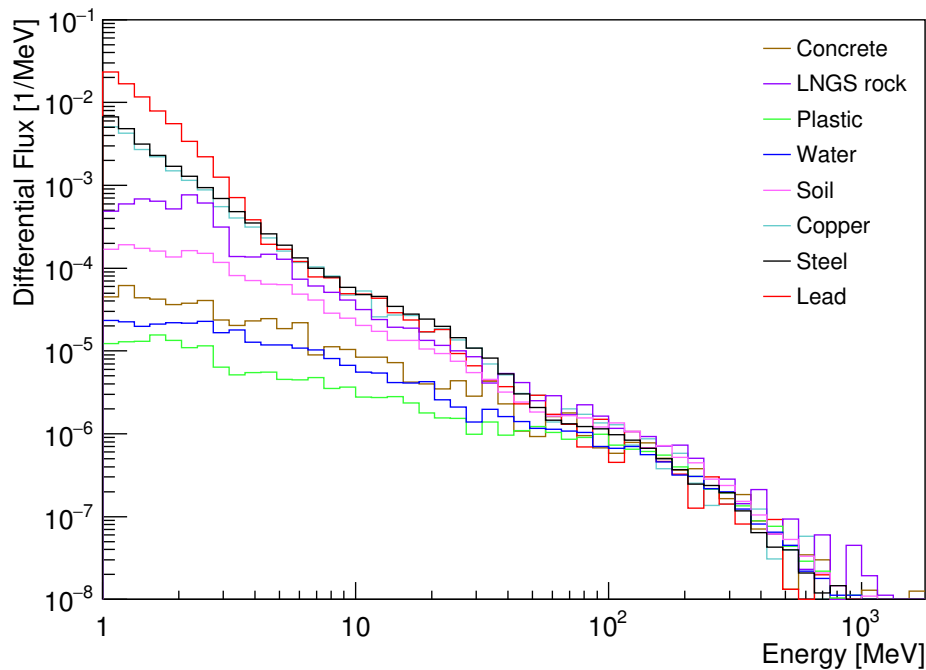


Figure 4.15: Muon-induced neutron energy spectrum for μ^- which have penetrated 2 m of different shielding materials.

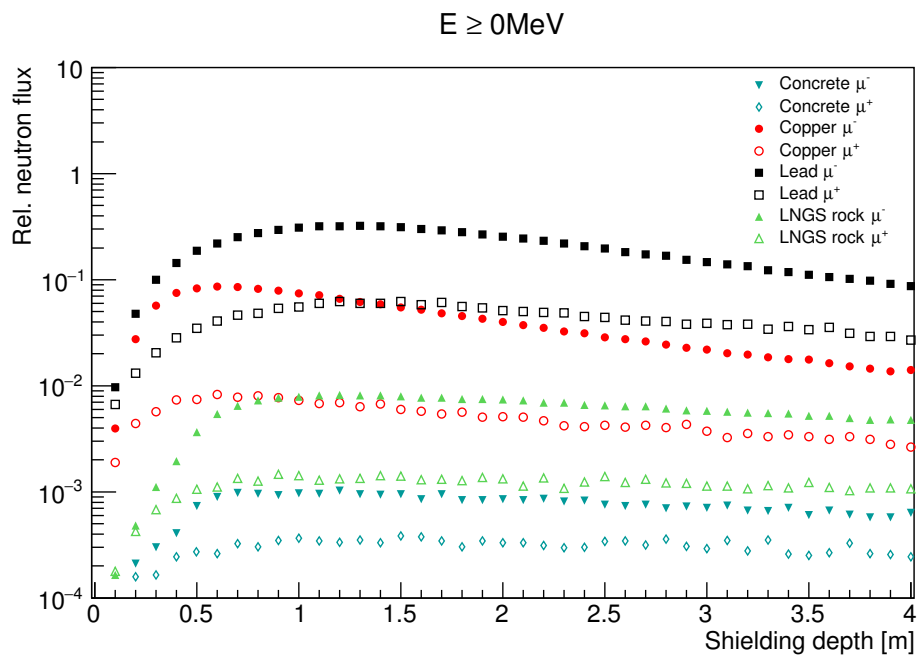


Figure 4.16: Muon-induced neutrons normalized to the incoming muons at different shielding depths.

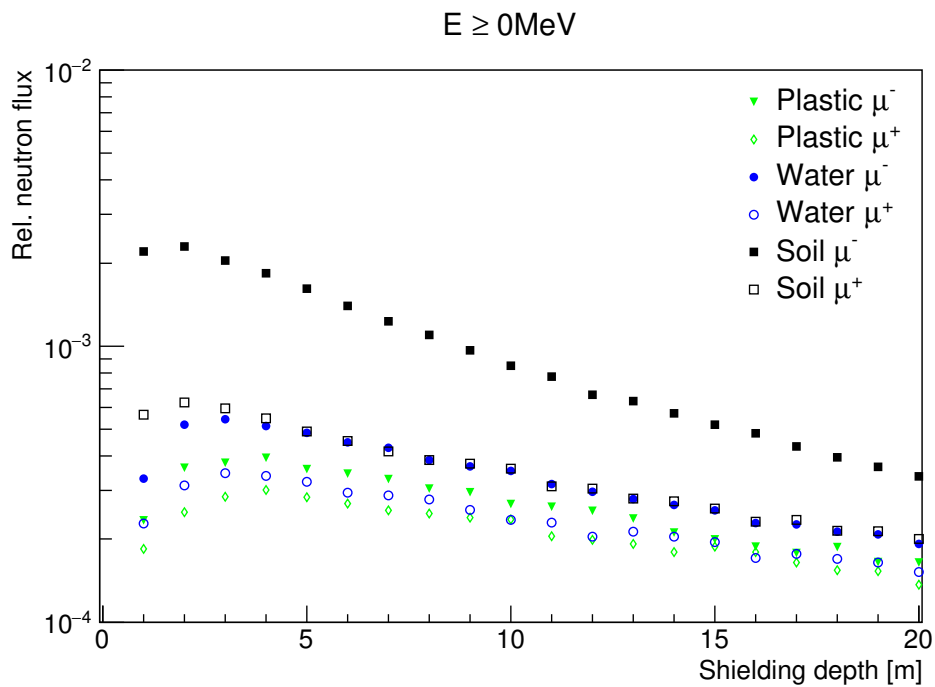


Figure 4.17: Muon-induced neutron flux at different depths of light shielding materials.

Table 4.8: Depths d_{max} at which the muon-induced neutron flux is the highest for different materials and the attenuation indices s in [1/m] and [1/mwe] if no energy cut is set.

Material	Muon	d_{max} [m]	d_{max} [mwe]	s [m ⁻¹]	s [mwe ⁻¹]
Plastic	μ^+	4 ± 1	3.7 ± 0.9	-0.0193 ± 0.0008	-0.0210 ± 0.0009
	μ^-	3 ± 1	2.8 ± 0.9	-0.0246 ± 0.0008	-0.0267 ± 0.0009
Water	μ^+	3 ± 1	3 ± 1	-0.021 ± 0.001	-0.021 ± 0.001
	μ^-	3 ± 1	3 ± 1	-0.0271 ± 0.0007	-0.0271 ± 0.0007
Soil	μ^+	2 ± 1	3 ± 2	-0.0264 ± 0.0009	-0.0160 ± 0.0005
	μ^-	2 ± 1	3 ± 2	-0.045 ± 0.001	-0.0276 ± 0.0006
Concrete	μ^+	1.2 ± 0.1	2.8 ± 0.2	-0.041 ± 0.008	-0.018 ± 0.004
	μ^-	1.1 ± 0.1	2.5 ± 0.2	-0.079 ± 0.004	-0.034 ± 0.002
LNGS rock	μ^+	1.1 ± 0.1	3.0 ± 0.3	-0.038 ± 0.006	-0.014 ± 0.002
	μ^-	1.2 ± 0.1	3.3 ± 0.3	-0.085 ± 0.003	-0.032 ± 0.001
Steel	μ^+	0.6 ± 0.1	4.8 ± 0.8	-0.046 ± 0.004	-0.0058 ± 0.0005
	μ^-	0.7 ± 0.1	5.5 ± 0.8	-0.065 ± 0.002	-0.0082 ± 0.0003
Copper	μ^+	0.7 ± 0.1	6.3 ± 0.9	-0.134 ± 0.005	-0.0149 ± 0.0006
	μ^-	0.6 ± 0.1	5.4 ± 0.9	-0.256 ± 0.003	-0.0285 ± 0.0003
Lead	μ^+	1.4 ± 0.1	16 ± 1	-0.122 ± 0.006	-0.0108 ± 0.0005
	μ^-	1.3 ± 0.1	15 ± 1	-0.238 ± 0.002	-0.0210 ± 0.0002

Figure 4.16 and Fig. 4.17 show the muon-induced neutron flux normalized to the incoming muons flux for different materials at different depths. More neutrons are produced if materials with higher atomic mass number are penetrated by muons. Also more neutrons are produced by μ^- than by μ^+ . The number of muon-induced neutrons differs for μ^+ and μ^- at all depths shown in Fig. 4.16 and Fig. 4.17. However, the difference becomes smaller at larger depths. This can be explained by the stopping muon rate. Since the mean muon energy increases with increasing depth (see chapter 3), also less neutrons are produced by muon capture and the difference between μ^- and μ^+ -induced neutrons decreases.

Also the depth d_{max} at which the muon-induced neutron flux reaches its maximum depends on the shielding material. A polynomial fit was applied to obtain the depths where the muon-induced neutron flux reaches its maximum. The results are shown in Table 4.8 if no energy cut on the neutrons is set. For different energy thresholds see Appendix E. It can be seen that d_{max} is smaller for materials with higher atomic mass number. Since the energy spectra of μ^+ and μ^- are similar (see Fig. 4.10), also the depth with the maximum muon-induced neutron flux is similar.

Table 4.8 also shows the attenuation indices s for muon-induced neutrons. The fit of Eq. 3.5 was applied to the muon-induced neutron fluxes. See Appendix F for the

attenuation indices if a cut on the neutron energy is set. The attenuation indices s for μ^- are smaller than for μ^+ . Like the cosmic-ray neutron and muon shielding indices, the attenuation indices of muon-induced neutrons are smaller for material with higher atomic mass number—except for lead. The attenuation indices for different energy thresholds are similar (see Appendix F). Comparing Table 4.8 with Table 4.6, it can be seen that attenuation indices of muon-induced neutrons are larger than shielding indices of cosmic-ray neutrons. This means that the muon-induced neutron flux starts to dominate the total neutron flux at a certain depth.

4.5 Total Neutron Flux

Before calculating the total neutron rate at given shielding depth, the total muon-induced neutron rate has to be calculated from the μ^+ and μ^- simulations. The muon charge ratio at sea-level is $\mu^+/\mu^- \sim 1.25$ [56]. From this ratio it follows that 55.6% of all muons are μ^+ and that 44.4% of all muons are μ^- . Figure 4.18 shows the μ^+ -induced, the μ^- -induced and the total muon-induced neutron fluxes calculated with this muon charge ratio. All fluxes are normalized to the incoming muon fluxes. It can be seen from Fig. 4.18 that the total muon flux resembles more the μ^- -induced neutron flux than the μ^+ -induced neutron flux, although there are more μ^+ than μ^- .

To calculate the total number of neutrons from the results of the neutron and muon simulations, the relative ratio of muons to neutrons has to be used. The relative ratio of the secondaries charge pions:protons:electrons:neutrons:muons is about 1:13:340:480:1420 at sea level [57]. From this it follows that 63% of the particles are muons and 21% are neutrons which means that the ratio of neutrons to muons is $\sim 1 : 3$. Therefore the cosmic-ray neutron results are weighted by a factor of 0.25, the μ^+ -results by a factor of 0.417 and the μ^- -results by a factor of 0.333.

In Fig. 4.19 the total simulated neutron energy spectrum is shown together with the energy spectra of cosmic-ray neutrons and total muon-induced neutrons. All energy spectra has been normalized to the total fluxes. It can be seen that only at low energies all spectra are similar.

In Fig. 4.20, the total neutron flux for lead at different shielding depths is shown together with the cosmic-ray neutron flux and the muon-induced neutron flux. The number of incoming cosmic-ray neutrons was chosen for normalization. It can clearly be seen that the muon-induced neutron flux becomes larger than the cosmic-ray neutron flux at a given depth. For small shielding depths, the total neutron flux is dominated by cosmic-ray secondary neutrons. With increasing shielding depth, the total neutron flux is dominated by muon-induced neutrons.

Table 4.9 shows the shielding depths d_{eq} at which the muon-induced neutron flux becomes equal to the cosmic-ray neutron flux for different shielding materials and for different energy thresholds if the cosmic-ray neutrons were distributed according to the

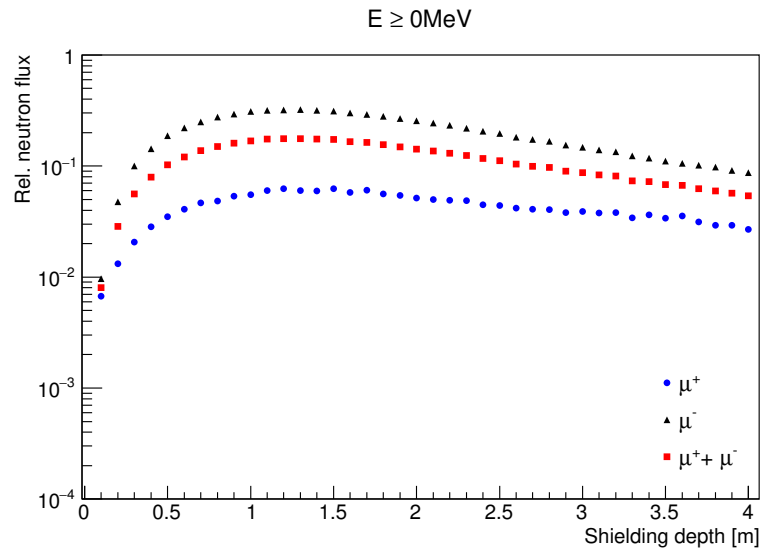


Figure 4.18: Total muon-induced, μ^+ -induced and μ^- -induced neutron flux normalized to the incoming muons at different shielding depths if lead is penetrated.

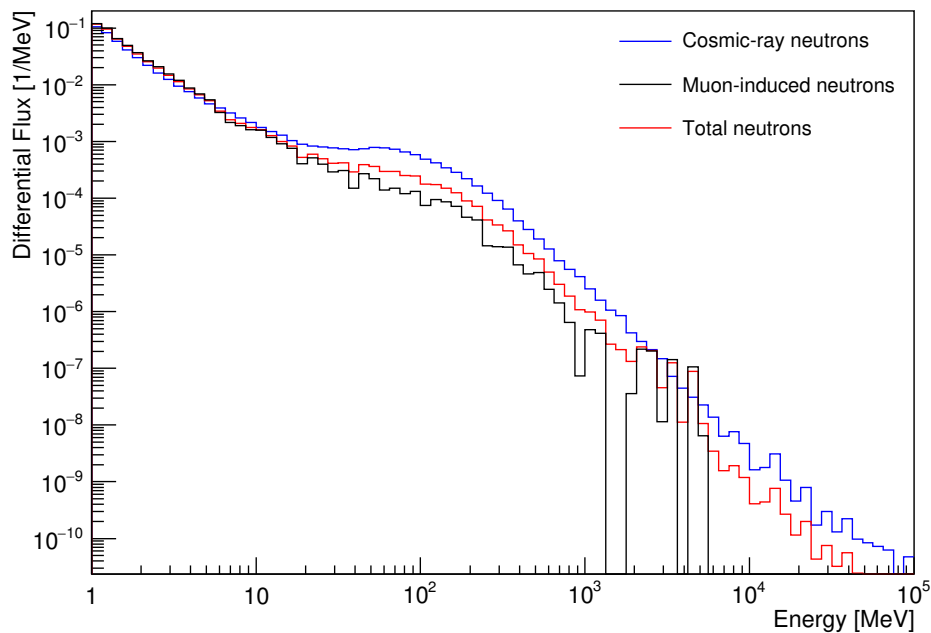


Figure 4.19: Energy spectra comparison at 3 dm if copper is penetrated. For the cosmic-ray neutrons only vertically downwards going neutrons were injected. All energy spectra are normalized to the total fluxes.

Table 4.9: Shielding depth d_{eq} at which the cosmic neutron flux and the muon-induced neutron flux are equal and the total neutron flux (per arriving cosm. neutron) at this depth for different energy thresholds. The cosmic-ray neutrons were injected according to a distribution suggested by Nesterenok for high energetic neutrons.

Material	Threshold [MeV]	Depth [m]	Depth [mwe]	Total neutron flux
Plastic	0	8.0 ± 0.5	7.4 ± 0.5	0.00183 ± 0.00003
	1	8.0 ± 0.5	7.4 ± 0.5	0.00167 ± 0.00003
	20	9.0 ± 0.5	8.3 ± 0.5	0.00088 ± 0.00002
	200	8.0 ± 0.5	7.4 ± 0.5	0.00037 ± 0.00001
Water	0	8.0 ± 0.5	8.0 ± 0.5	0.00164 ± 0.00003
	1	8.0 ± 0.5	8.0 ± 0.5	0.00140 ± 0.00003
	20	8.0 ± 0.5	8.0 ± 0.5	0.00112 ± 0.00003
	200	8.0 ± 0.5	8.0 ± 0.5	0.00029 ± 0.00001
Soil	0	5.0 ± 0.5	8.3 ± 0.8	0.00455 ± 0.00004
	1	5.0 ± 0.5	8.3 ± 0.8	0.00302 ± 0.00004
	20	5.0 ± 0.5	8.3 ± 0.8	0.00191 ± 0.00004
	200	5.0 ± 0.5	8.3 ± 0.8	0.00040 ± 0.00002
Concrete	0	3.20 ± 0.05	7.4 ± 0.1	0.00286 ± 0.00006
	1	3.30 ± 0.05	7.6 ± 0.1	0.00221 ± 0.00005
	20	3.60 ± 0.05	8.3 ± 0.1	0.00115 ± 0.00004
	200	3.50 ± 0.05	8.1 ± 0.1	0.00034 ± 0.00002
LNGS rock	0	2.60 ± 0.05	7.0 ± 0.1	0.0217 ± 0.0002
	1	2.90 ± 0.05	7.9 ± 0.1	0.00708 ± 0.00009
	20	3.30 ± 0.05	8.9 ± 0.1	0.00194 ± 0.00005
	200	3.20 ± 0.05	8.7 ± 0.1	0.00041 ± 0.00002
Steel	0	1.00 ± 0.05	7.9 ± 0.4	0.2577 ± 0.0004
	1	0.90 ± 0.05	7.1 ± 0.4	0.0395 ± 0.0002
	20	1.30 ± 0.05	10.3 ± 0.4	0.00249 ± 0.00004
	200	1.30 ± 0.05	10.3 ± 0.4	0.00037 ± 0.00002
Copper	0	0.90 ± 0.05	8.1 ± 0.4	0.2459 ± 0.0006
	1	0.90 ± 0.05	8.1 ± 0.4	0.0306 ± 0.0002
	20	1.20 ± 0.05	10.8 ± 0.4	0.00251 ± 0.00006
	200	1.20 ± 0.05	10.8 ± 0.4	0.00034 ± 0.00002
Lead	0	1.70 ± 0.05	19.3 ± 0.6	0.962 ± 0.001
	1	1.00 ± 0.05	11.3 ± 0.6	0.1065 ± 0.0003
	20	1.20 ± 0.05	13.6 ± 0.6	0.00244 ± 0.00004
	200	1.30 ± 0.05	14.7 ± 0.6	0.00030 ± 0.00002

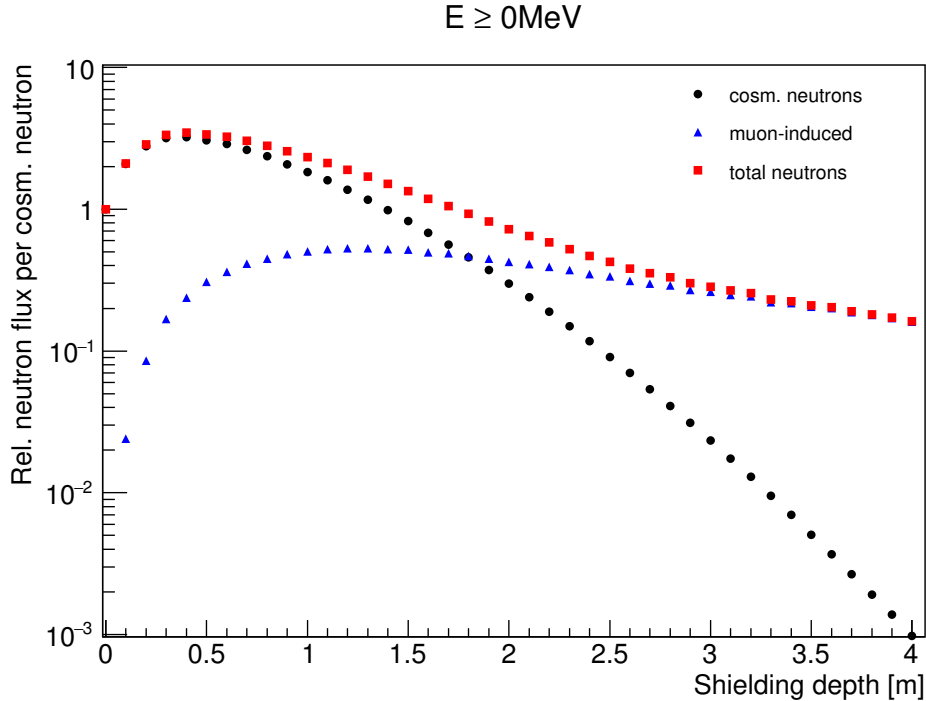


Figure 4.20: Total neutron flux at different shielding depths for lead normalized to the incoming cosmic-ray neutrons. All cosmic-ray neutrons were injected vertically downwards going.

distribution suggested by Nesterenok. For only vertically downwards going neutrons and the isotropically distribution see Appendix G. It can be seen that the muon-induced neutron flux starts to dominate at smaller depths for materials with higher atomic mass number. No relation between the set neutron energy threshold and the shielding depth at which the cosmic-ray and muon-induced neutron fluxes are equal could be found. In Table 4.9, also the total neutron fluxes at these depths are shown. The total neutron fluxes at d_{eq} are higher for materials with higher atomic mass. For materials with lower atomic mass, less neutrons are shielded but also less neutrons are induced by muons (see section 4.2 and section 4.4).

In Fig. 4.21 and Fig. 4.22, the total neutron fluxes for different materials are shown if no threshold and a threshold of 20 MeV are set on the neutron energy. If no energy threshold is set, there are less neutrons if concrete is used as shielding material than if other materials are used. For neutrons with energies higher than 20 MeV this is not the case. There are less neutrons with $E \geq 20$ MeV if copper, lead or steel is used as shielding material. This shows that the best choice of shielding material depends on the neutron energy which has to be shielded.

For the production of ^{60}Co and ^{68}Ge , which are the most dangerous isotopes mainly produced above ground, only fast neutrons are relevant [69]. Thus, steel which was chosen as shielding material for GERDA Phase II material transport [6] is a good choice.

For the shielding design simulations, only cosmic-ray neutrons and protons were con-

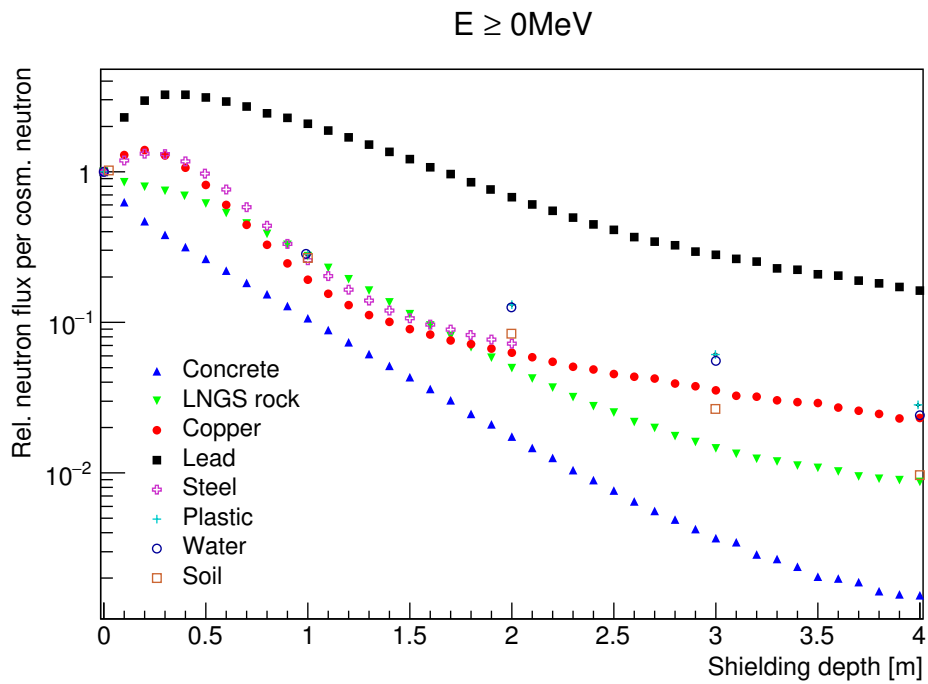


Figure 4.21: Total neutron flux at different shielding depths for different materials. The outgoing neutrons were normalized to the incoming cosmic-ray neutrons which were distributed by Eq. 3.3 (suggested by Nesterenok).

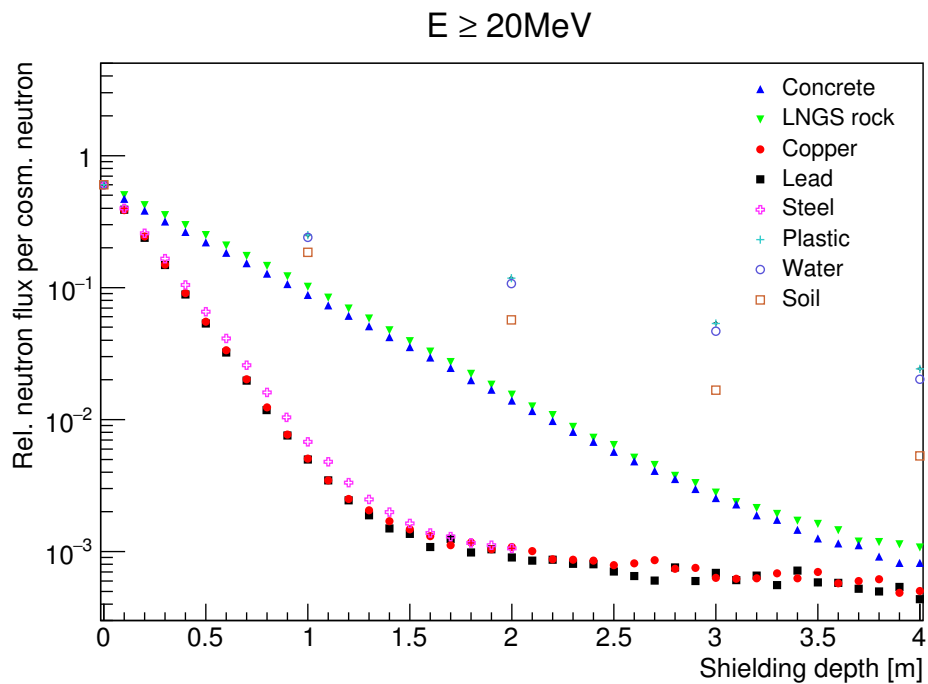


Figure 4.22: Total neutron flux with $E \geq 20\text{ MeV}$ at different shielding depths for different materials. The outgoing neutrons were normalized to the incoming cosmic-ray neutrons which were distributed by Eq. 3.3 (suggested by Nesterenok).

sidered, since muon-induced neutrons would only contribute with 2% [69]. However, this is only true for very small shielding thicknesses. From Fig. 4.20 it can be seen that the muon-induced neutron contribution increases to 10% if a lead shield of 50 cm thickness is used and to even 25% if a lead shield of 1 m thickness is used. Thus also muon-induced neutrons have to be considered for further optimizing shielding designs.

Chapter 5

The MINIDEX Experiment

Muon-induced neutrons may limit future low-background experiments due to the production of radioisotopes. Therefore reliable Monte Carlo simulations are needed for designing such experiments and for background estimations. However, the muon-induced neutron production rates especially for high-Z materials are not well understood and Monte Carlo simulations do not always reproduce the data well (see section 3.3). In this chapter, the **Muon-Induced Neutron Indirect Detection EXperiment MINIDEX** [5] is presented. MINIDEX aims to investigate the muon-induced neutron production in different high-Z materials with two germanium detectors at shallow underground laboratories. It is running in the Tübingen Shallow Underground Laboratory since July 2015.

The principle and the setup of MINIDEX is described in section 5.1. The different run configurations and the analysis are described in section 5.2 and section 5.3.

For comparing MINIDEX data with Monte Carlo simulations, the muon energy spectra and angular distributions inside the laboratory are needed. Muon simulations with MaGe were conducted to get these distributions: a simplified and a more detailed simulation were conducted. These have been used as an input for the MINIDEX simulations (see [75]). The results of the cosmic-ray simulations are presented in section 5.4. In section 5.5 the angular distributions from Monte Carlo simulations are compared to the muon flux map inside the laboratory measured by A. Hegai [76].

5.1 Principle and Setup

MINIDEX aims to measure the muon-induced neutron rate. The principle of MINIDEX is illustrated by Fig. 5.1. The neutrons are produced inside a target which surrounds a water container and two germanium detectors. Water is used to thermalize the muon-induced neutrons which are then captured on hydrogen. If neutrons gets captured on hydrogen, 2.2 MeV neutron capture gammas are emitted which can be detected by the germanium detectors. For identification of passing muons, plastic scintillators above and below the target are used. They trigger if a muon is passing through the setup.

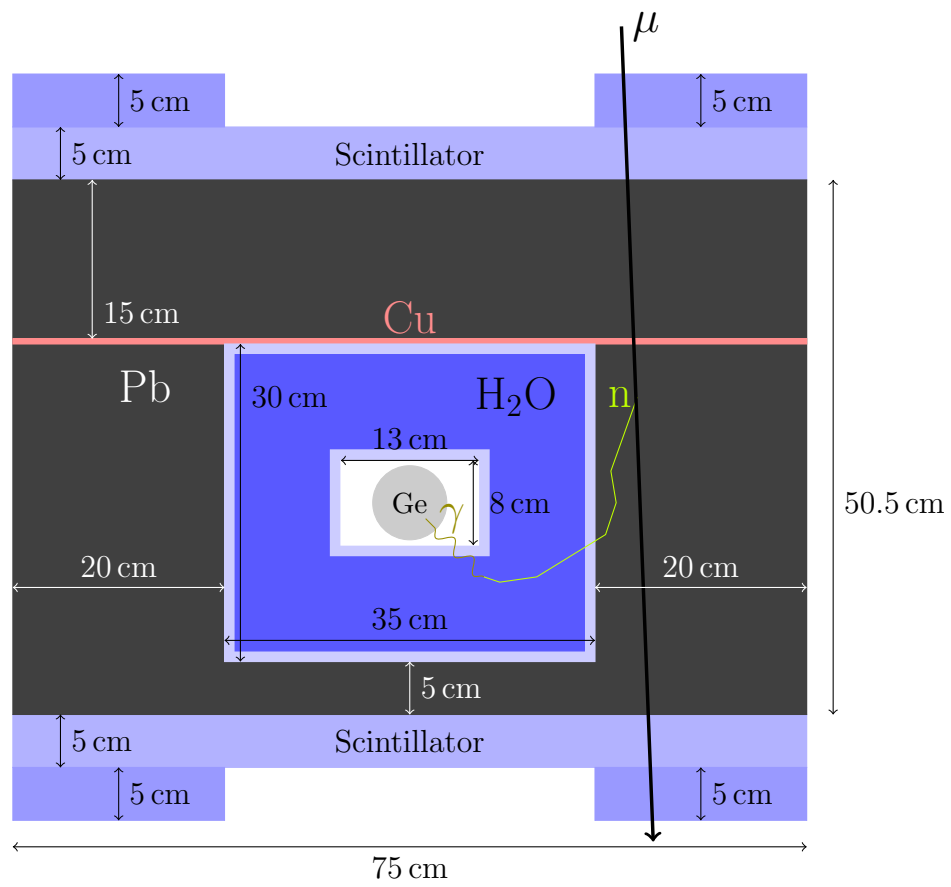


Figure 5.1: Sketch of the MINIDEX concept.

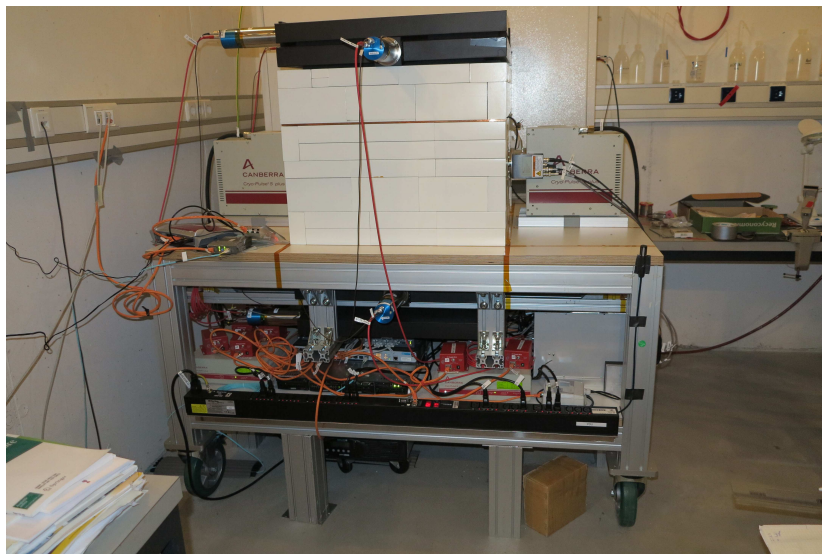


Figure 5.2: The MINIDEX setup. Photo from Raphael Kneißl.

The MINIDEX setup (see Fig. 5.2) is located at the Tübingen Shallow Underground Laboratory which has an overburden of ~ 16 mwe [75]. For the first runs, lead was chosen as target material. The outer dimensions of the lead castle are $65\text{ cm} \times 75\text{ cm} \times 50.5\text{ cm}$. It is placed on top of an aluminum table and surrounds a water container made of plastic ($\text{C}_{10}\text{H}_8\text{O}_4$). The outer dimensions of the water container are $55\text{ cm} \times 35\text{ cm} \times 30\text{ cm}$. The thickness of the plastic container walls are 1 cm. As support for the lead bricks above the water container, a 0.5 cm thick copper plate is placed on top of the water container.

To detect the neutron capture gammas, two high-purity germanium detectors (HPGe) are used which are commercial Extended Range Coaxial Ge Detectors (XtRa) produced by CANBERRA. They are p-type detectors with a diameter of $\sim 7\text{ cm}$, a length of $\sim 6.35\text{ cm}$ and an energy resolution of 2 keV at 1.3 MeV. Both detectors are electrically cooled and are operated with +3000 V and +3500 V on the n+ contact. They are placed inside a central rectangular hole which runs along the entire water container length facing each other. The hole has a length of 55 cm and has a rectangular shape with 8 cm height and 13 cm width.

For muon event identification, plastic scintillators from Saint-Gobain are placed on top of the lead castle and underneath the tabletop. Two big scintillator panels with $65\text{ cm} \times 75\text{ cm} \times 5\text{ cm}$ are placed above and below the target material. Four smaller scintillator panels with $65\text{ cm} \times 20\text{ cm} \times 5\text{ cm}$ are used additionally to distinguish muons penetrating only lead from muons passing through lead and water. Two of the small scintillators are placed on top and the other two are placed on the bottom of the target material.

All detector signals from the germanium detectors and the scintillators are recorded independently. The time correlation analysis is done off-line.

5.2 Run Configurations

In run I (July 15th – November 25th, 2015), only the two big scintillator panels were used: one placed on top, the other placed below. Therefore it could not be distinguished between muons passing only through lead and muons passing through lead and water. This distinction is possible since run II (January 27th – November 11st, 2016).

During run II, also a fast neutron detector of the Tshinghua University, which was filled with organic liquid scintillator doped with gadolinium, was placed next to the MINIDEX set-up. In contrast to MINIDEX, which detects signals only from thermalized neutrons, it can detect signatures from thermal as well as from fast neutrons.

In run III (November 16th, 2016 – May 5th, 2017), one side of the lead castle was replaced by copper.

5.3 Analysis and Background

The energy resolution is constantly evaluated using the ^{40}K line at 1460 keV. The water level as well as the water temperature are measured constantly. [5]

The signal is a 2.2 MeV gamma from the neutron capture on hydrogen which appears within a short time window ($\sim \mu\text{s}$) after a through-going muon. The time window is much smaller than the mean time between two muons. The size of the time window is not fixed but is varied for the analysis. The number of neutron captures is determined by fitting a Gaussian plus a first order polynomial. [5]

Any energy depositions of 2.2 MeV in one of the two germanium detectors is background. Background can be produced by cosmic-ray neutrons, natural radioactivity, muon capture and non-triggered muons. Since outside the signal window only background events occur, the background can be measured between the end of the signal window time and the time of the next through-going muon.

Within the signal window, signal and background events occur. With the determined background rate, the signal rate can be calculated by subtracting the background rate. The measured neutron production rate can be compared to Monte Carlo predictions.

5.4 Cosmic-Ray Simulations

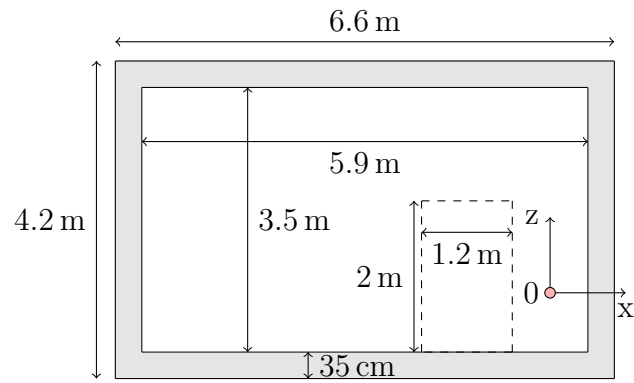
The Monte Carlo simulations of MINIDEX are divided into two steps. In the first step, the passage of cosmic-ray muons and neutrons through the overburden of the Tübingen Shallow Underground Laboratory is simulated to get the energy spectra and the angular distributions inside the laboratory. These simulations are described in this section. The results serve as input for further simulations in which the interactions of muons and neutrons with the MINIDEX setup are simulated. The analysis of the second Monte Carlo step is similar to the data analysis described in section 5.3. For more details see [5].

Flat Overburden As starting point, cosmic-ray μ^+ , μ^- and neutrons passing through a flat overburden corresponding to 16 mwe above the laboratory were simulated with MaGe using GEANT4 version 9.6 patch 2. The dimensions of the laboratory are shown in Fig. 5.3. The origin of the coordinate system was chosen to be in the middle between the two germanium detectors of the MINIDEX setup.

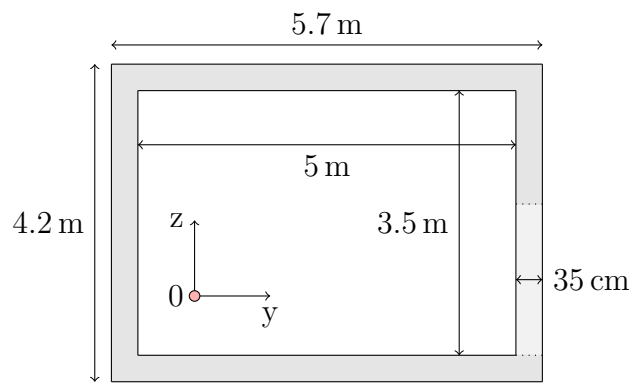
For the 35 cm thick concrete walls, a density of $\rho = 3.56 \text{ g cm}^{-3}$ is assumed. If a soil overburden with a density of $\rho = 1.65 \text{ g cm}^{-3}$ is assumed, a thickness of 9 m soil is needed to reach 16 mwe.

A soil overburden with $8.6 \text{ m} \times 7.7 \text{ m} \times 9 \text{ m}$ was placed above the laboratory. The generation plane was located above the soil hill and has an area of

$$A_{gen} = 8.6 \text{ m} \times 7.7 \text{ m} = 66.22 \text{ m}^2. \quad (5.1)$$



(a) x-z plane



(b) y-z plane

Figure 5.3: Sketch of the Tübingen Shallow Underground Laboratory.

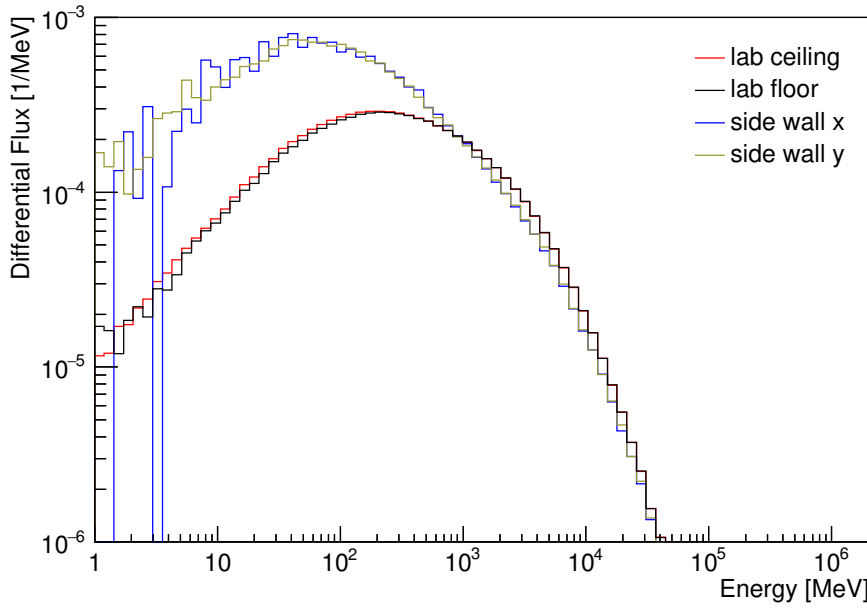


Figure 5.4: Energy spectra of μ^+ at different laboratory planes. All spectra are normalized to 1.

For each particle kind (cosmic-ray neutrons, μ^+ and μ^-), $N_{gen} = 9.999 \cdot 10^7$ particles were generated. The muon energy spectrum of [59] was used for the muon simulations. For the cosmic-ray neutron simulations, the energy spectrum of [60] and the angular distribution suggested by A. Nesterenok [61] was used (see section 3.1).

Only 106 cosmic-ray neutrons reach the laboratory ceiling which is $\sim 10^{-6}$ of the injected neutrons. The number of muon-induced neutrons is two orders of magnitude larger: the fraction of μ^+ -induced neutrons to injected μ^+ is $1.63 \cdot 10^{-4}$ and the fraction of μ^- -induced neutrons to injected μ^- is $7.16 \cdot 10^{-4}$. Thus, the cosmic-ray neutron component is negligible.

Figure 5.4 shows the energy spectra of μ^+ crossing different laboratory planes. The energy spectra of μ^- are similar (see section 4.3). It can be seen from Fig. 5.4 that the energy spectra of muons passing the side walls differ from the spectra of muons passing the ceiling or the floor.

The nadir angle θ and the azimuth angle φ can be calculated from the stored momentum information:

$$\theta = \arccos\left(-\frac{p_z}{p}\right) \quad (5.2)$$

$$\varphi = \begin{cases} \arccos\left(\frac{p_x}{p_{xy}}\right) + \pi, & p_y > 0 \\ \pi - \arccos\left(\frac{p_x}{p_{xy}}\right), & p_y \leq 0 \end{cases} \quad \text{with } p_{xy} = \sqrt{p_x^2 + p_y^2} \quad (5.3)$$

with the momentum in x , y and z -direction, the total momentum p and the projection in the xy -plane p_{xy} .

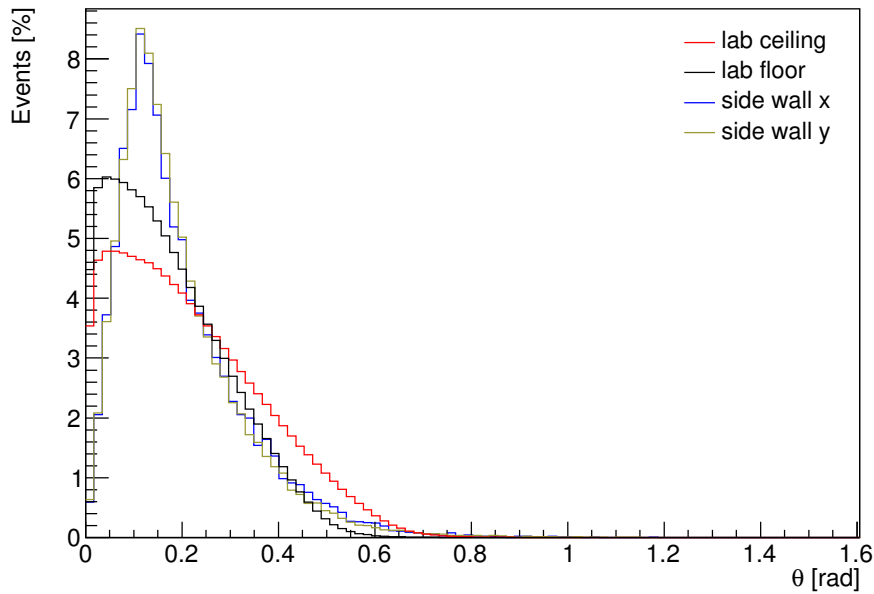


Figure 5.5: Nadir angle θ distributions of μ^- at different laboratory plans. Spectra are normalized to 1.

In Fig. 5.5 the nadir-angle distributions of μ^- passing different laboratory planes are shown. It can clearly be seen that the distribution depends on the entering plane. High θ -values are more unlikely at the side walls than at the ceiling. This may indicate that the generation plane is not large enough, since one would expect it vice versa.

Figure 5.6 shows the azimuth-angle distributions of muons passing different laboratory planes. Since no azimuth distribution was set for the simulations, the φ -values should be equally distributed at the laboratory ceiling and at the floor. From Fig. 5.6 it can be seen that this is not the case, since there are variations of the order of $\sim 20\%$. Thus, the generation plane must be enlarged.

Hill Overburden For a generation plane larger than the area of the laboratory, the shape of the laboratory overburden has to be considered. The approximated shape of the hill overburden made of soil was included in the used geometry of the Monte Carlo simulations. The implemented overburden with its dimensions is shown in Fig. 5.7. Also the tunnel which leads to the laboratory was included.

The generation plane has an area of $A_{gen} = 50 \text{ m} \times 50 \text{ m}$ and is centered 9 m above MINIDEX located at the origin of the coordinate system. For each muon charge (μ^+ and μ^-), $N_{gen} = 2 \cdot 10^8$ particles were injected.

It was investigated how large the generation plane has to be to include all muons which can reach the laboratory. For each started muon track, it was calculated whether

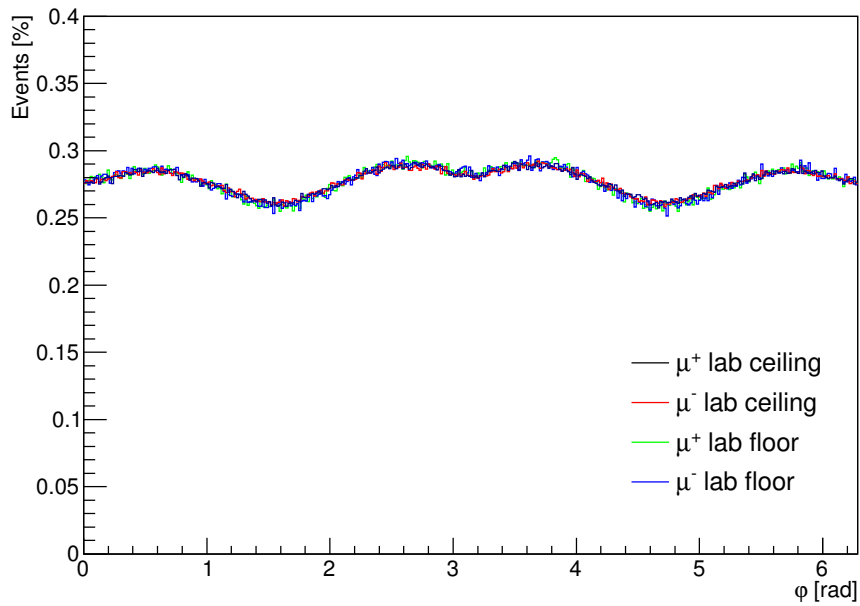
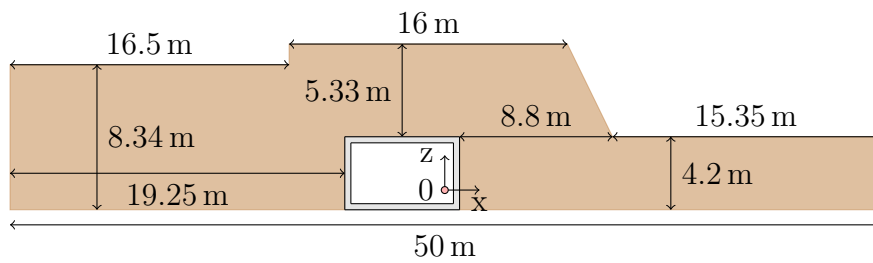
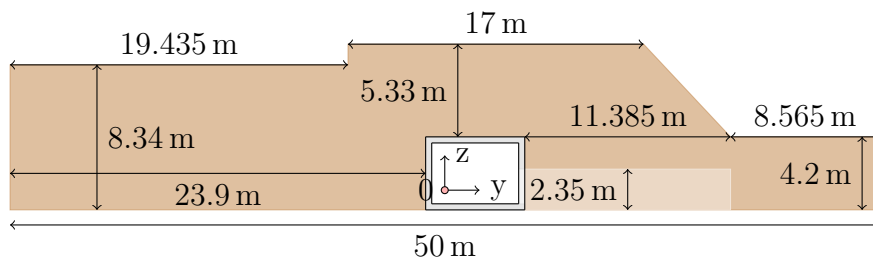


Figure 5.6: Azimuth angle φ distributions of muons at different laboratory planes. Spectra are normalized to 1.



(a) x-z plane



(b) y-z plane

Figure 5.7: Sketch of the Tübingen Shallow Underground Laboratory overburden.

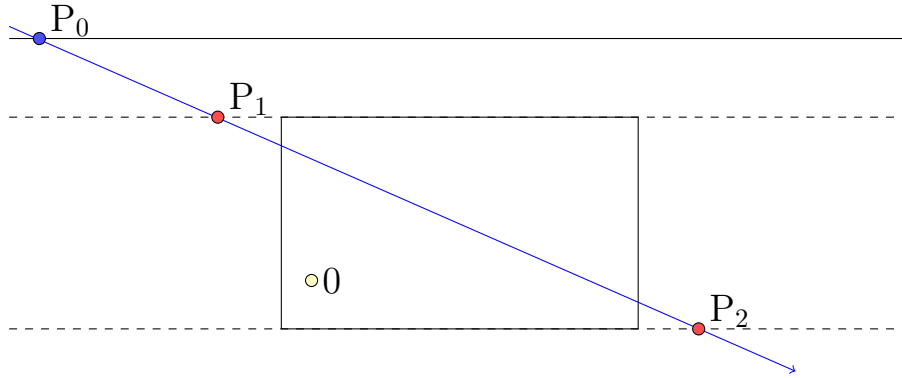


Figure 5.8: Illustration of the interception investigation.

the muon is going towards the laboratory or not. Since the location where the injected particle is entering the hill geometry

$$P_0 = \begin{pmatrix} x_0 \\ y_0 \\ z_0 \end{pmatrix} \quad (5.4)$$

and its momentum at this point

$$p = \begin{pmatrix} p_x \\ p_y \\ p_z \end{pmatrix} \quad (5.5)$$

are known, the muon track can be parameterized by

$$f(z) = \begin{pmatrix} m \cdot z + a \\ n \cdot z + b \\ z \end{pmatrix} \quad (5.6)$$

with

$$m = \frac{p_x}{p_z}, \quad n = \frac{p_y}{p_z}, \quad a = x_0 - m \cdot z_0, \quad b = y_0 - n \cdot z_0. \quad (5.7)$$

The investigation of the interception with the laboratory is illustrated in Fig. 5.8. The interception points at the level of the laboratory ceiling (P_1) and the laboratory floor (P_2) were calculated. If these points do not belong to the laboratory ceiling or floor, also the interception points with the sidewalls were calculated. If there are interception points with the laboratory boundary, the momentum of the started muon points towards the laboratory.

Table 5.1 shows the fraction of muons which are going towards or through the laboratory for different planes. Around half of the muons entering the laboratory are generated inside an area of the size smaller than $10 \text{ m} \times 10 \text{ m}$. However, it can be seen from Table 5.1

Table 5.1: Number of muons which are going towards or through the laboratory for different planes divided by the values of $50\text{ m}\times 50\text{ m}$ in [%].

	10 m×10 m	20 m×20 m	30 m×30 m	40 m×40 m
μ^+ towards lab	51.4	88.4	98.2	99.9
μ^+ inside lab	58.3	92.4	99.1	100
μ^- towards lab	51.4	88.5	98.2	99.9
μ^- inside lab	58.4	92.4	99.1	100.0

that a generation plane of $30\text{ m}\times 30\text{ m}$ is needed for containing nearly all generation points of muons which are going towards the laboratory.

To determine the fluxes of incoming muons and muon-induced particles, particles entering the laboratory from all walls were counted and the fluxes of each wall were determined. For calculating the particle fluxes inside the laboratory Φ_{lab} , the simulated time t_{sim} has to be calculated from N_{gen} , A_{gen} and the particle flux Φ_{ground} on ground:

$$t_{sim} = \frac{N_{gen}}{\Phi_{ground} \cdot A_{gen}}. \quad (5.8)$$

The particle flux Φ at the walls of the laboratory is given by

$$\Phi = \frac{N}{A \cdot t_{sim}} = \frac{N \cdot A_{gen}}{N_{gen} \cdot A} \cdot \Phi_{ground}. \quad (5.9)$$

with A being the area of the wall and N the number of particles passing through this area.

At sea level, the muon flux of muons with an energy higher than 1 GeV is

$$\Phi_{\mu} = 135.2\text{ m}^{-2}\text{ s}^{-1} \quad [77]. \quad (5.10)$$

Muon with energies less than 1 GeV are shielded before reaching the laboratory. Considering a muon charge ratio of

$$\frac{\mu^+}{\mu^-} \sim 1.25 \quad [56], \quad (5.11)$$

the μ^+ and μ^- fluxes at sea level are

$$\Phi_{\mu^+} = 75.11\text{ m}^{-2}\text{ s}^{-1}, \quad \Phi_{\mu^-} = 60.09\text{ m}^{-2}\text{ s}^{-1}. \quad (5.12)$$

The area of the ceiling and the floor is 29.5 m^2 and for the side walls $A_{side\ x} = 20.65\text{ m}^2$ and $A_{side\ y} = 17.5\text{ m}^2$. For the side wall containing the doorway (side wall x_2), the area of the laboratory door (2.4 m^2) was subtracted, since no particles were stored at this area. The area of this side wall is therefore 18.25 m^2 .

Table 5.2: Fluxes of entering muons and muon-induced neutrons in [$\text{m}^{-2} \text{s}^{-1}$] at different laboratory planes.

Location	Φ_{μ^+}	Φ_n by μ^+	Φ_{μ^-}	Φ_n by μ^-
Lab Ceiling	48.065 ± 0.039	0.2901 ± 0.0030	38.495 ± 0.031	1.4848 ± 0.0061
Side wall x_1	1.5943 ± 0.0085	0.0697 ± 0.0018	1.2752 ± 0.0068	$0.3417 \pm 0, 0035$
Side wall x_2	6.353 ± 0.018	0.2587 ± 0.0036	5.051 ± 0.014	1.3354 ± 0.0074
Side wall y_1	6.379 ± 0.019	0.2596 ± 0.0037	5.112 ± 0.015	1.3437 ± 0.0076
Side wall y_2	0.8293 ± 0.0067	0.0501 ± 0.0016	0.6675 ± 0.0054	0.2402 ± 0.0032

The muon and muon-induced neutron fluxes are shown in Table 5.2. The μ^+ fluxes are higher than the μ^- fluxes due to the higher μ^+ flux above the overburden. The μ^+/μ^- ratio has not been changed (see also section 4.3). The muon flux from the ceiling is dominating. The contributions from each side wall is up to about 13% of the muon flux at the ceiling. In contrast to the muon flux, the contributions from the walls for muon-induced neutrons are of the same order as from the ceiling.

The number of μ^- entering the laboratory at different locations on the respective walls is shown in Fig. 5.9. At the ceiling, the muons are nearly equally distributed with deviations from the average flux of about 14%. The deviations at the side walls are much larger. There are much less muons at the lower part (up to ~ 80 cm above the floor). These muons can not create a trigger in MINIDEX which is placed 90.5 cm above the floor. The deviations at the upper wall part are still in the order of $\sim 30\%$ and can not be neglected.

The energy spectrum of μ^- entering at different laboratory planes is shown in Fig. 5.10. It can be seen that the energy spectra of muons entering at different planes hardly differ.

The μ^+ and μ^- -induced neutron energy spectra at the ceiling are compared with each other in Fig. 5.11. It can clearly be seen that they differ significantly. The fraction of low energetic neutrons is larger for the μ^+ -induced neutrons. For μ^- -induced neutrons, the fraction of high energetic neutrons is larger. Since only μ^- can be captured resulting in the creation of further neutrons (see section 3.2), this difference is attributed to neutrons created by muon capture.

The azimuth angle φ distributions of μ^- and μ^- -induced neutrons entering the laboratory from different sides are shown in Fig. 5.12. The distributions from the μ^+ -induced neutrons do not differ from the distributions from the μ^- -induced neutrons. From Fig. 5.12 it can be seen that particles are uniformly distributed at the ceiling as expected. The structure of the side wall distributions is due to the fact that only for certain φ values the particle is going inside the laboratory depending on the side wall.

The nadir angle θ distribution of μ^- and μ^- -induced neutrons entering the laboratory from different sides is shown in Fig. 5.13. For the ceiling and the floor, not all θ values

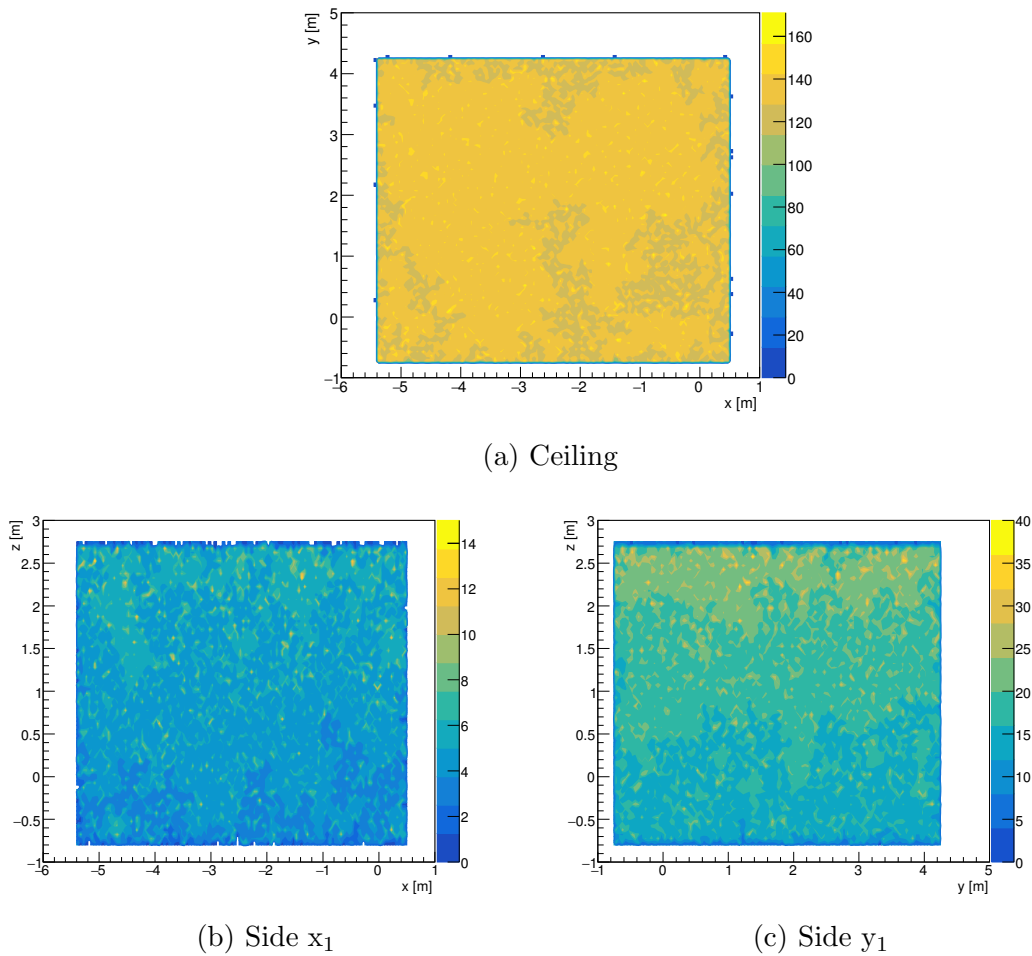


Figure 5.9: Location of the μ^- entry points at the laboratory ceiling and the side walls x_1 and y_1 .

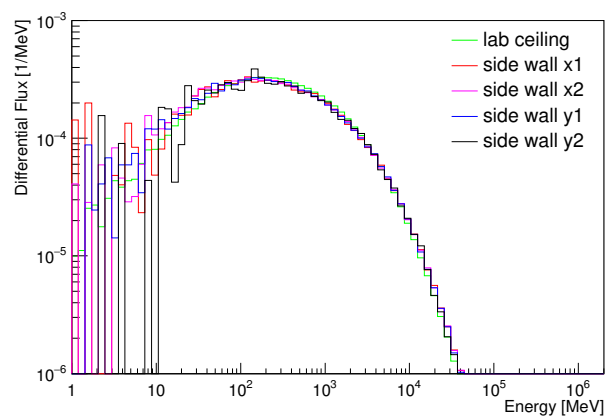


Figure 5.10: Energy spectrum of μ^- entering the laboratory from different sides. All spectra are normalized to 1.

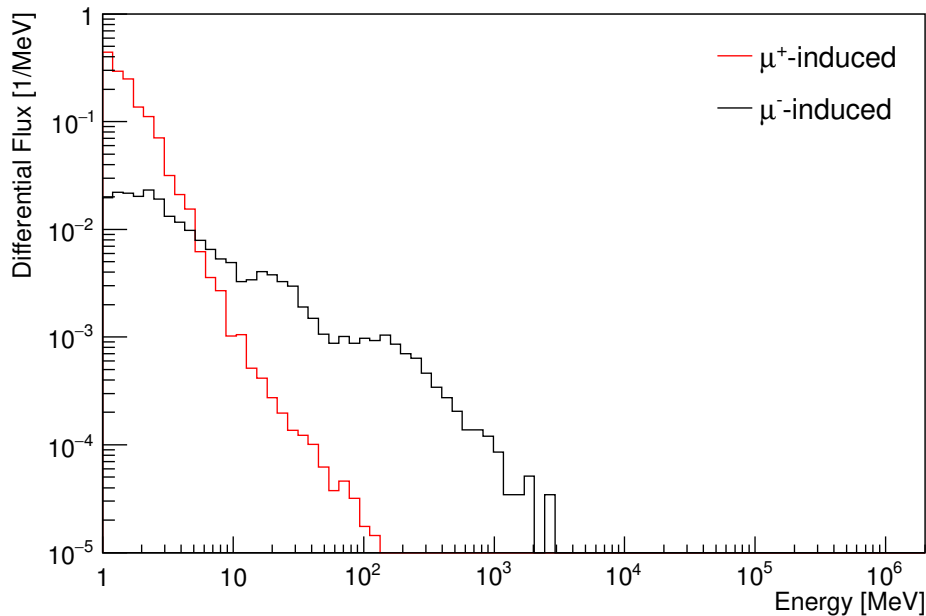


Figure 5.11: Energy spectrum of muon-induced neutrons at the ceiling. All spectra are normalized to 1.

are possible, since only particles with $\theta < \frac{\pi}{2}$ enter the laboratory (ceiling) and particles with $\theta > \frac{\pi}{2}$ leave the laboratory (floor). Most muons have small θ values, since muons on ground follow a $\cos^2(\theta)$ distribution and therefore small θ values are more likely. Also muons with small θ values have traveled a shorter distance than muons with a higher θ values. Thus, less muons are shielded by the overburden.

As the φ distributions, also the θ distributions do not differ for μ^+ - and μ^- -induced neutrons. From Fig. 5.13 it can be seen that the θ distributions of muon-induced neutrons are much broader. Contrary to the muon distributions where more particles are going downwards, the information of the incident muon direction gets lost for muon-induced neutrons and the number of upwards going neutrons is nearly equal to the number of downwards going neutrons.

Also the $\theta - \varphi$ correlation was investigated. In Fig. 5.14, θ is plotted against φ . It can be seen that for a given θ value all φ values have the same possibility. No significant correlation can be seen. Therefore it is safe to assume that θ and φ are independent. Since the φ distribution is isotropic for all particles, only the θ distributions are needed as an input for further MINIDEX simulations.

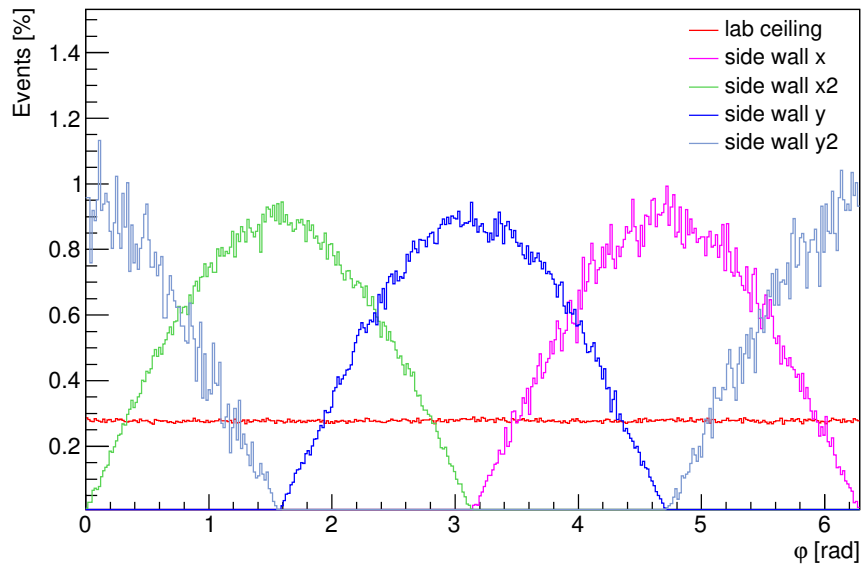
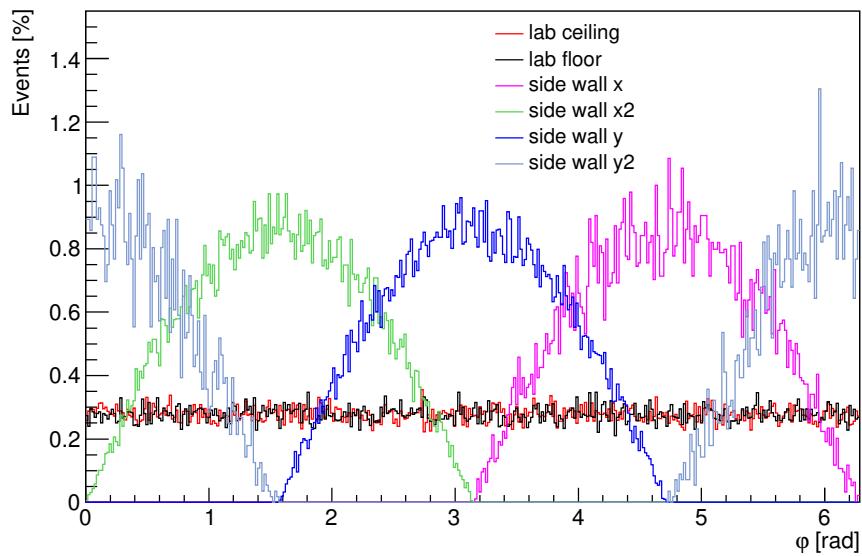
(a) μ^- (b) μ^- -induced neutrons

Figure 5.12: Azimuth angle φ distributions of μ^- and μ^- -induced neutrons entering the laboratory from different sides.

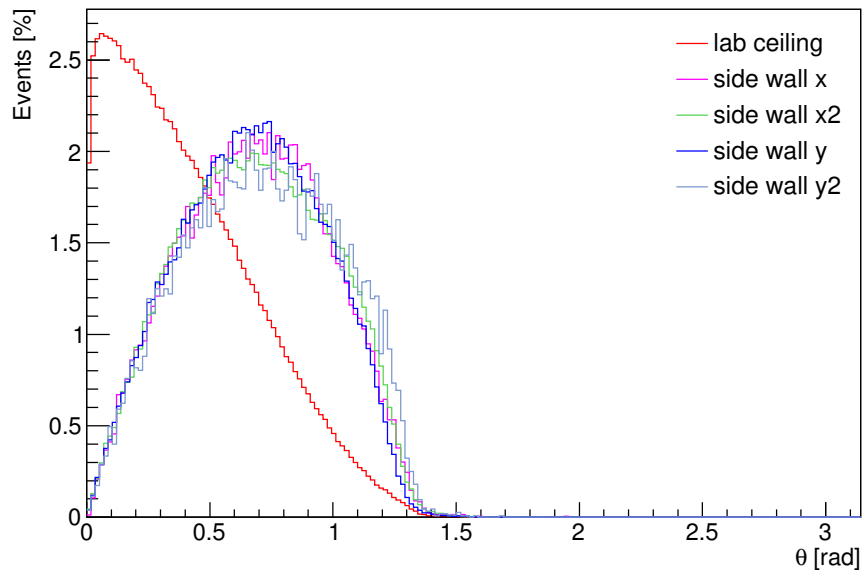
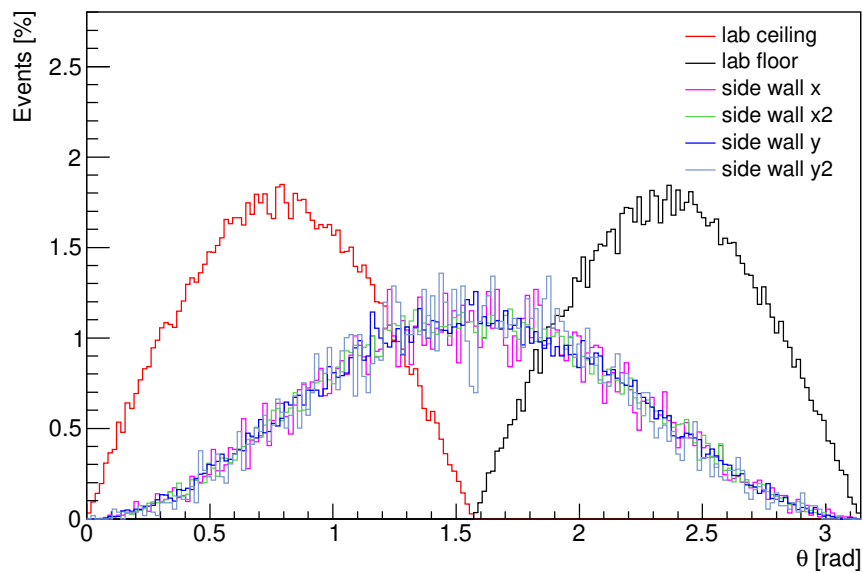
(a) μ^- (b) μ^- -induced neutrons

Figure 5.13: Nadir angle θ distribution of μ^- and μ^- -induced neutrons entering the laboratory from different sides.

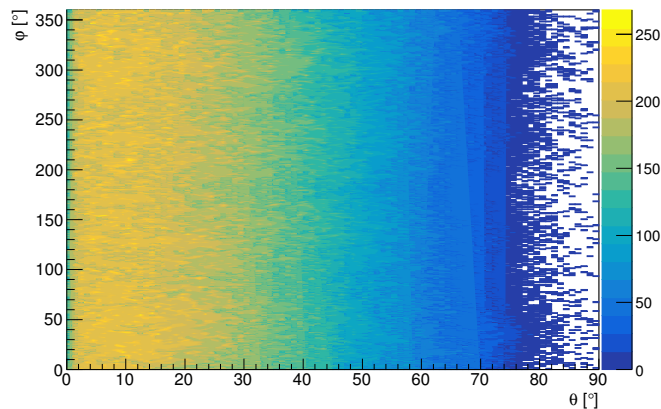


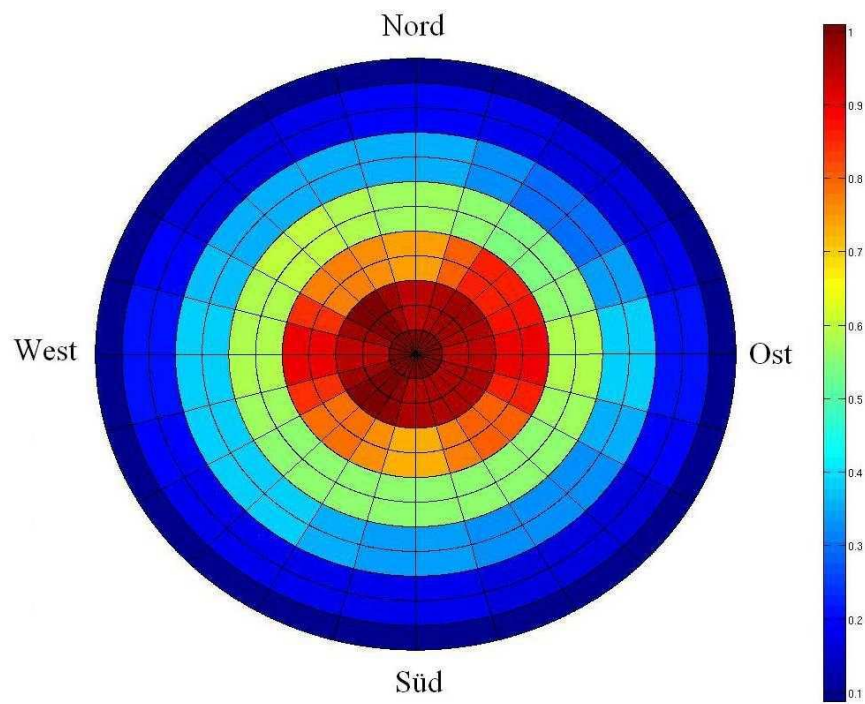
Figure 5.14: Nadir angle θ vs. azimuth angle φ for μ^- which enter the laboratory.

5.5 Comparison with Muon-Map Measurements

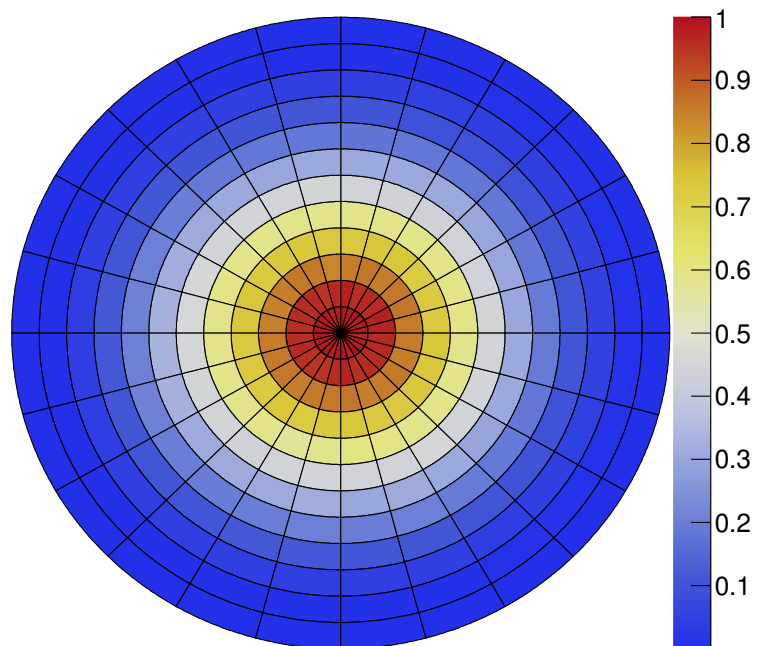
A measurement of the angular-dependent muon flux at the Tübingen Shallow Underground Laboratory to which the Monte Carlo simulations can be compared was conducted earlier [76]. For these measurements, two plastic scintillator panels equipped with PMTs were used. They were inserted parallel into a setup which could be rotated around the horizontal axis in 5° steps. The distance between the two scintillator panels was 77.5 cm. Both panels were 1 cm thick and had an area of $20\text{ cm} \times 10\text{ cm}$. The angular acceptance was $\pm 14.5^\circ$ and $\pm 7.5^\circ$, depending on the direction. For a muon signal, both scintillator panels had to deliver a signal. By rotating the panels and changing the orientation of the total setup, the muon rate for different θ and φ values were measured. [76]

To compare the Monte Carlo simulations with the measured muon map, a similar map with the same binning was created using μ^+ and μ^- entering the laboratory from the ceiling. The muon flux maps from the measurements and the simulations are shown in Fig. 5.15. The binning of θ is 7.5° and 15° for φ . All bins are normalized to the vertical muon rate. When comparing the simulated with the measured muon flux map, one has to keep in mind that buildings in the surrounding were not included in the simulations. Also the angular acceptance of the setup (29° and 15°) is twice as much as the used binning. Therefore any θ - φ pair is contained in more than one bin. Moreover the position inside the laboratory where the measurement of [76] was conducted was not provided in [76]. Therefore only a rough comparison between the measurement and the Monte Carlo simulations is possible.

Half of the measured muons have a value of $\theta \leq 30^\circ$ [76]. In the simulations $\sim 68\%$ have a value of $\theta \leq 30^\circ$. Also the muon rate of $(70.7 \pm 0.9)\text{ m}^{-2}\text{ s}^{-1}$ measured with two larger plastic scintillator panels ($2\text{ m} \times 0.5\text{ m} \times 3\text{ cm}$) [76] is smaller than the simulated muon rate of $(86.56 \pm 0.05)\text{ m}^{-2}\text{ s}^{-1}$ at the ceiling; the deviation is $\sim 20\%$.



(a) Measured muon flux map [76]



(b) Simulated muon flux map

Figure 5.15: Measured and simulated muon flux map of the Tübingen Shallow Underground Laboratory. For the simulated muon flux map, μ^+ and μ^- entering the laboratory from the ceiling were weighted with the charge ratio.

For the measured muon flux map, Fig. 5.15 shows that values for φ deviate by up to $\sim 15\%$ for fixed θ values. The simulations are isotropic in φ with deviations between bins below 3%.

Deviations between the measured and the simulated muon flux map could be due to different positions in the laboratory and due to uncertainties of the soil density as well as the buildings missing in the simulation.

5.6 Discussion

The results of the passage of cosmic-ray muons through the overburden to the Tübingen Shallow Underground Laboratory serves as input for a second step in which the interactions of muons and (muon-induced) neutrons with the MINIDEX setup are simulated. Comparing first data of MINIDEX with Monte Carlo simulations of the MINIDEX experiment shows that the muon-induced neutron production in lead is higher by a factor of 3 – 4 than the simulated production rates [5]. For this first comparison (see [5] and [75]), energy spectra and angular distributions of muons and muon-induced neutrons at the ceiling from the flat overburden simulations done in the framework of this thesis were used. The generation plane was placed 35 cm above the top scintillator of the setup assuming that the fluxes hardly change between the ceiling and the MINIDEX setup [75]. However, deviations of the muon flux at the side walls are of the order of $\sim 30\%$ (see section 5.4) and thus not negligible. This systematic error can be reduced by using a generation sphere around MINIDEX with the corresponding input energy spectra and angular distributions.

Furthermore, only a flat overburden of 16 mwe above the laboratory was considered. However, the overburden of the laboratory in a radius of ~ 15 m around MINIDEX has to be implemented, since muons which can reach the laboratory are created inside an area of 30 m \times 30 m (see section 5.4).

Comparisons of the cosmic-ray muon simulations with an angular-dependent muon flux measurement at the Tübingen Shallow Underground Laboratory [76] show that the muon rates deviate by 20% even if a large generation plane of 50 m \times 50 m is used (see section 5.5). The flux deviations could either be due to different positions and height inside the laboratory or due to a different overburden density and composition which are not precisely known. Furthermore, the flux of the Monte Carlo simulations was not corrected to the altitude of the laboratory site.

To improve the accuracy of the Monte Carlo simulations, further systematic have to be studied. The results of this chapter serve as reference for further simulations. Another Monte Carlo campaign with FLUKA is currently ongoing to investigate further systematics.

Chapter 6

The GERDA Experiment

The **GER**manium **D**etector **A**rray (GERDA) experiment [78] is located at the Laboratori Nazionali del Gran Sasso (LNGS) in Italy and is searching for the $0\nu\beta\beta$ decay of ^{76}Ge :



For this purpose, **H**igh **P**urity **G**ermanium (HPGe) detectors enriched in ^{76}Ge ($\sim 87\%$) are used. Since the expected signal rates are very low (see chapter 2), the background rate has to be as low as possible. Therefore the selection of materials used in the experiment is important; the used materials should have very low radio-contaminations [57]. For germanium detectors, the achievable radio-purity is very high, since germanium is one of the cleanest available materials [57].

Background can not only originate from intrinsic contaminations in the detector and shielding material, but also from the environmental radioactivity, the airborne activity (radon), cosmic rays and neutrons from natural fission, (α, n) reactions and muon interactions [57]. More neutrons are produced in high-Z materials than in low-Z materials (see section 4.4). Therefore low-Z materials are used for shielding purposes in GERDA instead of the commonly used lead. Also the amount of materials used for the support is minimized [78].

The GERDA germanium detectors are operated in liquid argon which serves as cooling medium and as shielding against external radiation at the same time. In Phase II, the liquid argon is additionally used as active veto (see next section).

In section 6.1, the GERDA set-up is described. In section 6.2 and section 6.3, the analysis and the background of the GERDA experiment are discussed.

6.1 Set-Up

In the GERDA experiment, two different detector types are implemented: coaxial detectors from previous experiments and **B**road **E**nergy **G**ermanium (BEGe) detectors which were newly produced for Phase II. All detectors are p-type HPGe detectors. In Fig. 6.1,

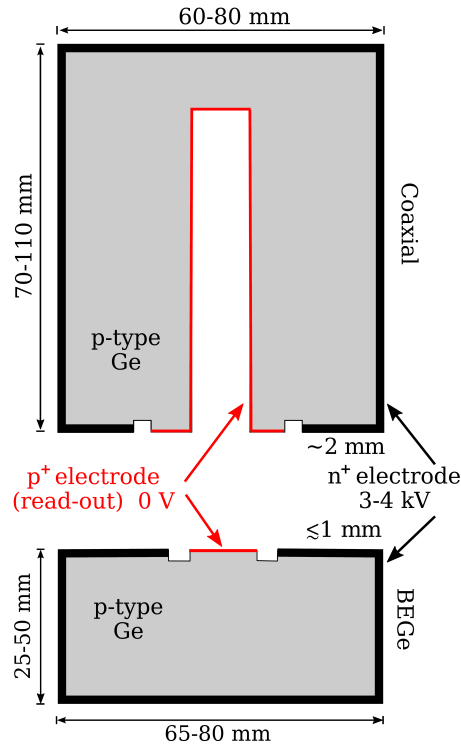


Figure 6.1: Schematic sketch of a coaxial HPGe detector (top) and a BEGe detector (bottom) (drawings not to scale) [79].

a schematic sketch of a coaxial and a BEGe detector is shown. The high voltage (up to +4600 V) is applied to the n+ electrode and the read-out is connected to the p+ electrode for the normal¹ DC readout. Both electrodes are separated by an insulating groove.

Eight enriched detectors from the previous Heidelberg-Moscow experiment [80] and the International Germanium Experiment (IGEX) [81] were used in Phase I. Also coaxial detectors with natural germanium composition from the GENIUS Test Facility [82] were used. The detectors from previous experiments are closed-end coaxial detectors and had been refurbished before the start of GERDA Phase I.

Figure 6.2 shows a sketch of the GERDA experiment. In Phase I and Phase II, different detector array configurations were used. In Phase I, the eight enriched coaxial and the three natural coaxial detectors from previous experiments were placed inside GERDA. During Phase I, two of the natural coaxial detectors were removed and five BEGe detectors were implemented instead. Since Phase II, 40 detectors are used in total: 30 BEGe detectors, 7 enriched coaxial detectors and 3 coaxial detectors with a natural isotopic composition. The detectors are arranged in one array of detector strings which are lowered into liquid argon (LAr): Four strings with 2 – 3 detectors each (Phase I) and seven strings with 3 – 8 detectors each (Phase II) are used.

To limit the collection of ^{42}K ions (resulting from the decay of cosmogenic produced

¹For an alternative readout, the n+ electrode is grounded and the p+ electrode is biased with a negative high voltage (AC coupling).

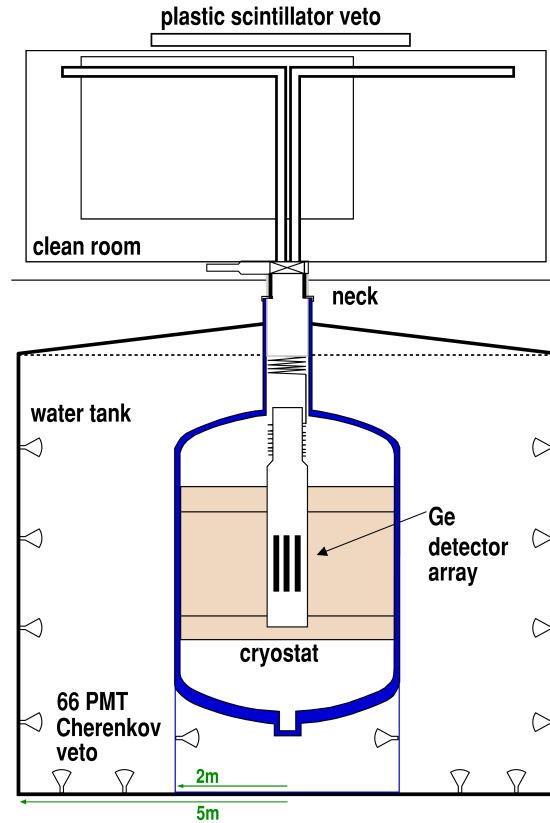


Figure 6.2: Sketch of the GERDA experiment [83].

^{42}Ar) on the detector surface, the detector strings were surrounded by a cylindrical $60\ \mu\text{m}$ thick copper foil (called mini-shroud) in Phase I [78]. In Phase II, each string is enclosed by nylon instead of copper [46] since the LAr is also used as an active veto.

To detect energy depositions inside the liquid argon in Phase II, a cylindrical volume of $0.5\ \text{m}$ diameter and $2.2\ \text{m}$ height around the detector array is instrumented with light sensors. The veto consists of a curtain of wavelength shifting fibers which are read-out with 90 silicon photomultipliers (SiPM). In addition, 16 3-inch low-background photomultiplier tubes (PMTs) are placed at the top and bottom surfaces. The PMTs are designed for cryogenic operation. [46]

To avoid the transportation of ^{222}Rn into the central volume of $3\ \text{m}$ height and $750\ \text{mm}$ diameter, this volume is separated by a $30\ \mu\text{m}$ thick copper foil (called radon shroud) from the rest of the LAr volume [78].

In total, $64\ \text{m}^3$ radio-pure liquid argon is used. The LAr cryostat consists of two coaxial vessels made of steel with $4200\ \text{mm}$ and $4000\ \text{mm}$ outer diameter and $4\ \text{m}$ height with an internal copper shield. The necks of the vessels are $1.7\ \text{m}$ high and the inner vessel has an inner diameter of $800\ \text{mm}$. The internal copper shield of the cryostat is made of 60 plates of high purity oxygen free, radio-pure copper with a total mass of $16\ \text{t}$. It is centered at $4\ \text{m}$ height. The central ring is $2\ \text{m}$ high and $6\ \text{cm}$ thick. In a range of $40\ \text{cm}$ above and below this central ring, the copper shield is $3\ \text{cm}$ thick. [78]

The LAr cryostat is surrounded by ultra-pure water which acts as an additional shield. The 3 m thick water layer also moderates and absorbs neutrons [78]. Furthermore, the external gamma flux is attenuated by the water. The water serves also as a Cherenkov medium for muons. Since muons can induce background, it is important to identify muon events. For this purpose, 66 8" PMTs are mounted on the walls of the water tank to detect the Cherenkov light. To improve the photon detection efficiency and therefore also the muon detection efficiency, the tank is covered with a 206 μm thick VM200 foil which has a reflectivity of $> 99\%$. The water tank is cylindrical with a diameter of 10 m and a height of 8.3 m. It has a capacity of 590 m^3 and is divided into two parts: the main part equipped with 60 PMTs and a smaller part below the cryostat region equipped with 6 PMTs. For a muon veto trigger, at least 5 PMTs in the main water tank or 3 PMTs in the second Cherenkov detector must see a signal. [78]

To cover also the neck of the cryostat, 36 plastic scintillator panels with the dimensions 200 cm \times 50 cm \times 3 cm are used. They cover an area of 4 m \times 3 m centered at the neck and are placed in three layers with 12 plastic scintillator modules per layer. [78]

The scintillator panel part of the muon veto system is located on top of the clean room above the water tank. The interior of the LAr cryostat can only be assessed by the lock system which is used to lower the detector strings and the calibration sources into the liquid argon. Calibration measurements with ^{228}Th sources are regularly performed (every one or two weeks) to check the energy resolution and the stability of the energy scale [53].

6.2 Analysis Results

The GERDA collaboration decided to perform blind analyses which means that the raw data of the blinding window around $Q_{\beta\beta}$ is not accessible until all parameters for the analysis are defined. Events within $Q_{\beta\beta} \pm 20$ keV [53] (± 25 keV in Phase II [46]) are not processed until the energy calibration and the background model has been finalized.

6.2.1 Analysis Cuts

To identify and remove background, different cuts are set. An anti-coincidence cut is performed: events with energy depositions in multiple detectors are discarded. Since the half-life of $0\nu\beta\beta$ decay is $> 10^{25}$ yr, it would be very unlikely that two $0\nu\beta\beta$ decays happen at the same time. Thus, loss in efficiency is negligible. Also events in coincidence within 10 μs with a muon veto signal are rejected; more than 99% of the muons are tagged having a dead time $< 0.1\%$ [46].

The measured mean cosmic muon rate of

$$I_{\mu}^0 = (3.477 \pm 0.002_{stat} \pm 0.067_{sys}) \cdot 10^{-4} \text{ m}^{-2} \text{ s}^{-1} \quad (6.2)$$

is in good agreement with rates measured by other experiments. A change of the muon flux due to seasonal modulations of the Earth's atmosphere and also from the CNGS neutrino beam (operating 2008 – 2013 during Phase I) has been observed. [83]

The rock overburden of 1400 m—which corresponds to ~ 3500 mwe—reduces the cosmic muon flux by approximate six orders of magnitude with a mean muon energy of 270 GeV [84]. The muon energy spectra and angular distribution have been measured by the MACRO (**M**onopole, **A**strophysics, and **C**osmic **R**ay **O**bservatory) experiment which was located at the LNGS in Hall B [84, 85].

To reject background events from ^{214}Bi – ^{214}Po cascade of the ^{222}Rn decay chain, events which were followed by another event in the same detector within 1 ms were excluded [53].

The range of electrons is short: in more than 90% the energy of both electrons of $0\nu\beta\beta$ decay is deposited within a few mm^3 [53]. Therefore no energy deposition due to $0\nu\beta\beta$ decays is expected inside the LAr veto. For background events, energy may be deposited in liquid argon which induces scintillation light. Since Phase II, this light can be detected and these kinds of events can be vetoed. The short range of electrons can also be used to reject background by analyzing the pulse shape of the detector signal [86].

6.2.2 Pulse Shape Discrimination

The pulse shape of single site events (SSE) for which the energy is deposited within a small volume (like $0\nu\beta\beta$ decay) and the pulse shape of multi site events (MSE) for which the energy is deposited at several locations are significantly different. If the energy is deposited at different locations, the drift times of the charged particles are different for different locations. [86]

BEGe detectors have a very good **P**ulse **S**hape **D**iscrimination (PSD) behavior due to their small area of the p+ contact leading to a very pronounced weighting potential. For MSE, two or more time-separated current pulses appear (see Figs. 6.3 and 6.4). Therefore the maximum of the current pulse A for MSEs will be smaller compared to SSEs. For a localized energy deposition, A will be proportional to the deposited energy E (corresponding to the integrated current over time) for most of the detector volume. The ratio A/E can be used for PSD. Surface events near the p+ electrode can be recognized. The current amplitude of these events is larger than standard SSE. Therefore these events have an increased A/E ratio. For n+ electrode events, the A/E ratio is reduced. A signal is accepted if A/E is in the range of $0.965 < A/E < 1.07$. [86]

The PSD behavior depends on the detector geometry. Coaxial detectors have a different electric field compared to BEGe detectors. The gradient of their weighting field is lower. Therefore a larger volume is relevant for the current signal. This makes the PSD more complicated compared to the PSD for BEGes. The A/E ratio by itself cannot be used with sufficient efficiency [86]. In the GERDA experiment, three different PSD methods are applied for coaxial detectors. For the main one, an artificial neural network

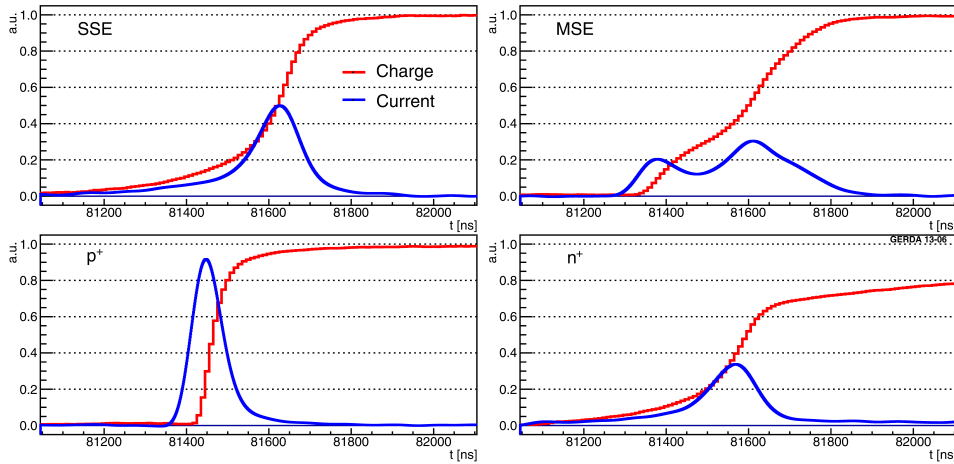


Figure 6.3: Candidate pulse traces taken from BEGe data for a **Single Site Event** (top, left), **Multi Site Event** (top right), **p+ electrode event** (bottom left) and **n+ surface event** (bottom right). The maximal charge pulse amplitudes are set equal to one for normalization and current pulses have equal integrals. The current pulses are interpolated. [86]

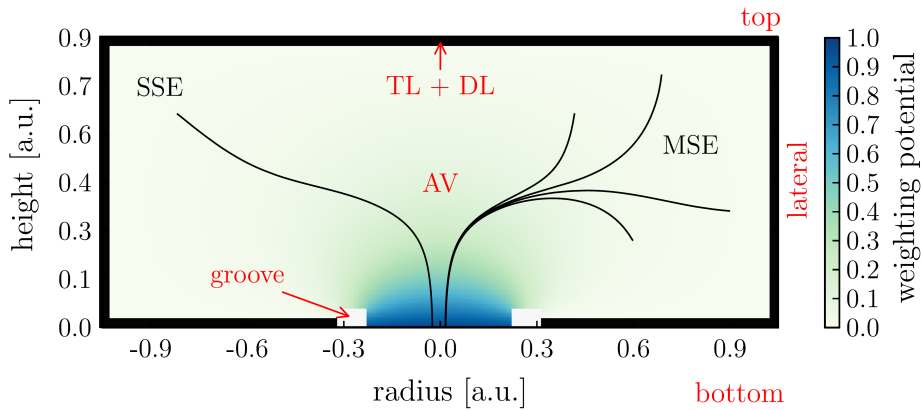


Figure 6.4: Generic view of a BEGe diode. The p+ read-out electrode (center, bottom) is separated from the n+ electrode by a groove covered by an insulating passivation layer. The n+ electrode consisting of an inactive dead (DL) and transition (TL) layer with reduced charge collection surrounds the AV. The dimensionless weighting potential is color-coded and strongest close to the p+ electrode. Examples of a single-site event (SSE) and of a multi-site event (MSE) are illustrated by means of the hole trajectories of the individual energy depositions. [6]

is used. It analyzes the rising part of the charge pulses. The second method is a likelihood method implemented on TMVA² which needs 8 input variables to discriminate SSE like and background events. The third method is based on the correlation between A/E and the pulse asymmetry. All three PSD methods identify a very similar set of events as background. [86]

6.2.3 Half-Life of Double Beta Decay

The half-life of $2\nu\beta\beta$ decay was determined with data taken from November 9th, 2011 till May 21st, 2013 and was found to be

$$T_{\frac{1}{2}}^{2\nu} = (1.926 \pm 0.094) \cdot 10^{21} \text{ yr [87]}. \quad (6.3)$$

6.2.4 Half-Life of Neutrinoless Double Beta Decay

Once a signal is observed, the half-life of $0\nu\beta\beta$ can be calculated from the number of observed signal events $N^{0\nu}$, the total exposure \mathcal{E} which is given by detector mass \times lifetime, the efficiency, the molar mass of the enriched material $m_{\text{enr}} = 75.6 \text{ g}$ and the Avogadro's constant N_A :

$$T_{\frac{1}{2}}^{0\nu} = \frac{(\ln 2)N_A}{m_{\text{enr}}N^{0\nu}} \mathcal{E}\epsilon. \quad (6.4)$$

The efficiency

$$\epsilon = f_{76}f_{\text{av}}\epsilon_{\text{FEP}}\epsilon_{\text{PSD}} \quad (6.5)$$

depends on the fraction of ^{76}Ge atoms f_{76} , the active volume fraction f_{av} , the full energy detection efficiency ϵ_{FEP} and the efficiency of the PSD ϵ_{PSD} . The full energy detection efficiency ϵ_{FEP} is determined with Monte Carlo simulations and is found to be 0.92 for semicoaxial and 0.90 for BEGe detectors. To get the number of $0\nu\beta\beta$ decays, a Gaussian peak (signal, mean at $Q_{\beta\beta} = 2039.01(5) \text{ keV}$ and standard deviation of σ_E) and a constant background term are fitted to the data. The free parameters are $1/T_{\frac{1}{2}}^{0\nu}$ and one background parameter for each data set. The data is divided into different sub-data sets, since the background depends on the history of the detectors. [53]

A frequentist and a Bayesian analysis based on an unbinned extended likelihood function are performed. If no signal is found, a limit on the half-life can be set from the confidence intervals of the signal $S = N^{0\nu}$ (frequentist analysis) or from the quantile of the marginalized posterior probability density function (Bayesian analysis). For the marginalization, the BAT toolkit [88] is used. A Markov chain Monte Carlo numerical integration is performed to get the one-dimensional posterior probability density function. The limit of the Bayesian analysis is the inverse of the 90% probability quantile for S . [46]

For getting the confidence intervals, possible realizations of the experiments are gen-

²Toolkit for Multivariate Data Analysis in ROOT

erated via Monte Carlo for a set of S values. The probability distribution $f(t_S|S_j)$ is calculated ($t_S = -2 \ln \lambda(S)$) with the profile likelihood $\lambda(S)$. The p -value of a certain S_j value is

$$p_S = \int_{t_{obs}}^{\infty} f(t_S|S_j) d(t_{S_j}) \quad (6.6)$$

with the value t_{obs} of the test statistic for S_j . The upper limit (90% C.L. is chosen) on the half-life from the frequentist analysis is the inverse of S_j for which the p -value is 0.1. [46]

Phase I During the data-taking time from November 2011 to May 2013, a 21.6 kg yr exposure was collected in total. The data was grouped into three subsets:

1. BEGe data set
2. golden data set: major part of semi-coaxial detectors
3. silver data set: two short periods with higher background levels after hardware operations.

No signal was observed. The profile likelihood fit result for a $0\nu\beta\beta$ signal is $N^{0\nu} = 0$ and the limit of the half-life is

$$T_{\frac{1}{2}}^{0\nu} > 2.1 \cdot 10^{25} \text{ yr (90\% C.L.)} \quad (6.7)$$

with the median sensitivity of $2.4 \cdot 10^{25}$ yr. The best fit of the Bayesian analysis is $N^{0\nu} = 0$ resulting in

$$T_{\frac{1}{2}}^{0\nu} > 1.9 \cdot 10^{25} \text{ (90\% credible interval CI).} \quad (6.8)$$

The median sensitivity of the Bayesian analysis is $2.0 \cdot 10^{25}$ yr. The $0\nu\beta\beta$ claim of part the HDM collaboration is strongly disfavored with a Bayes factor³ of 0.024. The upper limit on the effective neutrino mass $m_{\beta\beta}$ is 0.2 – 0.4 keV. [53]

Phase II The second data-taking phase with the upgraded detector array and the LAr veto started in December 2015. The goal of this phase is to reach a half-life sensitivity of $> 10^{26}$ yr for which a 100 kg yr exposure with a background index (BI) of 10^{-3} cts/(keV kg yr) is needed. The mass has been doubled compared to Phase I: now 37 detectors with enriched germanium (35.6 kg) are used. Seven coaxial and 30 BEGe detectors are arranged in six strings which surround a central string with three coaxial detectors with natural isotopic composition. [46]

The background level could be reduced by an order of magnitude due to the LAr veto and the improved PSD performance. Events in the germanium detectors with a coincident signal from the LAr veto within $5 \mu\text{s}$ are rejected. Most of the photons are expected to occur within this time window. The accidental coincidence between LAr veto

³Ratio of likelihood probabilities of two competing models

and germanium detectors results in a dead time of $(2.3 \pm 0.1)\%$. The blinding window in Phase II is $Q_{\beta\beta} \pm 25$ keV. [46]

Data taken from December 2015 – April 2017 with additional data from Phase I taken in 2013 has been unblinded and analyzed together with data from Phase I. A frequentist and a Bayesian analysis based on an unbinned extended likelihood function have been performed. Again, no signal was observed which results in

$$T_{\frac{1}{2}}^{0\nu} > 8.0 \cdot 10^{25} \text{ yr (90\% C.L.)} \quad (6.9)$$

with an experimental median sensitivity of $5.8 \cdot 10^{25}$ yr. The limit on the half-life from the Bayesian analysis is

$$T_{\frac{1}{2}}^{0\nu} > 5.1 \cdot 10^{25} \text{ yr (90\% CI)} \quad (6.10)$$

with a median sensitivity of $4.5 \cdot 10^{25}$ yr. [89]

6.3 Background in GERDA

Background can not only come from internal contaminations of the setup (like in the germanium detectors, the support materials or the liquid argon), but also from environmental radioactivity or cosmic rays.

To reduce the internal background, the used material was screened and only high radio-pure material was chosen. Radiation from the cryostat vessel made of steel is reduced by the copper lining (see section 6.1). External radiation from the environment (like from the rock) can be shielded with the water and the liquid argon. [78]

Cosmic rays can produce prompt and delayed background. Muons and muon-induced neutrons can deposit energy around $Q_{\beta\beta}$ in the detector. This prompt background can be reduced by the muon veto [90]. Furthermore, most neutrons produced outside the setup are moderated and absorbed by the water. This reduces the production of radio-isotopes (which contributes to the delayed background) close to the detector array.

To avoid the production of long-lived radio-isotopes, the exposure to cosmic rays has to be avoided. Therefore the detectors had been kept underground whenever it was possible [78]. Since the coaxial detectors of the former HDM and IGEX experiments have been stored underground for a long time, they have a lower intrinsic activity compared to the newly produced BEGe detectors. For the newly produced BEGe detectors, efforts were made to reduce their exposure to cosmic-rays during processing as much as possible; the enriched germanium was shielded by a cylindric steel container during transportation [6].

Figure 6.5 shows the energy spectrum of Phase I and Phase II for events with only energy depositions inside one detector and which are not vetoed by the muon or the LAr veto. The background at the low energy region is dominated by the beta decay of ^{39}Ar which has an endpoint energy of 565 keV. It has a long half-life of 269 years and

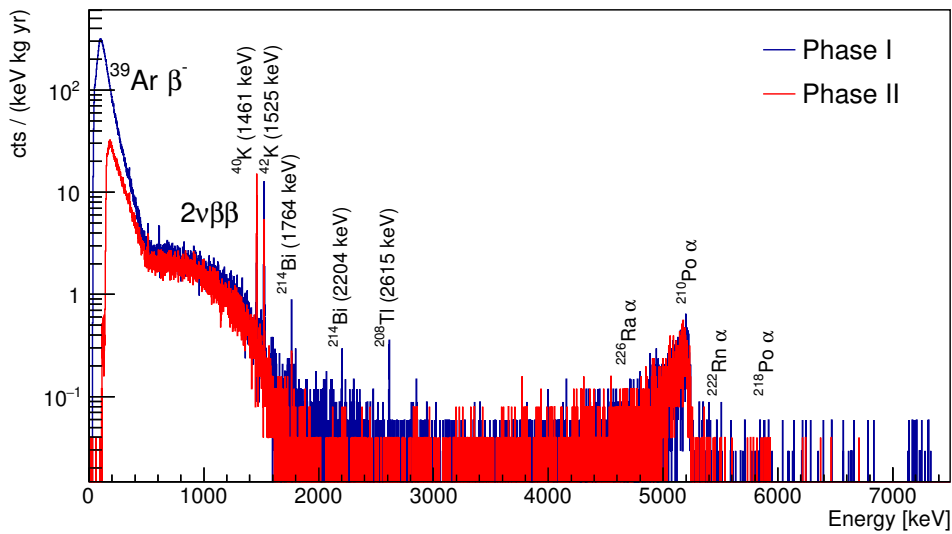


Figure 6.5: Energy spectrum of Phase I and Phase II. Only events with energy depositions inside one detector and which are not vetoed by the muon veto (and LAr veto for Phase II data) are included.

is produced by cosmogenic activation of natural argon in the atmosphere. The found activity in GERDA is

$$A(^{39}\text{Ar}) = (1.01 \pm 0.002_{stat} \pm 0.08_{sys}) \text{ Bq/kg}. \quad (6.11)$$

The energy range from 600 keV to 1500 keV is dominated by the $2\nu\beta\beta$ decay spectrum. In Fig. 6.5, γ lines from ^{40}K , ^{42}K , ^{214}Bi and ^{208}Tl are clearly visible. Above 3.5 MeV which is the Q-value of ^{42}K the main contribution comes from α decays which are mainly from the ^{226}Ra decay chain. The peak-like structure around 5.3 MeV comes from ^{210}Po decay on the detector p^+ surface. Other peak-like structures at 4.7 MeV, 5.4 MeV and 5.9 MeV come from α decays of ^{226}Ra , ^{222}Rn and ^{218}Po . Another background component comes from ^{42}K ($T_{1/2} = 12.36$ h, $Q_\beta = 3525.4$ keV [35]). It is produced by the decay of ^{42}Ar inside the LAr. Since it is ionized, it drifts inside electric fields and can thus decay on the detector surface. [79]

For Phase I data, a background fit in the energy range of 570 keV–7500 keV was done [79] in order to predict the background in the blinded region of interest. Contributions from $2\nu\beta\beta$ decay, ^{40}K , ^{60}Co , ^{228}Th , ^{228}Ac , ^{214}Bi , ^{42}K and α -emitters in the ^{226}Ra decay chain were considered. A flat background was predicted by the background model in the region of interest (ROI). By interpolating from the background model [79] to the ROI, the background index for coaxial detectors is $(1.75^{+0.26}_{-0.24} \times 10^{-2})$ cts/(keV kg yr) and $(3.6^{+1.3}_{-1.0} \times 10^{-2})$ cts/(keV kg yr) for the BEGe detectors. [79]

In Phase I, a background index (BI) of

$$2.0_{-0.4}^{+0.6} \cdot 10^{-2} \text{ cts}/(\text{keV kg yr}) \quad (6.12)$$

was reached after applying all cuts which is an order of magnitude improvement compared to the previous HDM and IGEX experiments [78]. In Phase II, the BI for BEGe's at $Q_{\beta\beta}$ is

$$1.0_{-0.4}^{+0.6} \cdot 10^{-3} \text{ cts}/(\text{keV kg yr}) \quad (6.13)$$

which means that also the background index goal of Phase II has been achieved [89].

6.4 Next Generation of ^{76}Ge Experiments

In order to be sensitive for a higher $T_{1/2}^{0\nu}$, a larger detector mass with even reduced background is needed. The newly formed LEGEND collaboration (**L**arge **E**nriched **G**ermanium **E**xperiment for **N**eutrinoless $\beta\beta$ **D**ecay) aims to build a tonne-scale ^{76}Ge experiment to reach a sensitivity of $T_{1/2}^{0\nu} \sim 10^{28}$ yr corresponding to a sensitivity on the effective Majorana neutrino mass of (15 – 50) meV. To reach this sensitivity, the background must be less than 0.1 cts/(FWHM · t · yr) (corresponds to 10^{-5} cts/(keV kg yr). Thus, the background has to be further reduced by two orders of magnitude to reach the sensitivity goal. [91]

Presently it is planned to use a shielding strategy comparable to that used by the GERDA experiment: only low- Z materials should be used as shielding and the germanium detectors should be operated in liquid argon. The amount of radio-impurities in the direct surrounding of the detector has to be further reduced and the background recognition has to be improved. An increased mass per detector helps to reduce the background since fewer detectors and thus read-out channels are needed. [91]

A tonne-scale experiment also requires a new infrastructure. So far, the location of the LEGEND setup has not been settled. Possible sites are SNOLAB (Canada, 2000 m rock overburden), SURF (United States, 1480 m overburden [92]) and CJPL (China, 2400 m rock overburden). [91]

Depending on the chosen site of the experiment, the background produced by cosmic-rays may limit the sensitivity. Therefore a detailed understanding of cosmic-ray-induced background is important and a reduced cosmic-ray flux would be advantageous.

Chapter 7

Muon-Induced Radionuclide Search in GERDA

In this chapter, the search for muon-induced radionuclides in the GERDA experiment is described. The goal is to estimate the background index of $^{77(m)}\text{Ge}$ β^- decay in the ROI and the integrated neutron flux from muon-induced neutron production. Monte Carlo simulations predict that $^{77(m)}\text{Ge}$ β^- decay is the highest contribution to the muon-induced radionuclide background component in the ROI [3]. It is produced by neutron capture on ^{76}Ge .

The muon-induced background is not the dominant background for the ^{76}Ge $0\nu\beta\beta$ decay search of GERDA after all vetoes and cuts have been applied (see chapter 6). The background index (BI) of GERDA Phase II is of the order of 10^{-3} cts/(keV kg yr) while Monte Carlo simulations predict a BI from ^{77}Ge and ^{77m}Ge decays ($^{77(m)}\text{Ge}$) of

$$(1.1 \pm 0.2) \cdot 10^{-4} \text{ cts}/(\text{keV kg yr}) [3] \quad (7.1)$$

and

$$(4.0 \pm 0.4) \cdot 10^{-5} \text{ cts}/(\text{keV kg yr}) [4] \quad (7.2)$$

depending on the Geant4 version and the implemented geometry. For future experiments like LEGEND, the background must be further reduced to 10^{-5} cts/(keV kg yr) which is lower than the BI predictions for $^{77(m)}\text{Ge}$ [4]. Monte Carlo simulations predict that the BI can be reduced to $(2.7 \pm 0.3) \cdot 10^{-6}$ cts/(keV kg yr) by applying a delayed coincidence cut [4]. This BI would be small enough. However, the difference between both Monte Carlo simulations (one order of magnitude) is very large. It is also known that muon-induced neutron production is not well reproduced by GEANT4 (see chapter 3 and chapter 5). Therefore the BI after the delayed coincidence cut could be of the order of the LEGEND BI goal if the $^{77(m)}\text{Ge}$ production rate is higher than the expected one in [4].

Since the muon-induced background becomes more relevant for future $0\nu\beta\beta$ experiments and the uncertainties of the simulated production rates are large, the radionuclide production rates should be estimated from data. This would not only allow to calculate the BI in the ROI, but also to test and improve the reliability of Monte Carlo simulations. Signatures for neutron capture on ^{76}Ge ($^{76}\text{Ge}(n,\gamma)^{77(m)}\text{Ge}$) and on ^{74}Ge ($^{74}\text{Ge}(n,\gamma)^{75(m)}\text{Ge}$) in enriched germanium detectors as well as neutron capture on argon ^{40}Ar ($^{40}\text{Ar}(n,\gamma)^{41}\text{Ar}$) were investigated and are described in section 7.1. All investigated signatures of the three radionuclide are due to muon-induced neutrons which are captured by the nuclei (first part of the signature) followed by a delayed energy deposition from the decay of the radionuclide (second part of the signature).

Monte Carlo simulations were conducted to get the information (like the efficiencies, energy spectra for example) needed to extract the radionuclide production rates, the $^{77(m)}\text{Ge}$ BI and the integrated neutron flux from the number of observed neutron captures. The simulations are described in section 7.2.

7.1 Signatures

Three different muon-induced radionuclides were investigated: muon-induced $^{77(m)}\text{Ge}$ production due to neutron capture on ^{76}Ge , $^{75(m)}\text{Ge}$ production due to neutron capture on ^{74}Ge and ^{41}Ar production due to neutron capture on ^{40}Ar . Latter is the most abundant isotope in LAr which surrounds the germanium detectors.

Since most of the muon-induced background is predicted to be from $^{77(m)}\text{Ge}$ β^- decay [3] whose Q-value is larger than $Q_{\beta\beta}$, the estimation of the $^{77(m)}\text{Ge}$ production rate is of great interest to determine the BI in the ROI from data.

Muon-induced $^{77(m)}\text{Ge}$ is produced by neutron capture on ^{76}Ge which is the most abundant germanium isotope ($\sim 88\%$) in the enriched germanium detectors. Its decay scheme is shown in Fig. 7.1. After neutron capture on ^{76}Ge , the produced ^{77}Ge nucleus is highly excited and de-excites by the emission of gammas. If the gamma cascade ends in the ground-state, 6072.6 keV are released during the gamma cascade. If the gamma cascade ends in the meta-stable state at $E_{\text{IT}} = 159.7$ keV, 5912.9 keV are released. The meta-stable state has a half-life of 52.9 s and decays via β^- decay to ^{77}As with a branching ratio of 81% or via isomeric transition (IT) with a branching ratio of 19% to the ground state of ^{77}Ge which has a half-life of 11.3 h. While from β^- decay a continuous energy spectrum up to the Q-value of 2861 keV is expected, a fixed energy of 159.7 keV is released due to the IT. Latter produces a peak in the energy spectrum and hence gives a good signature.

The combination of the rather short half-life of the meta-stable state and the well-defined energy deposition from the IT lead to a small stochastic background. Thus, the chosen signature for the $^{77(m)}\text{Ge}$ production is a signal from neutron capture ($E > E_{\text{cut}}$) accompanied by a signal from the muon veto followed by a delayed signal from the IT

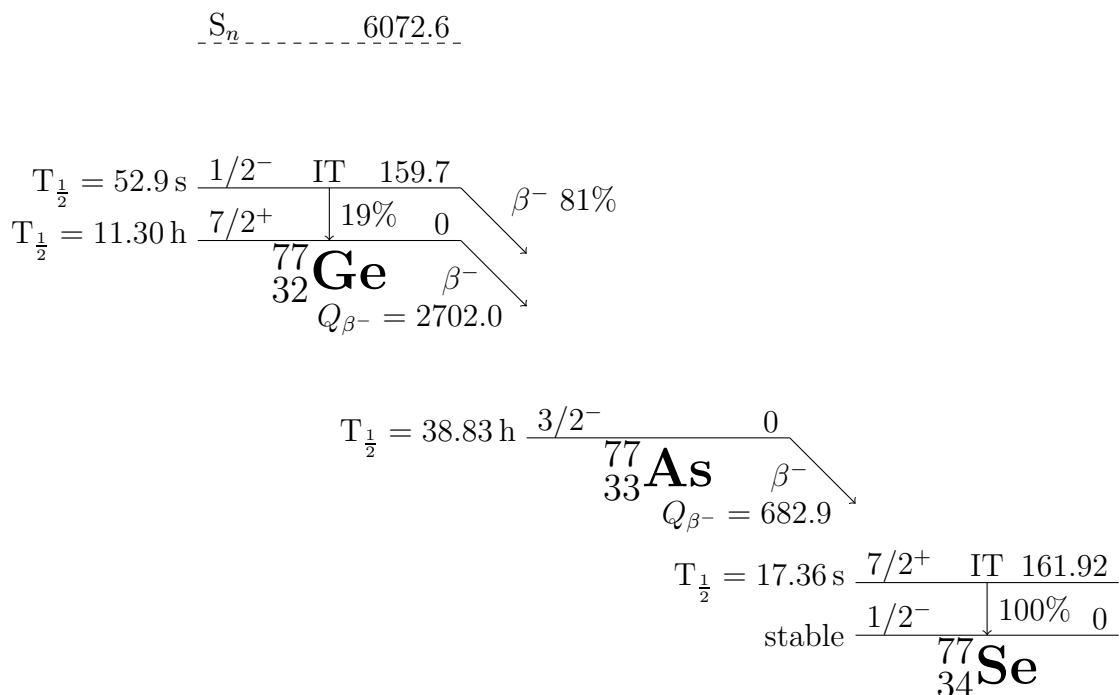


Figure 7.1: Decay of ${}^{77}\text{Ge}$ (left: J^π ; right: E in keV). Values are taken from [35].

($E \in [E_{\text{IT}} \pm \Delta E]$). An energy cut, E_{cut} , on the energy deposition from the neutron capture cascade is set to reduce the background from random coincidences. A small energy window for the IT gamma search is used to take the energy resolution of the germanium detectors into account.

The second most abundant germanium isotope in the enriched germanium detectors is ${}^{74}\text{Ge}$ ($\sim 12\%$). If a neutron gets captured on ${}^{74}\text{Ge}$, ${}^{75}\text{Ge}$ is produced. The decay scheme of ${}^{75}\text{Ge}$ is shown in Fig. 7.2. Since its Q -value is much lower than $Q_{\beta\beta}$, it does not contribute to the BI in the ROI. It has also a meta-stable state which can undergo β^- decay or IT—like ${}^{77}\text{Ge}$. The half-life of 47.7 s and the IT energy of 139.69 keV are of the same order as for ${}^{77(m)}\text{Ge}$. Therefore a similar signature can be chosen. The branching ratio for IT of ${}^{75m}\text{Ge}$ is with 99.97% and thus much higher than the IT branching ratio of ${}^{77m}\text{Ge}$. This may be compensate the lower abundance of ${}^{74}\text{Ge}$.

The germanium detectors are surrounded by liquid argon whose most abundant isotope is ${}^{40}\text{Ar}$ (99.6% [35]). If a neutron is captured on ${}^{40}\text{Ar}$, ${}^{41}\text{Ar}$ is produced. The decay scheme of ${}^{41}\text{Ar}$ is shown in Fig. 7.3. Its half-life is 109.34 min and it decays via β^- decay to ${}^{41}\text{K}$ with a Q -value of 2491.6 keV. Since its Q -value is larger than $Q_{\beta\beta}$, it can contribute to the background in the ROI. However, ${}^{41}\text{Ar}$ is not produced inside the germanium detectors like ${}^{77(m)}\text{Ge}$ but outside the germanium detectors. Therefore the probability that energy from its β^- decay of the order of $Q_{\beta\beta}$ is deposited inside one of the germanium detectors is smaller than for ${}^{77(m)}\text{Ge}$ β^- decay.

Unlike ${}^{77}\text{Ge}$ and ${}^{75}\text{Ge}$, ${}^{41}\text{Ar}$ has no meta-stable state. However, a 1293.6 keV gamma is released in nearly all of its β^- decays (99.1% branching ratio). Therefore the ${}^{41}\text{Ar}$

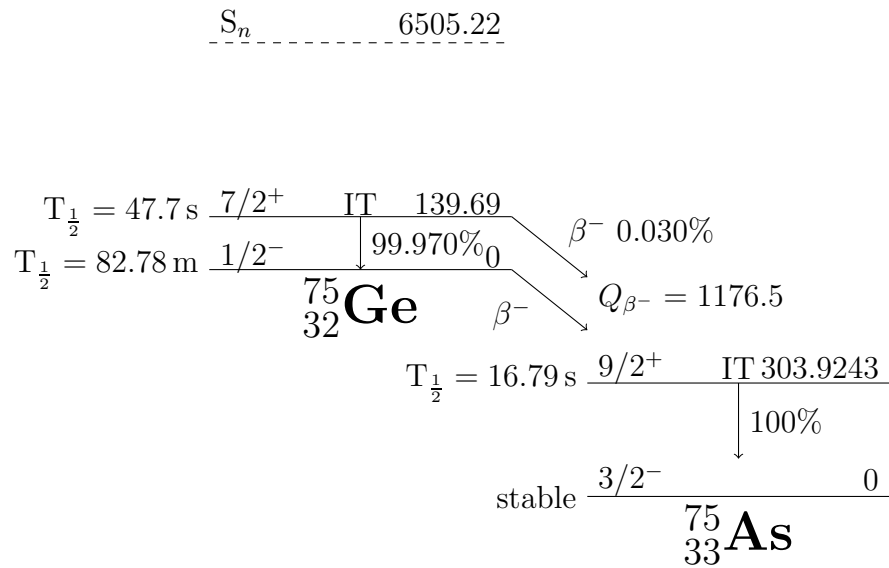


Figure 7.2: Decay of ${}^{75}\text{Ge}$ (left: J^π ; right: E in keV). Values are taken from [35].

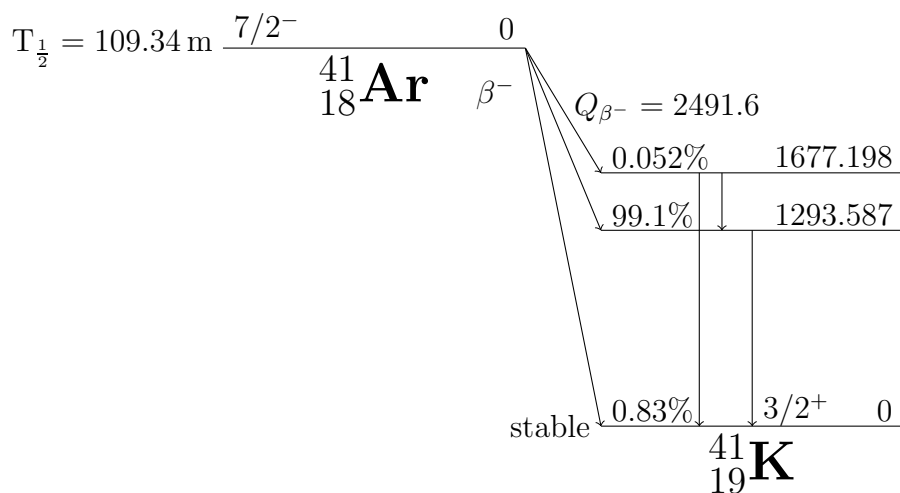


Figure 7.3: Decay of ${}^{41}\text{Ar}$ (left: J^π ; right: E in keV). Values are taken from [35].

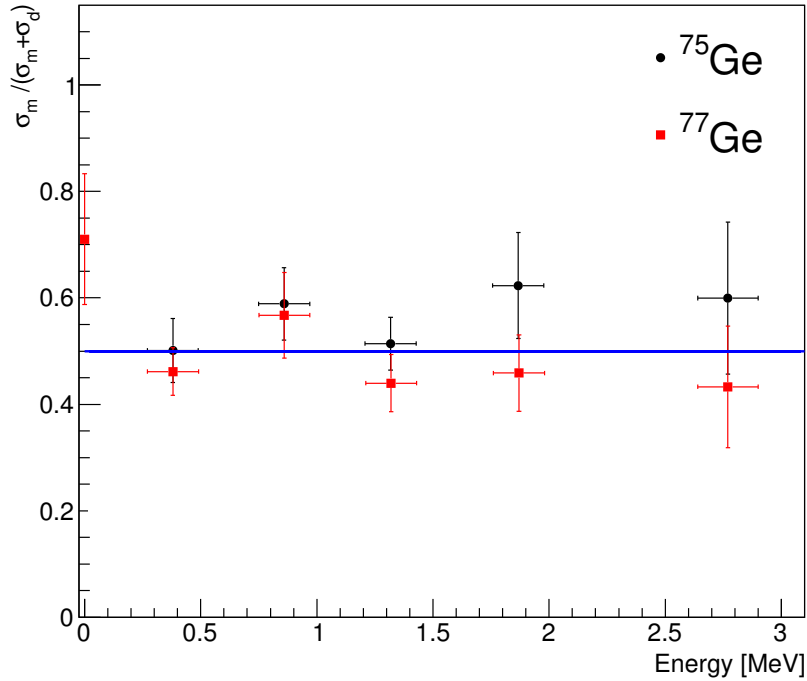


Figure 7.4: Ratio of the meta-stable state production cross section to the meta-stable and direct ground state production cross section. Data was taken from [93] and [94].

production can be investigated by looking for the full energy deposition of the 1293.6 keV gamma in one of the germanium detectors.

In order to obtain the $^{77(m)}\text{Ge}$ and $^{75(m)}\text{Ge}$ production rates from the number of observed neutron capture signals followed by the IT, the ratio of meta-stable state to direct ground state production f_m has to be known. The cross sections for meta-stable state and direct ground-state production by neutron capture have been measured for ^{76}Ge [93] [94] and ^{74}Ge [94]. Figure 7.4 shows the ratio between the meta-stable state to direct ground-state production f_m for different neutron energies. For both isotopes and at all energies, the ratio is $f_m \approx 0.5$.

The $^{77(m)}\text{Ge}$ and $^{75(m)}\text{Ge}$ production rates can then be calculated from the number of found IT signatures using the ratio of the meta-stable state to direct ground state production f_m , the IT branching factor f_{IT} and the efficiency for detecting the signature ϵ . For obtaining the integrated neutron flux calculation, not only the neutron energy spectrum is needed which is determined using Monte Carlo simulations (see section 7.2), but also the energy-dependent cross-section distribution. The ENDF/B-VII database [95] contains only the cross-section distributions for total ground-state production of ^{77}Ge and ^{75}Ge via neutron capture. The energy-dependent cross-section distributions for meta-stable state production can be calculated from the branching ratio f_m , since the total number of produced ground state nuclei N_t is given by the number of directly produced nuclei in ground states N_d and the number of produced meta-stable states N_m which

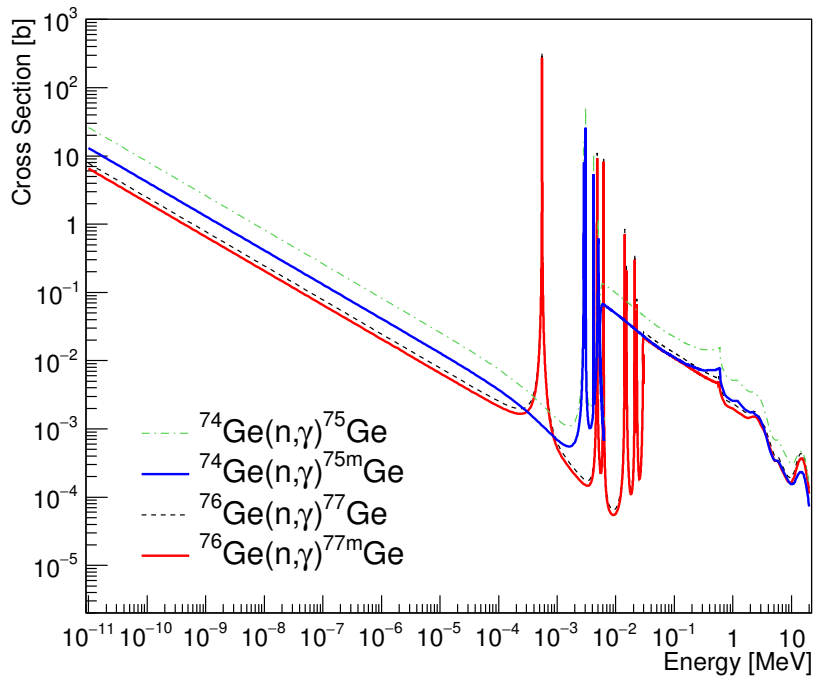


Figure 7.5: Cross sections from the ENDF/B-VII data libraries [95] for the total ground state production of ^{77}Ge and ^{75}Ge via neutron capture and calculated cross sections for the meta-stable state production.

undergo IT to the ground state with the branching ratio f_{IT}

$$N_t = N_d + f_{\text{IT}} \cdot N_m = (1 - f_m) \cdot N + f_{\text{IT}} \cdot f_m \cdot N \quad (7.3)$$

with the total number of captures N . Thus, the meta-stable state to total ground-state production ratio is

$$\frac{N_m}{N_t} = \frac{f_m \cdot N}{(1 - f_m) \cdot N + f_{\text{IT}} \cdot f_m \cdot N} = \frac{1}{\frac{1}{f_m} - 1 + f_{\text{IT}}} \quad (7.4)$$

which becomes

$$\frac{N_m}{N_t} = \frac{1}{1 + f_{\text{IT}}} \quad (7.5)$$

for $f_m = 0.5$.

The ENDF/B-VII cross sections for the total ground-state production and the calculated cross-section distributions for the meta-stable state production are shown in Fig. 7.5. It can be seen that not only thermalized neutrons can be captured but also intermediate and fast neutrons.

The ^{41}Ar production rate can be directly calculated from the number of observed delayed 1293.6 keV gammas using the known branching ratio, its detection rate and the efficiency for detecting 1293.6 keV gammas which is determined using Monte Carlo simulations.

7.2 Monte Carlo Simulations

Monte Carlo simulations were conducted to determine

- energy deposition spectra which are not from neutron capture cascade, the neutron capture time distribution and the neutron energy spectrum around the germanium detector array
- energy deposition spectra from neutron capture cascade
- the efficiencies for the full IT gamma detection and the energy deposition spectra from ^{77m}Ge β^- decay inside the germanium detectors
- energy deposition spectra from ^{77}Ge β^- decay inside the germanium detectors
- the efficiencies for detecting the ^{41}Ar β^- decay gamma at 1293.6 keV

The neutron energy spectrum around the germanium detector array is needed for the integrated neutron flux calculation. The energy depositions from neutron capture cascade (E_{cas}) and the distribution of all other energy depositions (E_{dep}) are needed to determine the efficiencies to detect the neutron capture. These other energy depositions can be induced by muons, by scattering of neutrons or by nuclear recoils for example. The neutron capture time distribution can be used to reduce background, since it takes time for the neutron to be captured while most of the muon-induced background of the neutron capture signature will appear prompt after the muon passage. The energy deposition spectra from ^{77m}Ge and ^{77}Ge β^- decay inside the germanium detectors are needed for determining the BI of $^{77(m)}\text{Ge}$ β^- decay in the ROI.

Neutron Capture on Germanium To get the efficiencies and the needed distributions, Monte Carlo simulations with MaGe were conducted using GEANT4.10.3. In this version, the simulation of the energy depositions from neutron capture events (from neutron capture cascade and other energy depositions) has to be separated into two simulations¹. The total energy depositions has to be calculated afterwards from the energy depositions of the neutron capture cascade E_{cas} and the distribution of other energy depositions E_{dep}

$$E_{tot} = E_{dep} + E_{cas} . \quad (7.6)$$

¹The neutron gamma cascades of ^{77}Ge and ^{75}Ge end before the meta-stable or the ground state is reached. This would lead to missing energy.

To get the distribution of E_{dep} , the neutron energy spectrum around the detector array and the neutron capture time, $1.5 \cdot 10^8$ muons were generated above the GERDA water tank. The cosmic-ray generator of MaGe was chosen for this purpose. It generates muons according to the muon energy spectrum and the muon angular distribution measured by the MACRO experiment at the Gran Sasso underground laboratory [85] [84]. The circular generator plane was located 5 m above the detector array and had a radius of 5 m. Since the detector mass differences of different GERDA phases are small compared to the total set-up mass, it is expected that the radionuclide production rates will be the same for all GERDA phases. The much smaller volumes of BEGe detectors compared to coaxial detectors and thus different detection efficiencies are expected to be more relevant. Therefore only the GERDA Phase Ib set-up with 14 detectors (coaxial and BEGe) was simulated.

The passage of muons and the capture of induced neutrons were simulated. Energy depositions from the capture cascade are investigated with another simulation separately. All gammas which are emitted by nuclei produced by neutron capture were discarded to avoid energy depositions from the capture cascade. Energy depositions in the germanium detectors as well as the neutron capture vertices were recorded to estimate the E_{dep} distribution. The quenching of the nuclear recoil is not considered in the simulations. However, the fraction of the nuclear recoil to the total energy deposition which are not from neutron capture cascade is less than 10%.

The neutron capture time as well as the neutron creation time and energy for all produced neutrons were recorded. The energy of neutrons crossing a sphere with a 30 cm radius centered in the middle of the detector array were recorded as well to get the neutron energy spectrum. These simulations can also be used to determine the radionuclide production rate (e.g the $^{75(m)}\text{Ge}$ which has not been investigated so far).

To simulate the de-excitation of the radionuclides after neutron capture and to get the energy depositions from the neutron capture cascade, 10^6 excited nuclei at the energy level of S_n were uniformly generated inside the germanium detectors for each isotope ($^{77}\text{Ge}/^{75}\text{Ge}$) and for each detector type (coaxial/BEGe detectors). The energy depositions inside the germanium detectors were recorded. To determine if the meta-stable or the ground state is reached after the de-excitation, also the energy of the emitted gammas was recorded.

To estimate the fraction of full energy depositions of the IT gamma, 10^6 meta-stable states were generated inside the germanium detectors for each isotope and each detector type. The energy deposition inside the germanium detectors were recorded. The same simulations were conducted using GEANT4 9.4 for comparison.

The ^{77m}Ge simulations can also be used to determine the energy depositions from ^{77m}Ge β^- decay. To get the energy depositions inside the germanium detectors from ^{77}Ge β^- decays, the decay of 10^6 ^{77}Ge nuclei were simulated.

The recorded energy of neutrons passing the sphere around the detector array were used to get the normalized neutron energy spectrum which is shown in Fig. 7.6. This energy spectrum will be used to obtain the average cross section (see chapter 8).

The distribution of times that passed between the neutron capture (t_{cap}) and either muon generation (t_0), neutron creation (t_{cr}) or the last inelastically interaction of the neutron (t_{li}) is shown in Fig. 7.7. It can be seen from Fig. 7.7 that all three distributions are very similar. This shows that the time needed for the neutron to be captured is much larger than the time between the muon generation and the neutron creation. Also the last inelastic interaction of neutrons happen shortly after their creations. Afterwards, they only undergo elastic scattering until they are captured.

From Fig. 7.7 it can be seen that most of the neutrons are captured on germanium within $10 \mu\text{s}$. However, 20.63% of all neutron captures happen after $10 \mu\text{s}$. Thus, these neutron capture events will not be tagged as vetoed by the muon veto.

In total 159 $^{75(m)}\text{Ge}$ and 349 $^{77(m)}\text{Ge}$ nuclei were produced in the simulation. The lifetime of the simulation corresponds to 127.73 yr and the enriched mass of the implemented set-up is 21.3 kg. The production rate of $^{75(m)}\text{Ge}$ is found to be $(0.0584 \pm 0.0046_{stat.})$ nuclei/(kg yr). The systematic uncertainty for muon-induced isotope production was estimated to be 35% [4]. By adding this systematic uncertainty in quadrature, the $^{75(m)}\text{Ge}$ production rate is

$$(0.06 \pm 0.02) \text{ nuclei}/(\text{kg yr}). \quad (7.7)$$

The $^{77(m)}\text{Ge}$ production rate is

$$(0.13 \pm 0.05) \text{ nuclei}/(\text{kg yr}) \quad (7.8)$$

which is smaller than the values of the other two Monte Carlo simulations:

$$(0.51 \pm 0.09) \text{ nuclei}/(\text{kg yr}) [3] \quad \text{and} \quad (0.21 \pm 0.01) \text{ nuclei}/(\text{kg yr}) [4]. \quad (7.9)$$

In [3] an older GEANT4 version was used while in [4] the $^{77(m)}\text{Ge}$ cross section was artificially increased by 68%. Also the Phase II set-up was used. If the $^{77(m)}\text{Ge}$ production rate of Eq. 7.8 is increased by 68%, this results in a production rate of 0.22 nuclei/(kg yr) which is within the uncertainty range of the $^{77(m)}\text{Ge}$ production rate from [4]. Thus, the production rate of the Phase Ib and of Phase II set-up should be the same within their uncertainties. The implemented cross section in the Monte Carlo simulation affects only the production rate of the radionuclides but not the shapes of the investigated distributions.

The distribution of the total energy deposition $E_{tot} = E_{dep} + E_{cas}$ is shown in Fig. 7.8. Most of the energy deposition comes from the capture cascade. However, it can be seen from Fig. 7.8 that other energy depositions are not negligible for the efficiency determination. It can also be seen from Fig. 7.8 that in average less energy is deposited inside

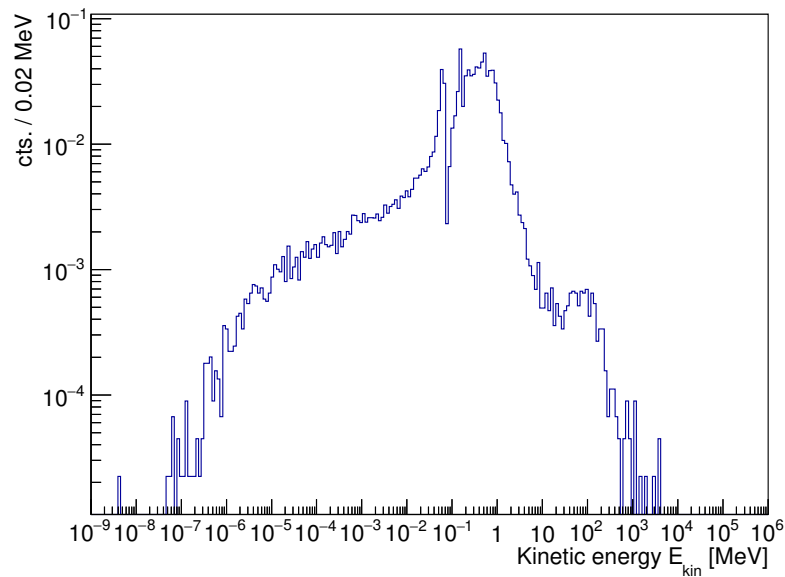


Figure 7.6: Normalized simulated neutron energy spectrum around the germanium detector array for neutrons crossing a sphere with a radius of $r = 30$ cm.

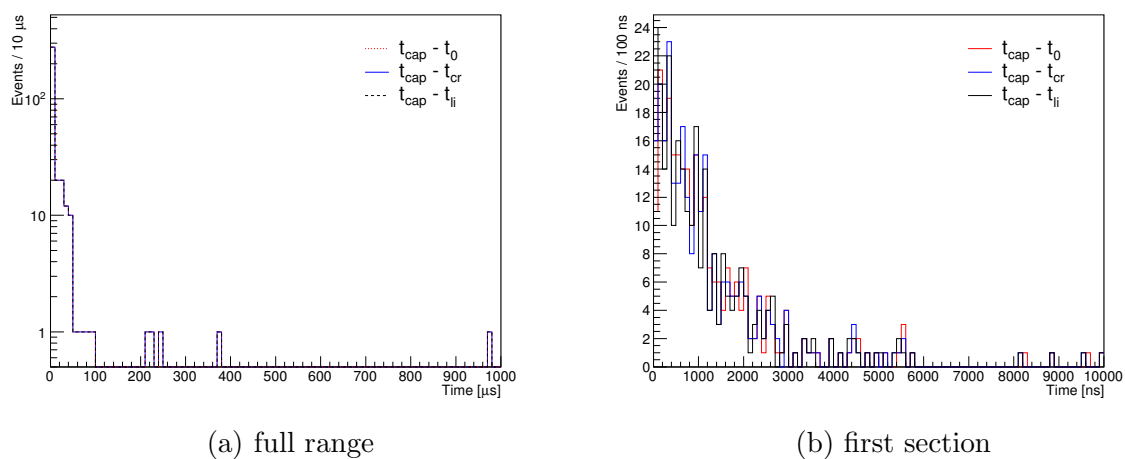


Figure 7.7: Simulated time distributions. The time differences of time of the capture on germanium t_{cap} to the simulation start time t_0 , to the neutron creation time t_{cr} and to the time of the last inelastic scattering t_{li} are shown.

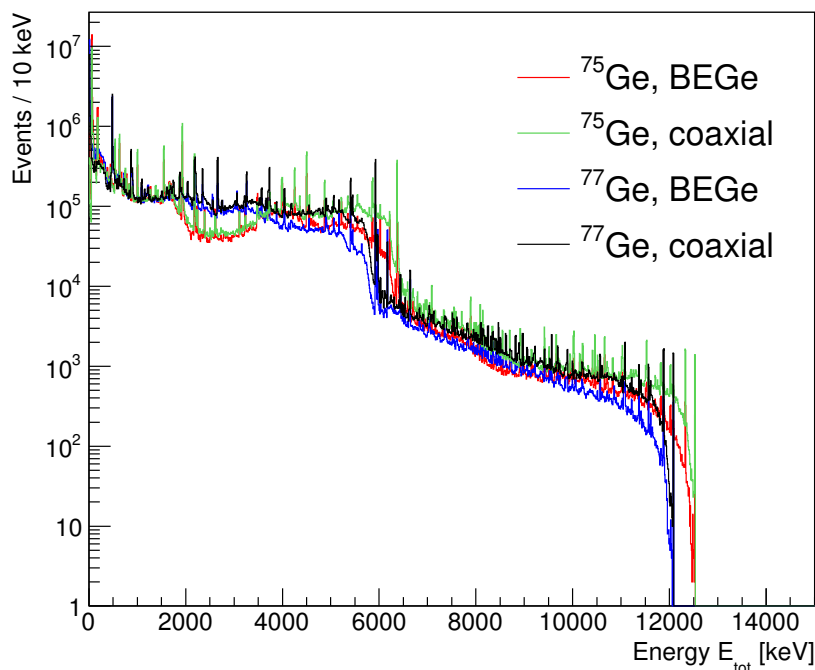


Figure 7.8: Total energy deposition E_{tot} in the detector where the neutron is captured on different isotopes for different detector types (BEGe or coaxial).

BEGe detectors than in coaxial detectors.

The efficiency to detect the high energy deposition from the neutron capture ($E > E_{cut}$) can be determined by estimating the fraction of energy depositions above E_{cut} . Thus, the efficiency depends on the cut value E_{cut} and decreases for increasing E_{cut} values. The neutron capture efficiency ϵ_{ncap} depending on E_{cut} is shown in Fig. 7.9. The efficiency values as a function of E_{cut} are summarized in Appendix H.

Since ϵ_{ncap} decreases with increasing E_{cut} , E_{cut} should be as low as possible. On the other hand the background for the muon-induced radionuclide search increases with decreasing E_{cut} . Thus, E_{cut} should be larger than the Q-value of $2\nu\beta\beta$ decay and should lie above the ^{208}Tl gamma line at 2615 keV.

The normalized energy spectra from ^{77m}Ge and ^{77}Ge β^- decay are shown in Fig. 7.10 for BEGe and coaxial detectors. It can be seen that BEGe detectors have in average more energy depositions at low energies but less energy depositions at high energies compared to coaxial detectors. This can be explained by the much smaller detector volume of BEGe detectors. The probability that a high energy gamma deposit most or its full energy increases with increasing detector volume.

The efficiency that the IT gamma energy is fully deposited inside the detector volume ϵ_{IT} is calculated by dividing the number of events where the full energy of the IT gamma was deposited with the number of simulated events. The results are shown in Table 7.1. It can be seen that both GEANT4 versions agree within $\sim 1\%$. The value of

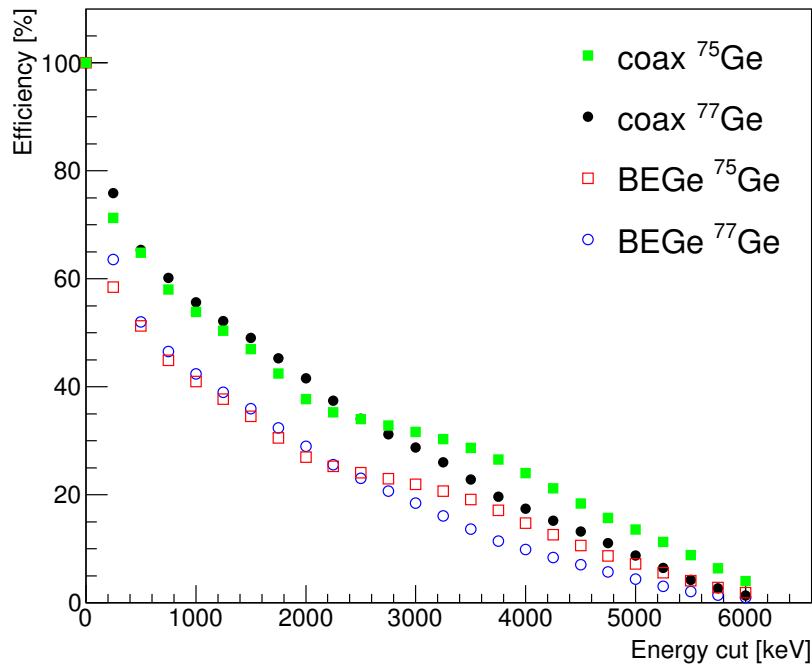


Figure 7.9: Total neutron capture detection efficiencies.

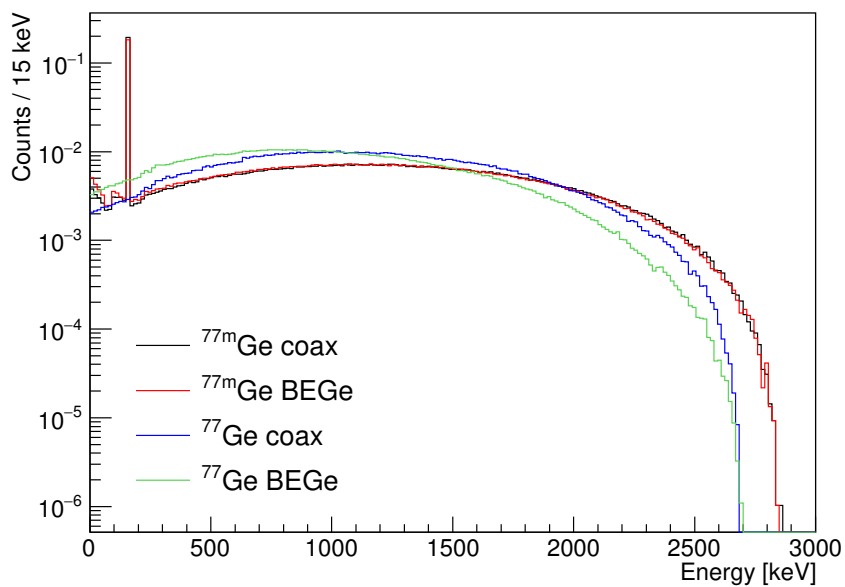
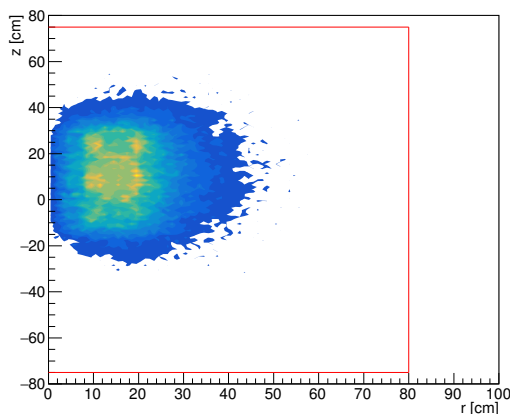


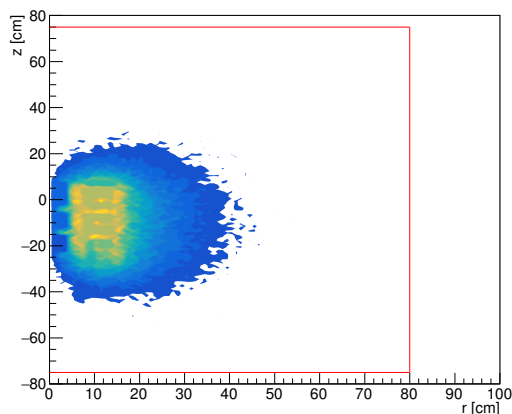
Figure 7.10: Normalized distribution of the energy depositions in coaxial or BEGe detectors due to ^{77m}Ge and ^{77}Ge β^- decay. The energy depositions from ^{77m}Ge can also be due to IT which appear as a peak in the energy spectrum.

Table 7.1: Full IT energy deposition detection efficiencies ϵ_{IT} in [%].

Isotope	Detector	Geant4 9.4.3	Geant4 10.3.0	ϵ_{IT}
^{77m}Ge	Coaxial	88.48 ± 0.07	87.96 ± 0.07	88.0 ± 0.6
	BEGe	83.30 ± 0.08	82.22 ± 0.09	82 ± 1
^{75m}Ge	Coaxial	93.42 ± 0.02	93.13 ± 0.03	93.1 ± 0.3
	BEGe	90.35 ± 0.03	89.59 ± 0.03	89.6 ± 0.8



(a) Phase I, 14 detectors



(b) Phase II

Figure 7.11: Generation vertex distribution for events with fully detected ^{41}Ar 1293.6 keV gammas. The border of the generation volume is shown as a red line.

the GEANT4 10.3 is chosen for ϵ_{IT} . The deviation to the other GEANT4 version is used as systematic uncertainty. As for ϵ_{ncap} , ϵ_{IT} is larger for coaxial detectors than for BEGe detectors.

Argon Gamma Search To determine the efficiency of detecting the 1293.6 keV gamma from ^{41}Ar β^- decay, GEANT4 10.3.2 and GEANT4 9.4.3 were used. Since ^{41}Ar is produced outside the germanium detectors, the detection efficiency depends on the array configuration. For the Phase Ib and for the Phase II set-up, 10^8 ^{41}Ar were generated. The nuclei were generated inside a cylindrical volume around the detector array which has a radius of 80 cm and a height of 1.5 m. The energy depositions inside the germanium detectors as well as the generation vertices were recorded.

Figure 7.11 shows the ^{41}Ar generation vertex distribution for all events with fully detected ^{41}Ar 1293.6 keV gammas. It can be seen that all these vertices are far away from the boundary of the generation volume. Thus, the fiducial volume is large enough for containing all detectable ^{41}Ar .

The gamma detection efficiency is calculated by dividing the number of events with 1293.6 keV energy deposition in one detector by the number of all simulated ^{41}Ar nuclei.

Table 7.2: Argon gamma detection efficiencies in [%] for Phase Ib (14 detectors) and Phase II.

Setup	Geant4 10.3.2	Geant4 9.4.3	ϵ_{Ar} [%]
Phase Ib	0.0685 ± 0.0003	0.0683 ± 0.0003	0.0685 ± 0.0005
Phase II	0.0959 ± 0.0003	0.0965 ± 0.0003	0.0959 ± 0.0009

The results are shown in Table 7.2. Similar results were delivered with both GEANT4 versions. From Table 7.2 it can be seen that the efficiency for detecting the ^{41}Ar 1293.6 keV gamma produced in the fiducial volume is below 1% and thus too low for an analysis. Therefore only signatures of neutron capture on ^{76}Ge and ^{74}Ge were used for the data analysis which is described in the next chapter.

Chapter 8

GERDA Muon-Induced Radionuclide Search Results

The muon-induced production rates of $^{77(m)}\text{Ge}$ and $^{75(m)}\text{Ge}$ due to neutron capture were investigated. The signature from the neutron capture is a high energy deposition

$$E > E_{cut} . \quad (8.1)$$

Since only the muon-induced production rate is investigated, the high energy deposition should be accompanied by a signal from the muon veto. To reduce background, a time cut t_{cut} is set on the time difference of the muon veto signal and the germanium detector signal from the neutron capture. Most of the background is expected to be prompt while the neutron capture needs some time (see section 7.2). Thus, events with time differences below t_{cut} are not considered.

The high energy deposition is followed by an energy deposition around the IT energy E_{IT} within few half-lives of the meta-stable state

$$E \in [E_{IT} \pm \Delta E] \quad \text{within} \quad t < 50 T_{1/2} \quad (8.2)$$

with the half of the IT energy window size ΔE and the time t which passes by between the neutron capture signal and the IT signal. The size of ΔE should be of the order of the energy resolution. If ΔE would be much larger, the background would be larger. If ΔE would be smaller than the energy resolution, signals would be cut away. Unlike neutron capture events where energy is likely be deposited in more than one germanium detector, the energy from IT is mostly deposited only in one detector. Therefore an anti-coincidences cut is set for the IT signature to reduce background. The IT event should not be vetoed by the muon veto or the LAr veto as well (only available for Phase II).

The number of expected signals can be calculated from the production rate R_c from neutron capture. The production rate of the meta-stable state is

$$R_m = f_m \cdot R_c \quad (8.3)$$

with f_m being the branching fraction of meta-stable state production which is $\sim 50\%$ for ^{77m}Ge and ^{75m}Ge production (see section 7.1). The ground state production rate via IT of the meta-stable state R_{IT} is

$$R_{\text{IT}} = f_{\text{IT}} \cdot R_m \quad (8.4)$$

with f_{IT} being the branching ratio of IT. The observed production rate is given by R_{IT} and the efficiency ϵ

$$R_{\text{obs}} = \epsilon \cdot R_{\text{IT}}. \quad (8.5)$$

The number of expected signals N_S can be calculated from the exposure \mathcal{E} of the used data and from the production rate

$$N_S = \mathcal{E} \cdot R_{\text{obs}} = \mathcal{E} \cdot \epsilon \cdot f_{\text{IT}} \cdot f_m \cdot R_c. \quad (8.6)$$

A binned extended-likelihood fit is conducted using the Bayesian toolkit BAT [88]. The likelihood for the analysis of the radionuclide production rate is given by

$$L = \prod_{i=1}^B e^{-\alpha_i} \frac{\alpha_i^{A_i}}{A_i!}. \quad (8.7)$$

with the number of bins B , the expected rate α_i and the rate for each bin

$$A_i = \frac{n_i}{\Delta x_i}. \quad (8.8)$$

Here n_i is the number of counts in bin i and Δx_i is the bin width. In order to be able to use the same equations for $^{77(m)}\text{Ge}$ and $^{75(m)}\text{Ge}$, the time t which passes by between the neutron capture signal and the IT signal is substituted with the number of half-life fractions x

$$t = x \cdot T_{\frac{1}{2}}. \quad (8.9)$$

The expected rate considers contributions from signal and background. Around E_{IT} , the dominant background component comes from ^{39}Ar decay which has a half-life of 269 years. Since this half-life is much longer than the half-lives of ^{77m}Ge and ^{75m}Ge , the background rate is approximately constant. The expected rate α_i is therefore

$$\alpha_i = \ln(2) \cdot \mathcal{E} \cdot \epsilon \cdot f_{\text{IT}} \cdot f_m \cdot R_c \cdot e^{-\ln(2) \cdot x_i^c} + A_{\text{bkg}} \quad (8.10)$$

with x_i^c being the value in the center of bin i and the constant background rate A_{bkg} . For the derivation of the likelihood function and Eq. 8.10 see Appendix I. The free parameters of the fit are the production rate R_c , the background rates A_{bkg} for each dataset and an efficiency deviation $\delta\epsilon$ to account for the systematic uncertainties ($\epsilon \rightarrow \epsilon + \delta\epsilon$). A Gaussian prior with a mean at zero and a sigma which is of the order of the efficiency uncertainties (see section 8.3) is chosen for $\delta\epsilon$. Also for the background rates, a Gaussian prior is chosen using information of the background fit (see section 8.2) for events with $t \in [10 T_{1/2}, 50 T_{1/2}]$. For R_c , a flat prior is chosen.

The data selection and used datasets are described in section 8.1. The signal and background extraction with all set cuts is presented in section 8.2. The composition of the total efficiency ϵ with their systematic uncertainties as well as the expected number of signals N_{obs} as a function of exposure is presented in section 8.3. The results of the data analysis are described in section 8.4.

8.1 Datasets and Data Selection

The GERDA raw data are processed offline with the data analysis framework GELATIO [96] which organizes the data analysis in multiple levels. The raw data from the DAQ are stored in Tier0 and are converted into the MGDO¹ format and then stored in Tier1. The signal traces, time stamps and DAQ flags etc. are stored in this level. The other levels (Tier2, Tier3 and Tier4) contain the analysis results of the data processing. In Tier2, the output of the signal trace analyses like the rise time and the amplitude of the pulse as well as the trigger position is stored. The calibrated energies and the quality cut flags are available in Tier3. Tier4 contains all parameters needed for the final $0\nu\beta\beta$ decay analysis.

For the muon-induced radionuclide search presented in this thesis, the information of Tier2 and Tier3 has been used. Since the number of germanium detectors implemented in the GERDA detector array (and thus possibly also the background) has been changed, GERDA data was divided into datasets containing data of periods with the same number of detectors. In GERDA Phase I which starts with run 26, the number of used detectors has been changed multiple times. From run 26 to run 32, 11 coaxial detectors were placed in the GERDA set-up. Run 31 was very unstable and is not considered in the analysis of this thesis. In run 33 and run 34, only 9 detectors were implemented in the detector array. Since the lifetime of these two runs is very short and run 33 is very unstable, these runs have not been considered either. From run 35 to run 46, 14 detectors (5 BEGe and 9 coaxial detectors) were placed inside the set-up. Phase II starts with run 53. The germanium trigger threshold had been increased to ~ 150 keV. Therefore these data can not be used for the search of ^{77m}Ge and ^{75m}Ge IT. The threshold has been lowered to

¹MGDO: Majorana-GERDA Data Objects

Table 8.1: Informations of used data sets.

	Phase Ia	Phase Ib	Phase IIb
Runs	26 – 30, 32	35 – 46	87 – 92
Detectors	11	14	40
Lifetime [d]	131.95	302.14	162.79
Det. mass [kg]	25.26	24.25	43.20
Enr. mass [kg]	17.66	21.29	35.60
BEGe mass [kg]	0	3.62	20.02
Active mass [kg]	23.38	20.48	38.73
Act. enr. mass [kg]	15.78	17.52	33.33
Act. BEGe mass [kg]	0	2.90	17.76
Act. coax mass [kg]	15.78	14.62	15.58
Act. f_{BEGe} [%]	0	16.56	53.27
Enr. exposure [kg yr]	5.70	14.50	14.87

~ 16 keV since run 87. The last run considered for this thesis is run 92. Information on the used datasets are shown in Table 8.1.

For the ^{77m}Ge and ^{75m}Ge IT search, the energy threshold must be well below E_{IT} . To determine the energy thresholds, the ^{39}Ar β^- decay spectrum from Monte Carlo simulations was fitted to the data for each run and channel. For Phase II run 87 – 92, also a peak-like structure around 25 keV appears in the data which was fitted with a Gaussian. The difference between the fit and the data was then fitted with the cumulative distribution $\Phi(E)$ of a generic normal distribution with the mean μ and deviation σ

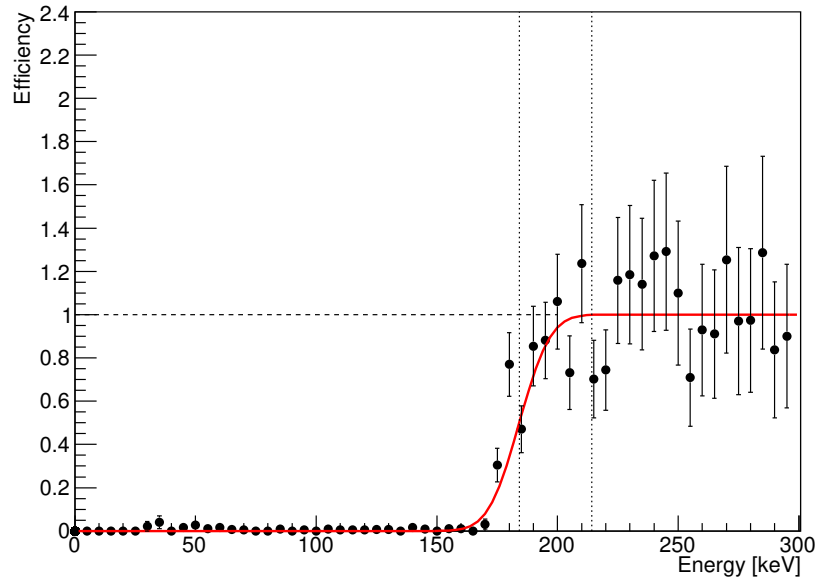
$$\Phi(E) = \frac{1}{2} \cdot \left[1 + \operatorname{erf} \left(\frac{E - \mu}{\sqrt{2}\sigma} \right) \right] \quad (8.11)$$

with E being the energy and with the error function

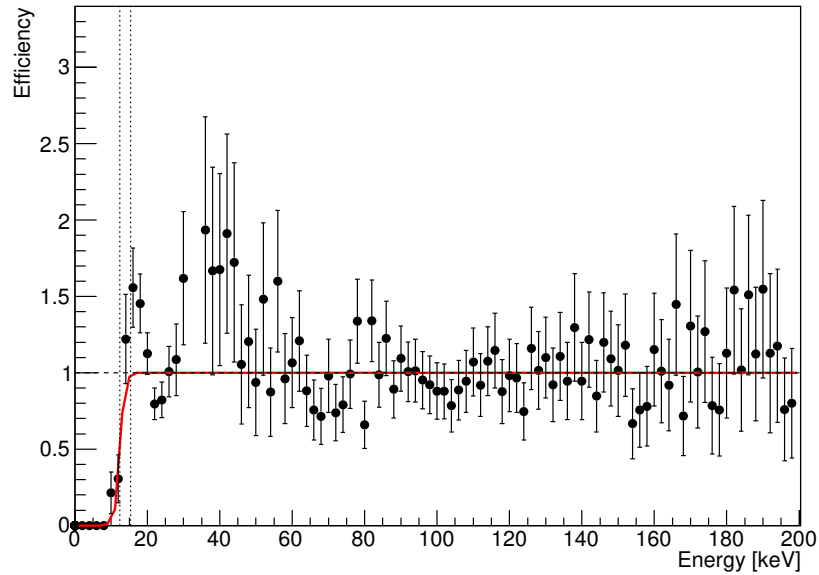
$$\operatorname{erf}(x) = \frac{2}{\sqrt{\pi}} \int_0^x e^{-t^2} dt \quad (8.12)$$

to get μ and σ . In Fig. 8.1, the energy reconstruction efficiency distribution fit for Phase II with a high and a low germanium detector energy trigger threshold setting are shown. It can be seen that for a high germanium detector energy trigger threshold as set for run 53 – 86, the energy threshold is around E_{IT} . Except for runs of Phase II with the higher energy trigger threshold, it is well below E_{IT} for all detectors in all runs considered in this analysis (for fit results see Appendix J).

For the efficiency of detecting the high energy deposition from the neutron capture, also the energy at which the germanium detectors go into saturation E_{sat} is crucial, since



(a) Phase II, run 53 ch 39



(b) Phase II, run 92 ch 31

Figure 8.1: Energy reconstruction efficiency distribution for Phase II with a high and a low germanium detector trigger threshold. The first dashed line indicates μ of the fitted cumulative distribution distribution of a generic normal distribution with the mean μ and deviation σ . The second dashed line indicates the value of $\mu + 3 \cdot \sigma$.

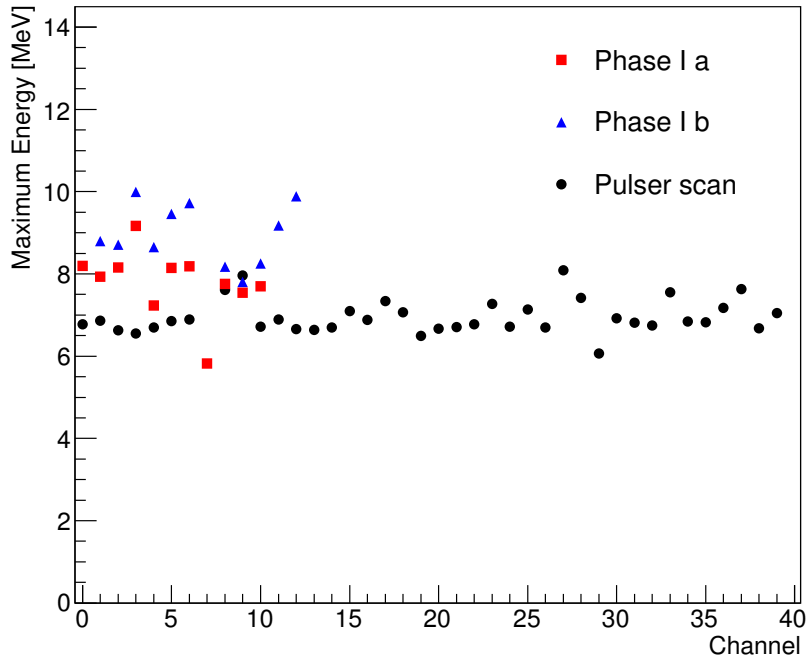


Figure 8.2: Maximal energies of the germanium detectors for Phase Ia and Phase Ib datasets and the maximum energy from Phase II pulser scan.

saturated events are cut away by quality cuts and are not contained in Tier3. To estimate this energy, the maximum energy of each channel was obtained for different datasets. For Phase II, data from pulser scans are available and were used instead. The maximum energies for each channel and dataset are shown in Fig. 8.2.

The efficiency ϵ_{sat} due to the saturation cut is given by the fraction of neutron capture events for which the deposited energy from the neutron capture event E_{tot} (see Fig. 7.8) is below E_{sat} . Since the deposited energy E_{tot} depends on the detector type, the ϵ_{sat} distribution as a function of E_{sat} depends on the BEGe to coaxial detector active mass fraction which is different for each dataset. The distributions for each dataset and each radionuclide are shown in Fig. 8.3. It can be seen that ϵ_{sat} increases with increasing E_{sat} . For all values shown in Fig. 8.2, the efficiency would be larger than 80% and for most of the values even higher than 90%.

To get the efficiency for each dataset, the efficiency $\epsilon_{sat,ch}$ of all used enriched detectors is weighted with their exposure $m_{ch} \cdot t_{ch}$:

$$\epsilon_{sat} = \sum_{ch} \epsilon_{sat,ch} \cdot \frac{m_{ch} \cdot t_{ch}}{m_{enr} \cdot t_{enr}} \quad (8.13)$$

with the total enriched exposure $m_{enr} \cdot t_{enr}$. For the detector configuration and exposure for the datasets see Appendix K. The results are shown in Table 8.2.

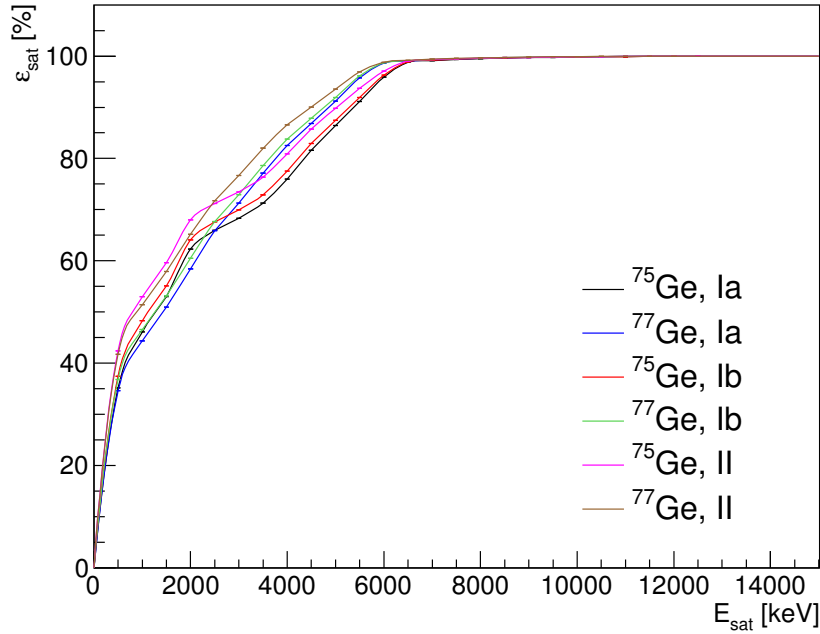


Figure 8.3: Saturation cut efficiencies ϵ_{sat} for different datasets (Phase Ia, Phase Ib and Phase II) depending on the saturation energy E_{sat} .

Table 8.2: Efficiencies ϵ_{sat} in [%] that the deposited energy from the neutron capture is below the saturation energy for different datasets. For Phase I data, the estimated maximum energy of each detector estimated by the data were used. For Phase II, the information of the pulser scan was used instead. The uncertainties due to the binning are estimated by moving the saturation energy E_{sat} by 10 keV.

Dataset	Phase Ia	Phase Ib	Phase II pulser scan
^{75}Ge	99.305 ± 0.006	99.722 ± 0.001	99.203 ± 0.007
^{77}Ge	99.503 ± 0.003	99.782 ± 0.001	99.392 ± 0.004

For the total detection efficiency, the active mass of the detector is relevant. Since these active masses are only known within a certain precision, the uncertainty of the active masses contributes to the systematic uncertainty. To calculate the active mass uncertainty, the active masses m_{ac} given in [79] were summed up for BEGe and coaxial detectors separately

$$m_{ac,coax} = (15326 \pm 951) \text{ g} \quad (8.14)$$

$$m_{ac,BEGe} = (3299 \pm 104) \text{ g}. \quad (8.15)$$

The relative systematic uncertainties of BEGe and coaxial detectors are added in quadrature to get the relative uncertainty of the active mass

$$\frac{\sigma_{sys,m_{ac}}}{m_{ac}} = \sqrt{\left(\frac{\sigma_{m_{ac},coax}}{m_{ac,coax}}\right)^2 + \left(\frac{\sigma_{m_{ac},BEGe}}{m_{ac,BEGe}}\right)^2} = 7\%. \quad (8.16)$$

8.2 Signal and Background Extraction

For the data analysis, information of Tier2 and Tier3 is used. If a muon-vetoed event with an high energy deposition ($E > 3 \text{ MeV}$) in one detector (for Phase II also with a signal from LAr veto) is followed by an IT like event ($E \in [E_{IT} \pm 10 \text{ keV}]$) with no energy depositions in other detectors or a signal from the muon veto (for Phase II: also no signal from the LAr veto) within $t < 50 \cdot T_{1/2}$ in the same detector, the energy depositions from the neutron capture and the IT like event as well as the time between these two events t is written to file for further analysis. Also the germanium trigger time t_{Ge} and the time of the muon veto signal $t_{\mu,t2}$ which are stored in Tier2 are written to file.

The prompt background induced by muons can be reduced by setting a cut on the time difference Δt between the muon veto and the germanium detector trigger time. Events with a smaller difference than a cut value t_{cut} are considered to be background.

The trigger time of the muon veto is not only recorded by the muon veto DAQ but it is also fed into the DAQ of the germanium detectors and stored in the Tier files. The recorded trace window of $(0 - 160) \mu\text{s}$ is recorder such that the trigger time is located in the middle of the trace around $80 \mu\text{s}$ for the trigger times recorded by the germanium DAQ t_{Ge} and the muon veto DAQ $t_{\mu,DAQ}$. However, the recored muon veto trigger times

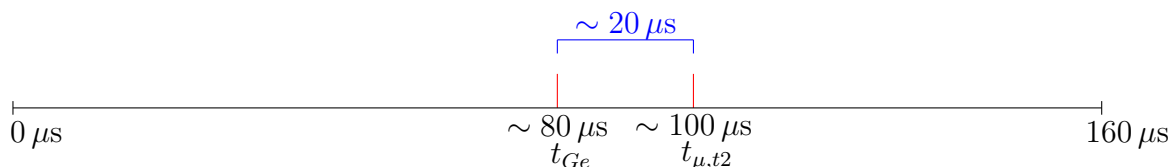


Figure 8.4: Sketch of the time difference between muon veto signal which is stored in Tier2 $t_{\mu,t2}$ and the germanium trigger time t_{Ge} .

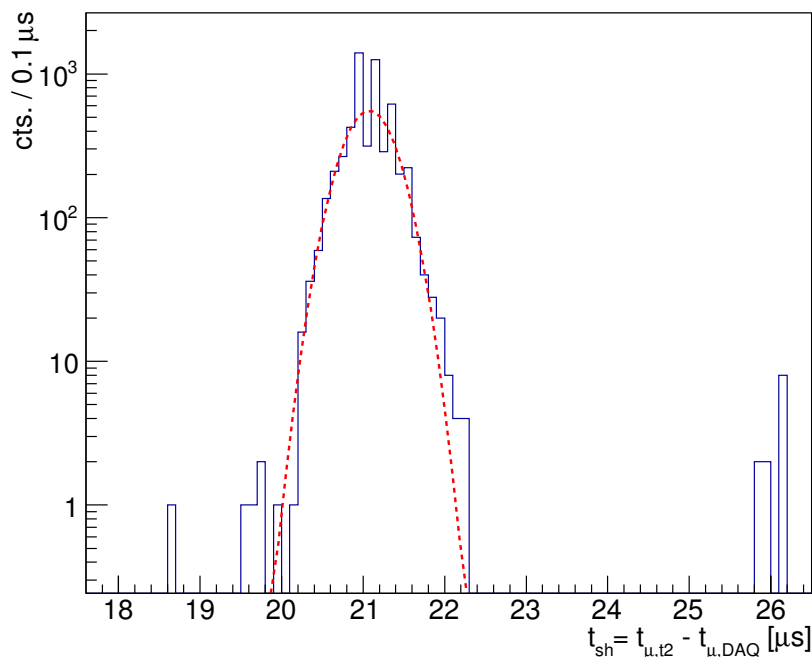


Figure 8.5: Time shifts t_{sh} between the muon veto signal of the germanium DAQ $t_{\mu,t2}$ and the muon veto DAQ $t_{\mu,DAQ}$. The red dashed line indicates the Gaussian fit.

in Tier2 ($t_{\mu,t2}$) have values around $100 \mu\text{s}$. Thus, the muon veto signal time of Tier2 ($t_{\mu,t2}$) is shifted by t_{sh} in relation to the recorded muon trigger time of the muon veto DAQ ($t_{\mu,DAQ}$). This is illustrated by Fig. 8.4.

The time shift t_{sh} between the recorded muon DAQ trigger time $t_{\mu,DAQ}$ and the stored time of the muon veto trigger time in the germanium DAQ $t_{\mu,t2}$ has been determined by using Phase I data. Events of run 26 – 30, run 32 and run 35 – 46 which are vetoed in time by the muon veto and which are not test pulses have been used. The time shifts between the muon veto DAQ $t_{\mu,DAQ}$ and Tier2 $t_{\mu,t2}$ are shown in Fig. 8.5. By fitting the distribution with a Gaussian, the time shift is determined to be

$$t_{sh} = (21.1 \pm 0.3) \mu\text{s}. \quad (8.17)$$

With this value, the corrected muon signal time t_{μ} can be calculated

$$t_{\mu} = t_{\mu,t2} - t_{sh}. \quad (8.18)$$

To choose a cut value t_{cut} for the time difference of the muon veto signal to the germanium detector signal Δt , background events chosen from the muon-induced radionuclide

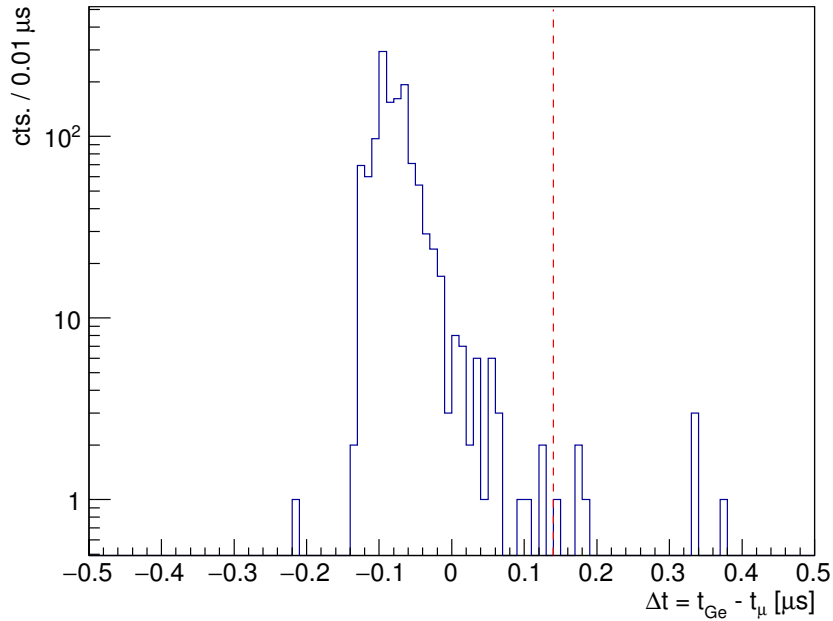


Figure 8.6: Time difference Δt of the germanium trigger time t_{Ge} of the neutron capture signal to the corrected muon veto signal time t_{μ} of selected background events with time differences between the neutron capture signal and the IT signal within $t \in [10 \cdot T_{1/2}, 50 \cdot T_{1/2}]$. The chosen value of $t_{cut} = 0.14 \mu s$ is indicated by the dashed red line.

search dataset were analyzed. Events with time differences between the neutron capture signal and the IT signal

$$t \in [10 \cdot T_{1/2}, 50 \cdot T_{1/2}] \quad (8.19)$$

were used. These events can be considered as background, since it is very unlikely that events with such large time difference result from neutron capture followed by IT of the meta-stable state. The time differences Δt of the germanium trigger time t_{Ge} to the corrected muon veto signal time t_{μ} for background events is shown in Fig. 8.6. From Fig. 8.6 it can be seen that for most background events this time difference is smaller than $0.14 \mu s$. For $t_{cut} = 0.14 \mu s$, $(99.4 \pm 0.2)\%$ of all background events can be removed while only $(6 \pm 1)\%$ of signal events are cut away.

The background rate A_{bkg} (counts per bin width) was determined by analyzing events with times between the neutron capture signal and the IT signal within the time window

$$t \in [10 \cdot T_{1/2}, 50 \cdot T_{1/2}] . \quad (8.20)$$

Different cuts on the energy of the neutron capture event E_{cut} and the half width of the IT window (ΔE), were set. No time cut t_{cut} on the time difference of the germanium trigger time of the neutron capture event and the muon veto signal time were set.

Figure 8.7 shows the background rate A_{bkg} in terms of events per half life as a function

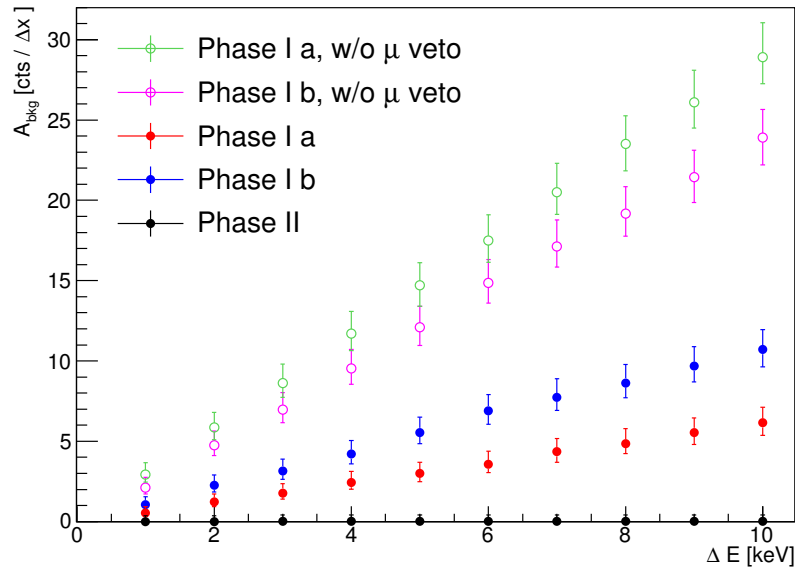
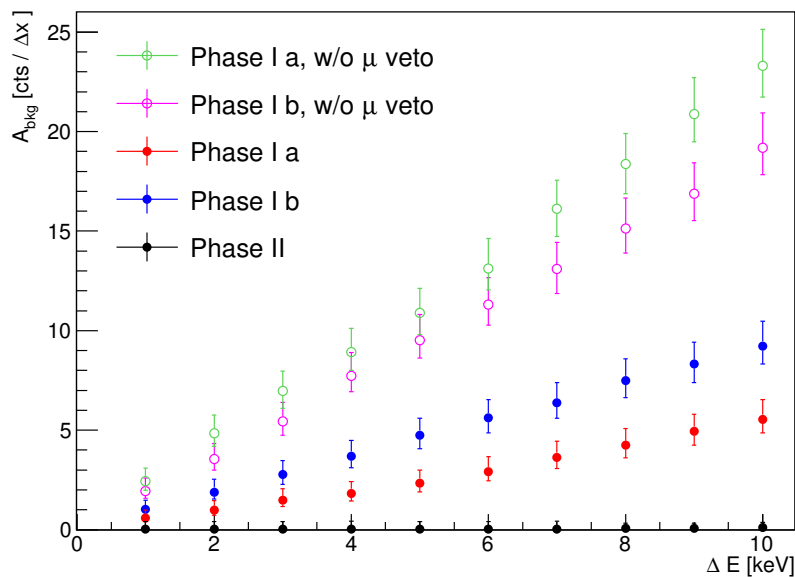
(a) ^{75}Ge (b) ^{77}Ge

Figure 8.7: Background counts per bin width A_{bkg} for $E_{cut} = 3$ MeV. For Phase Ia and Phase Ib, A_{bkg} is also shown if no muon veto signal is required for the neutron capture signal. For Phase II, also the LAr veto was used.

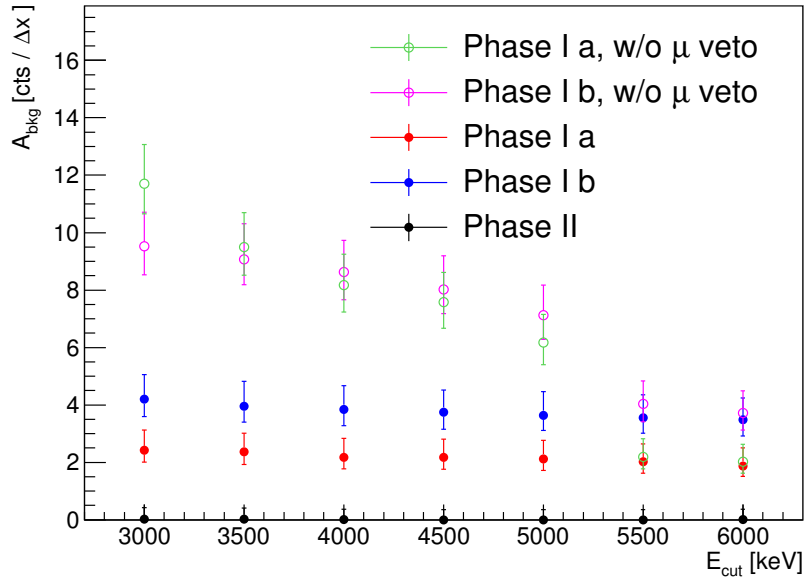
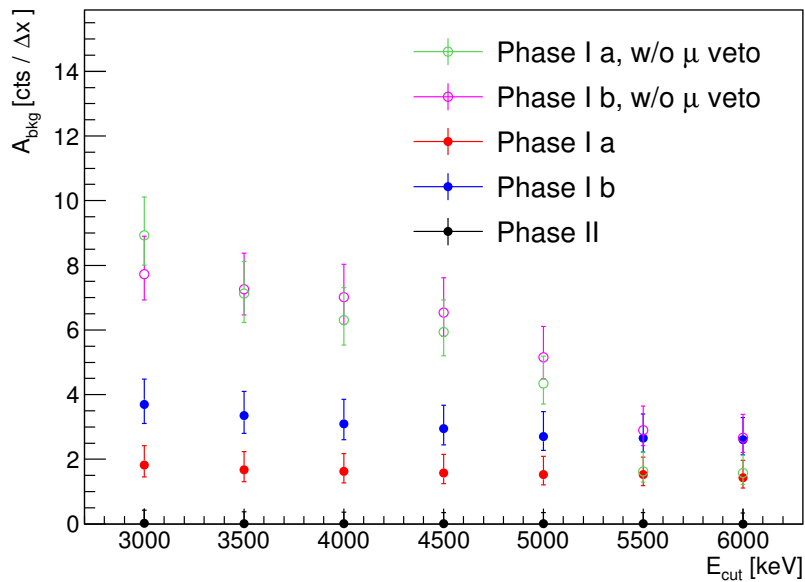
(a) ^{75}Ge (b) ^{77}Ge

Figure 8.8: Background counts per bin width A_{bkg} for $\Delta E = 4$ MeV. For Phase Ia and Phase Ib, A_{bkg} is also shown if no muon veto signal is required for the neutron capture signal. For Phase II, also the LAr veto was used.

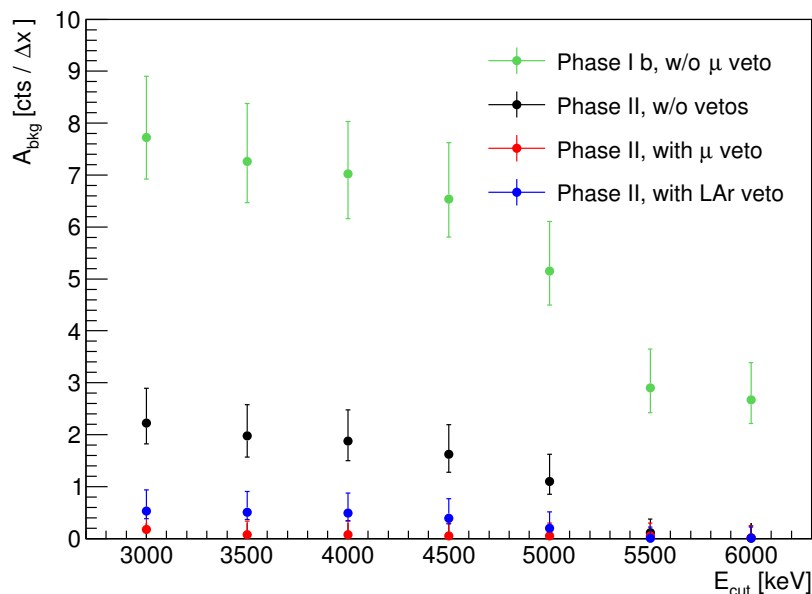


Figure 8.9: Background counts per bin width A_{bkg} for $\Delta E = 4$ keV for Phase II if the muon veto information is not used for the neutron capture signal and the LAr veto information is not used, if only the muon veto information is used for the neutron capture and the IT or if only the LAr information is used. Also the background rate for Phase Ib if no muon veto signal is required for the neutron capture signal is shown.

of ΔE for fixed E_{cut} . It can be seen that A_{bkg} increases linearly with ΔE as expected. ΔE is chosen such that it is in the order of the energy resolution to have a small background rate but no signals are cut. Since the background rates are not normalized to exposure, the background rate of Phase Ib is larger than the Phase Ia background rate due to its larger exposure. Phase II and Phase Ib have similar exposures. The usage of the LAr veto in Phase II further reduces A_{bkg} . For Phase Ia and Phase Ib, the background rate is shown as well if no muon veto is required for the neutron capture signal.

In Fig. 8.8, the background rate A_{bkg} as a function of E_{cut} is shown. If no muon veto signal is required for the neutron capture signal, the background rate decreases with increasing E_{cut} . Around the peak from α 's at 5 MeV, the A_{bkg} becomes significantly reduced. However, if a signal from the muon veto is required for the neutron capture signal, the background rate is nearly the same for all E_{cut} values. Since the efficiency decreases with increasing E_{cut} , $E_{cut} = 3$ MeV is chosen for the muon-induced radionuclide search.

In Fig. 8.9, the background rate for Phase II with differently set cuts is shown. Also the background rate of Phase Ib if no muon veto signal is required for the neutron capture event is shown. Although the exposure of Phase Ib and Phase II is similar, the background rate of Phase II is much smaller if the LAr veto information is not used as well as the muon veto information for the neutron capture but only for the IT signal (which should not be accompanied with a muon veto signal). This is due to a more efficient anti-coincidence

cut. Events with energy depositions in more than one detector are unlikely to be from IT and are discarded. Since much more detectors are used in Phase II than in Phase Ib, this cut becomes more efficient. If additionally the LAr veto information is used by requiring a LAr veto signal for neutron capture events and cut IT like events which are accompanied by a signal in the LAr veto (most likely background events), the background rate gets further reduced.

From Fig. 8.9 it can be seen that the usage of the muon veto information for the neutron capture signal reduces the background rate more than the usage of the LAr veto information for the neutron capture and the IT events. If both vetoes are used, nearly all background events are discarded (see Figs. 8.7 and 8.8).

For choosing ΔE , the energy resolution at E_{IT} has to be determined. The results of the GERDA super-calibration (for more information see [46]) can be used. Full width at half maximum as a function of energy is parameterized with

$$\text{FWHM} = \sqrt{a^2 + b \cdot E} \quad (8.21)$$

with the parameters a and b determined by the super calibration. The FWHM at 139.69 keV is (2.471 ± 0.008) keV for coaxial and (2.06 ± 0.01) keV for BEGe detectors. The FWHM at 159.7 keV is (2.485 ± 0.008) keV for coaxial detectors and (2.07 ± 0.01) keV for BEGe detectors.

The FWHM at 0 keV extrapolated by using the parameterization of Eq. 8.21 is 1.98 keV for BEGe detectors and 2.37 keV for coaxial detectors. These FWHM values can be compared to the results of a pulser scan done for Phase II. The average FWHM from pulser scan was determined for each detector. The average FWHM of BEGe and coaxial detectors were determined and found to be 2.718 keV for coaxial and 2.31 keV for BEGe detectors. Thus, the relative uncertainty is 15% for coaxial and 17% for BEGe detectors. The FWHM becomes therefore (2.5 ± 0.3) keV for coaxial and (2.1 ± 0.4) keV for BEGe detectors at 139.69 keV and (2.5 ± 0.4) keV for coaxial detectors and (2.1 ± 0.4) keV for BEGe detectors at 159.7 keV. Since the IT search window should be larger than the energy resolutions of all detectors, $\Delta E = 2.5$ keV is chosen.

With the chosen cut values $E_{cut} = 3$ MeV for the high energy deposition of the neutron capture signal, $\Delta E = 2.5$ keV for the IT gamma search window and $t_{cut} = 0.14 \mu\text{s}$ for the time difference of the germanium detector trigger to the trigger signal of the muon veto, the background rates A_{bkg} were determined for each dataset which are used for the prior information of the muon-induced radionuclide search fit. Since no event survived the cuts, only upper limits could be set. The upper limit is the same for all datasets and radionuclide searches and is 0.36 counts per half-life fraction x at 95% CI. As priors for the background rates A_{bkg} , Gaussian distributions with means at zero and standard deviations of $\sigma = 0.36/2 = 0.18$ are chosen.

Table 8.3: Efficiencies for different datasets. The efficiencies ϵ_{sat} , ϵ_{ncap} and ϵ_{IT} are without systematic uncertainties. The total efficiency for each dataset was determined using a toy Monte Carlo. All efficiencies were varied within their uncertainties. For the toy Monte Carlo, also systematic uncertainties due to the Monte Carlo uncertainties as well as the active mass uncertainty were considered.

Dataset	Efficiency	Phase Ia	Phase Ib	Phase II
^{75}Ge	ϵ_{sat}	99.305 ± 0.006	99.722 ± 0.001	99.203 ± 0.007
	ϵ_{ncap}	31.7 ± 0.5	30.1 ± 0.4	26.5 ± 0.3
	ϵ_{IT}	93.1 ± 0.3	30.1 ± 0.3	91.2 ± 0.4
	ϵ	21.5 ± 8.0	20.4 ± 7.6	17.1 ± 6.4
^{77}Ge	ϵ_{sat}	99.503 ± 0.003	99.782 ± 0.001	99.392 ± 0.004
	ϵ_{ncap}	28.8 ± 0.4	27.1 ± 0.3	23.3 ± 0.2
	ϵ_{IT}	88.0 ± 0.6	87.0 ± 0.5	84.8 ± 0.6
	ϵ	18.5 ± 6.9	17.3 ± 6.5	14.0 ± 5.2

8.3 Efficiencies and Expectation

For calculating the expected number of observed signal events N_S , the total efficiency ϵ is needed which depends on the dataset. The efficiency ϵ

$$\epsilon = \epsilon_{\mu} \cdot \epsilon_{\text{LAr}} \cdot \epsilon_{\Delta t} \cdot \epsilon_{sat} \cdot \epsilon_{ncap} \cdot \epsilon_{IT} \quad (8.22)$$

is a product of the efficiency of the muon veto $\epsilon_{\mu} = 0.991_{-0.004}^{+0.003}$ [79], the efficiency of the LAr veto $\epsilon_{\text{LAr}} = (97.7 \pm 0.1)\%$ [97], the efficiency of the cut on the time difference of the muon veto signal time and the germanium trigger time $\epsilon_{\Delta t}$, the efficiency that the high energy deposition of the neutron capture signal is below the saturation energy ϵ_{sat} , the efficiency ϵ_{ncap} that the energy deposition from neutron capture is above E_{cut} and the efficiency ϵ_{IT} to fully detect the IT energy. The LAr veto efficiency is only considered for Phase II.

The efficiency $\epsilon_{\Delta t}$ that $\Delta t \in [t_{cut}, 10 \mu\text{s}]$ was estimated by using the neutron capture time distribution determined by Monte Carlo simulations² (see Fig. 7.7 of section 7.2) and was found to be

$$\epsilon_{\Delta t} = (74 \pm 2_{stat} \pm 1_{sys})\%. \quad (8.23)$$

The systematic uncertainty of the neutron capture time distribution was estimated by comparing the fraction of events with neutron capture times $t \in [t_{cut}, 10 \mu\text{s}]$ with the fraction of the neutron creation time t_{cr} to the neutron capture time t_{cap} distribution.

The efficiencies ϵ_{sat} , ϵ_{ncap} and ϵ_{IT} depend on the coaxial and BEGe mass fractions and thus on the dataset. Their estimated values are shown in Table 8.3. The total efficiency ϵ

²Only events with $\Delta t < 10 \mu\text{s}$ are tagged to be vetoed by the muon veto.

for each dataset was determined using a toy Monte Carlo since the systematic uncertainties of ϵ_{sat} , ϵ_{ncap} and ϵ_{IT} are correlated. All three efficiencies depend on the active mass fraction which has an uncertainty of 7% (see section 8.1). The efficiency for detecting the energy deposition of the neutron capture also has a systematic uncertainty from the Monte Carlo simulations of 35% (see section 7.2). For the toy Monte Carlo, random numbers were generated following a Gaussian distribution with the means of the efficiency values and standard deviations of the efficiency uncertainties for all efficiencies. To consider the uncertainty due to the not precisely known active mass and the Monte Carlo, random numbers for uncertainties of the active mass and the Monte Carlo were generated following Gaussian distributions with the mean at zero and standard deviations in the order of the uncertainties of the active mass or of the Monte Carlo for each event. These values are added to the uncertainties of the efficiencies in quadrature before generating the random numbers of the efficiencies. In total 10^6 events were generated for each dataset. The total efficiencies were determined by estimating the mean and the standard deviation for each total efficiency distribution. The results are shown in Table 8.3.

The number of expected observed signals from ^{77m}Ge and ^{75m}Ge IT as a function of the exposure can be calculated from the simulated production rates R_c and the total detection efficiency ϵ . For the expected $^{77(m)}\text{Ge}$ production rate, the average of [3] and [4] which is (0.36 ± 0.15) nuclei/(kg yr) was chosen. The expected production rate of $^{75(m)}\text{Ge}$ is (0.06 ± 0.02) nuclei/(kg yr). For the total detection efficiency ϵ , the average value of all three datasets was used which is $(16.6 \pm 7)\%$ for ^{77m}Ge and $(20 \pm 8)\%$ for ^{75m}Ge . The number of expected signals as a function of exposure was calculated using a toy Monte Carlo. Random numbers of the production rate R_c and the efficiency ϵ were generated following Gaussian distributions with widths according to the uncertainties as described above. Also the number of maximally expected background events were calculated from the A_{bkg} limits. The results are shown in Fig. 8.10. The collected exposure of GERDA Phase Ia, Ib and II is shown as a dashed line. It can be seen from Fig. 8.10 that no signal is expected for the collected GERDA exposure and that only upper limits on the production rates can be set. However, for 5 years of data-taking with LEGEND-200 [91] which corresponds to an exposure of 1000 kg yr, it is very likely to see a signal and to determine the production rates of $^{77(m)}\text{Ge}$ and $^{75(m)}\text{Ge}$.

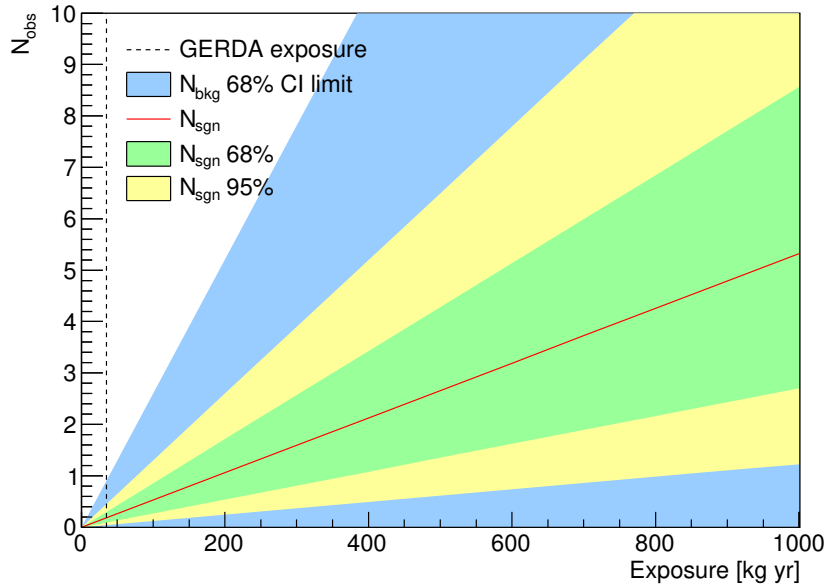
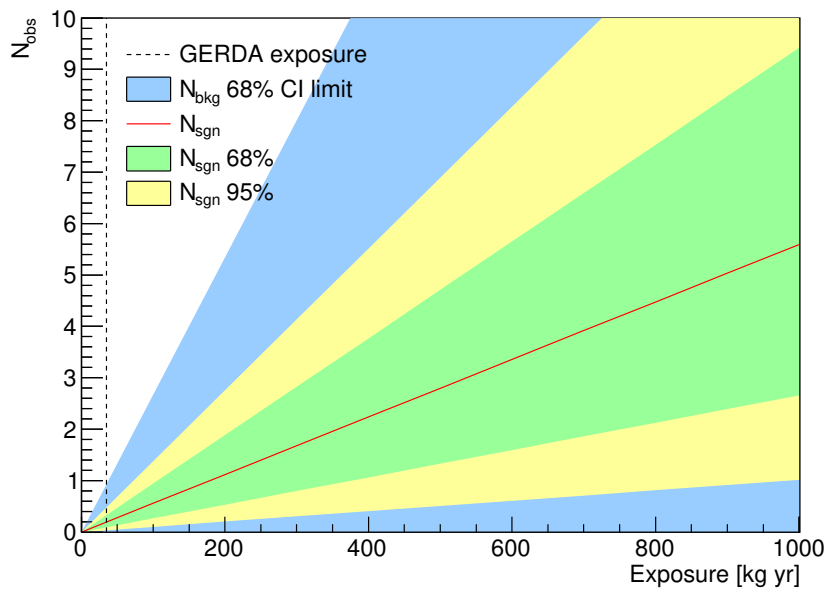
(a) ^{75m}Ge (b) ^{77m}Ge

Figure 8.10: Expected number of signal and background events for the ^{77m}Ge and ^{75m}Ge IT search as a function of the exposure. The expected signals are calculated from the production rate R_c and the efficiency ϵ using toy Monte Carlo simulations. For the expected number of background events, the average of the limits on the background rate A_{bkg} for each dataset was used. The collected GERDA exposure of Phase Ia, Phase Ib and Phase II is indicated by the dashed line.

8.4 Results

The Bayesian toolkit BAT [88] was used to extract upper limits for the muon-induced $^{77(m)}\text{Ge}$ and $^{75(m)}\text{Ge}$ production rates. The used priors and the posteriors of the two fits are shown in Fig. 8.11 and Fig. 8.12. As expected, no signal was observed and only upper limits on the production rates were set. The upper limit of the $^{77(m)}\text{Ge}$ production rate is

$$R_{\text{Ge}^{77(m)}} < 4.1 \text{ nuclei}/(\text{kg yr}) \quad 90\% \text{ CI} \quad (8.24)$$

and the upper limit on the $^{75(m)}\text{Ge}$ production rate is

$$R_{\text{Ge}^{75(m)}} < 0.63 \text{ nuclei}/(\text{kg yr}) \quad 90\% \text{ CI}. \quad (8.25)$$

Both limits are one magnitude larger than the expected production rates from Monte Carlo simulations. However, with LEGEND-200 it should be possible to determine the production rates (see Fig. 8.10 in section 8.3).

Background Index Limit From the upper limits on the $^{77(m)}\text{Ge}$ production rate, upper limits on the BI in the ROI due to $^{77(m)}\text{Ge}$ β^- decay can be determined for BEGe and coaxial detectors. For this purpose, the normalized energy spectra from β^- decay of ^{77}Ge and $^{77(m)}\text{Ge}$ were scaled with the $^{77(m)}\text{Ge}$ production rate limit and by determining the fraction in the ROI. The upper limit for the BI in the ROI is

$$\text{BI} < 9.4 \cdot 10^{-4} \text{ cts}/(\text{keV kg yr}) \quad 90\% \text{ CI} \quad (8.26)$$

for coaxial detectors and

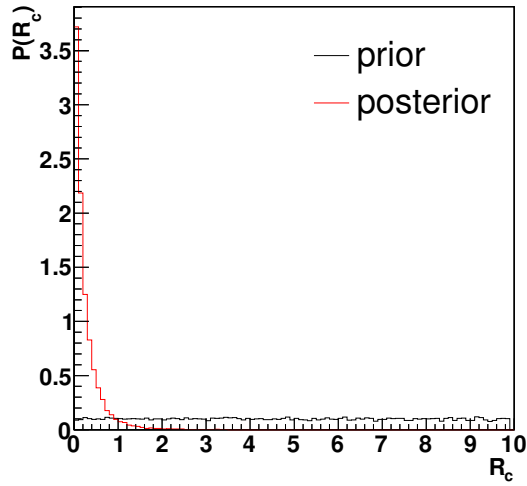
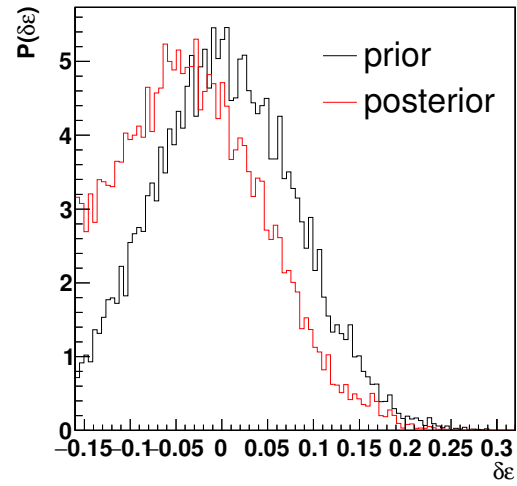
$$\text{BI} < 6.9 \cdot 10^{-4} \text{ cts}/(\text{keV kg yr}) \quad 90\% \text{ CI} \quad (8.27)$$

for BEGe detectors. These are the upper limits on the $^{77(m)}\text{Ge}$ BI if no analysis cuts are set. If detector anti-coincidence, LAr veto and PSD multi-site rejection cuts are applied, the ^{77}Ge BI is reduced to 9.5% and the ^{77m}Ge BI to 73% relative to the value before the cut application (see [4]). If these values are weighted with the ^{77}Ge and ^{77m}Ge β^- decay fractions which are 59.5% and 40.5%, the BI survival fraction becomes 35%. Taking this into account, the upper limits after cut application are

$$\text{BI} < 3.3 \cdot 10^{-4} \text{ cts}/(\text{keV kg yr}) \quad 90\% \text{ CI} \quad (8.28)$$

for coaxial detectors and

$$\text{BI} < 2.4 \cdot 10^{-4} \text{ cts}/(\text{keV kg yr}) \quad 90\% \text{ CI} \quad (8.29)$$

(a) $^{75(m)}\text{Ge}$ production rate

(b) efficiency uncertainty

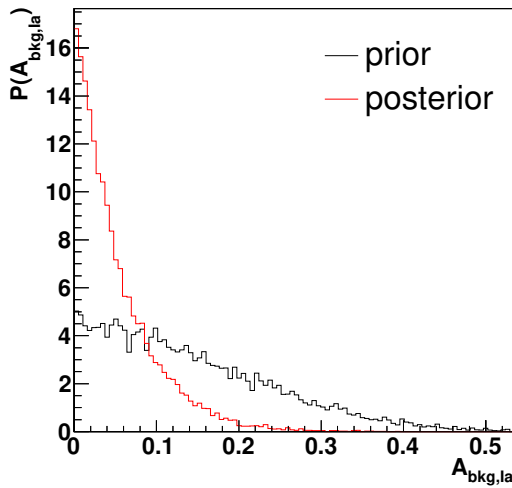
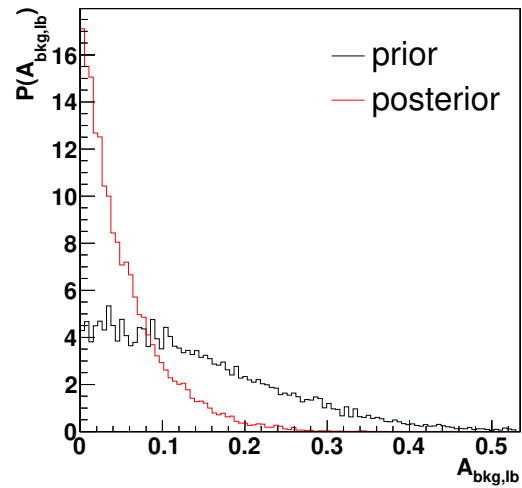
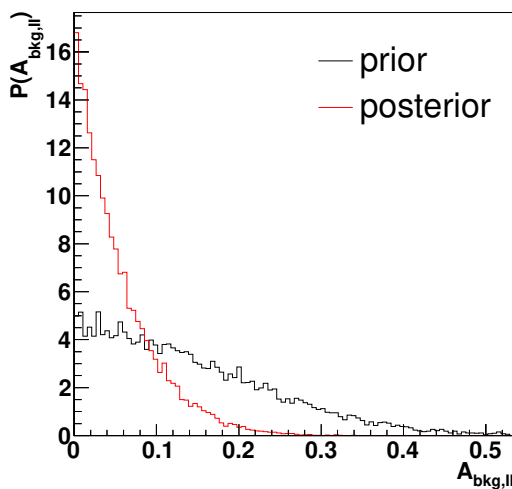
(c) Phase Ia A_{bkg} (d) Phase Ib A_{bkg} (e) Phase II A_{bkg}

Figure 8.11: Priors and posteriors of all parameters of the muon-induced $^{75(m)}\text{Ge}$ production rate in GERDA. The parameters are the production rate R_c , the systematic uncertainty of the efficiency $\delta\epsilon$ and the background rates for each dataset $A_{bkg,Ia}$, $A_{bkg,Ib}$ and $A_{bkg,II}$.

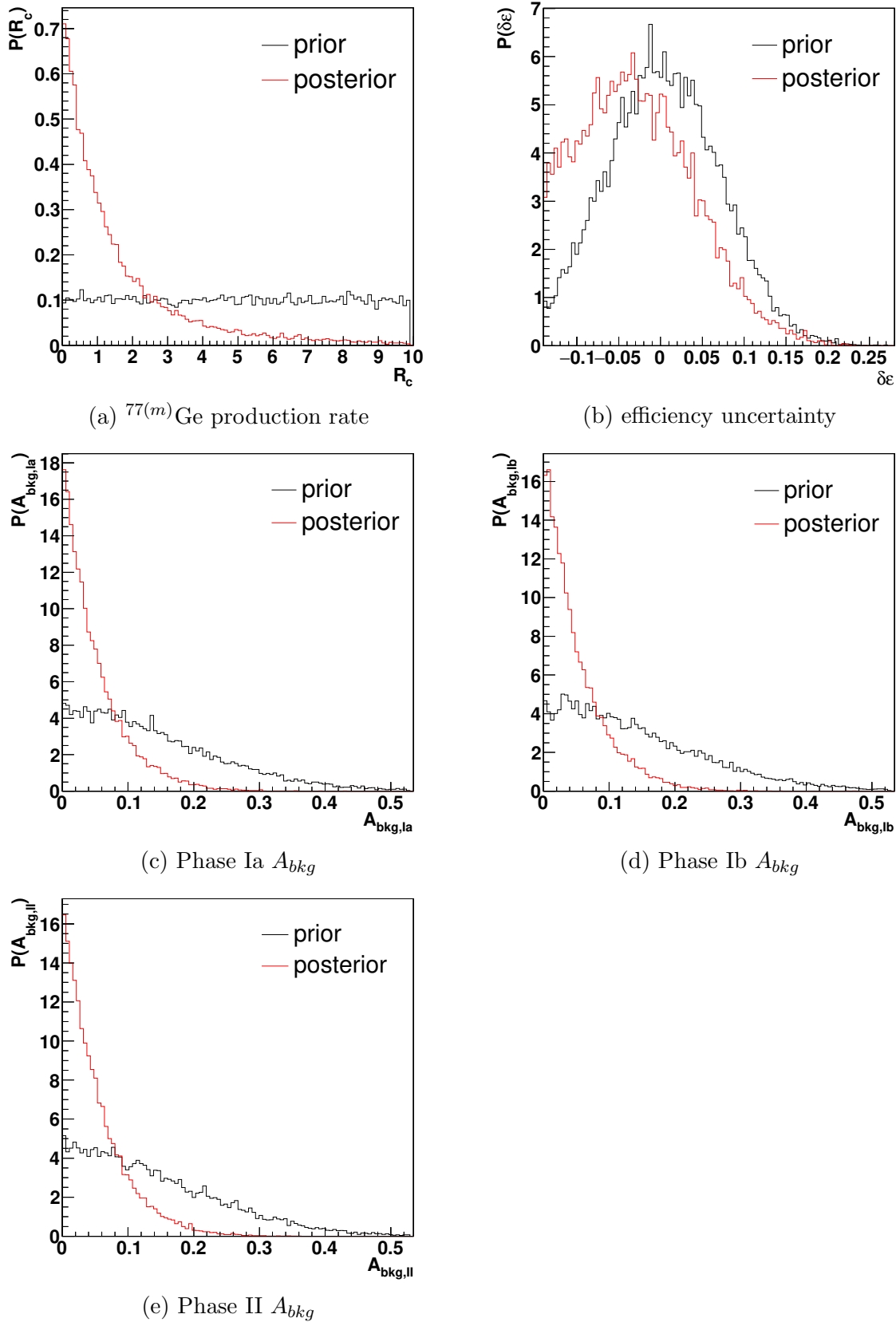


Figure 8.12: Priors and posteriors of all parameters of the muon-induced $^{77(m)}\text{Ge}$ production rate in GERDA. The parameters are the production rate R_c , the systematic uncertainty of the efficiency $\delta\epsilon$ and the background rates for each dataset $A_{bkg,Ia}$, $A_{bkg,Ib}$ and $A_{bkg,II}$.

for BEGe detectors. These limits are in the order of the total BI of the last GERDA Phase II datasets which are $6_{-3}^{+4} \cdot 10^{-4}$ cts/(keV kg yr) and $6_{-2}^{+4} \cdot 10^{-4}$ cts/(keV kg yr) for coaxial and BEGe detectors, respectively [97].

In [4], a delayed coincidence cut is suggested by which a survival fraction of 6.8% of the $^{77(m)}\text{Ge}$ BI is achieved. Events appearing within 6 min after a prompt ($< 10\mu\text{s}$) or delayed ($> 10\mu\text{s}$) coincidence tagging between the muon veto and the germanium detectors are discarded leading to a life-time loss of $< 4\%$ [4]. If this cut is applied as well, the upper limit on the BI from $^{77(m)}\text{Ge}$ β^- decay is

$$\text{BI} < 6.4 \cdot 10^{-5} \text{ cts}/(\text{keV kg yr}) \quad 90\% \text{ CI} \quad (8.30)$$

for coaxial detectors and

$$\text{BI} < 4.7 \cdot 10^{-5} \text{ cts}/(\text{keV kg yr}) \quad 90\% \text{ CI} \quad (8.31)$$

for BEGe detectors. These limits are larger than the total BI goal of LEGEND which is 10^{-5} cts/(keV kg yr). Therefore it is uncertain if a muon flux like the one at LNGS is low enough for LEGEND. Even if a delayed coincidence cut is applied, the induced background from $^{77(m)}\text{Ge}$ β^- decay may be too high for reaching the sensitivity goal of LEGEND.

If the average $^{77(m)}\text{Ge}$ production rate of both Monte Carlo simulations, which is (0.36 ± 0.15) nuclei/(kg yr), is used, the initial BI from $^{77(m)}\text{Ge}$ β^- decay is

$$(8 \pm 3) \cdot 10^{-5} \text{ cts}/(\text{keV kg yr}) \quad (8.32)$$

and

$$(6 \pm 3) \cdot 10^{-5} \text{ cts}/(\text{keV kg yr}) \quad (8.33)$$

for coaxial and BEGe detectors, respectively. After applying detector anti-coincidence, LAr veto and PSD multi-site rejection cuts, these BI get reduced to

$$(3 \pm 1) \cdot 10^{-5} \text{ cts}/(\text{keV kg yr}) \quad (8.34)$$

and

$$(2 \pm 1) \cdot 10^{-5} \text{ cts}/(\text{keV kg yr}). \quad (8.35)$$

Thus, the BI after applying these cuts would be too high for LEGEND. If the delayed coincidence cut suggested in [4] is applied as well, the BI contribution from $^{77(m)}\text{Ge}$ β^- decay becomes

$$(5 \pm 2) \cdot 10^{-6} \text{ cts}/(\text{keV kg yr}) \quad (8.36)$$

for coaxial and

$$(4 \pm 2) \cdot 10^{-6} \text{ cts}/(\text{keV kg yr}) \quad (8.37)$$

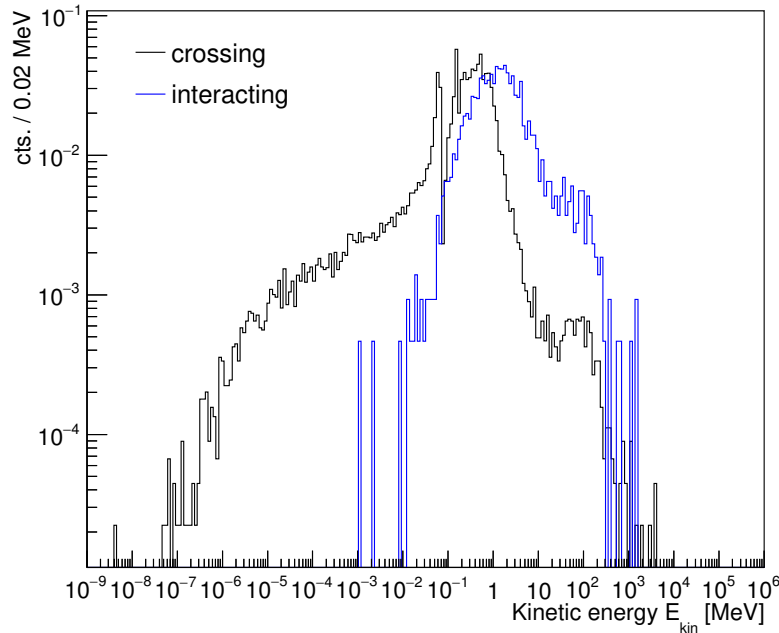


Figure 8.13: Normalized simulated neutron energy spectrum around the germanium detector array for neutrons crossing a sphere with a radius of $r = 30$ cm and for neutrons which interact by inelastic scattering within the spheric volume.

for BEGe detectors. Therefore the BI from $^{77(m)}\text{Ge}$ β^- decay after applying all cuts could be of the order of the LEGEND BI goal which would be too large. To make sure that the BI from $^{77(m)}\text{Ge}$ β^- decay is low enough, it would be preferable to run LEGEND in an underground laboratory with a lower muon flux than the one present at LNGS.

Integrated Neutron Flux Limit From the limit of the neutron production rates of $^{77(m)}\text{Ge}$ and $^{75(m)}\text{Ge}$, limits on the integrated neutron flux around the germanium detector array can be derived using the average cross section for the meta-stable state production, the meta-stable state production rates and the number of target nuclei N_{nuc} ($^{76}\text{Ge}/^{74}\text{Ge}$). The number of target nuclei is given by

$$N_{nuc} = f_n \cdot N_A \cdot \frac{m_{enr}}{M_{enr}} \quad (8.38)$$

with the target nuclei fraction f_n which is 0.877 for ^{76}Ge and 0.12 for ^{74}Ge , the Avogadro constant N_A , the mass of the enriched detectors m_{enr} and the molar mass of enriched germanium detectors which is 75.6 g/mol [53].

The average cross section is given by

$$\sigma_{av} = \frac{\int \sigma(E) \cdot f(E) dE}{\int f(E) dE} \quad (8.39)$$

with the energy dependent cross section for meta-stable state production $\sigma(E)$ and the

neutron energy distribution $f(E)$ around the detector array (see Fig. 7.6 in section 7.2). To investigate the influence of $f(E)$ on the uncertainty of the average cross section, the same calculation of the average cross section was done using the energy distribution obtained from neutrons which were interacting inside the spheric volume with a 30 cm radius and thus recorded by the output scheme of the Monte Carlo simulation (see Fig. 8.13). The deviation of the results is taken as systematic uncertainty of the average cross section. The average cross section is (0.009 ± 0.007) b for ^{77m}Ge production and (0.011 ± 0.007) b for ^{75m}Ge production.

The integrated neutron flux is given by

$$\Phi_n = \frac{R_m \cdot m_{enr}}{N_{nuc} \cdot \sigma_{av}} = \frac{f_m \cdot R_c \cdot m_{enr} \cdot M_{enr}}{f_n \cdot N_A \cdot m_{enr} \cdot \sigma_{av}} = \frac{f_m \cdot R_c \cdot M_{enr}}{f_n \cdot N_A \cdot \sigma_{av}}. \quad (8.40)$$

The 90% CI upper limit on the integrated neutron flux is calculated using a toy Monte Carlo. Random numbers for the average cross section are generated using a Gaussian distribution with the value of the calculated average cross section as mean and its uncertainty as standard deviation. The upper limit on the integrated neutron flux is

$$\Phi_n < 118 \text{ n/m}^2 \text{ h} \quad 90\% \text{ CI} \quad (8.41)$$

if the ^{77m}Ge production is used and

$$\Phi_n < 99 \text{ n/m}^2 \text{ h} \quad 90\% \text{ CI} \quad (8.42)$$

if the ^{75m}Ge production is used. The upper limits calculated from the limits on the $^{77(m)}\text{Ge}$ production and $^{75(m)}\text{Ge}$ production are similar. The large uncertainty of the integrated neutron flux is due to the large systematic uncertainty of the neutron energy spectrum around the detector array. If the $^{77(m)}\text{Ge}$ and $^{75(m)}\text{Ge}$ production rate limits are combined, the upper limit on the integrated neutron flux is

$$\Phi_n < 36 \text{ n/m}^2 \text{ h} \quad 90\% \text{ CI} \quad (8.43)$$

using the average cross section for ^{77m}Ge and ^{75m}Ge production of $\sigma_{av} = (0.020 \pm 0.007)$ b. This limit is smaller than the measured unshielded neutron flux in the underground laboratory of $137 \text{ m}^{-2} \text{ h}^{-1}$ [98] and one order of magnitude larger than the expected shielded flux in the GERDA set-up which is expected to be $5.7 \text{ m}^{-2} \text{ h}^{-1}$ [3] or $1.6 \text{ m}^{-2} \text{ h}^{-1}$ [4] depending on the Monte Carlo simulation. However, with LEGEND-200 it should be possible to determine the $^{77(m)}\text{Ge}$ and $^{75(m)}\text{Ge}$ production rates as well as the integrated neutron flux. This would allow to test the reliability of the Monte Carlo simulations.

Chapter 9

Conclusion and Outlook

The Lepton number violating process of neutrinoless double beta ($0\nu\beta\beta$) decay could answer the fundamental question regarding the nature of neutrinos: are they Dirac particles or Majorana particles and thus their own antiparticles? Experiments searching for $0\nu\beta\beta$ decay require very low background due to the very long expected half life. An important background contribution results from the activation of the setup material by cosmic rays. This can happen during the processing of the detector material above ground as well as in the underground laboratory. Most cosmogenic-induced isotopes are produced during processing [69]. By shielding the material during transportation, the production of the most dangerous cosmogenic isotopes ^{60}Co and ^{68}Ge can be reduced to a level which allows to reach a total background index of 10^{-3} cts/(keV kg yr) at the energy region of interest (ROI) for GERDA Phase II [6] [69].

For future experiments searching for $0\nu\beta\beta$ decays of ^{76}Ge like LEGEND, the background has to be further reduced to 10^{-5} cts/(keV kg yr). Background rejection techniques as well as a better shielding against cosmogenic activation can be used to reach a lower BI.

The shielding design used for the transportation of the detector material can be further optimized using more detailed simulations. For the GERDA Phase II shielding design [69], only cosmic-ray neutron and protons were considered. Furthermore, only the penetration of iron was simulated, since it seems the best choice from semi-empirical considerations [69]. In [66] also the penetration of other materials than iron were investigated including the contribution of muon-induced neutrons. However, backscattering of neutrons inside the shielding material was neglected leading to multiple counting of neutrons.

In this thesis, the multiple backscattering of neutrons was investigated for the materials used in [66] and was found to be not negligible. Counting the number of neutrons passing through defined borders inside a steel block as it was done in [66] leads to multiple counting of neutrons and thus to a factor of three more neutrons if compared to counting neutrons

leaving a shielding block of the same size. For this work, cosmic-ray neutrons, μ^+ and μ^- penetrating different commonly used shielding materials were simulated. Cosmic-ray showers inside high-Z materials like lead, copper and steel lead to neutron multiplication. For these shielding materials, the total number of neutrons after the penetration of a certain length of shielding material will be lower than the number of incident neutrons only behind a material dependent shielding depth. Also the number of muon-induced neutrons is higher for high-Z materials. The expected differential neutron flux behind different shielding depths has been investigated in this thesis. This is an important input for planning the shielding for future experiments.

The best choice for the shielding material depends on the material to be shielded and on the neutron energies at which dangerous long-lived isotopes can be produced. If low-energetic neutrons can produce dangerous long-lived isotopes which production should be avoided, concrete is the best choice, since the total neutron flux is the lowest for all shielding thicknesses. However, if only neutrons with $E > 20$ MeV are of concern for the long-lived isotope production, lead, copper and steel are the best choice. For the production of ^{60}Co and ^{68}Ge , which are the most dangerous cosmogenic isotopes for searching for the $0\nu\beta\beta$ decay of ^{76}Ge , only fast neutrons are relevant [69]. A steel container was used to shield the germanium material of GERDA Phase II during transportation. The investigations of this thesis show that this is indeed a good choice.

The shielding simulations can also be improved by understanding the muon-induced production rates. This information could then be used for improving the Monte Carlo simulations and for reducing the uncertainties of Monte Carlo simulations. The MINIDEX experiment aims to measure the muon-induced neutron production for different high-Z materials by identifying muon-induced neutrons through detection of gammas from neutron capture on hydrogen with two germanium detectors. To be able to compare the data with Monte Carlo simulations, the muon rate, angular distributions and the energy spectrum inside the Tübingen Shallow Underground Laboratory, where MINIDEX is located, are needed for μ^+ and μ^- . Monte Carlo simulations using the GEANT4-based framework MaGe were developed to get these informations which serve as input for further simulations. The spectra estimated in this thesis have been used to derive that the muon-induced neutron production in lead is by a factor of ~ 3 higher than the simulated production rates [5].

The Monte Carlo simulations can be compared to an angular-dependent muon rate measurement conducted earlier in the Tübingen Shallow Underground Laboratory [76]. The muon rates deviate by 20%. The measured vertical muon rate $(70.7 \pm 0.9) \text{ m}^{-2} \text{ s}^{-1}$ [76] is smaller than the simulated muon rate of $(86.56 \pm 0.05) \text{ m}^{-2} \text{ s}^{-1}$ at the ceiling. This may be due to the chosen overburden for the Monte Carlo simulations which composition and density is not precisely known. Also the muon φ distribution of the Monte Carlo simulations is more isotropic for fixed θ values (less than 3% deviation) while the measured φ distribution deviates up to $\sim 15\%$. The results of this thesis serve as reference for further

simulations.

For future tonne-scale experiments searching for $0\nu\beta\beta$ decay like LEGEND, muon-induced radionuclides produced in the underground laboratory becomes more relevant. The predicted background contribution from $^{77(m)}\text{Ge}$ is higher than 10^{-5} cts/(keV kg yr). Using available background rejection techniques this background can be efficiently discriminated [4]. However, the predicted $^{77(m)}\text{Ge}$ production rate differs for different Monte Carlo simulations (see [3] and [4]). Therefore the production rate of $^{77(m)}\text{Ge}$ needs to be determined to reliably estimate the BI in the ROI due to ^{77m}Ge and ^{77}Ge β^- decay.

Data were analyzed for the first time to investigate the $^{77(m)}\text{Ge}$ production rate as well as the production rates of other isotopes produced by neutron capture. For this purpose, signatures for ^{77m}Ge , ^{75m}Ge and ^{41}Ar production were investigated. The efficiency for detecting 1293.6 keV gammas from ^{41}Ar beta decay was found to be less than 1% and was not further investigated. The muon-induced production rates of $^{77(m)}\text{Ge}$ and $^{75(m)}\text{Ge}$ were investigated by looking for a high energy deposition from neutron capture ($E > 3\text{ MeV}$) accompanied by a signal from the muon veto and a delayed signal from the IT of the meta-stable state.

GERDA Phase I and Phase II data were analyzed by using the Bayesian toolkit BAT. No signal was observed and upper limits on the production rates were set. The upper limit for the $^{75(m)}\text{Ge}$ production is $R_{\text{Ge}^{75(m)}} < 0.63$ nuclei/(kg yr) (90% CI) and $R_{\text{Ge}^{77(m)}} < 4.1$ nuclei/(kg yr) (90% CI) for $^{77(m)}\text{Ge}$ production. The upper limit on the initial BI from $^{77(m)}\text{Ge}$ β^- decay in the ROI is $\text{BI} < 9.4 \cdot 10^{-4}$ cts/(keV kg yr) for coaxial detectors and $\text{BI} < 6.9 \cdot 10^{-4}$ cts/(keV kg yr) for BEGe detectors. Using available background rejection techniques like detector anti-coincidence, LAr veto and PSD multi-site rejection cuts, these limits become $\text{BI} < 3.3 \cdot 10^{-4}$ cts/(keV kg yr) and $\text{BI} < 2.4 \cdot 10^{-4}$ cts/(keV kg yr) for coaxial and BEGe detectors, respectively. These limits are in the order of the total BI reached for the last GERDA Phase II dataset. If also the delayed coincidence cut suggested in [4] is applied, the upper limit on the BI from $^{77(m)}\text{Ge}$ β^- decay is $\text{BI} < 6.4 \cdot 10^{-5}$ cts/(keV kg yr) for coaxial detectors and $\text{BI} < 4.7 \cdot 10^{-5}$ cts/(keV kg yr) for BEGe detectors. These limits are larger than the BI goal of LEGEND which is 10^{-5} cts/(keV kg yr). Also the $^{77(m)}\text{Ge}$ production rates estimated from Monte Carlo simulations do not exclude that the background contribution from $^{77(m)}\text{Ge}$ is of the order of the LEGEND BI goal. Therefore it is still uncertain if a muon flux comparable with the flux at the LNGS would be low enough for LEGEND even if all available background rejection techniques including a delayed coincidence cut are applied.

Also upper limits on the integrated neutron flux were derived. The upper limit of the integrated neutron flux is $\Phi_n < 118$ n/m² h if the ^{77m}Ge production is used and $\Phi_n < 99$ n/m² h if the ^{75m}Ge production is used. If the $^{77(m)}\text{Ge}$ and $^{75(m)}\text{Ge}$ production rate limits are combined, the upper limit on the integrated neutron flux becomes $\Phi_n < 36$ n/m² h (90% CI). This limit is smaller than the measured unshielded neutron flux in the underground laboratory which is $137\text{ m}^{-2}\text{ h}^{-1}$ [98] showing that neutrons are

indeed shielded by the water tank and the LAr. The combined upper limit is also one order of magnitude larger than the expected shielded neutron flux close to the GERDA germanium detector array which is expected to be $5.7 \text{ m}^{-2} \text{ h}^{-1}$ [3] or $1.6 \text{ m}^{-2} \text{ h}^{-1}$ [4] depending on the Monte Carlo simulation.

LEGEND-200 has the capability to determine the $^{77(m)}\text{Ge}$ and $^{75(m)}\text{Ge}$ production rates as well as the BI from $^{77(m)}\text{Ge}$ β^- decay and the integrated neutron flux. This would also allow to test the reliability of the Monte Carlo simulations and to verify that the considered background components do not significantly alter the sensitivity of future tonne-scale experiments. However, few years data-taking with LEGEND-200 are needed for this purpose. To be on the safe side, it would be better to run LEGEND in an underground laboratory with a lower muon flux than the one at LNGS.

Appendix A

Used Physics Models and Cross Sections

Tables A.1-A.3 show the used physics models of GEANT4. The used neutron cross sections are shown in Table A.4. For the muons, the hadronic cross sections of Kokoulin-MuonNuclearXS in the energy range 0 eV–100 TeV are used.

Table A.1: Used GEANT4 models and their settings of the energy range for μ^+ .

Name of the model	Kind of model	E_{\min}	E_{\max}
WentzelVIUni	electromagnetic	0 eV	10 TeV
Bragg	electromagnetic	0 eV	200 keV
BetheBloch	electromagnetic	200 keV	1 GeV
MuBetheBloch	electromagnetic	1 GeV	10 TeV
MuBrem	electromagnetic	0 eV	10 TeV
muPairProd	electromagnetic	0 eV	10 TeV
eCoulombScattering	electromagnetic	0 eV	10 TeV
G4MuonVDNuclearModel	hadronic	0 eV	1000 TeV

Table A.2: Used GEANT4 models and their settings of the energy range for μ^- .

Name of the model	Kind of model	E_{\min}	E_{\max}
WentzelVIUni	electromagnetic	0 eV	10 TeV
ICRU73QO	electromagnetic	0 eV	200 keV
BetheBloch	electromagnetic	200 keV	1 GeV
MuBetheBloch	electromagnetic	1 GeV	10 TeV
MuBrem	electromagnetic	0 eV	10 TeV
muPairProd	electromagnetic	0 eV	10 TeV
eCoulombScattering	electromagnetic	0 eV	10 TeV
G4MuonVDNuclearModel	hadronic	0 eV	1000 TeV

Table A.3: Used hadronic models and their settings of the energy range for neutrons.

Name of the model	E_{\min} [GeV]	E_{\max} [GeV]
hElasticCHIPS	0.0195	100000
NeutronHPElastic	0	0.02
QGSP	12	100000
G4LENeutronInelastic	9.5	25
Bertini Cascade	0.0199	9.9
NeutronHPInelastic	0	0.02
G4LCapture	0.0199	20000
NeutronHPCapture	0	0.02
G4LFission	0.0199	20000
NeutronHPFission	0	0.02

Table A.4: Used neutron cross sections and in which energy range they are used.

Name	E_{\min} [GeV]	E_{\max} [GeV]
NeutronHPElasticXS	0	0.02
ChipsNeutronElasticXS	0	100000
GeishaElastic	0	100000
NeutronHPInelasticXS	0	0.02
Barashenkov-Glauber	0	100000
GeishaInelastic	0	100000
NeutronHPCaptureXS	0	0.02
GeishaCaptureXS	0	100000
NeutronHPFissionXS	0	0.02
GeishaFissionXS	0	100000

Appendix B

Material Compositions of Simulated Materials

Table B.4 shows only the composition of dry soil. For the soil simulations, water was added to the compositions listed in Table B.4 with the fraction 0.2 to 0.8.

Table B.1: Composition of concrete

Element	Fraction	Neutrons
Silicon	0.227915	14
Oxygen	0.60541	8
Hydrogen	0.09972	0
Calcium	0.04986	20
Aluminum	0.014245	14
Iron	0.00285	30

Table B.2: Composition of LNGS rock [99].

Element	Fraction	Neutrons
Carbon	0.1188	6
Oxygen	0.4892	8
Manganese	0.0558	30
Aluminum	0.0103	14
Silicon	0.0127	14
Potassium	0.0103	20
Calcium	0.3029	20

Table B.3: Some materials included in soil and their compositions.

Material	H	C	O	N
Cellulose	10	6	5	0
Lignin	12	10	3	0
Chitin	13	8	5	1

Table B.4: Composition of Soil

Material	Fraction	Neutrons
CaCO ₃	0.35	50
MgCO ₃	0.225	42
SiO ₂	0.15	30
Fe ₂ O ₃	0.07	84
SiC	0.06	20
Al ₂ O ₃	0.05	52
Cellulose	0.05	76
Lignin	0.04	84
Chitin	0.005	95

Table B.5: Composition of stainless steel.

Element	Fraction	Neutrons
Iron	0.67	30
Chromium	0.20	28
Nickel	0.10	30
Manganese	0.02	30
Silicon	0.01	14

Appendix C

Number of Simulated Neutrons

Table C.1: Number of simulated neutrons for each shielding materials and angular distribution. The step-size is 0.1 m.

Material	Distribution	Thicknesses [m]	Simulated neutrons
Concrete	Vertically downwards	0.1 – 4	10^6
	Isotropic	0.1 – 4	10^6
	Nesterenok	0.1 – 4	10^6
Copper	Vertically downwards	0.1 – 4	10^6
	Isotropic	0.1 – 4	10^6
	Nesterenok	0.1 – 4	10^6
LNGS rock	Vertically downwards	0.1 – 4	10^6
	Isotropic	0.1 – 4	10^6
	Nesterenok	0.1 – 4	10^6
Lead	Vertically downwards	0.1 – 0.9	10^5
		1 – 4	$7 \cdot 10^6$
	Isotropic	0.1 – 0.9	$7 \cdot 10^5$
		1 – 4	$7 \cdot 10^6$
	Nesterenok	0.1 – 0.8	$7 \cdot 10^5$
		0.9 – 4	$7 \cdot 10^6$
Steel	Isotropic	0.1 – 2	10^6
	Nesterenok	0.1 – 2	10^6

Table C.2: Number of simulated neutrons for each shielding materials and angular distribution. The step-size is 1 m.

Material	Distribution	Thicknesses [m]	Simulated neutrons
Steel	Vertically downwards	1 – 20	$9.99 \cdot 10^6$
Plastic	Vertically downwards Isotropic & Nesterenok	1 – 20	$9.99 \cdot 10^6$
		1 – 9	10^6
		10 – 13	$5 \cdot 10^6$
		14 – 15	10^7
Water	Vertically downwards Isotropic	1 – 20	$9.99 \cdot 10^6$
		1 – 9	10^6
		10 – 14	$5 \cdot 10^6$
		15	10^7
	Nesterenok	1 – 9	10^6
		10 – 13	$5 \cdot 10^6$
		14 – 15	10^7
Soil	Vertically downwards Isotropic	1 – 20	$9.99 \cdot 10^6$
		1 – 7	10^6
	Nesterenok	8 – 10	10^7
		1 – 7	10^6
		8 – 10	$5 \cdot 10^6$

Appendix D

Shielding Index s of Cosmic-Ray Neutrons

Table D.1: Shielding index s [1/m] for vertically downwards going neutrons.

Material	$E \geq 0$ MeV	$E \geq 1$ MeV	$E \geq 20$ MeV	$E \geq 200$ MeV
Concrete	-0.822 ± 0.006	-0.825 ± 0.006	-0.826 ± 0.006	-0.863 ± 0.007
Copper	-2.10 ± 0.02	-2.28 ± 0.02	-2.3 ± 0.02	-2.32 ± 0.02
Lead	-1.368 ± 0.009	-2.17 ± 0.01	-2.21 ± 0.01	-2.18 ± 0.03
LNGS rock	-0.850 ± 0.003	-0.842 ± 0.004	-0.846 ± 0.004	-0.915 ± 0.007
Plastic	-0.354 ± 0.003	-0.343 ± 0.004	-0.343 ± 0.004	-0.361 ± 0.004
Soil	-0.57 ± 0.01	-0.566 ± 0.007	-0.568 ± 0.007	-0.58 ± 0.01
Steel	-2.01 ± 0.02	-2.171 ± 0.008	-2.177 ± 0.008	-2.29 ± 0.02
Water	-0.372 ± 0.003	-0.365 ± 0.004	-0.365 ± 0.003	-0.381 ± 0.004

Table D.2: Shielding index s [1/m] for neutrons distributed by a distribution suggested by A. Nesterenok [61].

Material	$E \geq 0$ MeV	$E \geq 1$ MeV	$E \geq 20$ MeV	$E \geq 200$ MeV
Concrete	-0.855 ± 0.004	-0.856 ± 0.004	-0.853 ± 0.003	-0.871 ± 0.007
Copper	-2.15 ± 0.01	-2.40 ± 0.02	-2.41 ± 0.02	-2.46 ± 0.02
Lead	-1.39 ± 0.01	-2.26 ± 0.01	-2.325 ± 0.008	-2.362 ± 0.009
LNGS rock	-0.897 ± 0.005	-0.886 ± 0.003	-0.883 ± 0.003	-0.93 ± 0.01
Plastic	-0.366 ± 0.002	-0.361 ± 0.004	-0.361 ± 0.005	-0.384 ± 0.005
Soil	-0.584 ± 0.007	-0.567 ± 0.006	-0.563 ± 0.005	-0.584 ± 0.003
Steel	-2.12 ± 0.02	-2.20 ± 0.03	-2.22 ± 0.04	-2.4 ± 0.2
Water	-0.397 ± 0.007	-0.381 ± 0.002	-0.381 ± 0.002	-0.401 ± 0.004

Table D.3: Shielding index s [1/m] for isotropic distributed neutrons.

Material	$E \geq 0$ MeV	$E \geq 1$ MeV	$E \geq 20$ MeV	$E \geq 200$ MeV
Concrete	-0.91 ± 0.02	-0.91 ± 0.02	-0.91 ± 0.02	-0.96 ± 0.02
Copper	-2.22 ± 0.02	-2.56 ± 0.04	-2.55 ± 0.02	-2.72 ± 0.03
Lead	-1.42 ± 0.01	-2.43 ± 0.02	-2.48 ± 0.01	-2.73 ± 0.04
LNGS rock	-0.961 ± 0.009	-0.958 ± 0.005	-0.950 ± 0.004	-1.00 ± 0.02
Plastic	-0.388 ± 0.005	-0.386 ± 0.006	-0.385 ± 0.005	-0.411 ± 0.004
Soil	-0.611 ± 0.009	-0.598 ± 0.008	-0.604 ± 0.009	-0.57 ± 0.02
Steel	-2.33 ± 0.04	-2.39 ± 0.06	-2.45 ± 0.08	-2.44 ± 0.06
Water	-0.418 ± 0.005	-0.401 ± 0.008	-0.401 ± 0.009	-0.42 ± 0.01

Table D.4: Shielding index s [1/mwe] for vertically downwards going neutrons.

Material	$E \geq 0$ MeV	$E \geq 1$ MeV	$E \geq 20$ MeV	$E \geq 200$ Me
Concrete	-0.357 ± 0.003	-0.359 ± 0.003	-0.359 ± 0.003	-0.375 ± 0.003
Copper	-0.235 ± 0.002	-0.254 ± 0.003	-0.257 ± 0.003	-0.259 ± 0.002
Lead	-0.1206 ± 0.0008	-0.191 ± 0.001	-0.196 ± 0.003	-0.193 ± 0.003
LNGS rock	-0.314 ± 0.001	-0.311 ± 0.002	-0.312 ± 0.001	-0.338 ± 0.003
Plastic	-0.372 ± 0.004	-0.372 ± 0.004	-0.373 ± 0.004	-0.393 ± 0.004
Soil	-0.343 ± 0.004	-0.343 ± 0.004	-0.345 ± 0.004	-0.350 ± 0.006
Steel	-0.255 ± 0.002	-0.275 ± 0.001	-0.276 ± 0.001	-0.289 ± 0.002
Water	-0.365 ± 0.004	-0.365 ± 0.004	-0.365 ± 0.003	-0.381 ± 0.004

Table D.5: Shielding index s [1/mwe] for neutrons distributed by a distribution suggested by A. Nesterenok [61].

Material	$E \geq 0$ MeV	$E \geq 1$ MeV	$E \geq 20$ MeV	$E \geq 200$ MeV
Concrete	-0.372 ± 0.002	-0.372 ± 0.002	-0.371 ± 0.001	-0.379 ± 0.003
Copper	-0.240 ± 0.001	-0.268 ± 0.002	-0.256 ± 0.002	-0.275 ± 0.002
Lead	-0.122 ± 0.001	-0.1996 ± 0.0009	-0.208 ± 0.001	-0.2083 ± 0.0008
LNGS rock	-0.331 ± 0.002	-0.327 ± 0.001	-0.331 ± 0.002	-0.345 ± 0.005
Plastic	-0.391 ± 0.004	-0.392 ± 0.005	-0.393 ± 0.005	-0.417 ± 0.005
Soil	-0.357 ± 0.005	-0.344 ± 0.004	-0.341 ± 0.003	-0.354 ± 0.002
Steel	-0.268 ± 0.002	-0.279 ± 0.004	-0.281 ± 0.005	-0.30 ± 0.02
Water	-0.381 ± 0.002	-0.381 ± 0.002	-0.381 ± 0.002	-0.401 ± 0.004

Table D.6: Shielding index s [1/mwe] for isotropic distributed neutrons.

Material	$E \geq 0$ MeV	$E \geq 1$ MeV	$E \geq 20$ MeV	$E \geq 200$ MeV
Concrete	-0.396 ± 0.007	-0.397 ± 0.007	-0.395 ± 0.007	-0.42 ± 0.01
Copper	-0.248 ± 0.002	-0.285 ± 0.004	-0.284 ± 0.003	-0.303 ± 0.003
Lead	-0.125 ± 0.001	-0.215 ± 0.002	-0.219 ± 0.001	-0.241 ± 0.003
LNGS rock	-0.355 ± 0.003	-0.353 ± 0.002	-0.351 ± 0.001	-0.370 ± 0.009
Plastic	-0.418 ± 0.007	-0.419 ± 0.006	-0.419 ± 0.006	-0.447 ± 0.005
Soil	-0.363 ± 0.007	-0.362 ± 0.005	-0.366 ± 0.006	-0.35 ± 0.01
Steel	-0.295 ± 0.005	-0.303 ± 0.008	-0.31 ± 0.01	-0.308 ± 0.007
Water	-0.400 ± 0.007	-0.401 ± 0.008	-0.401 ± 0.009	-0.42 ± 0.01

Appendix E

Maximum Muon-Induced Neutron Flux Depths

Table E.1: Depths d_{max} at which the muon-induced neutron flux is highest for different materials and energy thresholds.

Material	Threshold[MeV]	Muon	Maximum [m]	Maximum [mwe]
Plastic	0	μ^+	4 ± 1	3.7 ± 0.9
		μ^-	3 ± 1	2.8 ± 0.9
	1	μ^+	4 ± 1	3.7 ± 0.9
		μ^-	3 ± 1	2.8 ± 0.9
	20	μ^+	4 ± 1	3.7 ± 0.9
		μ^-	4 ± 1	3.7 ± 0.9
200	μ^+	3 ± 1	2.8 ± 0.9	
	μ^-	4 ± 1	3.7 ± 0.9	
Water	0	μ^+	3 ± 1	3 ± 1
		μ^-	3 ± 1	3 ± 1
	1	μ^+	3 ± 1	3 ± 1
		μ^-	3 ± 1	3 ± 1
	20	μ^+	4 ± 1	4 ± 1
		μ^-	3 ± 1	3 ± 1
200	μ^+	4 ± 1	4 ± 1	
	μ^-	3 ± 1	3 ± 1	
Soil	0	μ^+	2 ± 1	3 ± 2
		μ^-	2 ± 1	3 ± 2
	1	μ^+	2 ± 1	3 ± 2
		μ^-	2 ± 1	3 ± 2
	20	μ^+	2 ± 1	3 ± 2
		μ^-	2 ± 1	3 ± 2
200	μ^+	3 ± 1	5 ± 2	
	μ^-	2 ± 1	3 ± 2	

Table E.2: Depths d_{max} at which the muon-induced neutron flux is highest for different materials and energy thresholds.

Material	Threshold[MeV]	Muon	Maximum [m]	Maximum [mwe]
Concrete	0	μ^+	1.2 ± 0.1	2.8 ± 0.2
		μ^-	1.1 ± 0.1	2.5 ± 0.2
	1	μ^+	1.2 ± 0.1	2.8 ± 0.2
		μ^-	1.2 ± 0.1	2.8 ± 0.2
	20	μ^+	1.3 ± 0.1	3.0 ± 0.2
		μ^-	1.2 ± 0.1	2.8 ± 0.2
	200	μ^+	1.3 ± 0.1	3.0 ± 0.2
		μ^-	1.0 ± 0.1	2.3 ± 0.2
Copper	0	μ^+	0.7 ± 0.1	6.3 ± 0.9
		μ^-	0.6 ± 0.1	5.4 ± 0.9
	1	μ^+	0.5 ± 0.1	4.5 ± 0.9
		μ^-	0.4 ± 0.1	3.6 ± 0.9
	20	μ^+	0.5 ± 0.1	4.5 ± 0.9
		μ^-	0.4 ± 0.1	3.6 ± 0.9
	200	μ^+	0.5 ± 0.1	4.5 ± 0.9
		μ^-	0.4 ± 0.1	3.6 ± 0.9
Lead	0	μ^+	1.4 ± 0.1	16 ± 1
		μ^-	1.3 ± 0.1	15 ± 1
	1	μ^+	0.5 ± 0.1	6 ± 1
		μ^-	0.5 ± 0.1	6 ± 1
	20	μ^+	0.5 ± 0.1	6 ± 1
		μ^-	0.5 ± 0.1	6 ± 1
	200	μ^+	0.5 ± 0.1	6 ± 1
		μ^-	0.5 ± 0.1	6 ± 1
LNGS rock	0	μ^+	1.1 ± 0.1	3.0 ± 0.3
		μ^-	1.2 ± 0.1	3.3 ± 0.3
	1	μ^+	1.0 ± 0.1	2.7 ± 0.3
		μ^-	1.2 ± 0.1	3.3 ± 0.3
	20	μ^+	1.0 ± 0.1	2.7 ± 0.3
		μ^-	1.3 ± 0.1	3.5 ± 0.3
	200	μ^+	1.0 ± 0.1	2.7 ± 0.3
		μ^-	1.2 ± 0.1	3.3 ± 0.3
Steel	0	μ^+	0.6 ± 0.1	4.8 ± 0.8
		μ^-	0.7 ± 0.1	5.5 ± 0.8
	1	μ^+	0.5 ± 0.1	4.0 ± 0.8
		μ^-	0.5 ± 0.1	4.0 ± 0.8
	20	μ^+	0.5 ± 0.1	4.0 ± 0.8
		μ^-	0.5 ± 0.1	4.0 ± 0.8
	200	μ^+	0.7 ± 0.1	5.5 ± 0.8
		μ^-	0.5 ± 0.1	4.0 ± 0.8

Appendix F

Attenuation Index s of Muon-induced Neutrons

Table F.1: Attenuation index s of muon-induced neutrons in [1/m].

Material	Threshold[MeV]	μ^+ [m ⁻¹]	μ^- [m ⁻¹]
Plastic	0	-0.0193 ± 0.0008	-0.0246 ± 0.0008
	1	-0.0190 ± 0.0009	-0.023 ± 0.001
	20	-0.0189 ± 0.0009	-0.022 ± 0.001
	200	-0.018 ± 0.001	-0.022 ± 0.002
Water	0	-0.021 ± 0.001	-0.0271 ± 0.0007
	1	-0.021 ± 0.001	-0.0255141 ± 0.0008
	20	-0.021 ± 0.001	-0.021 ± 0.001
	200	-0.020 ± 0.002	-0.019 ± 0.001
Soil	0	-0.0264 ± 0.0009	-0.045 ± 0.001
	1	-0.0261 ± 0.0008	-0.042 ± 0.001
	20	-0.0262 ± 0.0008	-0.031 ± 0.001
	200	-0.025 ± 0.001	-0.024 ± 0.002
Concrete	0	-0.041 ± 0.008	-0.079 ± 0.004
	1	-0.040 ± 0.008	-0.068 ± 0.005
	20	-0.042 ± 0.009	-0.046 ± 0.007
	200	-0.05 ± 0.02	-0.02 ± 0.01
LNGS rock	0	-0.038 ± 0.006	-0.085 ± 0.003
	1	-0.032 ± 0.008	-0.087 ± 0.003
	20	-0.019 ± 0.008	-0.061 ± 0.006
	200	-0.01 ± 0.01	-0.06 ± 0.01
Steel	0	-0.046 ± 0.004	-0.065 ± 0.002
	1	-0.043 ± 0.006	-0.064 ± 0.002
	20	-0.048 ± 0.008	-0.055 ± 0.003
	200	-0.05 ± 0.01	-0.043 ± 0.006
Copper	0	-0.134 ± 0.005	-0.256 ± 0.003
	1	-0.122 ± 0.008	-0.247 ± 0.004
	20	-0.115 ± 0.009	-0.183 ± 0.009
	200	-0.11 ± 0.02	-0.11 ± 0.02
Lead	0	-0.122 ± 0.006	-0.238 ± 0.002
	1	-0.09 ± 0.02	-0.226 ± 0.006
	20	-0.07 ± 0.03	-0.17 ± 0.02
	200	-0.11 ± 0.04	-0.18 ± 0.03

Table F.2: Attenuation index s of muon-induced neutrons in [1/mwe].

Material	Threshold[MeV]	μ^+ [mwe ⁻¹]	μ^- [mwe ⁻¹]
Plastic	0	-0.0210 ± 0.0009	-0.0267 ± 0.0009
	1	-0.021 ± 0.001	-0.025 ± 0.001
	20	-0.021 ± 0.001	-0.024 ± 0.001
	200	-0.019 ± 0.001	-0.024 ± 0.002
Water	0	-0.021 ± 0.001	-0.0271 ± 0.0007
	1	-0.021 ± 0.001	-0.0255 ± 0.0008
	20	-0.021 ± 0.001	-0.021 ± 0.001
	200	-0.020 ± 0.002	-0.019 ± 0.001
Soil	0	-0.0160 ± 0.0005	-0.0276 ± 0.0006
	1	-0.0158 ± 0.0005	-0.0253 ± 0.0006
	20	-0.0159 ± 0.0005	-0.0188 ± 0.0007
	200	-0.0154 ± 0.0008	-0.014 ± 0.001
Concrete	0	-0.018 ± 0.004	-0.034 ± 0.002
	1	-0.017 ± 0.004	-0.030 ± 0.002
	20	-0.018 ± 0.004	-0.020 ± 0.003
	200	-0.023 ± 0.007	-0.008 ± 0.006
LNGS rock	0	-0.014 ± 0.002	-0.032 ± 0.001
	1	-0.012 ± 0.003	-0.032 ± 0.001
	20	-0.007 ± 0.003	-0.023 ± 0.002
	200	-0.003 ± 0.005	-0.021 ± 0.004
Steel	0	-0.0058 ± 0.0005	-0.0082 ± 0.0003
	1	-0.0055 ± 0.0007	-0.0082 ± 0.0003
	20	-0.006 ± 0.001	-0.0069 ± 0.0004
	200	-0.007 ± 0.001	-0.0054 ± 0.0007
Copper	0	-0.0149 ± 0.0006	-0.0285 ± 0.0003
	1	-0.0136 ± 0.0009	-0.0276 ± 0.0004
	20	-0.013 ± 0.001	-0.020 ± 0.001
	200	-0.012 ± 0.002	-0.013 ± 0.002
Lead	0	-0.0108 ± 0.0005	-0.0210 ± 0.0002
	1	-0.008 ± 0.001	-0.0199 ± 0.0006
	20	-0.006 ± 0.002	-0.015 ± 0.002
	200	-0.010 ± 0.004	-0.016 ± 0.003

Appendix G

Depth of Equality of the Neutron Fluxes

Table G.1: Shielding depth at which the cosmic-ray neutron flux and the muon-induced neutron flux are equal and the total neutron flux (per arriving cosm. neutron) at this depth for different energy thresholds. The cosmic-ray neutrons were injected vertically downwards going.

Material	Threshold [MeV]	Depth [m]	Depth [mwe]	Total neutron flux
Plastic	0	9.0 ± 0.5	8.3 ± 0.5	0.00148 ± 0.00001
	1	9.0 ± 0.5	8.3 ± 0.5	0.00134 ± 0.00001
	20	9.0 ± 0.5	8.3 ± 0.5	0.00116 ± 0.00001
	200	9.0 ± 0.5	8.3 ± 0.5	0.000314 ± 0.000006
Water	0	8.0 ± 0.5	8.0 ± 0.5	0.00207 ± 0.00002
	1	8.0 ± 0.5	8.0 ± 0.5	0.00180 ± 0.00001
	20	9.0 ± 0.5	9.0 ± 0.5	0.00093 ± 0.00001
	200	8.0 ± 0.5	8.0 ± 0.5	0.000404 ± 0.000007
Soil	0	5.0 ± 0.5	8.3 ± 0.8	0.00562 ± 0.00003
	1	5.0 ± 0.5	8.3 ± 0.8	0.00391 ± 0.00002
	20	6.0 ± 0.05	9.9 ± 0.8	0.00123 ± 0.00001
	200	6.0 ± 0.05	9.9 ± 0.8	0.000260 ± 0.000006
Concrete	0	3.50 ± 0.05	8.1 ± 0.1	0.00262 ± 0.00006
	1	3.70 ± 0.05	8.5 ± 0.1	0.00188 ± 0.00005
	20	3.90 ± 0.05	9.0 ± 0.1	0.00102 ± 0.00004
	200	3.90 ± 0.05	9.0 ± 0.1	0.00027 ± 0.00002
LNGS rock	0	2.90 ± 0.05	7.9 ± 0.1	0.0193 ± 0.0002
	1	3.10 ± 0.05	8.4 ± 0.1	0.00685 ± 0.00009
	20	3.60 ± 0.05	9.8 ± 0.1	0.00184 ± 0.00005
	200	3.60 ± 0.05	9.8 ± 0.1	0.00033 ± 0.00002
Steel	0	1.10 ± 0.05	8.7 ± 0.4	0.2323 ± 0.0002
	1	1.00 ± 0.05	7.9 ± 0.4	0.03703 ± 0.00007
	20	1.40 ± 0.05	11.1 ± 0.4	0.00240 ± 0.00002
	200	1.40 ± 0.05	11.1 ± 0.4	0.000385 ± 0.000009
Copper	0	1.00 ± 0.05	9.0 ± 0.4	0.2202 ± 0.0005
	1	0.90 ± 0.05	8.1 ± 0.4	0.0378 ± 0.0002
	20	1.30 ± 0.05	11.6 ± 0.4	0.00247 ± 0.00006
	200	1.30 ± 0.05	11.6 ± 0.4	0.00036 ± 0.00002
Lead	0	1.80 ± 0.05	20.4 ± 0.6	0.9273 ± 0.0009
	1	1.10 ± 0.05	12.5 ± 0.6	0.0974 ± 0.0003
	20	1.30 ± 0.05	14.7 ± 0.6	0.00238 ± 0.00004
	200	1.40 ± 0.05	15.9 ± 0.6	0.00031 ± 0.00002

Table G.2: Shielding depth at which the cosmic neutron flux and the muon-induced neutron flux are equal and the total neutron flux (per arriving cosm. neutron) at this depth for different energy thresholds. The cosmic-ray neutrons were injected isotropically.

Material	Threshold [MeV]	Depth [m]	Depth [mwe]	Total neutron flux
Plastic	0	7.0 ± 0.5	6.4 ± 0.5	0.00171 ± 0.00004
	1	7.0 ± 0.5	6.4 ± 0.5	0.00155 ± 0.00004
	20	7.0 ± 0.5	6.4 ± 0.5	0.00135 ± 0.00004
	200	7.0 ± 0.5	6.4 ± 0.5	0.00034 ± 0.00002
Water	0	7.0 ± 0.5	7.0 ± 0.5	0.00168 ± 0.00004
	1	7.0 ± 0.5	7.0 ± 0.5	0.00141 ± 0.00004
	20	7.0 ± 0.5	7.0 ± 0.5	0.00113 ± 0.00003
	200	6.0 ± 0.5	6.0 ± 0.5	0.00041 ± 0.00002
Soil	0	4.0 ± 0.5	6.6 ± 0.8	0.00584 ± 0.00008
	1	4.0 ± 0.5	6.6 ± 0.8	0.00399 ± 0.00007
	20	5.0 ± 0.5	8.3 ± 0.8	0.00120 ± 0.00003
	200	4.0 ± 0.5	6.6 ± 0.8	0.00120 ± 0.00003
Concrete	0	2.70 ± 0.05	6.2 ± 0.1	0.00309 ± 0.00007
	1	2.80 ± 0.05	6.4 ± 0.1	0.00230 ± 0.00006
	20	3.00 ± 0.05	6.9 ± 0.1	0.00141 ± 0.00005
	200	2.90 ± 0.05	6.7 ± 0.1	0.00038 ± 0.00003
LNGS rock	0	2.20 ± 0.05	6.0 ± 0.1	0.0223 ± 0.0002
	1	2.40 ± 0.05	6.5 ± 0.1	0.0079 ± 0.0001
	20	2.80 ± 0.05	7.6 ± 0.1	0.00210 ± 0.00006
	200	2.70 ± 0.05	7.3 ± 0.1	0.00041 ± 0.00003
Steel	0	0.90 ± 0.05	7.1 ± 0.4	0.2468 ± 0.0006
	1	0.80 ± 0.05	6.3 ± 0.4	0.0356 ± 0.0002
	20	1.10 ± 0.05	8.7 ± 0.4	0.00276 ± 0.00006
	200	1.10 ± 0.05	8.7 ± 0.4	0.00042 ± 0.00002
Copper	0	0.80 ± 0.05	7.2 ± 0.4	0.2387 ± 0.0007
	1	0.70 ± 0.05	6.3 ± 0.4	0.0377 ± 0.0003
	20	1.00 ± 0.05	9.0 ± 0.4	0.00294 ± 0.00007
	200	1.00 ± 0.05	9.0 ± 0.4	0.00041 ± 0.00003
Lead	0	1.50 ± 0.05	17.0 ± 0.6	0.999 ± 0.001
	1	0.90 ± 0.05	10.2 ± 0.6	0.1007 ± 0.0005
	20	1.00 ± 0.05	11.3 ± 0.6	0.00274 ± 0.00005
	200	1.00 ± 0.05	11.3 ± 0.6	0.00045571 ± 0.00002

Appendix H

Total Neutron Capture Detection Efficiencies

Table H.1: Total ^{77}Ge neutron capture detection efficiency ϵ in % for coaxial detectors.

E_{cut} [keV]	Calculation	Random number	Difference [%]
250	74.8634	75.866 ± 0.004	1
500	64.5741	65.366 ± 0.005	1
750	59.3214	60.170 ± 0.005	0.8
1000	54.8388	55.635 ± 0.005	0.8
1250	51.4386	52.170 ± 0.005	0.7
1500	48.3523	49.042 ± 0.005	0.7
1750	44.7277	45.292 ± 0.005	0.6
2000	41.0057	41.575 ± 0.005	0.6
2250	36.9125	37.425 ± 0.005	0.5
2500	33.6606	34.129 ± 0.005	0.5
2750	30.7827	31.191 ± 0.005	0.4
3000	28.3639	28.754 ± 0.005	0.4
3250	25.6519	26.009 ± 0.004	0.4
3500	22.5764	22.878 ± 0.004	0.3
3750	19.3792	19.627 ± 0.004	0.2
4000	17.2377	17.471 ± 0.004	0.2
4250	15.0225	15.219 ± 0.004	0.2
4500	13.0275	13.191 ± 0.003	0.2
4750	10.9147	11.037 ± 0.003	0.1
5000	8.70537	8.798 ± 0.003	0.09
5250	6.39194	6.448 ± 0.002	0.06
5500	4.1959	4.224 ± 0.002	0.03
5750	2.67522	2.693 ± 0.002	0.02
6000	1.36303	1.377 ± 0.001	0.01

Table H.2: Total ^{77}Ge neutron capture detection efficiency ϵ in % for BEGe detectors.

E_{cut} [keV]	Calculation	Random number	Difference [%]
250	62.786	63.553 ± 0.005	0.8
500	51.4519	52.043 ± 0.005	0.6
750	45.8651	46.516 ± 0.005	0.7
1000	41.7675	42.367 ± 0.005	0.6
1250	38.4259	38.973 ± 0.005	0.5
1500	35.4505	35.952 ± 0.005	0.5
1750	32.0085	32.426 ± 0.005	0.4
2000	28.5608	28.956 ± 0.005	0.4
2250	25.251	25.603 ± 0.004	0.4
2500	22.7516	23.073 ± 0.004	0.3
2750	20.449	20.703 ± 0.004	0.3
3000	18.2691	18.510 ± 0.004	0.2
3250	15.8931	16.104 ± 0.004	0.2
3500	13.5029	13.673 ± 0.003	0.2
3750	11.3282	11.474 ± 0.003	0.1
4000	9.76859	9.898 ± 0.003	0.1
4250	8.29494	8.394 ± 0.003	0.1
4500	6.97736	7.063 ± 0.003	0.09
4750	5.6934	5.757 ± 0.002	0.06
5000	4.34498	4.389 ± 0.002	0.04
5250	3.07354	3.100 ± 0.002	0.03
5500	2.08652	2.103 ± 0.001	0.02
5750	1.45466	1.468 ± 0.001	0.01
6000	0.985955	0.998 ± 0.001	0.01

Table H.3: Total ^{75}Ge neutron capture detection efficiency ϵ in % for coaxial detectors.

E_{cut} [keV]	Calculation	Random number	Difference [%]
250	70.3123	71.258 ± 0.005	0.9
500	63.9009	64.809 ± 0.005	0.9
750	57.2892	57.988 ± 0.005	0.7
1000	53.4369	53.870 ± 0.005	0.4
1250	49.6438	50.365 ± 0.005	0.7
1500	46.3039	46.975 ± 0.005	0.7
1750	41.9332	42.493 ± 0.005	0.6
2000	37.1455	37.694 ± 0.005	0.5
2250	34.7791	35.301 ± 0.005	0.5
2500	33.5477	34.053 ± 0.005	0.5
2750	32.3297	32.821 ± 0.005	0.5
3000	31.1846	31.660 ± 0.005	0.5
3250	29.8474	30.296 ± 0.005	0.4
3500	28.2799	28.693 ± 0.005	0.4
3750	26.1762	26.543 ± 0.004	0.4
4000	23.6933	24.010 ± 0.004	0.3
4250	21.0833	21.186 ± 0.004	0.1
4500	18.4731	18.369 ± 0.004	0.1
4750	15.5437	15.750 ± 0.004	0.2
5000	13.3907	13.560 ± 0.003	0.2
5250	11.1715	11.301 ± 0.003	0.1
5500	8.75883	8.854 ± 0.003	0.09
5750	6.37351	6.426 ± 0.002	0.05
6000	4.04357	4.068 ± 0.002	0.02

Table H.4: Total ^{75}Ge neutron capture detection efficiency ϵ in % for BEGe detectors.

E_{cut} [keV]	Calculation	Random number	Difference [%]
250	57.7486	58.446 ± 0.005	0.7
500	50.5783	51.269 ± 0.005	0.7
750	44.347	44.892 ± 0.005	0.5
1000	40.592	40.986 ± 0.005	0.4
1250	37.2157	37.737 ± 0.005	0.5
1500	34.0669	34.542 ± 0.005	0.5
1750	30.1744	30.540 ± 0.005	0.4
2000	26.6316	27.020 ± 0.004	0.4
2250	24.8899	25.258 ± 0.004	0.4
2500	23.7852	24.140 ± 0.004	0.4
2750	22.6738	23.012 ± 0.004	0.3
3000	21.6697	21.989 ± 0.004	0.3
3250	20.3703	20.666 ± 0.004	0.3
3500	18.9057	19.164 ± 0.004	0.3
3750	16.8913	17.108 ± 0.004	0.2
4000	14.6145	14.784 ± 0.004	0.2
4250	12.528	12.601 ± 0.003	0.07
4500	10.6333	10.591 ± 0.003	0.04
4750	8.61836	8.727 ± 0.003	0.1
5000	7.12596	7.208 ± 0.003	0.08
5250	5.52267	5.574 ± 0.002	0.05
5500	4.06341	4.102 ± 0.002	0.04
5750	2.80675	2.829 ± 0.002	0.02
6000	1.83429	1.851 ± 0.001	0.02

Table H.5: Total neutron capture detection efficiencies ϵ . The errors including the statistic and the systematic errors.

E_{cut} [keV]	^{77}Ge ϵ_{coax} [%]	^{77}Ge ϵ_{BEGe} [%]	^{75}Ge ϵ_{coax} [%]	^{75}Ge ϵ_{BEGe} [%]
250	76 ± 1	63.6 ± 0.8	71 ± 1	58.4 ± 0.7
500	65.4 ± 0.8	52.0 ± 0.6	64.8 ± 0.9	51.3 ± 0.7
750	60.2 ± 0.9	46.5 ± 0.7	58.0 ± 0.7	44.9 ± 0.5
1000	55.6 ± 0.8	42.4 ± 0.6	53.9 ± 0.4	41.0 ± 0.4
1250	52.2 ± 0.7	39.0 ± 0.6	50.4 ± 0.7	37.7 ± 0.5
1500	49.0 ± 0.7	36.0 ± 0.5	47.0 ± 0.7	34.5 ± 0.5
1750	45.3 ± 0.6	32.4 ± 0.4	42.5 ± 0.6	30.5 ± 0.4
2000	41.6 ± 0.6	29.0 ± 0.4	37.7 ± 0.6	27.0 ± 0.4
2250	37.4 ± 0.5	25.6 ± 0.4	35.3 ± 0.5	25.3 ± 0.4
2500	34.1 ± 0.5	23.1 ± 0.3	34.1 ± 0.5	24.1 ± 0.4
2750	31.2 ± 0.4	20.7 ± 0.3	32.8 ± 0.5	23.0 ± 0.3
3000	28.8 ± 0.4	18.5 ± 0.2	31.7 ± 0.5	22.0 ± 0.3
3250	26.0 ± 0.4	16.1 ± 0.2	30.3 ± 0.5	20.7 ± 0.3
3500	22.9 ± 0.3	13.7 ± 0.2	28.7 ± 0.4	19.2 ± 0.3
3750	19.6 ± 0.3	11.5 ± 0.2	26.5 ± 0.4	17.1 ± 0.2
4000	17.5 ± 0.2	9.9 ± 0.1	24.0 ± 0.3	14.8 ± 0.2
4250	15.2 ± 0.2	8.4 ± 0.1	21.2 ± 0.1	12.60 ± 0.07
4500	13.2 ± 0.2	7.06 ± 0.09	18.4 ± 0.1	10.59 ± 0.04
4750	11.0 ± 0.1	5.76 ± 0.07	15.7 ± 0.2	8.7 ± 0.1
5000	8.8 ± 0.1	4.39 ± 0.05	13.6 ± 0.2	7.21 ± 0.08
5250	6.45 ± 0.06	3.10 ± 0.03	11.3 ± 0.1	5.58 ± 0.05
5500	4.22 ± 0.03	2.10 ± 0.02	8.9 ± 0.1	4.10 ± 0.04
5750	2.69 ± 0.02	1.47 ± 0.02	6.43 ± 0.05	2.83 ± 0.02
6000	1.38 ± 0.02	1.00 ± 0.01	4.07 ± 0.03	1.85 ± 0.02

Appendix I

Likelihood of the Radionuclide Search

For the data analysis of the muon-induced radionuclide search, a binned extended likelihood fit is conducted whose likelihood is given by

$$L = e^{-\nu} \frac{\nu^N}{N!} \cdot N! \prod_{i=1}^B \frac{P_i^{n_i}}{n_i!} = e^{-\nu} \nu^N \prod_{i=1}^B \frac{P_i^{n_i}}{n_i!} \quad (\text{I.1})$$

with the number of bins B , the number of observed events N , the number of expected events ν , the number of observed entries n_i in bin i and the expected probability P_i for an event to appear in bin i . The number of expected events in bin i is the product of the expected number of events ν and the expected probability P_i

$$\nu_i = P_i \cdot \nu. \quad (\text{I.2})$$

Using the relations

$$N = \sum_{i=1}^B n_i, \quad \nu = \sum_{i=1}^B \nu_i, \quad (\text{I.3})$$

the likelihood can be written with

$$L = e^{-\sum_{i=1}^B \nu_i} \cdot \nu^{\sum_{i=1}^B n_i} \prod_{i=1}^B \frac{1}{n_i!} \left(\frac{\nu_i}{\nu}\right)^{n_i} = \prod_{i=1}^B e^{-\nu_i} \frac{\nu^{n_i}}{n_i!} \left(\frac{\nu_i}{\nu}\right)^{n_i} = \prod_{i=1}^B e^{-\nu_i} \frac{\nu_i^{n_i}}{n_i!} \quad (\text{I.4})$$

The likelihood is thus the product of the Poisson probabilities for observing n_i events in bin i while ν_i events are expected.

The expected probability P_i for an event to appear in bin i is given by the integral over the probability density function $f(x_i; \vec{\theta})$ for the variable x with the parameters

$\vec{\theta}$ from the lower bin boundary x_i^{low} to the upper bin boundary:

$$P_i = \int_{x_i^{low}}^{x_i^{up}} f(x_i; \vec{\theta}) dx. \quad (\text{I.5})$$

If the number of events has a signal and a background component

$$\nu = \nu_S + \nu_B, \quad (\text{I.6})$$

the probability density function is a combination of the known probability density function of the signal $f_S(x)$ and the known probability density function $f_B(x)$

$$f(x; S) = S \cdot f_S(x) + (1 - S) f_B(x) \quad (\text{I.7})$$

with the known signal fraction S . The expected number of signal events is

$$\nu_S = S \cdot \nu \quad (\text{I.8})$$

and the expected number of background events is

$$\nu_B = (1 - S) \cdot \nu. \quad (\text{I.9})$$

Assuming that the probability density function is approximately constant in one bin, the probability density function becomes

$$f(x_i; S) \approx f(x_i^c; S) \quad (\text{I.10})$$

with x_i^c being the value in the center of bin i . The expected probability P_i in bin i can then be approximated with

$$P_i = f(x_i^c; S) \cdot (x_i^{up} - x_i^{low}) = f(x_i^c; S) \cdot \Delta x_i. \quad (\text{I.11})$$

with the bin width Δx_i of bin i and the number of expected events in bin i becomes

$$\nu_i = P_i \cdot \nu = f(x_i^c; S) \cdot \Delta x_i \cdot \nu. \quad (\text{I.12})$$

By inserting Eq.I.7 the number of expected events in bin i becomes

$$\nu_i = \Delta x_i \cdot \nu \cdot [S \cdot f_S(x_i^c) + (1 - S) \cdot f_B(x_i^c)] = \Delta x_i \cdot [\nu_S \cdot f_S(x_i^c) + \nu_B \cdot f_B(x_i^c)]. \quad (\text{I.13})$$

The likelihood given in Eq. I.4 is for an analysis where the number of observed entries n_i in bin i are fitted. If the number of observed entries n_i in bin i per bin width

$$A_i = \frac{n_i}{\Delta x_i} \quad (\text{I.14})$$

is fitted instead, the likelihood becomes

$$L = \prod_{i=1}^B e^{-\alpha_i} \frac{\alpha_i^{A_i}}{A_i!} \quad (\text{I.15})$$

with the expected count rate

$$\alpha_i = \frac{\nu_i}{\Delta x_i} = \nu_s \cdot f_S(x_i^c) + \nu_B \cdot f_B(x_i^c). \quad (\text{I.16})$$

For the muon-induced radionuclide search described in chapter 7 and chapter 8, the time needed by the meta-stable state to undergo IT is of interest. The probability that a IT happen at time t is described by an exponential distribution. The time dependent probability function of the signal is

$$f_S(t) = \frac{\ln(2)}{T_{1/2}^S} \cdot e^{-\frac{\ln(2)}{T_{1/2}^S} \cdot t} \quad (\text{I.17})$$

with the half-life of the meta-stable state $T_{1/2}^S$. The main background contribution comes from ^{39}Ar decay which has a half-life of $T_{1/2}^B = 269$ yr. The time-dependent probability function of the background is

$$f_B(t) = \frac{\ln(2)}{T_{1/2}^B} \cdot e^{-\frac{\ln(2)}{T_{1/2}^B} \cdot t}. \quad (\text{I.18})$$

If the fractions of half-lives

$$x = \frac{t}{T_{1/2}^S} \quad (\text{I.19})$$

is used as variable instead of the time t , the probability density function of the signal is given by

$$f_S(x) = \ln(2) \cdot e^{-\ln(2) \cdot x} \quad (\text{I.20})$$

and the probability density function of the background is given by

$$f_B(x) = \ln(2) \frac{T_{1/2}^S}{T_{1/2}^B} \cdot e^{-\ln(2) \frac{T_{1/2}^S}{T_{1/2}^B} \cdot x}. \quad (\text{I.21})$$

Since the half-life of ^{39}Ar decay is much longer than the half-lives of the meta-stable states of ^{77}Ge and ^{75}Ge and thus

$$T_{\frac{1}{2}}^B \gg t = x \cdot T_{\frac{1}{2}}^S, \quad (\text{I.22})$$

the probability density function of the background is approximately constant

$$f_B(x) \approx \ln(2) \frac{T_{\frac{1}{2}}^S}{T_{\frac{1}{2}}^B} \quad (\text{I.23})$$

for the investigated times and the expected rate α_i becomes

$$\alpha_i = \nu_s \cdot f_S(x_i^c) + \nu_B \cdot f_B(x_i^c) = \nu_s \cdot \ln(2) \cdot e^{-\ln(2) \cdot x_i^c} + \nu_B \cdot \ln(2) \frac{T_{\frac{1}{2}}^S}{T_{\frac{1}{2}}^B}. \quad (\text{I.24})$$

The expected number of signal events ν_S is equivalent to N_S in chapter 8 and can be calculated from the exposure \mathcal{E} of the used data and from the observed production rate R_{obs} :

$$\nu_S = N_S = \mathcal{E} \cdot R_{obs} = \mathcal{E} \cdot \epsilon \cdot f_{IT} \cdot f_m \cdot R_c \quad (\text{I.25})$$

with the efficiency for observing the signal ϵ , the IT branching fraction of the meta-stable state f_{IT} and the branching fraction of meta-stable state production. If the background component is substituted with

$$A_{bkg} = \nu_B \cdot \ln(2) \frac{T_{\frac{1}{2}}^S}{T_{\frac{1}{2}}^B}, \quad (\text{I.26})$$

the expected rate α_i becomes

$$\alpha_i = \ln(2) \cdot \mathcal{E} \cdot \epsilon \cdot f_{IT} \cdot f_m \cdot R_c \cdot e^{-\ln(2) \cdot x_i^c} + A_{bkg}. \quad (\text{I.27})$$

Appendix J

GERDA Energy Reconstruction Efficiencies

Table J.1: Energy reconstruction efficiency for Phase Ia run 26.

Run	Channel	μ [keV]	σ [keV]	χ^2/ndf	$\mu + 3\sigma$ [keV]
26	ch 0	83.5 ± 0.4	2.8 ± 0.4	0.60	92 ± 1
26	ch 1	86.4 ± 0.5	4.9 ± 0.5	0.89	101 ± 2
26	ch 2	42.6 ± 0.8	4 ± 1	1.67	54 ± 3
26	ch 3	96.8 ± 0.4	5.0 ± 0.4	0.74	112 ± 1
26	ch 4	56.0 ± 0.6	20.0 ± 0.1	1.83	116.0 ± 0.7
26	ch 5	92.7 ± 0.5	5.1 ± 0.4	0.84	108 ± 1
26	ch 6	90.8 ± 0.5	4.8 ± 0.5	0.66	105 ± 1
26	ch 7	88.6 ± 0.4	5.0 ± 0.4	0.60	104 ± 1
26	ch 8	83.5 ± 0.4	4.0 ± 0.4	0.89	95 ± 1
26	ch 9	80.9 ± 0.7	6.3 ± 0.6	0.83	100 ± 2
26	ch 10	83.7 ± 0.5	6.5 ± 0.5	0.67	103 ± 2

Table J.2: Energy reconstruction efficiency for Phase Ia run 27.

Run	Channel	μ [keV]	σ [keV]	χ^2/ndf	$\mu + 3\sigma$ [keV]
27	ch 0	85 ± 1	4 ± 1	0.49	96 ± 5
27	ch 1	85.0 ± 0.3	4.0 ± 0.7	0.45	97 ± 2
27	ch 2	58 ± 3	8.0 ± 0.5	0.70	82 ± 4
27	ch 3	100 ± 1	6 ± 1	0.32	117 ± 4
27	ch 4	58 ± 1	10.0 ± 0.3	0.96	88 ± 1
27	ch 5	96 ± 1	8 ± 2	0.39	120 ± 5
27	ch 6	90.0 ± 0.4	4.4 ± 0.8	0.65	103 ± 2
27	ch 7	-	-	-	-
27	ch 8	84 ± 1	5 ± 1	0.41	98 ± 4
27	ch 9	79 ± 1	5.0 ± 0.9	0.54	94 ± 3
27	ch 10	83 ± 1	6.0 ± 0.3	0.54	101 ± 2

Table J.3: Energy reconstruction efficiency for Phase Ia run 28.

Run	Channel	μ [keV]	σ [keV]	χ^2/ndf	$\mu + 3\sigma$ [keV]
28	ch 0	74 ± 1	4 ± 1	0.63	85 ± 4
28	ch 1	87.0 ± 0.2	4.6 ± 0.6	0.58	101 ± 2
28	ch 2	42 ± 4	11 ± 2	0.69	75 ± 8
28	ch 3	97.9 ± 0.9	5.2 ± 0.8	0.30	113 ± 3
28	ch 4	46 ± 3	9.0 ± 0.9	1.09	73 ± 4
28	ch 5	92.5 ± 0.8	4.6 ± 0.7	0.39	106 ± 2
28	ch 6	91.5 ± 0.9	5.0 ± 0.9	0.49	106 ± 3
28	ch 7	-	-	-	-
28	ch 8	84.7 ± 0.6	5.0 ± 0.4	0.67	100 ± 1
28	ch 9	79.0 ± 0.8	5.0 ± 0.4	0.48	94 ± 1
28	ch 10	87 ± 2	7 ± 1	0.58	109 ± 4

Table J.4: Energy reconstruction efficiency for Phase Ia run 29.

Run	Channel	μ [keV]	σ [keV]	χ^2/ndf	$\mu + 3\sigma$ [keV]
29	ch 0	35.6 ± 0.9	2 ± 1	0.59	43 ± 3
29	ch 1	41.1 ± 0.8	3.4 ± 0.8	1.57	51 ± 3
29	ch 2	43.1 ± 0.8	3 ± 1	1.34	52 ± 3
29	ch 3	41 ± 1	3 ± 1	1.15	49 ± 3
29	ch 4	44 ± 1	5 ± 1	1.61	58 ± 4
29	ch 5	37.8 ± 0.9	2.3 ± 0.8	1.55	45 ± 3
29	ch 6	44.1 ± 0.8	3 ± 1	0.94	52 ± 4
29	ch 7	-	-	-	-
29	ch 8	35.0 ± 0.7	1 ± 1	1.09	39 ± 4
29	ch 9	35 ± 1	1 ± 1	2.22	37 ± 3
29	ch 10	34.9 ± 0.6	0.9 ± 0.6	2.04	38 ± 2

Table J.5: Energy reconstruction efficiency for Phase Ia run 30.

Run	Channel	μ [keV]	σ [keV]	χ^2/ndf	$\mu + 3\sigma$ [keV]
30	ch 0	-	-	-	-
30	ch 1	41 ± 0.7	4 ± 1	1.57	51 ± 3
30	ch 2	42.8 ± 0.6	2.8 ± 0.6	1.19	51 ± 2
30	ch 3	41 ± 1	4 ± 1	1.28	52 ± 3
30	ch 4	44 ± 0.8	5 ± 1	1.74	58 ± 4
30	ch 5	38.7 ± 0.6	1.7 ± 0.6	1.80	44 ± 2
30	ch 6	45 ± 2	3.7 ± 0.6	1.59	56 ± 2
30	ch 7	-	-	-	-
30	ch 8	37.9 ± 0.8	3.5 ± 0.9	1.33	47 ± 3
30	ch 9	35.1 ± 0.5	2.2 ± 0.8	2.86	42 ± 2
30	ch 10	32.8 ± 0.4	1.5 ± 0.4	2.87	37 ± 1

Table J.6: Energy reconstruction efficiency for Phase Ia run 32.

Run	Channel	μ [keV]	σ [keV]	χ^2/ndf	$\mu + 3\sigma$ [keV]
32	ch 0	-	-	-	-
32	ch 1	39.7 ± 0.7	3.1 ± 0.6	1.39	49 ± 2
32	ch 2	43.0 ± 0.8	4 ± 1	1.40	55 ± 3
32	ch 3	41.3 ± 0.6	2.1 ± 0.5	1.17	47 ± 2
32	ch 4	45.0 ± 0.5	5.3 ± 0.8	2.90	61 ± 2
32	ch 5	37.3 ± 0.8	2 ± 1	1.57	45 ± 4
32	ch 6	44 ± 1	4 ± 1	1.17	57 ± 3
32	ch 7	-	-	-	-
32	ch 8	35.2 ± 0.6	2 ± 1	1.43	42 ± 3
32	ch 9	33.0 ± 0.5	1.6 ± 0.8	2.76	38 ± 2
32	ch 10	31.1 ± 0.5	1.1 ± 0.5	3.02	35 ± 2

Table J.7: Energy reconstruction efficiency for Phase Ib run 35.

Run	Channel	μ [keV]	σ [keV]	χ^2/ndf	$\mu + 3\sigma$ [keV]
35	ch 0	-	-	-	-
35	ch 1	42.5 ± 0.9	3 ± 1	0.75	53 ± 4
35	ch 2	45 ± 1	4 ± 1	1.22	56 ± 4
35	ch 3	43 ± 2	5 ± 2	1.38	58 ± 6
35	ch 4	48 ± 2	8.0 ± 0.5	1.70	72 ± 2
35	ch 5	40.3 ± 0.9	2 ± 1	1.28	47 ± 3
35	ch 6	45 ± 2	5 ± 3	1.08	61 ± 8
35	ch 7	-	-	-	-
35	ch 8	37.6 ± 0.6	1.68896 ± 0.8	1.39	43 ± 3
35	ch 9	32.7 ± 1	4 ± 3	0.54	44 ± 8
35	ch 10	35 ± 1	3 ± 2	0.66	44 ± 7
35	ch 11	35.0 ± 0.5	4 ± 22	0.67	46 ± 7
35	ch 12	39.0 ± 0.6	3 ± 1	0.50	47 ± 4

Table J.8: Energy reconstruction efficiency for Phase Ib run 36.

Run	Channel	μ [keV]	σ [keV]	χ^2/ndf	$\mu + 3\sigma$ [keV]
36	ch 0	-	-	-	-
36	ch 1	43.0 ± 0.8	5 ± 1	2.21	57 ± 4
36	ch 2	46.2 ± 0.5	2.3 ± 0.4	1.82	53 ± 1
36	ch 3	42.9 ± 0.7	3.9 ± 0.7	1.71	55 ± 2
36	ch 4	47.3 ± 0.6	3.3 ± 0.7	2.24	57 ± 2
36	ch 5	41.2 ± 0.6	3.1 ± 0.7	2.04	50 ± 2
36	ch 6	44.2 ± 0.7	3.7 ± 0.9	1.39	55 ± 3
36	ch 7	-	-	-	-
36	ch 8	37.0 ± 0.5	2.0 ± 0.5	2.32	43 ± 1
36	ch 9	35 ± 0.5	2.9 ± 0.7	0.63	44 ± 2
36	ch 10	35.6 ± 0.3	1.0 ± 0.3	0.82	38.6 ± 0.9
36	ch 11	35.0 ± 0.3	2.6 ± 0.7	0.76	43 ± 2
36	ch 12	35.3 ± 0.5	1.1 ± 0.5	0.71	39 ± 2

Table J.9: Energy reconstruction efficiency for Phase Ib run 37.

Run	Channel	μ [keV]	σ [keV]	χ^2/ndf	$\mu + 3\sigma$ [keV]
37	ch 0	-	-	-	-
37	ch 1	44.0 ± 0.2	4.5 ± 0.7	2.15	58 ± 2
37	ch 2	46.8 ± 0.8	3 ± 1	1.55	56 ± 3
37	ch 3	42.2 ± 0.9	3.2 ± 0.9	1.42	51 ± 3
37	ch 4	46.4 ± 0.9	2.7 ± 0.7	2.41	55 ± 2
37	ch 5	40.1 ± 0.9	3 ± 1	1.54	50 ± 4
37	ch 6	44.7 ± 0.8	3.1 ± 0.9	0.94	54 ± 3
37	ch 7	-	-	-	-
37	ch 8	39 ± 1	2.9 ± 0.8	0.98	$47pm3$
37	ch 9	-	-	-	-
37	ch 10	35.4 ± 0.7	1.4 ± 0.9	0.60	40 ± 3
37	ch 11	33.7 ± 0.9	2 ± 1	0.72	40 ± 4
37	ch 12	36.5 ± 0.7	2 ± 1	0.52	41 ± 3

Table J.10: Energy reconstruction efficiency for Phase Ib run 38.

Run	Channel	μ [keV]	σ [keV]	χ^2/ndf	$\mu + 3\sigma$ [keV]
38	ch 0	-	-	-	-
38	ch 1	45 ± 2	5 ± 3	1.64	59 ± 8
38	ch 2	48 ± 1	5.0 ± 0.6	1.26	63 ± 2
38	ch 3	42 ± 2	5 ± 3	0.95	57 ± 10
38	ch 4	46.2 ± 0.9	3 ± 1	1.40	54 ± 4
38	ch 5	39.4 ± 0.8	1 ± 1	1.21	44 ± 3
38	ch 6	44.1 ± 0.9	3 ± 2	0.69	53 ± 5
38	ch 7	-	-	-	-
38	ch 8	37.4 ± 0.8	2.11474 ± 0.8	0.84	44 ± 2
38	ch 9	35 ± 2	3 ± 2	0.46	44 ± 6
38	ch 10	39 ± 1	4 ± 2	0.58	50 ± 5
38	ch 11	-	-	-	-
38	ch 12	35 ± 2	3 ± 3	0.55	44 ± 9

Table J.11: Energy reconstruction efficiency for Phase Ib run 39.

Run	Channel	μ [keV]	σ [keV]	χ^2/ndf	$\mu + 3\sigma$ [keV]
39	ch 0	-	-	-	-
39	ch 1	48 ± 1	9.0 ± 0.8	1.95	75.3233 ± 3
39	ch 2	49.8 ± 0.9	7.0 ± 0.9	1.70	70.7766 ± 3
39	ch 3	44 ± 1	7 ± 5	1.60	65 ± 14
39	ch 4	47.8 ± 0.9	5.0 ± 0.3	2.45	63 ± 1
39	ch 5	42.4 ± 0.8	3 ± 1	1.15	50 ± 3
39	ch 6	46 ± 1	5 ± 1	1.06	60 ± 4
39	ch 7	-	-	-	-
39	ch 8	42 ± 1	4.0 ± 0.9	1.65	54 ± 3
39	ch 9	33.8 ± 0.6	1.3 ± 0.6	0.50	38 ± 2
39	ch 10	35.7 ± 0.8	3 ± 2	0.78	44 ± 5
39	ch 11	33.5 ± 0.6	1.1 ± 0.6	0.82	37 ± 2
39	ch 12	36.5 ± 0.7	1.9 ± 0.9	0.57	42 ± 3

Table J.12: Energy reconstruction efficiency for Phase Ib run 40.

Run	Channel	μ [keV]	σ [keV]	χ^2/ndf	$\mu + 3\sigma$ [keV]
40	ch 0	-	-	-	-
40	ch 1	48.1 ± 0.9	8 ± 0.2	2.75	72 ± 1
40	ch 2	49 ± 2	6 ± 2	2.29	65 ± 5
40	ch 3	43.9 ± 0.7	3 ± 2	1.64	54 ± 5
40	ch 4	46.6 ± 0.6	3.0 ± 0.6	2.36	56 ± 2
40	ch 5	41.0 ± 0.5	1.7 ± 0.5	1.96	46 ± 2
40	ch 6	45 ± 1	5 ± 2	1.30	59 ± 5
40	ch 7	-	-	-	-
40	ch 8	40.5 ± 0.7	3.4 ± 0.65	1.70	51 ± 2
40	ch 9	33.4 ± 0.8	2.1 ± 0.8	0.78	40 ± 2
40	ch 10	35.5 ± 0.6	1.4 ± 0.6	0.62	40 ± 2
40	ch 11	32.9 ± 0.8	1.9 ± 0.7	0.61	39 ± 2
40	ch 12	34.9 ± 0.6	2 ± 1	0.89	39 ± 3

Table J.13: Energy reconstruction efficiency for Phase Ib run 41.

Run	Channel	μ [keV]	σ [keV]	χ^2/ndf	$\mu + 3\sigma$ [keV]
41	ch 0	-	-	-	-
41	ch 1	48.1 ± 0.9	5.0 ± 0.3	1.68	63 ± 1
41	ch 2	47 ± 2	6 ± 2	1.92	65 ± 6
41	ch 3	46 ± 1	6.0 ± 0.6	1.42	64 ± 2
41	ch 4	47.5 ± 0.9	5.0 ± 0.7	1.78	63 ± 2
41	ch 5	41.4 ± 0.8	3 ± 1	1.94	50 ± 3
41	ch 6	45.8437 ± 2	4 ± 3	1.32	59 ± 8
41	ch 7	-	-	-	-
41	ch 8	39.2 ± 0.8	3 ± 1	1.04	49 ± 4
41	ch 9	33 ± 1	2 ± 2	0.75	40 ± 6
41	ch 10	36.0 ± 0.9	3 ± 2	0.65	45 ± 7
41	ch 11	32.6 ± 0.9	2 ± 1	0.69	40 ± 4
41	ch 12	36 ± 1	3 ± 1	0.54	45 ± 4

Table J.14: Energy reconstruction efficiency for Phase Ib run 42.

Run	Channel	μ [keV]	σ [keV]	χ^2/ndf	$\mu + 3\sigma$ [keV]
42	ch 0	-	-	-	-
42	ch 1	43.9 ± 0.7	3.5 ± 0.8	1.96	54 ± 2
42	ch 2	45.9 ± 0.7	5.0 ± 0.6	2.64	61 ± 2
42	ch 3	42.2 ± 0.6	3.0 ± 0.9	1.49	51 ± 3
42	ch 4	47.0 ± 0.9	3.5 ± 0.8	2.44	57 ± 3
42	ch 5	40.6 ± 0.8	2.9 ± 0.7	1.89	49 ± 2
42	ch 6	46 ± 1	5 ± 1	1.33	60 ± 3
42	ch 7	-	-	-	-
42	ch 8	39.7 ± 0.7	3.8 ± 0.7	1.82	51 ± 2
42	ch 9	34.5 ± 0.7	2 ± 1	0.66	40 ± 3
42	ch 10	35.3 ± 0.8	3 ± 2	0.66	44 ± 5
42	ch 11	33 ± 1	3 ± 2	0.76	42 ± 6
42	ch 12	35.6 ± 0.6	1.5 ± 0.7	0.81	40 ± 2

Table J.15: Energy reconstruction efficiency for Phase Ib run 43.

Run	Channel	μ [keV]	σ [keV]	χ^2/ndf	$\mu + 3\sigma$ [keV]
43	ch 0	-	-	-	-
43	ch 1	47.0 ± 0.8	5.0 ± 0.6	1.40	62 ± 2
43	ch 2	47 ± 1	4 ± 1	1.06	60 ± 4
43	ch 3	46 ± 2	6 ± 2	1.80	62 ± 6
43	ch 4	53 ± 3	12.0 ± 0.2	1.44	89 ± 3
43	ch 5	44 ± 1	4 ± 1	1.99	55 ± 4
43	ch 6	45 ± 1	4 ± 2	0.80	56 ± 6
43	ch 7	-	-	-	-
43	ch 8	44 ± 1	4.93123 ± 1	1.33	59 ± 4
43	ch 9	36.0 ± 0.6	3 ± 1	0.62	46 ± 3
43	ch 10	36 ± 1	2 ± 1	0.60	42 ± 4
43	ch 11	34.0 ± 0.9	3 ± 2	0.66	43 ± 6
43	ch 12	35.8 ± 0.7	1.2 ± 0.6	0.54	40 ± 2

Table J.16: Energy reconstruction efficiency for Phase Ib run 44.

Run	Channel	μ [keV]	σ [keV]	χ^2/ndf	$\mu + 3\sigma$ [keV]
44	ch 0	-	-	-	-
44	ch 1	50 ± 0.2	6.0 ± 0.8	1.36	68 ± 2
44	ch 2	48.3 ± 0.9	5.5 ± 0.4	1.33	65 ± 2
44	ch 3	43.6 ± 0.9	4 ± 1	1.42	56 ± 3
44	ch 4	46.9 ± 0.6	2.0 ± 0.8	1.63	53 ± 2
44	ch 5	42.2 ± 0.7	1.6 ± 0.8	1.72	47 ± 3
44	ch 6	-	-	-	-
44	ch 7	-	-	-	-
44	ch 8	50.0 ± 0.3	9.0 ± 0.2	1.10	77.0 ± 0.7
44	ch 9	35 ± 1	4 ± 3	0.46	46 ± 8
44	ch 10	36.3 ± 0.7	1.9 ± 0.9	0.86	42 ± 3
44	ch 11	33.5 ± 0.7	1.2 ± 0.7	0.79	37 ± 2
44	ch 12	36.0 ± 0.8	5 ± 2	0.71	51 ± 8

Table J.17: Energy reconstruction efficiency for Phase Ib run 45.

Run	Channel	μ [keV]	σ [keV]	χ^2/ndf	$\mu + 3\sigma$ [keV]
45	ch 0	-	-	-	-
45	ch 1	48.8 ± 0.9	7.0 ± 0.3	1.66	70 ± 1
45	ch 2	47 ± 1	5 ± 1	1.39	63 ± 3
45	ch 3	43.3 ± 0.7	3.3 ± 0.7	1.58	53 ± 2
45	ch 4	47.1 ± 0.6	2.0 ± 0.7	2.70	53 ± 2
45	ch 5	42.7 ± 0.9	3.7 ± 0.8	2.76	54 ± 3
45	ch 6	-	-	-	-
45	ch 7	-	-	-	-
45	ch 8	44 ± 1	5 ± 1	1.54	59 ± 3
45	ch 9	33.2 ± 0.8	3 ± 1	0.72	41 ± 3
45	ch 10	36.8 ± 0.7	2.0 ± 0.7	0.73	43 ± 2
45	ch 11	33.2 ± 0.6	1.1 ± 0.5	0.81	36 ± 2
45	ch 12	36.8 ± 0.7	2 ± 1	0.66	42 ± 3

Table J.18: Energy reconstruction efficiency for Phase Ib run 46.

Run	Channel	μ [keV]	σ [keV]	χ^2/ndf	$\mu + 3\sigma$ [keV]
46	ch 0	-	-	-	-
46	ch 1	46 ± 1	4 ± 1	1.33	58 ± 4
46	ch 2	46.4 ± 0.9	3.0 ± 0.8	1.24	55 ± 3
46	ch 3	42.2 ± 0.8	3 ± 1	0.68	50 ± 3
46	ch 4	49 ± 1	4 ± 1	1.49	60 ± 4
46	ch 5	42 ± 1	5 ± 2	1.26	57 ± 5
46	ch 6	-	-	-	-
46	ch 7	-	-	-	-
46	ch 8	43 ± 1	4 ± 1	0.98	56 ± 3
46	ch 9	35.0 ± 0.6	5 ± 2	0.52	49 ± 5
46	ch 10	35 ± 1	3 ± 2	0.58	46 ± 6
46	ch 11	37 ± 1	5 ± 2	0.40	53 ± 7
46	ch 12	35 ± 1	2 ± 1	0.58	41 ± 4

Table J.19: Energy reconstruction efficiency for Phase IIa run 53.

Run	Channel	μ [keV]	σ [keV]	χ^2/ndf	$\mu + 3\sigma$ [keV]
53	ch 0	148 ± 1	1.6 ± 0.6	0.91	153 ± 2
53	ch 1	148 ± 1	3 ± 2	0.92	157 ± 5
53	ch 2	144.0 ± 0.9	2.1 ± 0.6	0.65	150 ± 2
53	ch 3	-	-	-	-
53	ch 4	143 ± 1	3 ± 1	1.09	152 ± 3
53	ch 5	148 ± 2	6 ± 2	0.85	166 ± 5
53	ch 6	147 ± 1	5 ± 1	0.61	161 ± 4
53	ch 7	148 ± 1	4 ± 1	0.89	161 ± 4
53	ch 8	-	-	-	-
53	ch 9	-	-	-	-
53	ch 10	147.1 ± 0.7	4.4 ± 0.7	0.77	160 ± 2
53	ch 11	149 ± 2	3 ± 2	0.64	158 ± 5
53	ch 12	-	-	-	-
53	ch 13	145 ± 1	4.5 ± 0.6	0.68	159 ± 2
53	ch 14	144 ± 1	3 ± 1	0.82	154 ± 4
53	ch 15	168.2 ± 0.8	3.0 ± 0.8	0.85	177 ± 2
53	ch 16	-	-	-	-
53	ch 17	150 ± 42	3 ± 2	0.72	159 ± 42
53	ch 18	-	-	-	-
53	ch 19	142 ± 1	5 ± 1	0.83	157 ± 4
53	ch 20	141 ± 1	3.2 ± 0.8	0.76	151 ± 3
53	ch 21	146.6 ± 0.8	3 ± 1	0.55	155 ± 4
53	ch 22	143 ± 1	2.0 ± 0.6	0.73	149 ± 2
53	ch 23	-	-	-	-
53	ch 24	146 ± 2	4 ± 2	0.535789	159 ± 6
53	ch 25	-	-	-	-
53	ch 26	-	-	-	-
53	ch 27	-	-	-	-
53	ch 28	-	-	-	-
53	ch 29	149.5 ± 0.9	4.0 ± 0.9	0.72	162 ± 3
53	ch 30	150.0 ± 0.6	7 ± 4	0.69	170 ± 11
53	ch 31	-	-	-	-
53	ch 32	-	-	-	-
53	ch 33	-	-	-	-
53	ch 34	-	-	-	-
53	ch 35	145 ± 1	2.6 ± 0.8	0.30	153 ± 3
53	ch 36	161.4 ± 0.9	4.4 ± 0.9	0.67	175 ± 3
53	ch 37	168 ± 1	5 ± 1	1.15	183 ± 4
53	ch 38	-	-	-	-
53	ch 39	182 ± 2	8 ± 1	0.89	206 ± 4

Table J.20: Energy reconstruction efficiency for Phase IIb run 87.

Run	Channel	μ [keV]	σ [keV]	χ^2/ndf	$\mu + 3\sigma$ [keV]
87	ch 0	12 ± 1	3 ± 2	1.32	23 ± 5
87	ch 1	10 ± 4	4.0 ± 0.6	1.16	22 ± 4
87	ch 2	11 ± 1	4.0 ± 0.3	1.23	23 ± 1
87	ch 3	13.3 ± 0.4	1.1 ± 0.4	1.04	17 ± 1
87	ch 4	15 ± 1	4.0 ± 0.6	1.21	27 ± 2
87	ch 5	-	-	-	-
87	ch 6	-	-	-	-
87	ch 7	-	-	-	-
87	ch 8	15.2 ± 0.3	1.5 ± 0.3	3.21	19.7 ± 0.8
87	ch 9	14.6 ± 0.4	1.5 ± 0.4	2.04	19 ± 1
87	ch 10	15.1 ± 0.3	2.10 ± 0.05	2.36	21.4 ± 0.3
87	ch 11	14 ± 2	6 ± 3	1.17	31 ± 8
87	ch 12	14.1 ± 0.2	2.5 ± 0.3	0.84	22 ± 1
87	ch 13	16.1 ± 0.1	4.2 ± 0.9	1.37	29 ± 3
87	ch 14	11.2 ± 0.4	1.0 ± 0.4	1.10	14 ± 1
87	ch 15	14.3 ± 0.4	2.3 ± 0.1	0.99	21.2 ± 0.6
87	ch 16	13.7 ± 0.5	1.2 ± 0.5	0.76	17 ± 2
87	ch 17	13.1 ± 0.6	1.2 ± 0.6	1.23	17 ± 2
87	ch 18	13.0 ± 0.4	1.1 ± 0.4	1.18	16 ± 1
87	ch 19	11.9 ± 0.8	2 ± 1	0.86	19 ± 3
87	ch 20	12.5 ± 0.5	2.2 ± 0.3	0.96	19.1 ± 0.9
87	ch 21	10.2 ± 0.5	1.6 ± 0.5	1.13	15 ± 2
87	ch 22	11.4 ± 0.4	1.1 ± 0.4	0.97	15 ± 1
87	ch 23	14.2 ± 0.5	1.4 ± 0.5	0.58	18 ± 2
87	ch 24	12.9 ± 0.6	1.5 ± 0.7	0.97	17 ± 2
87	ch 25	14.3 ± 0.7	1.6 ± 0.7	0.66	19 ± 2
87	ch 26	10.0 ± 0.4	2.4 ± 0.2	1.20	17.2 ± 0.8
87	ch 27	15.7 ± 0.3	1.3 ± 0.3	1.89	20 ± 1
87	ch 28	15.2 ± 0.3	1.1 ± 0.3	1.57	18 ± 1
87	ch 29	12.8 ± 0.3	2.10 ± 0.09	1.88	19.1 ± 0.4
87	ch 30	11.1 ± 0.8	2.1 ± 0.7	0.73	17 ± 2
87	ch 31	12.1 ± 0.4	1.8 ± 0.2	0.99	17.5 ± 0.7
87	ch 32	-	-	-	-
87	ch 33	11 ± 2	3 ± 1	1.04	20 ± 5
87	ch 34	11.3 ± 0.5	1.0 ± 0.4	0.94	14 ± 1
87	ch 35	14.3 ± 0.7	2.6 ± 0.4	0.75	22 ± 1
87	ch 36	16.4 ± 0.6	1.8 ± 0.6	1.22	22 ± 2
87	ch 37	13.0 ± 0.3	2.50 ± 0.06	1.78	20.5 ± 0.3
87	ch 38	-	-	-	-
87	ch 39	-	-	-	-

Table J.21: Energy reconstruction efficiency for Phase IIb run 88.

Run	Channel	μ [keV]	σ [keV]	χ^2/ndf	$\mu + 3\sigma$ [keV]
88	ch 0	14.6 ± 0.6	2.1 ± 0.6	1.30	21 ± 2
88	ch 1	11.4 ± 0.6	0.9 ± 0.5	0.89	14 ± 2
88	ch 2	13.4 ± 0.5	2.2 ± 0.2	0.97	12.0 ± 0.7
88	ch 3	13.2 ± 0.5	1.3 ± 0.7	0.82	17 ± 2
88	ch 4	12.9 ± 0.7	1.2 ± 0.8	0.96	16 ± 2
88	ch 5	-	-	-	-
88	ch 6	-	-	-	-
88	ch 7	-	-	-	-
88	ch 8	15.3 ± 0.3	1.3 ± 0.3	2.56	19.2 ± 0.8
88	ch 9	15.1 ± 0.4	2.3 ± 0.2	1.65	22.0 ± 0.6
88	ch 10	14.1 ± 0.4	1.7 ± 0.5	2.09	19 ± 1
88	ch 11	14.0 ± 0.4	3 ± 1	0.90	22 ± 4
88	ch 12	12.9 ± 0.6	2.5 ± 0.3	0.89	20 ± 1
88	ch 13	13.7 ± 0.5	2.2 ± 0.2	1.02	20.3 ± 0.7
88	ch 14	12.0 ± 0.2	1.8 ± 0.3	0.96	17.4 ± 0.9
88	ch 15	12 ± 1	2 ± 1	0.80	17 ± 4
88	ch 16	14.0 ± 0.6	1.4 ± 0.6	0.65	18 ± 2
88	ch 17	12 ± 1	2 ± 1	0.62	19 ± 4
88	ch 18	12.2 ± 0.7	1.6 ± 0.5	1.03	17 ± 2
88	ch 19	10 ± 4	1.4 ± 0.7	1.11	14 ± 5
88	ch 20	11.5 ± 0.6	1.0 ± 0.5	0.76	15 ± 2
88	ch 21	10.0 ± 0.4	1.3 ± 0.5	1.21	14 ± 2
88	ch 22	12.7 ± 0.2	1.8 ± 0.3	0.97	18 ± 1
88	ch 23	13.7 ± 0.6	1.7 ± 0.4	0.94	19 ± 1
88	ch 24	12 ± 1	2 ± 1	0.86	18 ± 5
88	ch 25	15.0 ± 0.7	1.1 ± 0.8	0.70	18 ± 2
88	ch 26	11.4 ± 0.4	2.4 ± 0.1	1.05	18.6 ± 0.5
88	ch 27	15.0 ± 0.4	1.2 ± 0.5	1.42	19 ± 1
88	ch 28	15.0 ± 0.4	1.1 ± 0.4	1.30	18 ± 1
88	ch 29	11.4 ± 0.3	1.0 ± 0.3	2.10	14 ± 1
88	ch 30	12.0 ± 0.5	2 ± 1	0.89	18 ± 3
88	ch 31	12.0 ± 0.6	2.1 ± 0.5	0.95	18 ± 2
88	ch 32	-	-	-	-
88	ch 33	12 ± 1	2 ± 1	0.96	18 ± 4
88	ch 34	12.0 ± 0.6	1.8 ± 0.5	0.87	17 ± 2
88	ch 35	13.8 ± 1	2.5 ± 0.9	0.80	21 ± 3
88	ch 36	16.0 ± 0.5	1.7 ± 0.7	0.78	21 ± 2
88	ch 37	12.5 ± 0.3	1.1 ± 0.5	1.69	16 ± 2
88	ch 38	-	-	-	-
88	ch 39	15.4 ± 0.3	1.0 ± 0.2	1.59	18.4 ± 0.7

Table J.22: Energy reconstruction efficiency for Phase IIb run 89.

Run	Channel	μ [keV]	σ [keV]	χ^2/ndf	$\mu + 3\sigma$ [keV]
89	ch 0	22.0 ± 0.6	7 ± 2	0.90	43 ± 6
89	ch 1	17.0 ± 0.4	5 ± 4	0.88	31 ± 13
89	ch 2	11 ± 2	2.0 ± 0.6	1.22	17 ± 3
89	ch 3	14.0 ± 0.8	2.0 ± 0.9	0.62	20 ± 3
89	ch 4	19 ± 7	6 ± 2	1.22	37 ± 9
89	ch 5	-	-	-	-
89	ch 6	-	-	-	-
89	ch 7	-	-	-	-
89	ch 8	13.9 ± 0.7	1 ± 0.5	1.2	17 ± 2
89	ch 9	15 ± 1	1.8 ± 0.9	1.7	20 ± 3
89	ch 10	13 ± 2	2.0 ± 0.9	0.95	19 ± 4
89	ch 11	14 ± 2	4 ± 3	0.60	26 ± 9
89	ch 12	13 ± 2	2 ± 2	0.61	20 ± 5
89	ch 13	13 ± 3	2 ± 2	0.50	20 ± 6
89	ch 14	13 ± 3	2 ± 1	0.77	19 ± 4
89	ch 15	14 ± 2	2.5 ± 0.9	0.56	21 ± 4
89	ch 16	16 ± 2	3 ± 1	0.61	24 ± 5
89	ch 17	12 ± 4	2 ± 1	0.80	18 ± 6
89	ch 18	15 ± 1	2 ± 1	0.56	21 ± 4
89	ch 19	14 ± 2	2 ± 1	0.54	21 ± 4
89	ch 20	12 ± 3	3 ± 2	0.99	21 ± 6
89	ch 21	13 ± 2	3.0 ± 0.7	0.62	22 ± 3
89	ch 22	12 ± 2	2.5 ± 0.5	0.73	20 ± 3
89	ch 23	14 ± 1	2.4 ± 0.6	1.51	22 ± 2
89	ch 24	12 ± 3	2.7 ± 0.6	0.68	20 ± 4
89	ch 25	14 ± 1	2.3 ± 0.4	0.48	21 ± 2
89	ch 26	11.0 ± 0.7	2 ± 1	0.62	17 ± 3
89	ch 27	15.6 ± 0.8	2.1 ± 0.8	0.85	22 ± 2
89	ch 28	15.5 ± 0.7	1.9 ± 0.7	0.67	21 ± 2
89	ch 29	12 ± 1	2 ± 1	0.86	18 ± 3
89	ch 30	11 ± 4	1.9 ± 0.6	0.66	17 ± 4
89	ch 31	12.1274 ± 1	1.9 ± 0.6	0.75	18 ± 2
89	ch 32	12 ± 3	1.9 ± 0.8	0.62	18 ± 4
89	ch 33	11 ± 4	1.9 ± 0.6	0.72	17 ± 4
89	ch 34	13 ± 3	2.2 ± 0.4	0.49	19 ± 3
89	ch 35	13 ± 3	2.2 ± 0.4	0.66	20 ± 3
89	ch 36	13 ± 4	3 ± 1	0.70	22 ± 6
89	ch 37	12 ± 1	1.9 ± 0.9	0.95	18 ± 3
89	ch 38	16 ± 1	1.9 ± 0.6	0.85	22 ± 2
89	ch 39	14 ± 1	2 ± 1	0.85	20 ± 3

Table J.23: Energy reconstruction efficiency for Phase IIb run 90.

Run	Channel	μ [keV]	σ [keV]	χ^2/ndf	$\mu + 3\sigma$ [keV]
90	ch 0	14.4 ± 0.3	1.0 ± 0.5	1.44	17 ± 2
90	ch 1	12.3 ± 0.4	1 ± 1	0.84	15 ± 3
90	ch 2	10.8 ± 0.9	1.8 ± 0.6	0.86	16 ± 2
90	ch 3	13.2 ± 0.6	1.2 ± 0.6	1.10	17 ± 2
90	ch 4	14.2 ± 0.5	1.3 ± 0.7	0.76	18 ± 2
90	ch 5	-	-	-	-
90	ch 6	-	-	-	-
90	ch 7	-	-	-	-
90	ch 8	15.6 ± 0.3	1.9 ± 0.3	3.57	21.2 ± 0.9
90	ch 9	15.5 ± 0.4	1.9 ± 0.1	1.85	21.2 ± 0.6
90	ch 10	14.2 ± 0.4	1.6 ± 0.4	1.72	19 ± 1
90	ch 11	10.9 ± 0.9	2.8 ± 0.9	0.79	19 ± 3
90	ch 12	12.2 ± 0.7	2.1 ± 0.8	0.87	19 ± 2
90	ch 13	-	-	-	-
90	ch 14	11.2 ± 0.3	1.0 ± 0.3	0.89	14.2 ± 0.8
90	ch 15	13.3 ± 0.4	1.0 ± 0.4	0.94	16 ± 1
90	ch 16	14.4 ± 0.5	1.4 ± 0.7	0.80	19 ± 2
90	ch 17	13.3 ± 0.6	1.1 ± 0.9	0.69	17 ± 3
90	ch 18	13.0 ± 0.3	1.0 ± 0.4	1.18	16 ± 1
90	ch 19	11.1 ± 0.5	1.3 ± 0.9	0.95	15 ± 3
90	ch 20	12.9 ± 0.6	2 ± 1	1.08	19 ± 3
90	ch 21	12 ± 0.1	1.4 ± 0.6	1.06	16 ± 2
90	ch 22	12 ± 0.2	1.1 ± 0.5	1.03	15 ± 1
90	ch 23	14.3 ± 0.5	1.3 ± 0.6	0.73	18 ± 2
90	ch 24	13.0 ± 0.6	1.4 ± 0.7	0.85	17 ± 2
90	ch 25	15.0 ± 0.7	2.6 ± 0.5	0.93	23 ± 2
90	ch 26	10.5 ± 0.3	1.0 ± 0.8	1.11	13 ± 3
90	ch 27	15.2 ± 0.4	1.5 ± 0.5	2.20	20 ± 2
90	ch 28	14.9 ± 0.3	1.2 ± 0.4	1.27	18 ± 1
90	ch 29	12.4 ± 0.3	1.3 ± 0.4	1.67	16 ± 1
90	ch 30	12.9 ± 0.4	1.0 ± 0.9	1.22	16 ± 3
90	ch 31	12.6 ± 0.4	1.2 ± 0.9	1.25	16 ± 3
90	ch 32	12.2 ± 0.5	1 ± 1	0.96	15 ± 4
90	ch 33	13.3 ± 0.5	1.1 ± 0.4	1.01	17 ± 1
90	ch 34	12.5 ± 0.4	1 ± 0.9	0.87	15 ± 3
90	ch 35	13.6 ± 0.6	1.8 ± 0.4	0.94	19 ± 1
90	ch 36	16.4 ± 0.5	1.7 ± 0.8	1.27	21 ± 2
90	ch 37	11.9 ± 0.3	1.0 ± 0.8	1.69	15 ± 3
90	ch 38	-	-	-	-
90	ch 39	14.6 ± 0.4	1.7 ± 0.5	1.88	20 ± 2

Table J.24: Energy reconstruction efficiency for Phase IIb run 91.

Run	Channel	μ [keV]	σ [keV]	χ^2/ndf	$\mu + 3\sigma$ [keV]
91	ch 0	14.7 ± 0.3	1.0 ± 0.2	1.45	17.7 ± 0.7
91	ch 1	12.3 ± 0.6	1.9 ± 0.8	1.23	18 ± 2
91	ch 2	11.1 ± 0.8	1.9 ± 0.6	1.06	17 ± 2
91	ch 3	13.2 ± 0.5	2.4 ± 0.2	1.39	20.4 ± 0.7
91	ch 4	13.4 ± 0.7	2.0 ± 0.9	2.23	19 ± 3
91	ch 5	-	-	-	-
91	ch 6	-	-	-	-
91	ch 7	-	-	-	-
91	ch 8	15.4 ± 0.3	1.8 ± 0.3	4.29	21 ± 1
91	ch 9	14.6 ± 0.3	1.0 ± 0.9	3.32	18 ± 3
91	ch 10	14.3 ± 0.3	1.5 ± 0.3	1.91	19 ± 1
91	ch 11	13.2 ± 0.5	1 ± 1	0.98	16 ± 4
91	ch 12	12.7 ± 0.3	1.0 ± 0.6	0.92	16 ± 2
91	ch 13	13.1 ± 0.5	1 ± 1	1.09	16 ± 3
91	ch 14	10.7 ± 0.3	1.0 ± 0.5	1.02	14 ± 2
91	ch 15	12.3 ± 0.7	1.4 ± 0.9	0.74	17 ± 3
91	ch 16	13.1 ± 0.9	2 ± 1	0.90	19 ± 3
91	ch 17	12 ± 1	2 ± 1	0.81	17 ± 5
91	ch 18	11.7 ± 0.5	1.4 ± 0.5	0.97	16 ± 2
91	ch 19	10.9 ± 0.6	2 ± 1	0.97	17 ± 4
91	ch 20	11.1 ± 0.5	1.3 ± 0.5	0.94	15 ± 2
91	ch 21	10.5 ± 0.4	1 ± 1	0.96	14 ± 4
91	ch 22	11.5 ± 0.3	1 ± 0.1	0.91	14.5 ± 0.5
91	ch 23	13 ± 1	3 ± 1	0.87	21 ± 4
91	ch 24	12.4 ± 0.8	2 ± 1	0.97	17 ± 3
91	ch 25	14.3 ± 0.9	3 ± 2	0.78	22 ± 5
91	ch 26	10.0 ± 0.3	1.2 ± 0.4	1.31	14 ± 1
91	ch 27	15.0 ± 0.3	1.2 ± 0.5	2.59	19 ± 2
91	ch 28	14.7 ± 0.3	1.5 ± 0.4	1.62	19 ± 1
91	ch 29	12.2 ± 0.3	1.0 ± 0.5	1.70	15 ± 1
91	ch 30	13.3 ± 0.3	1.0 ± 0.2	0.85	16.3 ± 0.6
91	ch 31	11.9 ± 0.5	1.4 ± 0.5	1.00	16 ± 2
91	ch 32	12.7 ± 0.3	1.0 ± 0.4	0.77	16 ± 1
91	ch 33	12.8 ± 0.5	1.3 ± 0.6	1.09	17 ± 2
91	ch 34	11.5 ± 0.4	1.0 ± 0.9	0.89	14 ± 3
91	ch 35	14.8 ± 0.5	1 ± 1	0.82	18 ± 4
91	ch 36	15.1 ± 0.7	1 ± 1	1.48	18 ± 4
91	ch 37	12.5 ± 0.3	1.5 ± 0.4	1.62	17 ± 1
91	ch 38	16.7 ± 0.4	1.6 ± 0.5	1.10	21 ± 1
91	ch 39	13.9 ± 0.4	1.1 ± 0.4	3.07	17 ± 1

Table J.25: Energy reconstruction efficiency for Phase IIb run 92.

Run	Channel	μ [keV]	σ [keV]	χ^2/ndf	$\mu + 3\sigma$ [keV]
92	ch 0	12.0 ± 0.9	3.1 ± 0.8	1.26	21 ± 3
92	ch 1	10.9 ± 0.7	1.9 ± 0.5	0.88	17 ± 2
92	ch 2	11.2 ± 0.6	1.4 ± 0.6	0.87	15 ± 2
92	ch 3	13.2 ± 0.4	1.2 ± 0.5	0.80	17 ± 2
92	ch 4	14.1 ± 0.7	2.2 ± 0.4	0.74	21 ± 1
92	ch 5	-	-	-	-
92	ch 6	-	-	-	-
92	ch 7	-	-	-	-
92	ch 8	15.6 ± 0.3	1.6 ± 0.4	3.88	20 ± 1
92	ch 9	14.9 ± 0.4	1.4 ± 0.6	1.29	19 ± 2
92	ch 10	13.9 ± 0.4	1.7 ± 0.5	1.81	19 ± 1
92	ch 11	12.9 ± 0.4	1.0 ± 0.6	0.95	16 ± 2
92	ch 12	13.0 ± 0.6	1.4 ± 0.6	1.11	17 ± 2
92	ch 13	13.3 ± 0.4	1.0 ± 0.4	0.90	16 ± 1
92	ch 14	11.4 ± 0.3	1.0 ± 0.2	0.89	14.4 ± 0.7
92	ch 15	13.2 ± 0.5	1.1 ± 0.5	1.03	16 ± 2
92	ch 16	12.6 ± 0.8	2 ± 1	0.82	17 ± 3
92	ch 17	13.1 ± 0.7	1.4 ± 0.7	0.85	17 ± 2
92	ch 18	11.3 ± 0.8	2.3 ± 0.6	1.13	18 ± 2
92	ch 19	11.6 ± 0.7	2.6 ± 0.8	0.86	19 ± 3
92	ch 20	12.6 ± 0.4	1 ± 1	0.70	16 ± 3
92	ch 21	10.8 ± 0.6	1.4 ± 0.6	0.98	15 ± 2
92	ch 22	12.0 ± 0.3	1.1 ± 0.5	0.82	15 ± 2
92	ch 23	14.7 ± 0.4	1.0 ± 0.9	0.74	18 ± 3
92	ch 24	13.0 ± 0.7	1.2 ± 0.8	0.83	16 ± 2
92	ch 25	14.4 ± 0.8	1 ± 1	0.73	19 ± 3
92	ch 26	10.4 ± 0.3	1.0 ± 0.3	0.84	13 ± 1
92	ch 27	15.2 ± 0.4	1.6 ± 0.6	2.45	20 ± 2
92	ch 28	14.6 ± 0.3	1.0 ± 0.4	2.86	18 ± 1
92	ch 29	12.1 ± 0.3	1.0 ± 0.5	1.44	15 ± 1
92	ch 30	12.9 ± 0.4	1.0 ± 0.8	1.18	16 ± 2
92	ch 31	12 ± 1	2.3 ± 0.4	0.87	19 ± 2
92	ch 32	12.4 ± 0.5	1.4 ± 0.6	0.83	17 ± 2
92	ch 33	14.7 ± 0.3	1.0 ± 0.5	1.14	18 ± 1
92	ch 34	12.0 ± 0.7	1.4 ± 0.7	0.80	16 ± 2
92	ch 35	13 ± 1	3 ± 1	0.80	21 ± 4
92	ch 36	16.9 ± 0.5	1.6 ± 0.6	1.23	22 ± 2
92	ch 37	11.4 ± 0.4	1.3 ± 0.4	2.56	15 ± 1
92	ch 38	-	-	-	-
92	ch 39	14.1 ± 0.6	1.6 ± 0.9	1.82	19 ± 3

Appendix K

Data Set Detector Configurations

Table K.1: Configuration and exposure information of dataset Phase Ia.

Channel	Name	Mass [kg]	Exposure [kg d]
ch 0	ANG1	0.958	71.2803
ch 1	ANG2	2.833	373.814
ch 2	ANG3	2.391	315.492
ch 3	ANG4	2.372	312.985
ch 4	ANG5	2.746	362.334
ch 5	RG1	2.11	278.414
ch 6	RG2	2.166	285.803
ch 7	RG3	2.087	81.9773
ch 8	GTF112	2.965	391.231
ch 9	GTF45	2.321	306.255
ch 10	GTF32	2.312	305.068

Table K.2: Configuration and exposure information of dataset Phase Ib.

Channel	Name	Mass [kg]	Exposure [kg d]
ch 0	ANG1	0.958	0
ch 1	ANG2	2.833	855.951
ch 2	ANG3	2.391	722.407
ch 3	ANG4	2.372	716.667
ch 4	ANG5	2.746	829.666
ch 5	RG1	2.11	637.507
ch 6	RG2	2.166	654.427
ch 7	RG3	2.087	0
ch 8	GTF112	2.965	895.833
ch 9	GD32B	0.716	199.531
ch 10	GD32C	0.743	224.487
ch 11	GD32D	0.72	207.546
ch 12	GD35B	0.81	244.73
ch 13	GD35C	0.634	0

Table K.3: Configuration and exposure information of dataset Phase IIb.

Channel	Name	Mass [kg]	Exposure [kg d]
ch 0	GD91A	0.627	102.068
ch 1	GD35B	0.81	131.859
ch 2	GD02B	0.625	101.743
ch 3	GD00B	0.697	113.464
ch 4	GD61A	0.731	118.998
ch 5	GD89B	0.62	0
ch 6	GD02D	0.662	0
ch 7	GD91C	0.627	0
ch 8	ANG5	2.746	447.017
ch 9	RG1	2.11	343.484
ch 10	ANG3	2.391	389.227
ch 11	GD02A	0.545	88.7197
ch 12	GD32B	0.716	116.557
ch 13	GD32A	0.458	60.1696
ch 14	GD32C	0.743	120.952
ch 15	GD89C	0.595	96.8591
ch 16	GD61C	0.634	103.208
ch 17	GD76B	0.384	62.5108
ch 18	GD00C	0.815	132.673
ch 19	GD35C	0.634	103.208
ch 20	GD76C	0.824	134.138
ch 21	GD89D	0.526	85.6267
ch 22	GD00D	0.813	132.347
ch 23	GD79C	0.812	132.184
ch 24	GD35A	0.768	125.022
ch 25	GD91B	0.65	105.812
ch 26	GD61B	0.751	122.254
ch 27	ANG2	2.833	461.18
ch 28	RG2	2.166	352.6
ch 29	ANG4	2.372	386.134
ch 30	GD00A	0.496	80.7431
ch 31	GD02C	0.788	128.277
ch 32	GD79B	0.736	75.7849
ch 33	GD91D	0.693	112.812
ch 34	GD32D	0.72	117.208
ch 35	GD89A	0.524	85.3011
ch 36	ANG1	0.958	155.951
ch 37	GTF112	2.965	482.668
ch 38	GTF32	2.312	95.3573
ch 39	GTF45	2.321	300.766

List of Figures

2.1	Mass parabola for A=76	11
2.2	The effective Majorana mass as function of the smallest neutrino mass . . .	13
3.1	The all-particle spectrum from air shower measurements [18]	18
3.2	Measured muon energy spectrum on ground	20
3.3	Measured neutron energy spectrum on ground	20
3.4	Angular distribution for high-energy neutrons on ground	20
3.5	Vertical muon intensity vs depth [18]	21
3.6	Differential muon intensity	24
3.7	Average muon energy spectrum	24
3.8	Muon energy spectrum	24
4.1	Illustration of the backscattering effect investigation	31
4.2	Backscattered neutrons	32
4.3	Neutron energy spectrum at different depths for steel	33
4.4	Neutron energy spectrum for different materials	34
4.5	Neutron energy spectrum for different angular distributions	35
4.6	Neutron flux at different shielding depths (in m) for different materials . .	36
4.7	Neutron flux at different shielding depths in mwe	36
4.8	Neutron flux for lead with different energy cuts	38
4.9	Muon energy spectrum at different depths	40
4.10	Comparison of the μ^- and μ^+ energy spectrum	40
4.11	Muon energy spectra for different materials	41
4.12	Muon flux at different shielding depth for LNGS rock	42
4.13	Muon-induced neutron energy spectrum at different depths	43
4.14	Energy spectra of μ^- -induced and μ^+ -induced neutrons	44
4.15	Muon-induced neutron energy spectrum at 2 m for different materials . . .	44
4.16	Muon-induced neutron flux at different shielding depths	45
4.17	Muon-induced neutron flux at different depths of light shielding materials .	45
4.18	Total muon-induced neutron flux	48
4.19	Neutron energy spectra comparison	48
4.20	Total neutron flux at different shielding depths	50

4.21	Comparison of the total neutron flux for different materials	51
4.22	Comparison of the total neutron flux for $E \geq 20$ MeV	51
5.1	Sketch of the MINIDEX concept	54
5.2	The MINIDEX setup	54
5.3	Sketch of the Tübingen Shallow Underground Laboratory	57
5.4	Muon energy spectra at different laboratory planes	58
5.5	Nadir angle θ distributions of μ^- at different laboratory plans	59
5.6	Azimuth angle φ distributions of muons at different laboratory planes . . .	60
5.7	Sketch of the Tübingen Shallow Underground Laboratory overburden . . .	60
5.8	Illustration of the interception investigation	61
5.9	Location of the μ^- entry points at different laboratory planes	64
5.10	Energy spectrum of μ^- entering the laboratory from different sides	64
5.11	Energy spectrum of muon-induced neutrons at the ceiling	65
5.12	Azimuth angle distributions of μ^- and μ^- -induced neutrons	66
5.13	Nadir angle distribution of of μ^- and μ^- -induced neutrons	67
5.14	Nadir angle θ vs. azimuth angle φ	68
5.15	Measured and simulated muon flux map of the Tübingen laboratory	69
6.1	Schematic sketch of a coaxial and BEGe detector [79]	72
6.2	Sketch of the GERDA experiment [83]	73
6.3	Candidate pulse traces taken from BEGe data [86]	76
6.4	Examples of a single-site and multi-site event [6]	76
6.5	GERDA energy spectrum of Phase I and Phase II	80
7.1	Decay of ^{77}Ge	85
7.2	Decay of ^{75}Ge	86
7.3	Decay of ^{41}Ar	86
7.4	Cross-section ratios of neutron capture on ^{76}Ge and ^{74}Ge	87
7.5	ENDF/B-VII cross sections	88
7.6	Neutron energy spectrum around the detector array	92
7.7	Simulated germanium neutron capture time distributions.	92
7.8	Total energy deposition E_{tot}	93
7.9	Total neutron capture detection efficiencies	94
7.10	Energy depositions distributions due to ^{77m}Ge and ^{77}Ge β^- decay	94
7.11	Vertex distribution of fully detected 1293.6 keV gammas	95
8.1	Energy reconstruction efficiency distribution	101
8.2	Maximum energies for different channels and datasets	102
8.3	Saturation cut efficiencies depending on the saturation energy	103
8.4	Time difference between the muon veto and germanium detector signal . .	104

8.5	Time shifts of the muon veto signal between different DAQ's	105
8.6	Time difference to the muon veto signal for background events	106
8.7	Background counts per bin width for fixed E_{cut}	107
8.8	Background counts per bin width for Phase II	108
8.9	Background rate comparison for Phase II	109
8.10	Expected number of signal and background events	113
8.11	Priors and posteriors of all parameters of the $^{75(m)}\text{Ge}$ production rate fit . .	115
8.12	Priors and posteriors of all parameters of the $^{77(m)}\text{Ge}$ production rate fit . .	116
8.13	Neutron energy spectra comparison	118

List of Tables

2.1	Half-lives of the $2\nu\beta\beta$ decay for different isotopes	12
2.2	Isotopes undergoing $2\nu\beta\beta$ decay	14
2.3	Limits on the half-lives of the $0\nu\beta\beta$ decay and $m_{\beta\beta}$	15
3.1	Muon-induced isotope production and background index estimated by [3] .	28
4.1	Properties of different materials	30
4.2	Results of the backscattering-effect analysis	32
4.3	Depths at which the the equilibrium has been reached	34
4.4	Depths at which there are less neutrons than arriving neutrons	37
4.5	Depths at which the neutron flux is highest	38
4.6	Shielding index s [1/m] for different angular distributions	39
4.7	Muon shielding index s for different materials in [1/m] and [1/mwe]	41
4.8	Muon-induced neutron attenuation index and d_{max}	46
4.9	Neutron flux equality (Nesterenok)	49
5.1	Number of muon entry points belonging to different planes	62
5.2	Particle fluxes at different laboratory planes	63
7.1	Full IT energy deposition detection efficiencies	95
7.2	Argon gamma detection efficiencies	96
8.1	Used datasets	100
8.2	Efficiency from saturation	103
8.3	Efficiencies for different datasets	111
A.1	Used models for μ^+	125
A.2	Used models for μ^-	125
A.3	Used hadronic models for neutrons	126
A.4	Used neutron cross sections	126
B.1	Composition of concrete	127
B.2	Composition of LNGS rock [99].	127
B.3	Some materials included in soil and their compositions.	128

B.4	Composition of Soil	128
B.5	Composition of stainless steel.	128
C.1	Number of simulated neutrons for simulations with step-size 0.1 m	129
C.2	Number of simulated neutrons for simulations with step-size 1 m	130
D.1	Shielding index s [1/m] for vertically downwards going neutrons	131
D.2	Shielding index s [1/m] for the Nesterenok neutron distribution	131
D.3	Shielding index s [1/m] for isotropic distributed neutrons	132
D.4	Shielding index s [1/mwe] for vertically downwards going neutrons	132
D.5	Shielding index s [1/mwe] for the Nesterenok neutron distribution	133
D.6	Shielding index s [1/mwe] for isotropic distributed neutrons	133
E.1	Depths with the highest muon-induced neutron flux for different E_{cut}	135
E.2	Depths with the highest muon-induced neutron flux for different E_{cut}	136
F.1	Attenuation index of muon-induced neutrons in [1/m] for different E_{cut}	137
F.2	Attenuation index of muon-induced neutrons in [1/mwe] for different E_{cut}	138
G.1	Neutron flux equality (vertically downwards going neutrons)	140
G.2	Neutron flux equality (isotropic distribution)	141
H.1	Total ^{77}Ge neutron capture detection efficiency for coaxial detectors	143
H.2	Total ^{77}Ge neutron capture detection efficiency for BEGe detectors	144
H.3	Total ^{75}Ge neutron capture detection efficiency for coaxial detectors	145
H.4	Total ^{75}Ge neutron capture detection efficiency for BEGe detectors	146
H.5	Total neutron capture detection efficiencies	147
J.1	Energy reconstruction efficiency for Phase Ia run 26	153
J.2	Energy reconstruction efficiency for Phase Ia run 27	154
J.3	Energy reconstruction efficiency for Phase Ia run 28	154
J.4	Energy reconstruction efficiency for Phase Ia run 29	155
J.5	Energy reconstruction efficiency for Phase Ia run 30	155
J.6	Energy reconstruction efficiency for Phase Ia run 32	156
J.7	Energy reconstruction efficiency for Phase Ib run 35	156
J.8	Energy reconstruction efficiency for Phase Ib run 36	157
J.9	Energy reconstruction efficiency for Phase Ib run 37	157
J.10	Energy reconstruction efficiency for Phase Ib run 38	158
J.11	Energy reconstruction efficiency for Phase Ib run 39	158
J.12	Energy reconstruction efficiency for Phase Ib run 40	159
J.13	Energy reconstruction efficiency for Phase Ib run 41	159
J.14	Energy reconstruction efficiency for Phase Ib run 42	160
J.15	Energy reconstruction efficiency for Phase Ib run 43	160

J.16	Energy reconstruction efficiency for Phase Ib run 44	161
J.17	Energy reconstruction efficiency for Phase Ib run 45	161
J.18	Energy reconstruction efficiency for Phase Ib run 46	162
J.19	Energy reconstruction efficiency for Phase IIa run 53	163
J.20	Energy reconstruction efficiency for Phase IIb run 87	164
J.21	Energy reconstruction efficiency for Phase IIb run 88	165
J.22	Energy reconstruction efficiency for Phase IIb run 89	166
J.23	Energy reconstruction efficiency for Phase IIb run 90	167
J.24	Energy reconstruction efficiency for Phase IIb run 91	168
J.25	Energy reconstruction efficiency for Phase IIb run 92	169
K.1	Configuration and exposure information of dataset Phase Ia.	171
K.2	Configuration and exposure information of dataset Phase Ib.	172
K.3	Configuration and exposure information of dataset Phase IIb.	173

Bibliography

- [1] Ettore Majorana. Teoria simmetrica dell'elettrone e del positrone. *Nuovo Cim.*, 14:171–184, 1937.
- [2] J. Schechter and J. W. F. Valle. Neutrinoless Double beta Decay in SU(2) x U(1) Theories. *Phys. Rev.*, D25:2951, 1982.
- [3] L. Pandola et al. Monte Carlo evaluation of the muon-induced background in the GERDA double beta decay experiment. *Nucl. Instrum. Meth.*, A570:149–158, 2007.
- [4] C. Wiesinger, L. Pandola, and S. Schönert. Virtual depth by active background suppression: Revisiting the cosmic muon induced background of GERDA Phase II. *arXiv*, 1802.05040 [hep-ex], February 2018.
- [5] I. Abt et al. The Muon-Induced Neutron Indirect Detection EXperiment, MINIDEX. *Astropart. Phys.*, 90:1–13, 2017.
- [6] M. Agostini et al. Production, characterization and operation of ^{76}Ge enriched BEGe detectors in GERDA. *Eur. Phys. J.*, C75(2):39, 2015.
- [7] C. L. Cowan, F. Reines, F. B. Harrison, H. W. Kruse, and A. D. McGuire. Detection of the Free Neutrino: a Confirmation. *Science*, Volume 124:103–104, 1956.
- [8] G. Danby, J. M. Gaillard, Konstantin A. Goulianos, L. M. Lederman, Nari B. Mistry, M. Schwartz, and J. Steinberger. Observation of High-Energy Neutrino Reactions and the Existence of Two Kinds of Neutrinos. *Phys. Rev. Lett.*, 9:36–44, 1962.
- [9] Martin L. Perl et al. Evidence for Anomalous Lepton Production in $e^+ - e^-$ Annihilation. *Phys. Rev. Lett.*, 35:1489–1492, 1975.
- [10] K. Kodama et al. Observation of tau neutrino interactions. *Phys. Lett.*, B504:218–224, 2001.
- [11] Ch. Kraus et al. Final results from phase II of the Mainz neutrino mass search in tritium beta decay. *Eur. Phys. J.*, C40:447–468, 2005.
- [12] V. N. Aseev et al. An upper limit on electron antineutrino mass from Troitsk experiment. *Phys. Rev.*, D84:112003, 2011.

-
- [13] Raymond Davis, Jr., Don S. Harmer, and Kenneth C. Hoffman. Search for neutrinos from the sun. *Phys. Rev. Lett.*, 20:1205–1209, 1968.
- [14] B. T. Cleveland, Timothy Daily, Raymond Davis, Jr., James R. Distel, Kenneth Lande, C. K. Lee, Paul S. Wildenhain, and Jack Ullman. Measurement of the solar electron neutrino flux with the Homestake chlorine detector. *Astrophys. J.*, 496:505–526, 1998.
- [15] Q. R. Ahmad et al. Direct evidence for neutrino flavor transformation from neutral current interactions in the Sudbury Neutrino Observatory. *Phys. Rev. Lett.*, 89:011301, 2002.
- [16] B. Pontecorvo. Inverse beta processes and nonconservation of lepton charge. *Sov. Phys. JETP*, 7:172–173, 1958. [Zh. Eksp. Teor. Fiz.34,247(1957)].
- [17] Ziro Maki, Masami Nakagawa, and Shoichi Sakata. Remarks on the unified model of elementary particles. *Prog. Theor. Phys.*, 28:870–880, 1962.
- [18] C. Patrignani et al. Review of Particle Physics. *Chin. Phys.*, C40(10):100001, 2016.
- [19] Paul A. M. Dirac. The quantum theory of the electron. *Proc. Roy. Soc. Lond.*, A117:610–624, 1928.
- [20] S. M. Bilenky. Neutrinoless double beta-decay. *Phys. Part. Nucl.*, 41:690–715, 2010.
- [21] M. Fukugita and T. Yanagida. Baryogenesis Without Grand Unification. *Phys. Lett.*, B174:45–47, 1986.
- [22] W. H. Furry. On transition probabilities in double beta-disintegration. *Phys. Rev.*, 56:1184–1193, 1939.
- [23] M. Goeppert-Mayer. Double Beta-Disintegration. *Phys. Rev.*, 48:512–516, 1935.
- [24] M. G. Inghram and J. H. Reynolds. Double beta-decay of Te-130. *Phys. Rev.*, 78:822–823, 1950.
- [25] A. S. Barabash. Double beta decay: Present status. *Phys. Atom. Nucl.*, 73:162–178, 2010.
- [26] R. Arnold et al. Measurement of the double-beta decay half-life and search for the neutrinoless double-beta decay of ^{48}Ca with the NEMO-3 detector. *Phys. Rev.*, D93(11):112008, 2016.
- [27] M. Agostini et al. Measurement of the half-life of the two-neutrino double beta decay of ^{76}Ge with the GERDA experiment. *J. Phys.*, G40:035110, 2013.

- [28] R. Arnold et al. First results of the search of neutrinoless double beta decay with the NEMO 3 detector. *Phys. Rev. Lett.*, 95:182302, 2005.
- [29] J. Argyriades et al. Measurement of the two neutrino double beta decay half-life of Zr-96 with the NEMO-3 detector. *Nucl. Phys.*, A847:168–179, 2010.
- [30] R. Arnold et al. Measurement of the $2\nu\beta\beta$ Decay Half-Life and Search for the $0\nu\beta\beta$ Decay of ^{116}Cd with the NEMO-3 Detector. *Phys. Rev.*, D95(1):012007, 2017.
- [31] C. Alduino et al. Measurement of the two-neutrino double-beta decay half-life of ^{130}Te with the CUORE-0 experiment. *Eur. Phys. J.*, C77(1):13, 2017.
- [32] J. B. Albert et al. Improved measurement of the $2\nu\beta\beta$ half-life of ^{136}Xe with the EXO-200 detector. *Phys. Rev.*, C89(1):015502, 2014.
- [33] R. Arnold et al. Measurement of the $2\nu\beta\beta$ decay half-life of ^{150}Nd and a search for $0\nu\beta\beta$ decay processes with the full exposure from the NEMO-3 detector. *Phys. Rev.*, D94(7):072003, 2016.
- [34] F. Capozzi, E. Lisi, A. Marrone, D. Montanino, and A. Palazzo. Neutrino masses and mixings: Status of known and unknown 3ν parameters. *Nucl. Phys.*, B908:218–234, 2016.
- [35] S.Y.F. Chu, L.P. Ekström, and R.B. Firestone. WWW Table of Radioactive Isotopes, database version 1999-02-28 from URL <http://nucldata.nuclear.lu.se/nucldata/toi/>.
- [36] A. A. Kwiatkowski et al. New determination of double- β -decay properties in ^{48}Ca : High-precision $Q_{\beta\beta}$ -value measurement and improved nuclear matrix element calculations. *Phys. Rev.*, C89(4):045502, 2014.
- [37] G. Douysset, T. Fritioff, C. Carlberg, I. Bergstrom, and M. Bjorkhage. Determination of the Ge-76 double beta decay Q value. *Phys. Rev. Lett.*, 86:4259–4262, 2001.
- [38] David L. Lincoln et al. First direct double- β decay Q -Value measurement of ^{82}Se in support of understanding the nature of the Neutrino. *Phys. Rev. Lett.*, 110(1):012501, 2013.
- [39] K. Gulyuz et al. Determination of the direct double- β -decay Q value of Zr96 and atomic masses of Zr90–92,94,96 and Mo92,94–98,100. *Phys. Rev.*, C91(5):055501, 2015.
- [40] S. Rahaman et al. Q value of the Mo-100 Double-Beta Decay. *Phys. Lett.*, B662:111–116, 2008.

-
- [41] S. Rahaman et al. Double-beta decay Q values of ^{116}Cd and ^{130}Te . *Phys. Lett.*, B703:412–416, 2011.
- [42] M. Redshaw, E. Wingfield, J. McDaniel, and E. G. Myers. Mass and double-beta-decay Q value of Xe-136. *Phys. Rev. Lett.*, 98:053003, 2007.
- [43] V. S. Kolhinen et al. Double-beta decay Q value of Nd-150. *Phys. Rev.*, C82:022501, 2010.
- [44] O. Cremonesi and M. Pavan. Challenges in Double Beta Decay. *Adv. High Energy Phys.*, 2014:951432, 2014.
- [45] M. Auger et al. Search for Neutrinoless Double-Beta Decay in ^{136}Xe with EXO-200. *Phys. Rev. Lett.*, 109:032505, 2012.
- [46] M. Agostini et al. Background free search for neutrinoless double beta decay with GERDA Phase II. *Nature*, Volume 544:5–132, 2017.
- [47] K. Alfonso et al. Search for Neutrinoless Double-Beta Decay of ^{130}Te with CUORE-0. *Phys. Rev. Lett.*, 115(10):102502, 2015.
- [48] A. Gando et al. Limit on Neutrinoless $\beta\beta$ Decay of ^{136}Xe from the First Phase of KamLAND-Zen and Comparison with the Positive Claim in ^{76}Ge . *Phys. Rev. Lett.*, 110(6):062502, 2013.
- [49] Laura Segui. The SNO+ Project. *Nucl. Part. Phys. Proc.*, 273-275:2654–2656, 2016.
- [50] S. Umehara et al. Neutrino-less double- β decay of ^{48}Ca studied by $\text{CaF}_2(\text{Eu})$ scintillators. *Phys. Rev.*, C78:058501, 2008.
- [51] R. Arnold et al. Results of the search for neutrinoless double- β decay in ^{100}Mo with the NEMO-3 experiment. *Phys. Rev.*, D92(7):072011, 2015.
- [52] H. V. Klapdor-Kleingrothaus and I. V. Krivosheina. The evidence for the observation of $0\nu\beta\beta$ decay: The identification of $0\nu\beta\beta$ events from the full spectra. *Mod. Phys. Lett.*, A21:1547–1566, 2006.
- [53] M. Agostini et al. Results on Neutrinoless Double- β Decay of ^{76}Ge from Phase I of the GERDA Experiment. *Phys. Rev. Lett.*, 111(12):122503, 2013.
- [54] Pasquale Blasi. The Origin of Galactic Cosmic Rays. *Astron. Astrophys. Rev.*, 21:70, 2013.
- [55] Etienne Parizot. Cosmic Ray Origin: Lessons from Ultra-High-Energy Cosmic Rays and the Galactic/Extragalactic Transition. *Nucl. Phys. Proc. Suppl.*, 256-257:197–212, 2014.

- [56] W. R. Frazer, C. H. Poon, D. Silverman, and H. J. Yesian. Limiting fragmentation and the charge ratio of cosmic ray muons. *Phys. Rev.*, D5:1653–1657, 1972.
- [57] G. Heusser. Low-radioactivity background techniques. *Ann. Rev. Nucl. Part. Sci.*, 45:543–590, 1995.
- [58] B. C. Rastin. AN ACCURATE MEASUREMENT OF THE SEA LEVEL MUON SPECTRUM WITHIN THE RANGE 4-GEV/C TO 3000-GEV/C. *J. Phys.*, G10:1609–1628, 1984.
- [59] Matteo Duranti. *Measurement of the Atmospheric Muon Flux on Ground with the AMS-02 Detector*. PhD thesis, INFN, Perugia, 2012.
- [60] M. S. Gordon et al. Measurement of the Flux and Energy Spectrum of Cosmic-Ray Induced Neutrons on the Ground. *IEEE Trans. Nucl. Sci.*, 51:3427–3434, 2004.
- [61] Aleksandr Nesterenok. Numerical calculations of cosmic ray cascade in the Earth’s atmosphere: Results for nucleon spectra. *Nucl. Instrum. Meth.*, B295:99–106, 2013.
- [62] C. Adloff et al. The time structure of hadronic showers in highly granular calorimeters with tungsten and steel absorbers. *JINST*, 9:P07022, 2014.
- [63] A. S. Malgin. Phenomenology of muon-induced neutron yield. *Phys. Rev.*, C96(1):014605, 2017.
- [64] H. M. Araújo, V. A. Kudryavtsev, N. J. C. Spooner, and T. J. Sumner. Muon-induced neutron production and detection with GEANT4 and FLUKA. *Nucl. Instrum. Meth.*, A545:398–411, 2005.
- [65] L. Reichhart et al. Measurement and simulation of the muon-induced neutron yield in lead. *Astropart. Phys.*, 47:67–76, 2013.
- [66] Aaron Michel. Investigation of cosmic ray shielding properties of different materials at shallow depths. Diploma thesis, Technische Universität München, 2012.
- [67] Dongming Mei and A. Hime. Muon-induced background study for underground laboratories. *Phys. Rev.*, D73:053004, 2006.
- [68] D. F. Measday. The nuclear physics of muon capture. *Phys. Rept.*, 354:243–409, 2001.
- [69] I. Barabanov, S. Belogurov, Leonid B. Bezrukov, A. Denisov, V. Kornoukhov, and N. Sobolevsky. Cosmogenic activation of germanium and its reduction for low background experiments. *Nucl. Instrum. Meth.*, B251:115–120, 2006.
- [70] A. Best et al. Low energy neutron background in deep underground laboratories. *Nucl. Instrum. Meth.*, A812:1–6, 2016.

-
- [71] R. Lemrani, M. Robinson, V. A. Kudryavtsev, M. De Jesus, G. Gerbier, and N. J. C. Spooner. Low-energy neutron propagation in MCNPX and GEANT4. *Nucl. Instrum. Meth.*, A560:454–459, 2006.
- [72] S. Agostinelli et al. GEANT4: A Simulation toolkit. *Nucl. Instrum. Meth.*, A506:250–303, 2003.
- [73] Melissa Boswell et al. MaGe-a Geant4-based Monte Carlo Application Framework for Low-background Germanium Experiments. *IEEE Trans. Nucl. Sci.*, 58:1212–1220, 2011.
- [74] M. B. Chadwick et al. ENDF/B-VII.1 Nuclear Data for Science and Technology: Cross Sections, Covariances, Fission Product Yields and Decay Data. *Nucl. Data Sheets*, 112(12):2887–2996, 2011.
- [75] Matteo Palermo. *The Muon-Induced Neutron Indirect-Detection EXperiment: MINIDEX*. PhD thesis, LMU Munich (main), 2016.
- [76] Alexander Hegai. Gammaspektroskopie mit Germaniumdetektoren. Diploma thesis, Universität Tübingen, 2010.
- [77] Qing He and Kirk McDonald. Muon Rate in the MicroBooNE TPC. 2009.
- [78] K. H. Ackermann et al. The GERDA experiment for the search of $0\nu\beta\beta$ decay in ^{76}Ge . *Eur. Phys. J.*, C73(3):2330, 2013.
- [79] M. Agostini et al. The background in the $0\nu\beta\beta$ experiment GERDA. *Eur. Phys. J.*, C74(4):2764, 2014.
- [80] M. Günther et al. Heidelberg - Moscow $\beta\text{-}\beta$ experiment with ^{76}Ge : Full setup with five detectors. *Phys. Rev.*, D55:54–67, 1997.
- [81] C. E. Aalseth et al. The IGEX ^{76}Ge neutrinoless double-beta decay experiment: Prospects for next generation experiments. *Phys. Rev.*, D65:092007, 2002.
- [82] H. V. Klapdor-Kleingrothaus, L. Baudis, A. Dietz, G. Heusser, B. Majorovits, and H. Strecker. GENIUS-TF: A Test facility for the GENIUS project. *Nucl. Instrum. Meth.*, A481:149–159, 2002.
- [83] M. Agostini et al. Flux Modulations seen by the Muon Veto of the GERDA Experiment. *Astropart. Phys.*, 84:29–35, 2016.
- [84] M. Ambrosio et al. Measurement of the residual energy of muons in the Gran Sasso underground laboratories. *Astropart. Phys.*, 19:313–328, 2003.
- [85] M. Ambrosio et al. Vertical muon intensity measured with MACRO at the Gran Sasso Laboratory. *Phys. Rev.*, D52:3793–3802, 1995.

- [86] M. Agostini et al. Pulse shape discrimination for GERDA Phase I data. *Eur. Phys. J.*, C73(10):2583, 2013.
- [87] M. Agostini et al. Results on $\beta\beta$ decay with emission of two neutrinos or Majorons in ^{76}Ge from GERDA Phase I. *Eur. Phys. J.*, C75(9):416, 2015.
- [88] Allen Caldwell, Daniel Kollar, and Kevin Kröninger. BAT: The Bayesian Analysis Toolkit. *Comput. Phys. Commun.*, 180:2197–2209, 2009.
- [89] M. Agostini et al. Searching for neutrinoless double beta decay with GERDA. In *15th International Conference on Topics in Astroparticle and Underground Physics (TAUP 2017) Sudbury, Ontario, Canada, July 24-28, 2017*, 2017.
- [90] M. Knapp et al. The GERDA muon veto Cherenkov detector. *Nucl. Instrum. Meth.*, A610:280–282, 2009.
- [91] N. Abgrall et al. The Large Enriched Germanium Experiment for Neutrinoless Double Beta Decay (LEGEND). *AIP Conf. Proc.*, 1894(1):020027, 2017.
- [92] K. T. Lesko. The Sanford underground research facility at Homestake. *Eur. Phys. J. Plus*, 127:107, 2012.
- [93] G. Meierhofer et al. Thermal neutron capture cross-section of Ge-76. *Eur. Phys. J.*, A40:61–64, 2009.
- [94] Megha Bhike, B. Fallin, Krishichayan, and W. Tornow. Measurement of the neutron-capture cross section of ^{76}Ge and ^{74}Ge below 15 MeV and its relevance to $0\nu\beta\beta$ decay searches of ^{76}Ge . *Phys. Lett.*, B741:150–154, 2015.
- [95] Evaluated nuclear data file. <https://www-nds.iaea.org/exfor/endl.htm>. Accessed: 2017-12-15.
- [96] M. Agostini, L. Pandola, P. Zavarise, and O. Volynets. GELATIO: A General framework for modular digital analysis of high-purity Ge detector signals. *JINST*, 6:P08013, 2011.
- [97] A. J. Zsigmond. Neutrino 2018. <https://doi.org/10.5281/zenodo.1287604>.
- [98] P. Belli et al. Deep Underground Neutron Flux Measurement With Large Bf-3 Counters. *Nuovo Cim.*, A101:959–966, 1989.
- [99] H. Wulandari, J. Jochum, W. Rau, and F. von Feilitzsch. Neutron flux underground revisited. *Astropart. Phys.*, 22:313–322, 2004.

List of Publications

With peer review

1. The Muon-Induced Neutron Indirect Detection EXperiment, MINIDEX, I. Abt et al., *Astropart.Phys.* 90 (2017) 1-13, doi:10.1016/j.astropartphys.2017.01.011

Without peer review

1. Neutron Shielding Simulations and Muon-induced Neutrons, L. Vanhoefer et al., 16th International Workshop on Neutrino Telescopes (Neutel 2015), *Proceedings of Science NEUTEL2015(2015)085*
2. Neutron Shielding Simulations and Muon-induced Neutrons, L. Vanhoefer et al., Magellan Workshop (DESY-PROC-2016-05), doi:10.3204/DESY-PROC-2016-05/41

As part of the GERDA collaboration, I am also co-author of GERDA publications. A complete list can be found at the High-Energy Physics Literature Database (INSPIRE-HEP).

Acknowledgements

I would like to thank

- Priv.-Doz. Dr. Béla Majorovits for supervising this thesis and the other members of my Advisory Panel Prof. Dr. Lothar Oberauer and Dr. Oliver Kortner,
- all members of the GERDA collaboration, especially Luciano Pandola, Janina Hakemüller, Christoph Wiesinger and Ann-Kathrin Schütz for fruitful discussions,
- current and former members of the GERDA/GeDet group at the MPP, especially Dimitris Palioselitis, Oliver Schulz and Anna Julia Zsigmond for the discussions about my GERDA analysis,
- Mikko Meyer, Stefan Dahmke and Benjamin Büttner for reading the thesis and their comments,
- my family and Mikko for the great support during the last years.